CALIXARENES, CAVITANDS, AND ORGANIC CAGES UTILIZED TO CONSTRUCT POLYMER NETWORKS WITH VARIED POROSITIES

A Dissertation

by

JEREMY AARON WILLMAN

Submitted to the Office of Graduate and Professional Studies of
Texas A&M University
in partial fulfillment of the requirements for the degree of

DOCTOR OF PHILOSOPHY

Chair of Committee,	Hongcai Zhou
Committee Members,	Lei Fang
	Svetlana Sukhishvili
	Matthew Sheldon
Head of Department,	Simon North

December 2020

Major Subject: Chemistry

ABSTRACT

Calixarenes are a class of "cup-shaped" macrocyclic molecules which are notable for their modularity which permits the synthesis of many derivatives and their ability to bind small molecules which allows for their use in a range of applications such as sensing, catalysis, supramolecular assembly, host-guest chemistry, and separations. Several classes of these macrocyclic molecules were utilized to construct Porous Polymer Networks (PPNs), based on the hypothesis that the monomers' structures would modify the porosity of the resulting sorbents.

One series of phenol-aldehyde PPNs was constructed with "pre-structured" calixarene monomers and systematically compared to chemically similar "unstructured" porous Novalac resins. The pre-structured calixarene-derived polymers were found to be more microporous than their unstructured Novalac resin counterparts. Additional differences were observed between the PPNs pairs in morphology, dependence on linking aldehyde equivalents, zeta potentials, dye affinities, and resistance to chemical fouling.

Another series of PPNs derived from rigid bridged-calixarene cavitands were compared to flexible calixarene-derived polymers. The porosity of cavitand polymers were found to differ greatly from their flexible calixarene pairs, exhibiting a regular decrease in porosity with the length of the monomers' alkyl "feet" groups. The observations indicate that porosity of these PPNs was predominately defined by the rigid macrocyclic region of the cavitand while the attached functional groups occupied pore

volume. The cavitand bridging groups are suspected to labilize during the thermoset synthesis, acting as templates to the polymer network structures.

Finally, polymers were constructed from calixarenes that were pre-assembled into molecular capsules or “organic cages.” It was hypothesized that the polymers derived from organic cages would have porosities modified by the monomers’ molecular pores. While polymers were successfully derived from the organic cages through several different approaches, the products were found to be nonporous. The utilized organic cages may be unsuitable monomers for porous network formation due to steric considerations, and larger cages may have been more successful in this approach.

While this work focused on exploring synthesis and porosity PPNs constructed from calixarenes, their potential for easy modification and functionalization should allow for the targeted application of these materials with further investigation.

DEDICATION

This work is dedicated to entropy: the constant tendency towards randomness that contrasts the small pockets of order within the universe.

ACKNOWLEDGEMENTS

I would like to acknowledge and thank my committee chair, Dr. Hongcai Zhou, for giving me the opportunity to study at Texas A&M and pursue research in chemistry. I would also like to thank my committee members, Dr. Lei Fang, Dr. Svetlana Sukhishvili, and Dr. Matthew Sheldon, for their constructive insights and guidance through my oral exams.

I would like to thank my undergraduate research advisor Professor Fernando Uribe-Romo of the University of Central Florida's Department of Chemistry, who taught me much of what I know about chemistry research and giving presentations. I would also like to thank Dr. Yuen Lau and Dr. Jesus Cordova who were great mentors to me while they were postdoctoral researchers the University of Central Florida.

I would like to thank my TAMU research group members particularly, Hannah Drake, Dr. Kecheng "Kevin" Wang, and Dr. Zachary Perry, for their advice, stimulating discussions about chemistry and other topics, and for being my friends. I would like to thank Dr. Qiang Zhang for being a mentor and helping me get started in the Zhou group.

I would like to thank my friends, Chase Pectol, Christopher DeLaney, Dr. David Parobek, Dr. Adam Kabza, Dr. Drew Harding, and Richard Carranza for making my time at TAMU bearable. Without their conversation and company, surviving this program would have been immeasurably more tedious.

I would like to thank all the excellent chemistry teachers, lecturers, and professors I have been instructed by throughout my education; Dr. Fred White, Dr.

Donovan Dixon, Dr. Seth Elsheimer, Dr. Andres Campiglia, Dr. Fernando Uribe-Romo, Dr. Shengli Zou, Dr. Christian A. Clausen III, Dr. Matthew Rex, Dr. Mohammed Daoudi, Dr. David Richardson, Dr. Lei Feng, Dr. Svetlana Sukhishvili, Dr. Abraham Clearfield, and any others I neglected.

I would like to thank my grandfather Robert Obeid, who was a chemist and pharmacist for being inspirational to my early interest in chemistry.

Finally, I would also like to thank my brothers, Daniel, Gabriel, Michael, Joel, Johnathan, and Matthew Willman, for being model men whom I am proud to be numbered among.

CONTRIBUTORS AND FUNDING SOURCES

Contributors

This work was supervised by a dissertation committee consisting of Professor Hongcai Zhou (chair) and Professors Lei Fang and Matthew Sheldon of the Department of Chemistry and Professor Svetlana Sukhishvili of the Department of Materials Science and Engineering.

Dr. Vladimir Bakhmoutov collected and assisted in the analysis of the ssNMR spectra in Chapters II-IV. SEM micrographs were collected by Jialluo Li and Tianhao Yan. Hannah Drake assisted in collecting several BET gas isotherms, and Hannah Drake and Peiyu Cai for collected TGA measurements. Fan Chen collected zeta potential measurements.

Dr. Phuc Truong for collected M-DSC data and Dr. Bryan Tomlin for performed FNAA oxygen analyses.

All other work conducted for the dissertation was completed by the student independently.

Funding Sources

This graduate study was supported by teaching assistantship from Texas A&M University.

This work was also made possible by partial support from the Robert A. Welch Foundation endowed chair to HJZ A-0030. The author also received partial support from the U.S. Department of Energy's National Energy Technology Laboratory (DOE NETL) through award DE-FE0026472 and through the Penn State University Coalition for

Fossil Energy Research (UCFER) under award DE-FE0026825 subaward 5958-TAMU-DOE-6825. Its contents are solely the responsibility of the authors and do not necessarily represent the official views of the U.S. Department of Energy.

NOMENCLATURE

BET	Brunauer-Emmett-Teller (method/theory/adsorption)
IUPAC	International Union of Pure and Applied Chemistry
PSD	Pore Size Distributions
BJH	Barrett-Joyner-Halenda (algorithm)
NLDFT	Non-local Density Functional Theory (algorithm)
S_a	Surface Area
S_{BET}	BET Surface Area
PPN	Porous Polymer Network
AC	Activated Carbon
GO	Graphitic Oxide
OC	Organic Cage
PIM	Polymer of Intrinsic Microporosity
PAF	Porous Aromatic Framework
POP	Porous Organic Polymer
COP	Covalent Organic Polymer
HCP	Hyper-Crosslinked Polymer
COF	Covalent Organic Framework
MOF	Metal Organic Framework
C-PPN	Calixarene - Porous Polymer Network
C-PPN-n	n eqv. terephthalaldehyde C-PPN

N-PPN	Novolac resin - Porous Polymer Network
N-PPN-n	n eqv. terephthalaldehyde N-PPN-n
B-PPN	Bridged cavitand - Porous Polymer Network
OC-PPN	Organic Cage - Porous Polymer Network
GPC	Gel Permeation Chromatography
NMR	Nuclear Magnetic Resonance (spectroscopy)
ssNMR	solid state Nuclear Magnetic Resonance (spectroscopy)
CP-MAS	Cross Polarization - Magic Angle Spinning
HPDEC	high-powered decoupled
DSC	Differential Scanning Calorimetry
TGA	Thermo-Gravimetric Analysis
PXRD	Powder X-Ray Diffraction
PDF	Pair Distribution Function
XPS	X-Ray Photoelectron Spectroscopy
SEM	Scanning Electron Microscope
EDS	Energy-Dispersive x-ray Spectroscopy
IR	Infrared (spectroscopy)
FTIR-ATR	Fourier-Transform IR - Attenuated Total Reflection
UV-Vis	UltraViolet - Visible (spectroscopy)
FNAA	Fast Neutron Activation Analysis
EA	Elemental Analysis
ESI-MS	Electrospray Ionization - Mass Spectroscopy

FTMS-APCI	Fourier transform mass spectrometry atmospheric pressure chemical ionization
MeRsC	Methyl Resorcinarene Calixarene
PrRsC	Propyl Resorcinarene Calixarene
HeptRsC	Heptyl Resorcinarene Calixarene
B-MeRsC	Bridged - Methyl Resorcinarene Cavitand
B-PrRsC	Bridged - Propyl Resorcinarene Cavitand
B-HeptRsC	Bridged - Heptyl Resorcinarene Cavitand
Methyl C-PPN	Methyl Calixarene - Porous Polymer Network
Propyl C-PPN	Propyl Calixarene - Porous Polymer Network
Heptyl C-PPN	Heptyl Calixarene - Porous Polymer Network
Methyl B-PPN	Methyl Bridged cavitand - Porous Polymer Network
Propyl B-PPN	Propyl Bridged cavitand - Porous Polymer Network
Heptyl B-PPN	Heptyl Bridged cavitand - Porous Polymer Network
eqv.	equivalent(s)
[O]	Oxidation/Oxidized
[H]	Reduction/Reduced
RT	Room temperature
DI	Deionized
HCl	Hydrochloric acid
DMF	Dimethylformamide
THF	Tetrahydrofuran

EtOH	Ethanol
DMAc	Dimethylacetamide
n-BuLi	*n*-Butyllithium
B_2Pin_2	Bis(pinacolato)diboron
$Pd(dppf)Cl_2 \cdot CH_2Cl_2$	Bis(diphenylphosphino)ferrocene]dichloropalladium(II)·CH_2Cl_2
$SOCl_2$	Thionyl Chloride
$BrCH_2Cl$	Bromochloromethane
K_2CO_3	Potassium carbonate
TsOH	Tosylic acid
$AlCl_3$	Aluminum Chloride
$ZnCl_2$	Zinc Chloride
TFA	Trifluoroacetic Acid
I_2	Molecular Iodine
DBU	1,8-Diazabicyclo[5.4.0]undec-7-ene
MeB	Methylene Blue
MeO	Methyl Orange
RhB	Rhodamine B
PVP	Poly(VinylPyrrolidone)
POP	Persistent Organic Pollutant
PFCAs	Perfluorinated Carboxylic Acids
PCB	Poly Chlorinated Biphenyl
DCE	DiChloroEthane

4-OHPhRs-C	4-hydroxyphenylcalix[4]resorcinarenes
TFPB	1,3,5-tris(4-formylphenyl)benzene
DFBP	4,4'-diformylbiphenyl
MeOH	Methanol
DIPEA	N,N-Diisopropylethylamine or Hünig's base
TEA	Triethylamine
NaH	Sodium hydride
TFTN	tetrafluoroterephthalonitrile
PrRsC-OC	piperazinyl propyl resorcinarene organic cage

TABLE OF CONTENTS

Page

ABSTRACT ii

DEDICATION iv

ACKNOWLEDGEMENTS v

CONTRIBUTORS AND FUNDING SOURCES vii

NOMENCLATURE ix

TABLE OF CONTENTS xiv

LIST OF FIGURES xvi

CHAPTER I INTRODUCTION AND BACKGROUND 1

I.i The nature of porosity 1
I.ii A description of porosity 1
I.iii Porous materials 9
I.iv Porous polymers 20
I.v Macrocycle porous polymers 25
I.vi Calixarenes macrocycles 30
I.vii Novel calixarene porous polymers 44
I.viii Summary and forward 48

CHAPTER II PRE-STRUCTURED CALIXARENE-BASED PHENOLIC-ALDEHYDE POROUS POLYMER NETWORKS 50

II.i Introduction to porous Novolac resins and pre-structuring with calixarenes 50
II.ii Experimental 53
II.iii Results 60
II.iv Summary 78
II.v Supplemental information 79

CHAPTER III POROUS POLYMERS NETWORKS CONSTRUCTED FROM RIGID BRIDGED CAVITANDS 99

III.i Introduction to rigid cavitands and their polymer networks 99

III.ii Experimental 101
III.iii Results 108
III.iv Further work 119
III.v Summary 120
III.vi Supplemental information 122

CHAPTER IV POROUS POLYMER NETWORKS CONSTRUCTED FROM CALIXARENE-BASED ORGANIC CAGES 136

IV.i Introduction to organic cages and their polymer networks 136
VI.ii Experimental 138
IV.iii Results 143
IV.iv Further work 148
IV.v Summary 149
IV.vi Supplemental information 150

CHAPTER V CONCLUSIONS AND PROSPECTIVE 151

V.i Summary 151
V.ii Conclusions 152
V.iii Prospective 153

REFERENCES 154

LIST OF FIGURES

Page

Figure 1. Representations of spheres of varying porosity and surface areas 2

Figure 2. Internal or “intrinsic” versus external or “extrinsic” porosity 3

Figure 3. Example gas adsorption isotherm 6

Figure 4. Standard IUPAC gas adsorption isotherms.....8

Figure 5. Timeline of the discovery and use of porous material* [16,18–23].....9

Figure 6. Structure of amorphous carbon[24†], fullerene-like carbon[25†], and image of activated charcoal 11

Figure 7. Example zeolite structures[‡,37] and image of 3 Å molecular sieve pellets.....12

Figure 8. The chemical structure of weak cation ion-exchange resin and an image of Dowex® ion exchange beads 13

Figure 9. Structures of UIO-66[47], PCN-250[48], and MIL-101[49]*.....14

Figure 10. Structure and AA stacking model of COF-5[64*].....16

Figure 11. Synthesis and structure of COF-300[65†].....16

Figure 12. Structure and packing of imine organic cages, CC3, showing voids[77‡] 17

Figure 13. Chemical structure of PIM-1 and three-dimensional shape[81*].....18

Figure 14. Chemical structure of crown-ether functionalized OC and optical image of the free-flowing solution[16†].....19

Figure 15. The synthesis of an azo-linked soluble porous polymer, Azo-POP-7, and a comparison to similar but insoluble AG-azo-POP[86‡] 20

Figure 16. “Davankov resin” prepared from a styrene-based polymer[87]*.....21

Figure 17. Synthesis PPN-6-xSO_3Li and corresponding CO2 adsorption isotherms[93†] ..23

Figure 18. Large, rigid molecules utilized as monomers for porous polymers.....24

Figure 19. α-cyclodextrin, cucurbit[5]uril tetrahydroxycalix[4]arene, [2.2.2]paracyclophane macrocycles.....25

Figure 20. P-CDP, a cyclodextrin-based porous polymer[115‡] 26

Figure 21. Tribenzotriquinacene cage[118], [12+8] boronic ester cages[119,120], cofacial organic cage[121*].....27

Figure 22. Porous "pCAGE" polymers constructed from prismatic organic cages[122†]....29

Figure 23. Pillar[5]arene, tetrahydroxycalix[4]arene, calix[4]resorcinarene, and calix[4]pyrogallolarene.....32

Figure 24. Common synthesis of methylcalix[4]resorcinarene[113].....33

Figure 25. Common conformers of calixarenes with a depiction of the crown (*rccc*) conformers of calix[4]resorcinarene.....34

Figure 26. Cesium capture and retention by methylcalix[4]resorcinarene[131‡].....35

Figure 27. A hexameric hydrogen-bonded pyrogallolarene capsule[132] and several catalyzed isonitrile hydrations[133*].....35

Figure 28. Synthesis of three different phenylresorcinarene-based porous polymers, RN4-AZ-OH, RN4-OH, and RN4-F[135†] 36

Figure 29. Synthesis of porous P-PAP[*n*]s from pillar[*n*]arene (*n* = 5, 6) crosslinked by tetrafuoroterephthalonitrile[136‡].....37

Figure 30. Calix[4]arene-based CalP(*n*)s prepared via a Sonogashira−Hagihara cross-coupling[137*].....38

Figure 31. Calixarene-based cavitands with various bridging groups 38

Figure 32. Common methylene bridged cavitand synthesis utilizing bromochloromethane.....39

Figure 33. Crystal structures of enclathrated gases in the "0D pores" of dimethylsilyl-bridged cavitands[114†].....40

Figure 34. Selective monomethylation of alkylamines in a phosphate-bridged cavitand[108‡] 41

Figure 35. A calixarene-based PPN, CP-TFIN, utilized for haloform removal from water[139*] 42

Figure 36. Organic cages derived from one,[161] two,[162] and four calixarenes[167†] 43

Figure 37. Synthesis of a tetrameric organic cage based on four imine-linked calixarene-cavitands[167‡] 44

Figure 38. Phenylcalix[4]resorcinarene, methylene-bridged calix[4]resorcinarene cavitand, and piperazine pillared resorcinarene cage 45

Figure 39. (a) Resorcinarene macrocycle structure with variable R representing "foot" groups. (b) Bridged resorcinarene cavitand with R_2 representing rim-bridging group. (c) Resorcinarene cage with "—" representing the linking group. 46

Figure 40. Depictions of Calixarene and Novolac polymer networks 52

Figure 41. Synthesis of 4-OHPhRsC via HCl-catalyzed condensation 53

Figure 42. Synthesis of DFBP via a one-pot Suzuki-Miyaura coupling.....55

Figure 43. Synthesis of TFBP via an aldol cyclization and halo-lithium exchange 56

Figure 44. Blue (●)/ red (●) spheres indicate activated phenolic branch points and grey (●) spheres indicate formyl branch points. (a) Synthesis of 4-OHPhRsC macrocycle (depicted as the *rccc*-crown conformer) from 4-hydroxybenzaldehyde and resorcinol. (b) Subsequent condensation of 4-OHPhRsC and terephthalaldehyde to the C-PPN with concurrent oxidation (depicted as a proposed structures). (c) Direct condensation of 4-hydroxybenzaldehyde, resorcinol, and terephthalaldehyde to the unstructured Novolac resin, N-PPN with concurrent oxidation (depicted as a proposed structure showing a few of many possible branching geometries and linkages). 60

Figure 45. Solid and open marks indicate adsorption and desorption, respectively; blue (●)/ red (●) spheres indicate activated phenolic branch points and grey (●) spheres indicate formyl branch points. (a) N_2 adsorption isotherms of C-PPN-2s synthesized with acid catalysts. (b) N_2 adsorption isotherms of C-PPNs with increasing equivalents of terephthalaldehyde. (c) Comparison of N_2 adsorption isotherms of unstructured N-PPN-5 to resorcinarene-based C-PPN-5. (d) NLDFT N_2 adsorption pore size distribution of N-PPN-5 and C-PPN-5; inset of Barrett-Joyner-Halenda (BJH) N_2 desorption pore size distribution (f) N_2 adsorption isotherms of C-PPN-variants depicted with their aldehyde comonomers. 62

Figure 46. N_2 adsorption isotherms of repeated syntheses of (a) C-PPN-5 and (b).....65

Figure 47. N_2 Combined elemental analysis mass ratio for C-PPN-5 and N-PPN-5 (carbon and hydrogen determined via combustion and oxygen determined via FNAA) 67

Figure 48. (a) ^{13}C-CP-MAS-ssNMR experiments for C-PPN-5 and N-PPN-5. (b) Overlay of FTIR-ATR spectra of as-synthesized C-PPN-5 and N-PPN-5. (c) SEM image of the C-PPN-5 (100 μm scale). (d) SEM image of the N-PPN-5 (50 μm scale). 68

Figure 49. Comparison of normalized FTIR-ATR spectra of C-PPNs synthesized with varying equivalents of terephthalaldehyde 69

Figure 50. Comparison of normalized FTIR-ATR spectra of 5 eqv. C-PPN as synthesized, after oxidation [O], and after reduction [H] 70

Figure 51. Comparison of offset ^{13}C-CP-MAS-ssNMR spectra of C-PPN-5 and N-PPN-5 as synthesized, after oxidation [O], and after reduction [H] 71

Figure 52. M-DSC exotherms for C-PPN-5 heated at 10 °C/min to 300 °C under air and N_2 atmospheres 72

Figure 53. SEM micrographs of (a) PPN-2 (b) PPN-5 (c) PPN-9 of C-PPNs (blue) and N-PPNs (red) 73

Figure 54. Comparison thermal decomposition of C-PPN-5 and N-PPN-5 under nitrogen 74

Figure 55. (a) UV-Vis absorbance spectra of 110 ppm aqu. RhB adsorption onto 10 mg of C-PPN-5 over 45 min. (b) Desorption of 135 ppm RhB from 10 mg of C-PPN-5 by 1:1 ethanol:water solution of 1.5 M NaOH over 12 min. (c) Corresponding relative concentrations of RhB for adsorption/desorption experiments over 60 min from UV-Vis spectra 74

Figure 56. 1-week dye adsorption capacities of C-PPN-5 and N-PPN-5 for MeO, MeB, and RhB 75

Figure 57. Comparison of C-PPN-5 and N-PPN-5 dye adsorption capacities and percent removals of MeO, MeB, and RhB over 1 week 76

Figure 58. Zeta potential traces in triplicate for C-PPN-5. Comparison of measured zeta potentials for as C-PPN-5 and N-PPN-5, as well as C-PPN-5-[O] and C-PPN-5-[H] 76

Figure 59. Repeated removal of MeB dye from water by C-PPN-5 and N-PPN-5 in the absence (a) and presence (b) of a “macromolecular foulant” PVP 77

Figure 60. 500 MHz ^{1}H NMR spectra of 4-OHPhRsC in D_6-DMSO green and yellow overlays correspond to signals from the *rctt* and *rccc* diastereomers, respectively; blue overlay indicates water and purple overlay indicates residual solvent 79

Figure 61. Optical photograph of 4-OHPhRsC 80

Figure 62. 500 MHz ^{1}H NMR spectra of TFPB in $CDCl_3$, blue overlay indicates water and yellow overlay indicates residual solvent 80

Figure 63. N_2 isotherms of C-PPNs synthesized with varying equivalents of terephthalaldehyde 81

Figure 64. (a) Comparison of 77 K Ar isotherms for C-PPN-5 and N-PPN-5. (b) Comparison of calculated PSDs based on 77 K Ar 81

Figure 65. (a) Comparison of CO_2 isotherms for C-PPN-5 and N-PPN-5. (b) Comparison of calculated PSDs based on the CO_2 isotherms 82

Figure 66. Comparison of N_2 isotherms of C-PPN-5 produced with different HCl:Dioxane ratios 82

Figure 67. Comparison of N_2 isotherms of C-PPN-5 produced with different total volumes of dioxane and HCl 83

Figure 68. Comparison of N_2 isotherms of C-PPN-5 produced with different reaction temperatures 83

Figure 69. Comparison of normalized FTIR-ATR spectra of C-PPN-5 and N-PPN-5 84

Figure 70. Comparison of normalized offset FTIR-ATR spectra resorcinol, 4-OHPhRsC, terephthalaldehyde, and 4-hydroxybenzaldhyde 85

Figure 71. Comparison of FTIR-ATR normalized spectra offset by 0.5 of C-PPN-5-formaldehyde, C-PPN-5-isophthalaldehyde, C-PPN-5-DFBP, and C-PPN-5-TFPB 86

Figure 72. Comparison of offset ^{13}C-CP-MAS-ssNMR spectra of 5 eqv. C-PPN, 4-OHPhRsC, and terephthalaldehyde 87

Figure 73. Comparison of offset ^{13}C-CP-MAS-ssNMR spectra of C-PPNs synthesized with varying equivalents of terephthalaldehyde 88

Figure 74. Optical photograph of C-PPN-5 88

Figure 75. Comparison of offset ^{13}C-CP-MAS-ssNMR spectra of C-PPN-5 and N-PPN-5 89

Figure 76. Comparison thermal decomposition of C-PPNs under nitrogen 89

Figure 77. N_2 isotherms of N-PPNs synthesized with varying equivalents of terephthalaldehyde 90

Figure 78. Comparison of normalized FTIR-ATR spectra of N-PPNs synthesized with varying equivalents of terephthalaldehyde 90

Figure 79. Comparison of offset ^{13}C-CP-MAS-ssNMR spectra of N-PPNs synthesized with varying equivalents of terephthalaldehyde 91

Figure 80. Optical photograph of N-PPN-5 91

Figure 81. Comparison thermal decomposition of N-PPNs under nitrogen 92

Figure 82. Comparison of the thermal decomposition of C-PPN-5 under nitrogen and air 92

Figure 83. Thermal decomposition of C-PPN-5 under air with an isothermal hold at 250 °C for 4 h, followed by ramping to 600 °C 93

Figure 84. M-DSC exotherms for N-PPN-5 heated at 10 °C/min to 300 °C under air and N_2 atmospheres 93

Figure 85. Comparison of normalized FTIR-ATR spectra of N-PPN-5 as synthesized, after oxidation [O], and after reduction [H] 94

Figure 86. SEM micrographs of (a) C-PPN-1 (b) C-PPN-2 (c) C-PPN-3 95

Figure 87. SEM micrographs of (a) C-PPN-4 (b) C-PPN-5 (c) C-PPN-6 96

Figure 88. SEM micrographs of (a) C-PPN-7 (b) C-PPN-8 (c) C-PPN-9 97

Figure 89. SEM micrographs of (a) N-PPN-2 (b) N-PPN-5 (c) N-PPN-9 98

Figure 90. Depictions of polymer networks constructed from calixarenes (C-PPNs) and bridged cavitands (B-PPNs) 100

Figure 91. General synthesis of resorcinarenes ((R)RsC) 101

Figure 92. Chemical structures of methyl, *n*-propyl, and *n*-heptyl resorcinarenes from left to right (MeRsC, PrRsC, and HeptRsC respectively) 102

Figure 93. Optical photograph of PrRsC.....102

Figure 94. General synthesis of bridged resorcinarene cavitands (B-(R)RsC).....103

Figure 95. Chemical structures of bridged methyl, *n*-propyl, and *n*-heptyl resorcinarene cavitands from left to right (B-MeRsC, B-PrRsC, and B-HeptRsC respectively).....105

Figure 96. Optical photograph of Propyl C-PPN-3.....107

Figure 97. (a) Parent calixarene macrocycle (depicted as the *rccc*-crown conformer) and terephthalaldehyde condensed to form the C-PPNs, depicted as proposed structures. (b) Bridging of parent calixarenes into rigid cavitands by bromochloromethane. (c) Condensation of bridged cavitands into B-PPNs, depicted as expected structures.....108

Figure 98. N_2 isotherms of Propyl B-PPNs synthesized with varying equivalents of terephthalaldehyde.....110

Figure 99. N_2 isotherms of (a) B-PPN-4s and C-PPN-4s (b) B-PPN-5s and C-PPN-5s 111

Figure 100. (a) N_2 adsorption isotherms of the C-PPN-3s with different foot chain lengths (b) N_2 adsorption isotherms of the B-PPN-3s with different foot chain lengths. (c) A linear plot of the BET micropore surface areas, S_{BET}, of each B-PPN. (d) NLDFT N_2 adsorption pore size distribution of B-PPNs; inset of Barrett-Joyner-Halenda (BJH) N_2 desorption pore size distribution. 112

Figure 101. 273 K CO_2 isotherms of B-PPN-3s and NLDFT pore size distributions....114

Figure 102. 77 K Ar isotherms of B-PPN-3s and NLDFT pore size distributions 115

Figure 103. Comparison of normalized FTIR-ATR spectra of the bridged cavitand, B-HeptRsC, the Heptyl C-PPN-3, and Heptyl B-PPN-3.....116

Figure 104. Comparison of ^{13}C-CP-MAS-ssNMR spectra of (a) B-PrRsC, PrRsC, and Propyl B-PPN-3 (b) Propyl B- and Propyl C-PPN-3.....117

Figure 105. Comparison of the thermal decomposition of C- and B-PPN-3s under nitrogen.....118

Figure 106. (a) SEM image of the Methyl C-PPN-3 (100 μm scale). (b) SEM image of the Methyl B-PPN-3 (100 μm scale).....119

Figure 107. Chemical structures of the parent, bridged parent cavitand, and catechol-deepened cavitand from left to right (RsC, B-RsC, and D-(R)RsC respectively).....120

Figure 108. 500 MHz ^{1}H NMR spectra of MeRsC in D_6-DMSO, blue overlay indicates residual water and purple overlay indicates residual solvent DMSO 122

Figure 109. 500 MHz ^{1}H NMR spectra of B-MeRsC in D_6-DMSO, blue overlay indicates residual water, purple overlay indicates residual solvent, and green overlay indicates residual DMAc 123

Figure 110. 500 MHz ^{1}H NMR spectra of PrRsC in D_6-DMSO, blue overlay indicates residual water and purple overlay indicates residual solvent DMSO 124

Figure 111. 500 MHz ^{1}H NMR spectra of B-PrRsC in D_6-DMSO, blue overlay indicates residual water, purple overlay indicates residual DMSO, and green overlay indicates residual DMAc 125

Figure 112. 500 MHz ^{1}H NMR spectra of HeptRsC in $CDCl_3$, yellow overlay indicates residual solvent $CHCl_3$ 126

Figure 113. 500 MHz ^{1}H NMR spectra of B-HeptRsC in $CDCl_3$, yellow overlay indicates residual solvent $CHCl_3$ 127

Figure 114. N_2 isotherms of Propyl C-PPNs synthesized with varying equivalents of terephthalaldehyde 127

Figure 115. N_2 isotherms of Methyl C-PPNs and Methyl B-PPNs synthesized with varying equivalents of terephthalaldehyde 128

Figure 116. N_2 isotherms of Heptyl C-PPNs and Heptyl B-PPNs synthesized with varying equivalents of terephthalaldehyde 128

Figure 117. 77 K Ar isotherms of C-PPN-3s and derived NLDFT pore size distributions 129

Figure 118. 273 K CO_2 isotherms of C-PPN-3s and derived NLDFT pore size distributions 129

Figure 119. Comparison of normalized offset FTIR-ATR spectra of the bridged cavitands, B-MeRsC, B-PrRsC, and B-HeptRsC to the calixarenes, MeRsC, PrRsC, and HeptRsC 130

Figure 120. Comparison of normalized FTIR-ATR spectra of the bridged cavitand, B-MeRsC, the Methyl C-PPN-3, and Methyl B-PPN-3 131

Figure 121. Comparison of normalized FTIR-ATR spectra of the bridged cavitand, B-PrRsC, the Propyl C-PPN-3, and Propyl B-PPN-3 131

Figure 122. Comparison of ^{13}C-CP-MAS-ssNMR spectra bridged cavitand, Methyl B-and Methyl C-PPN-3 132

Figure 123. Comparison of ^{13}C-CP-MAS-ssNMR spectra bridged cavitand Heptyl B- and Heptyl C-PPN-3 132

Figure 124. SEM micrographs of (a) Methyl C-PPN-3 and (b) Methyl B-PPN-3 133

Figure 125. SEM micrographs of (a) Propyl C-PPN-3 and (b) Propyl B-PPN-3 134

Figure 126. SEM micrographs of (a) Heptyl C-PPN-3 and (b) Heptyl B-PPN-3 135

Figure 127. Depiction of polymer network constructed from organic cage, OC-PPNs, compared to C-PPNs 137

Figure 128. 500 MHz ^{1}H NMR spectra of PrRsC-OC in $CDCl_3$, yellow overlay indicates residual solvent 139

Figure 129. Optical photograph of PrRsC-OC 140

Figure 130. Synthesis of piperazinyl-pillared *n*-propyl resorcinarene organic cage, PrRsC-OC 143

Figure 131. Attempted model syntheses of polyethers, polyesters, and polyphosphazenes C-PPNs 144

Figure 132. N_2 gas adsorption/desorption isotherms for triazine-linked polyester PPN constructed from cyanuric chloride and 4-OHPhRsC 144

Figure 133. Attempted syntheses of triazine-linked polyethers PPNs from PrRsC and PrRsC-OC 145

Figure 134. Synthesis of a polyether OC-PPN utilizing TFTN 146

Figure 135. Comparison of normalized FTIR-ATR spectra of TFTN, PrRsC-OC, and OC-PPN 147

Figure 136. Comparison of offset ^{13}C-CP-MAS-ssNMR spectra of PrRsC-OC and OC-PPN 147

Figure 137. Distorted tetrahedron imine-linked cavitand organic cage[234] with a proposed polyamine synthesis* 148

Figure 138. Expected and experimental ESI mass spectra of PrRsC-OC 150

CHAPTER I

INTRODUCTION AND BACKGROUND

I.i The nature of porosity

Porosity is the term that describes empty space contained in voids, or "pores" within materials. While a simple void where material is missing may not seem like an exciting property in itself, focusing on the empty space contained reveals great utility. Bounded empty space can serve, most obviously, to store mater for myriad applications; alternatively, these spaces when left empty are natural insulators/ dielectrics, reducing the transport of heat and charge.

On a grand scale, the universe can be thought of as an infinite void that is expanding into nothing. Within this void all mater, energy, and all that we know is contained. In this thought experiment, the universe is a sort of "proto-pore:" a void that contains everything.

While a universal pore may be an interesting thought, the voids most commonly studied in porous materials are minute and their functions are similarly scaled.

I.ii A description of porosity

As a material property, porosity is often given as a fraction or percent of the bulk which is empty, a "void fraction," ϕ.[1] The higher the void fraction, the more porous the material, with a void fraction of one ($\phi = 1$) being the unrealistic case of a void bounded by surfaces of zero thickness.[2]

A consequence of porosity in a material is a change in surface area as compared to a closed solid of the same dimensions. Voids must be bounded by surfaces within a material and so the porosity and surface area, S_a, are linked.[3] However, there is not necessarily a linear relationship between surface area and void fraction. Considering a solid sphere as a non-porous starting point **(figure 1a**), a hollow version of this sphere with no surface thickness may have a void fraction of one ($\phi = 1$) and double the surface area of the starting sphere **(figure 1b**); however, if the sphere is contains many small voids, the void fraction may be less than one ($\phi < 1$) and the surface area may be greater than double the surface area of the starting sphere **(figure 1c**). From this description it can be seen that surface area is more a function of pore size (width) within a material, while void fraction is a somewhat independent metric of the porosity. Practically, surface area is oftentimes preferred to void fraction to gauge porous materials as it is more directly related to "useful porosity."

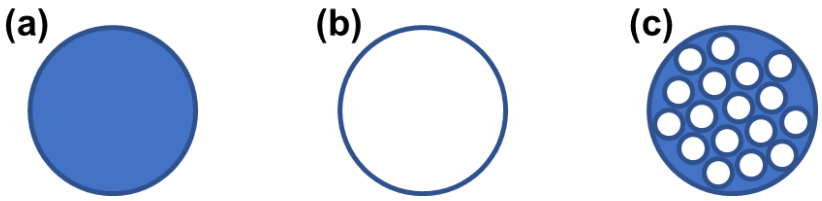

Figure 1. Representations of spheres of varying porosity and surface areas

Pore widths are commonly described as being microporous (< 2 nm), mesoporous (2 - 50 nm), or macroporous (> 50 nm).[4] Microporous materials are useful as "molecular sieves" for the adsorption and separation of small molecules. Solely microporous materials usually have highest surface areas of porous materials, as a result of the relationships previously described. Mesoporous materials are useful when

adsorption of larger species or an increase in flux is desired. Macropores, are mostly useful for fast transport kinetics, but do not provide a significant increase in useful surface area as micro/mesopores.

Porosity within materials may be described as internal or "intrinsic," arising from voids localized inside the bulk, or external or "extrinsic," being derived from empty space between packed particulates of the bulk **(figure 2a and b)**.[2,5–7] These descriptions are significant to how useful the materials are for various applications. Generally, extrinsically porous materials are not very desirable, as they require inherently small particle sizes and do not employ the bulk of the material towards porosity. The descriptors, intrinsic/extrinsic, can be further extended to molecular scale, where they will be useful for the description of molecular porosity in later sections.

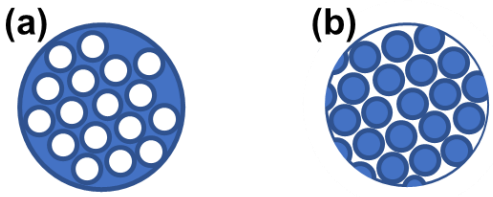

Figure 2. Internal or "intrinsic" versus external or "extrinsic" porosity

The void fraction and surface areas of real materials can be assessed through a variety of techniques. In several common methods, probe molecules are utilized to infiltrate voids and give an estimate of the empty space contained. The number of probe molecules at saturation and their cross-sectional areas and volumes can give a measure of the void fraction and surface area of the materials. As probe molecules infiltrate pores within a material, they will preferentially adhere to the surfaces of the pores

through interactions such as Van der Waals attractive forces. The process of substances adhering to surfaces is called “adsorption,” with the reverse process being “desorption.” These should be contrasted by the process called “absorption” where a substance is taken into a nonporous solid.[4] These terms are sometimes confused, but it is worth noting that most sorption processes are adsorptive rather than absorptive.[4,8] An example of absorptive process is hydrogen gas entering steel at high pressures.[9]

Adsorption processes can be modeled simply if there is assumed to be a single layer of adhering molecules (adsorbates) adsorbing to a surface. However, while a monolayer does preferentially form first, as excess adsorbate molecules infiltrate a porous material they will subsequently adsorb to the lower layer and form multilayers. This process will continue, layer on layer, till the pores are either filled or the concentration of the adsorbate (probe) molecules is high enough that they will interact with each other to cause condensation.[4]

A simple theory for monolayer adsorption is the Langmuir adsorption model.[10] This model makes several unrealistic assumptions such as the adsorbent surface is homogenous and has only one, equal interaction with all adsorbate molecules; additionally, that there are ideal, uniform interactions between adsorbate molecules within the monolayer.[3] However, this model is the basis several useful models of adsorptions behavior, including the Hill equation utilized in biochemistry for substrates binding to macromolecules[11,12] and Brunauer–Emmett–Teller (BET) theory which is a multi-layer adsorption model[4].

BET theory is the model most commonly utilized to describe adsorption on real materials. This model also relies on several assumptions, such as the ideal interaction between adsorbates. The BET model is most commonly applied to range of pressures of adsorbate (probe) molecules over a low-pressure regime to estimate the surface area of the first monolayer adsorbed.[2,3]

The process of dosing a sample of porous material with a probe gas is usually carried out under isothermal conditions and is called a "gas adsorption isotherm."[2,4] This process is often performed at the liquefaction temperature of the probe gas, but can be performed at many temperatures, as desired. In the standard process, a porous sample is placed in a sealed chamber of known volume and slowly dosed with the probe gas. After each dose, the pressure within the chamber is allowed to equilibrate. The difference between amount of gas dosed into the chamber and the equilibrium pressure can be used to determine the amount of gas adsorbed into the sample. Once the pressure of the gas within the chamber reaches saturation pressure, P_0, or vapor pressure of the gas at the temperature of measurement, the adsorption ceases; at this point, gas is usually removed from the chamber and pressure is allowed to equilibrate, in the reverse process to the adsorption measurement. This "desorption" process provides information about larger pores, flexibility, and reversibility of the adsorption process.[2,4]

When the relative pressure of the adsorbate gas is plotted versus the amount adsorbed by the sample, the shape of the plot or "isotherm" is diagnostic towards the porosity of the material **(figure 3)**. The low-pressure region, usually within the 0.0 - 0.3 relative pressure (P/P_0) range, is where monolayer adsorption will occur.[3,4] As the

pressure increases, multilayer adsorption will occur in any meso or macropores. If mesopores exist of the correct size and shape, capillary condensation of the adsorbate can occur in this region, below the saturation pressure of the bulk liquid. This is observed as a "step" in the isotherm, and the height, onset pressure, and shape of this step is indicative of the volume in the mesopores, size of the mesopores, and shape of the pores, respectively.[4] Sufficiently large mesopores and macropores will not exhibit capillary condensation at lower pressures, and the pressure increase till it approaches the saturation, P_0, where bulk condensation can occur.

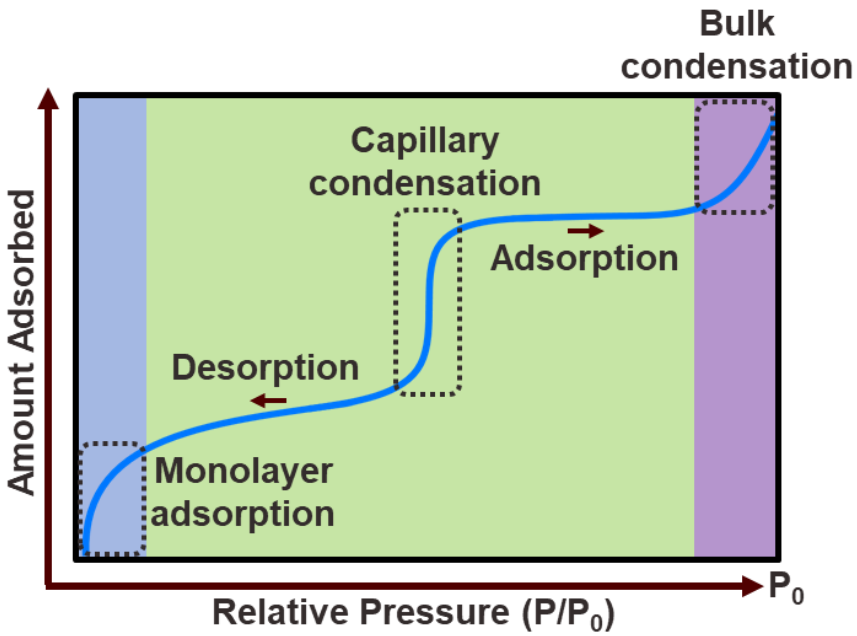

Figure 3. Example gas adsorption isotherm

The International Union of Pure and Applied Chemistry (IUPAC) has defined a set of standard isotherms which are useful for comparing to experimental observations **(figure 4)**.[4] According to this set, a Type I isotherm is observed for microporous

materials.[4] The shape of this isotherm is that of a "Langmuir isotherm," that is, only monolayers are adsorbed within the narrow micropores.[4] In these isotherms, the breadth of the inflection point reflects the width and distribution of pores within the material, with Type I(b) being a material with a broader distribution of pores than Type I(a).[4] Type II isotherms are usually characteristic of macroporous materials.[4] The height of the inflection point in these indicates the degree of monolayer adsorption. Type III isotherms are usually indicative of nonporous, finely divided materials with weak interactions to the adsorbates.[4] Type IV isotherms are characteristic of mesoporous materials with defined pore shapes where a pressure is reached which causes capillary condensation.[4] In the Type IV(a) isotherm, a hysteresis is observed between the adsorption and desorption phases of the cycle.[4] This is due to a lower pressure being required to overcome surface tension in condensate and cause desorption within narrow mesopores; the width of the "neck" of the pores dictates at which pressure the desorption will occur.[4] If the mesopores are significantly narrow as in Type IV(b), the isotherm will be reversible with no hysteresis, and the observed "step" for capillary condensation will be shifted to lower pressures.[4] While not a complete list of isotherms or isotherm features, this list is useful describing isotherms in comparison to these standard shapes. It should also be noted that many experimental isotherms will exhibit characteristics of multiple of these standard types, and these hybrids can be described as a combination of the standards.

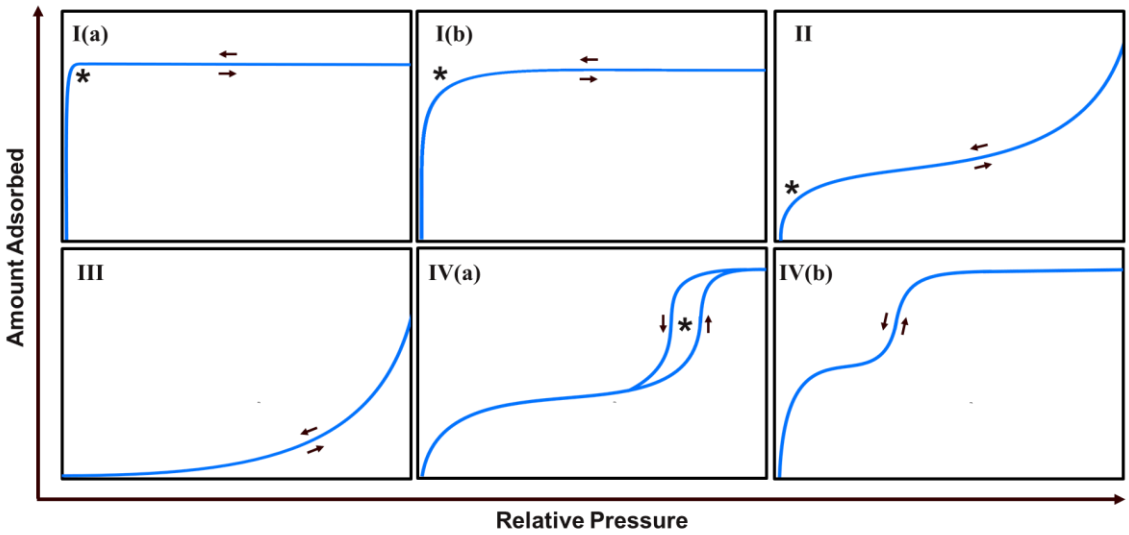

Figure 4. Standard IUPAC gas adsorption isotherms

While porosity is often viewed as a static feature of materials, flexibility, pressure, and stimuli can result in increases, reductions, or loss of porosity within materials. For certain flexible materials, increased gas pressure can result in a "gating" phenomenon where a critical pressure is reached which causes the opening of pores to adsorbates.[13,14] Likewise, flexible materials often display large hystereses during desorption due to changes material shape, etc.[15] These considerations are of importance in regard to porous polymers and other materials that are not entirely rigid.

Due to the dynamic of porosity in some materials, it is useful to define a term that is used in regard to porous materials: "permanent porosity" or "permanently porous" is used to describe materials that maintain their porosity under certain operating conditions.[5,16] This can be used to contrast between materials such as hydrogels and aerogels. Hydrogels are flexible polymeric materials that may be nonporous when in the solid, dry state; when these gels are exposed to water or other solvents, they can swell

taking on solvent and gaining a considerable void fractions. The removal of solvents from this type of material by ambient drying usually results in shrinkage and the return of the material to a nonporous state. These materials can be contrasted by aerogels, which are gel-like materials which have solvent removed by a supercritical fluid or freeze-drying.[17] Under these solvent removal conditions, the gel becomes a dry aerogel and maintains its shape and considerable void fraction. Aerogels will maintain "permanent porosity" when exposed to gases but can become gels again if wetted by solvent. Thus, the "permanence" of porosity should be qualified by a range of conditions under which the property is maintained.

I.iii Porous materials

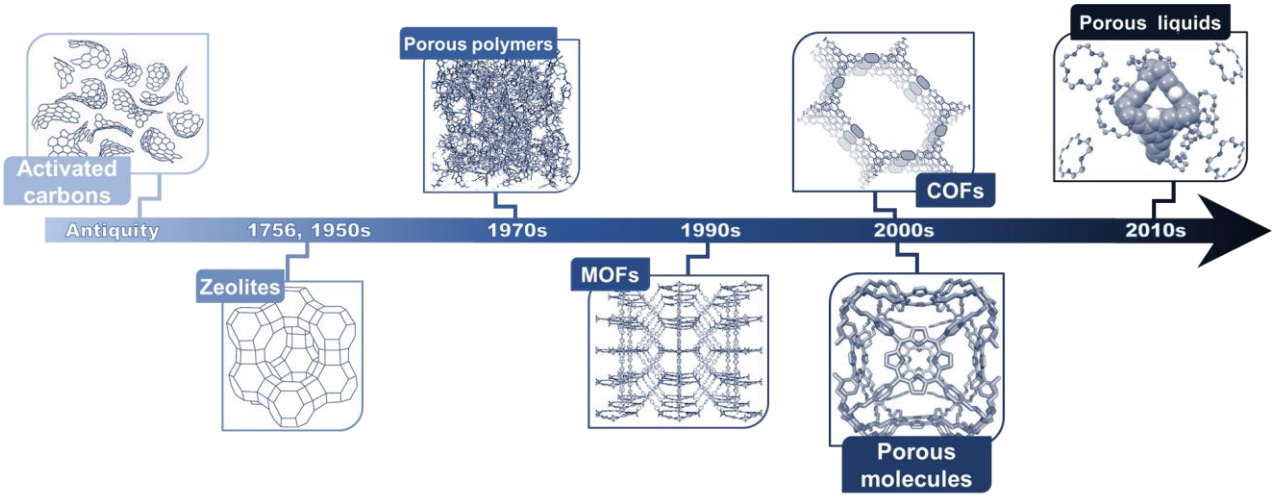

Figure 5. Timeline of the discovery and use of porous material* [16,18–23]

*Adapted with permission from (1) "Structure of Non-Graphitising Carbons" by Harris, P. J. F., *Int. Mater. Rev.*, 1997**.** *42* (5), 206–218, Copyright 1997 by Taylor & Francis.

*Adapted with permission from "Zeolite Y: Synthesis, Modification, and Properties—A Case Revisited" by Lutz, W., *Adv. Mater. Sci. Eng.*, 2014**.** *2014*, 724248, Copyright 2014 by Wolfgang Lutz.

*Adapted with permission from "Formation Mechanism of Ultra Porous Framework Materials" by Fayon, P.; Trewin, A., *Phys. Chem. Chem. Phys.*, 2016**.** *18* (25), 16840–16847, Copyright 2016 by Royal Society of Chemistry.

*Adapted with permission from "Highly Efficient Luminescent Metal–Organic Framework for the Simultaneous Detection and Removal of Heavy Metals from Water" by Rudd, N. D.; Wang, H.; Fuentes-Fernandez, E. M. A.; Teat, S. J.; Chen, F.; Hall, G.; Chabal, Y. J.; Li, J., *ACS Appl. Mater. Interfaces*, 2016**.** *8* (44), 30294–30303, Copyright 2016 by American Chemical Society.

*Adapted with permission from "Growth Rates and Water Stability of 2D Boronate Ester Covalent Organic Frameworks" by Smith, B. J.; Hwang, N.; Chavez, A. D.; Novotney, J. L.; Dichtel, W. R., *Chem. Commun.*, 2015**.** *51* (35), 7532–7535, Copyright 2015 by Royal Society of Chemistry.

*Adapted with permission from "Porphyrin Boxes: Rationally Designed Porous Organic Cages" by Hong, S.; Rohman, M. R.; Jia, J.; Kim, Y.; Moon, D.; Kim, Y.; Ko, Y. H.; Lee, E.; Kim, K., *Angew. Chemie - Int. Ed.*, 2015**.** *54* (45), 13241–13244, Copyright 2015 by John Wiley & Sons.

*Adapted with permission from "Liquids with Permanent Porosity" by Giri, N.; Del Pópolo, M. G.; Melaugh, G.; Greenaway, R. L.; Rätzke, K.; Koschine, T.; Pison, L.; Gomes, M. F. C.; Cooper, A. I.; James, S. L., *Nature*, 2015**.** *527* (7577), 216–220, Copyright 2015 by Springer Nature.

There are many types of porous materials **(figure 5)** and they will not be comprehensively described here, but several of note will be given in a brief overview.

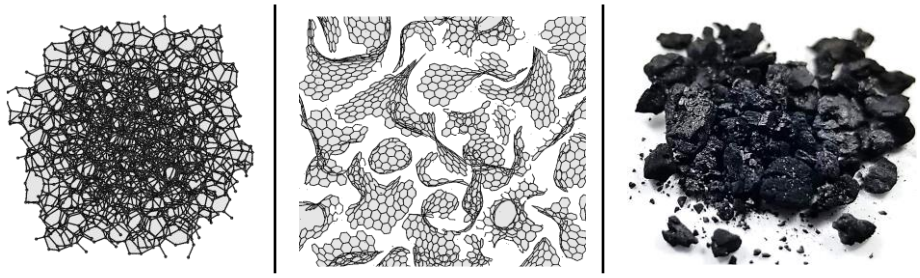

Figure 6. Structure of amorphous carbon[24†], fullerene-like carbon[25†], and image of activated charcoal

[†]Reprinted with permission from "Amorphous Carbon" by Ströck, M., https://upload.wikimedia.org/wikipedia/commons/9/90/Amorphous_Carbon.png, (accessed Oct 10, 2020), Copyright by Michael Ströck under CC BY-SA 3.0.

[†]Reprinted with permission from "Fullerene-Related Structure of Commercial Glassy Carbons" by Harris, P. J. F., *Philos. Mag.*, 2004. *84* (29), 3159–3167, Copyright 2004 by Taylor & Francis.

Porous or Activated Carbons (ACs) are formed via pyrolysis of organic materials **(figure 6)**.[26] These were some of the first porous materials to see use in human civilization. The ingestion of powdered "charcoal" or carbonized wood has been known as a method for treating poisoning via adsorption/sequestration since antiquity.[27,28] ACs usually consist of amorphous "graphitic" carbon ring systems, graphitic oxides, fullerene fragments, or foam-like structures, depending on the carbon source and the pyrolysis conditions **(figure 6)**.[26,29] Various organic sources may be selected to impart elemental and functional group doping in the carbon product, such as nitrogen-rich ACs derived from poly(acrylonitrile)[30] or amino acids[30]. On a basis of affordability and toxicity, porous carbons are generally considered safe and inexpensive enough to be utilized for

such applications as cosmetic and hygiene products as well as household water filtration systems. Modern research on porous carbons usually focuses on engineering the porosity through controlled pyrolysis and etching steps; additionally, many carbon sources have been explored such as coconut husks,[31] corn cobs/husks,[32–35] bamboo,[36] and other agricultural waste byproducts. These porous materials see use in many applications, and since they can be produced from many inexpensive organic sources.

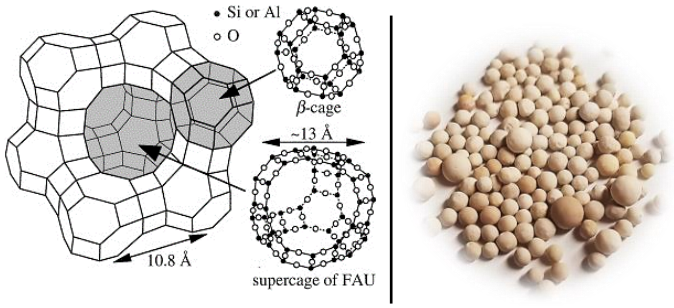

Figure 7. Example zeolite structures[‡,37] and image of 3 Å molecular sieve pellets

[‡]Reprinted with permission from "Magnetic and Optical Properties of K and Na Clusters Arrayed in a Diamond Structure in Zeolite FAU" by Ikemoto, Y.; Nakano, T.; Kuno, M.; Nozue, Y., *Phys. B Condens. Matter*, 2000**.** *281–282*, 691–693, Copyright 2000 by Elsevier Science B.V.

Zeolites are a class of crystalline, inorganic porous materials which occur naturally as minerals and are artificially produced **(figure 7)**.[38] Natural zeolites have been known since 1756, and research and production of artificial zeolites began in the 1950's.[38] Most zeolites are composed of aluminum, silicon, oxygen, and alkali metals; the addition of other elements such as phosphorous has been explored in artificial zeolites. Many zeolites are extremely thermally and chemically stable, due to their robust inorganic structures. Zeolites are essential to many industrial processes where

they are used as stable, high-temperature sorbents and catalysts. Zeolites are commercialized as multifunctional sorbents, and often sold in pellet form; chemists may be used to encountering and utilizing these as "molecular sieves" to removed water from organic solvents in the laboratory **(figure 7)**. Modern research on zeolites often focuses on synthetic techniques to access novel structures and methods to install catalytic sites.

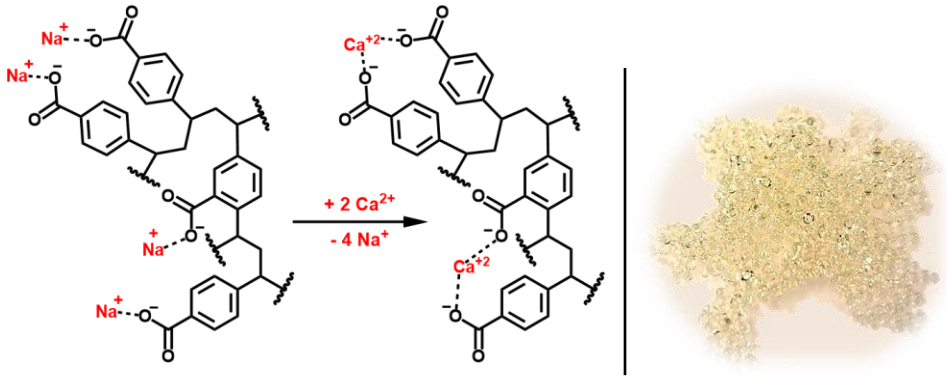

Figure 8. The chemical structure of weak cation ion-exchange resin and an image of Dowex® ion exchange beads

Porous polymers are amorphous materials based on repeating organic units.[39–43] The first porous polymers were made in the 1930's as ion exchange resins from phenol-aldehyde and later from crosslinked polystyrene **(figure 8)**.[44,45] These resins are gel-like and shrink to nonporous states when dry. The first permanently porous polymers were hypercrosslinked polystyrenes explored in the 1970's by Davankov, et al.[40,46] Porous polymers are notable for their relative ease of synthesis and their diverse structures. Porous polymers have been examined for many applications and stand-out for their potential affordability and scalability. These polymers have been commercialized as ion-exchange resins and hydrogels, such as Dowex® resins **(figure 8)**.[45] These polymers are utilized in research applications, and in water treatment devices, including household

"water softeners."[45] Research on porous polymers often focuses on processability, control of porosity, and targeted application. As the subject of this dissertation, these materials will be discussed further in the following sections.

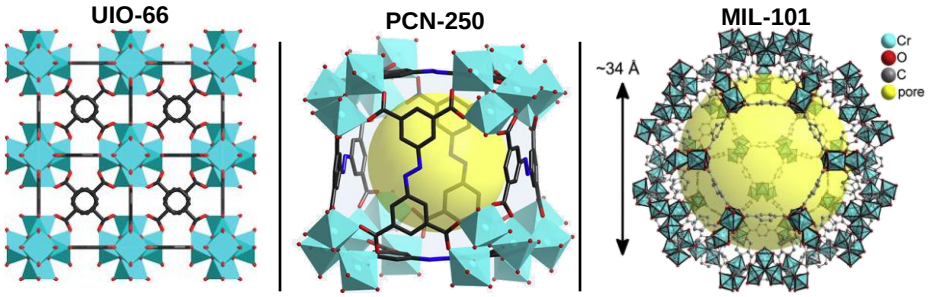

Figure 9. Structures of UIO-66[47], PCN-250[48], and MIL-101[49]*

*Reprinted with permission from "Stable Metal–Organic Frameworks: Design, Synthesis, and Applications" by Yuan, S.; Feng, L.; Wang, K.; Pang, J.; Bosch, M.; Lollar, C.; Sun, Y.; Qin, J.; Yang, X.; Zhang, P.; Wang, Q.; Zou, L.; Zhang, Y.; Zhang, L.; Fang, Y.; Li, J.; Zhou, H.-C., *Adv. Mater.*, 2018**.** *30* (37), 1704303, Copyright 2018 by John Wiley and Sons.

*Reprinted with permission from "PCN-250 under Pressure: Sequential Phase Transformation and the Implications for MOF Densification" by Yuan, S.; Sun, X.; Pang, J.; Lollar, C.; Qin, J. S.; Perry, Z.; Joseph, E.; Wang, X.; Fang, Y.; Bosch, M.; Sun, D.; Liu, D.; Zhou, H. C., *Joule*, 2017**.** *1* (4), 806–815, Copyright 2017 by Elsevier.

*Reprinted with permission from "Metal-Organic Framework (MIL-101) Stabilized Ruthenium Nanoparticles: Highly Efficient Catalytic Material in the Phenol Hydrogenation" by Ertas, I. E.; Gulcan, M.; Bulut, A.; Yurderi, M.; Zahmakiran, M., *Microporous Mesoporous Mater.*, 2016**.** *226*, 94–103, Copyright 2013 by Elsevier.

Metal Organic Frameworks (MOFs) are crystalline materials constructed from repeating organic ligands connecting metal nodes through coordination bonds **(figure 9)**.[50,51] These materials were first explored by Susumu Kitagawa, Omar Yaghi, Makoto Fujita, Gérard Férey, and coworkers beginning in the 1990's. Early MOFs were usually based on zinc and copper metals linked through carboxylate ligands and had low

chemical stability, such as MOF-5.[52] Further research in this field brought about advancement in the matching ligand and metal chemistries to enhance chemical stability. Hard base ligands, when matched with hard metal ions produce stable frameworks, such as zirconium-carboxylate linkages.[53,54] Alternatively, stable MOFs are also produced when soft base ligands are matched with soft metals such as nickel-pyrazolate-based frameworks.[55,56] MOFs have become ubiquitous among porous materials due to their diversity and tunability. A great deal of interest is directed towards these materials for application in separations, storage, and catalysis.[47] Such a diverse collection of these materials has been explored that they are difficult to summarize succinctly. A few types worth mentioning, include the zirconium, iron, and chromium-based MOFs bonded through carboxylate ligands. Notable individual examples in these categories include the ubiquitous zirconium-based UIO-66,[57,58] the iron-based PCN-250[59], and the chromium-based MIL-101[59] **(figure 9)**. These MOFs are noted for their stability and each has a great number of publications exploring their syntheses, modification, and application.

Covalent Organic Frameworks (COFs) are crystalline organic materials constructed from repeating organic units connected through covalent bonds.[60–63] COFs were first reported in the early 2000's by Omar Yaghi and coworkers, with early examples such as COF-5 being connected through labile boroxine linkages **(figure 10)**.[64]

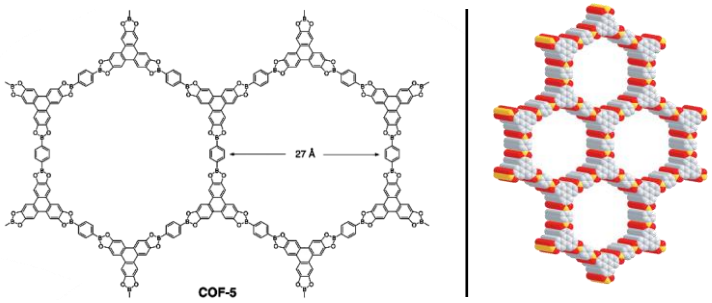

Figure 10. Structure and AA stacking model of COF-5[64*]

*Reprinted with permission from "Porous, Crystalline, Covalent Organic Frameworks" by Côté, A. P.; Benin, A. I.; Ockwig, N. W.; O'Keeffe, M.; Matzger, A. J.; Yaghi, O. M., *Science*, 2005**.** *310* (5751), 1166–1170, Copyright 2005 by The American Association for the Advancement of Science.

In further work, COFs have been developed which are linked through more-stable imine[65–67], hydrazone[68,69], aminal[70], triazine[71,72], and ethenyl linkages[51,73]. COFs are predominately known as two-dimensional materials, although there are notable three-dimensional examples, such as the interpenetrated COF-300 **(figure 11)**.[65]

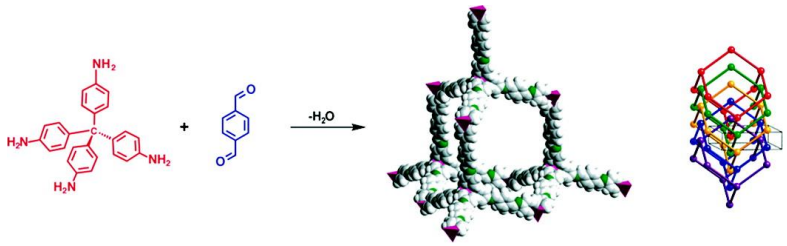

Figure 11. Synthesis and structure of COF-300[65†]

†Reprinted with permission from "A Crystalline Imine-Linked 3-D Porous Covalent Organic Framework" by Uribe-Romo, F. J.; Hunt, J. R.; Furukawa, H.; Klöck, C.; O'Keeffe, M.; Yaghi, O. M., *J. Am. Chem. Soc.*, 2009**.** *131* (13), 4570–4571, Copyright 2009 by American Chemical Society.

Most COFs are synthesized as crystalline powders with small particles sizes, however, there have been several reports of single-crystalline COFs accessed through

advanced synthetic techniques.[74,75] Single crystals of both two-dimensional COFs such as COF-5 and three-dimensional COFs like COF-300 have been produced with these methods.[75,76] These advances have the potential to propel the field forward, since large single crystals will allow for more advanced crystallographic characterization and novel application. COFs have mostly existed in the research phase and have been investigated for many of the same applications as other porous materials; however, COFs have potential advantages over other porous materials for some electronic and photonic applications.

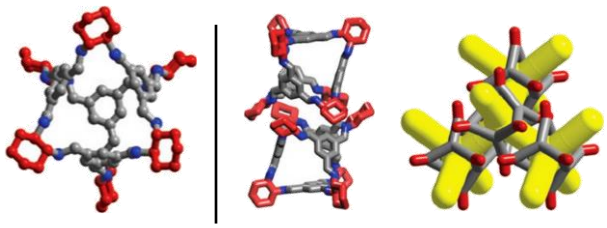

Figure 12. Structure and packing of imine organic cages, CC3, showing voids[77‡]

‡Reprinted with permission from "Porous Organic Cages" by Tozawa, T.; Jones, J. T. A.; Swamy, S. I.; Jiang, S.; Adams, D. J.; Shakespeare, S.; Clowes, R.; Bradshaw, D.; Hasell, T.; Chong, S. Y.; Tang, C.; Thompson, S.; Parker, J.; Trewin, A.; Bacsa, J.; Slawin, A. M. Z.; Steiner, A.; Cooper, A. I., *Nat. Mater.*, 2009**.** *8* (12), 973–978, Copyright 2009 by Springer Nature.

Porous molecules are molecular compounds which have enclosed volumes result in porosity **(figure 12)**.[77,78] As molecular compounds, porous molecules are not strictly materials; however, porous molecules can be utilized in the production of many types of porous materials, whether blended into hybrid materials to impart porosity or used to as building units in the construction of bulk materials. Porous molecules derive their porosity from rigid, three-dimensional structures where intermolecular packing does not

result in a loss of the void fraction. Much work has been focused on porous molecules and materials derived from them. Of note amongst these are Organic Cages (OCs) developed by Cooper, et al. which are constructed from imine-linked organic units **(figure 12)**.[5,7,77,79,80] These cages are soluble in organic solvents and can be crystalized into a variety polymorphic crystals.

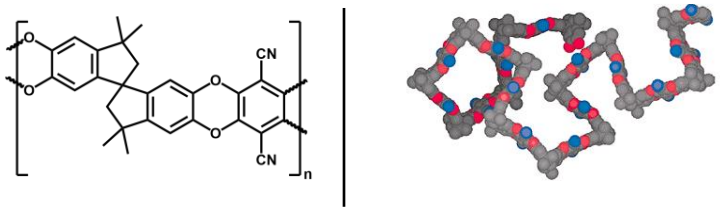

Figure 13. Chemical structure of PIM-1 and three-dimensional shape[81*]

*Reprinted with permission from "Polymers of Intrinsic Microporosity (PIMs): Robust, Solution-Processable, Organic Nanoporous Materials" by Budd, P. M.; Ghanem, B. S.; Makhseed, S.; McKeown, N. B.; Msayib, K. J.; Tattershall, C. E., *Chem. Commun.*, 2004**.** *4* (2), 230–231, Copyright 2004 by Royal Society of Chemistry.

Additionally, there are porous polymeric macromolecules, Polymers of Intrinsic Microporosity (PIMs) which have been studied by McKeown, et al. and are notable for being solution processible **(figure 13)**.[6,82,83] The porosity in PIMs arises from their alternating "bent" structures which cannot efficiently pack on the molecular-scale, leaving micropores within the bulk **(figure 13)**. PIMs have seen particular interest as matrix materials for porous membranes for gas separations.[84] Porous molecules as building units of porous materials will be discussed further in a later section.

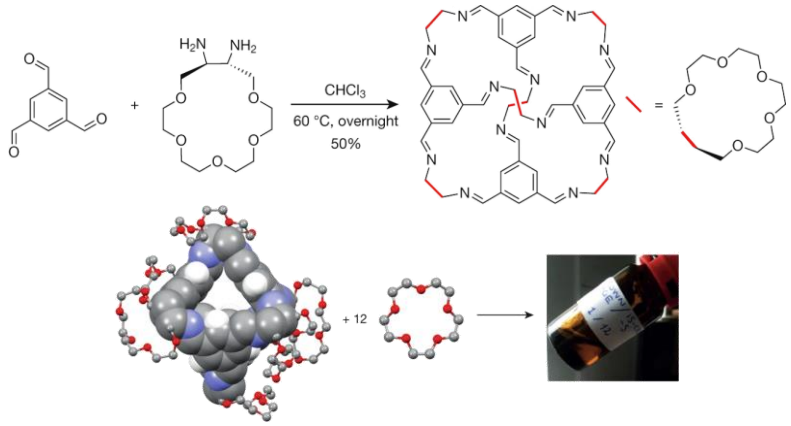

Figure 14. Chemical structure of crown-ether functionalized OC and optical image of the free-flowing solution[16†]

[†]Reprinted with permission from "Liquids with Permanent Porosity" by Giri, N.; Del Pópolo, M. G.; Melaugh, G.; Greenaway, R. L.; Rätzke, K.; Koschine, T.; Pison, L.; Gomes, M. F. C.; Cooper, A. I.; James, S. L., *Nature*, 2015**.** *527* (7577), 216–220, Copyright 2015 by Springer Nature.

Porous liquids are emerging materials where porosity arises from large solvent molecules which are unable in infiltrate pores of suspended or dissolved sorbents.[7] These types of materials were first reported by Cooper, et al. in 2015.[16] In their report, an organic cage functionalized with crown-ether functional groups, was dissolved in a free-flowing crown-ether solvent to produce a porous liquid capable of adsorbing methane **(figure 14)**.[16] Stable dispersions of microparticulate porous materials in bulky liquids which are incapable of infiltrating the pores have also been reported.[85] These materials have not yet seen practical application, however, a free-flowing porous material may have advantages in some engineering applications in the future.

I.iv Porous polymers

To further focus on porous polymers, these materials can be broadly divided into two categories: soluble and insoluble polymers.

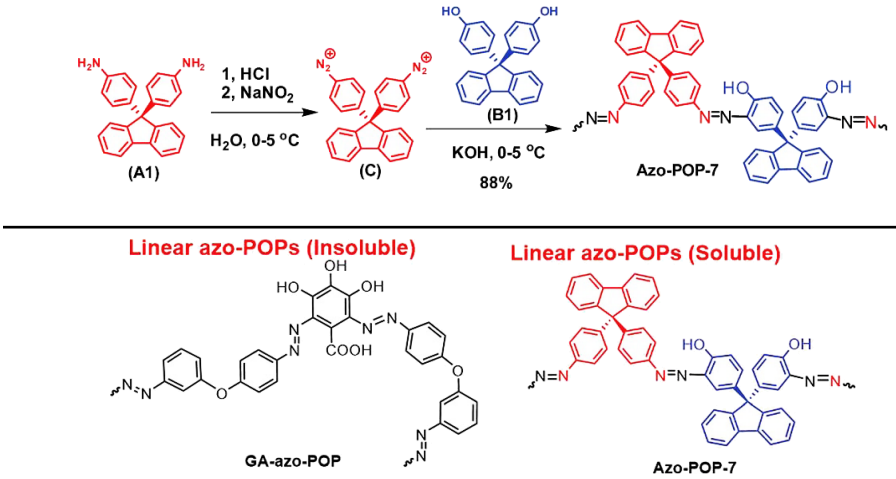

Figure 15. The synthesis of an azo-linked soluble porous polymer, Azo-POP-7, and a comparison to similar but insoluble AG-azo-POP[86‡]

‡Reprinted with permission from "A Soluble Porous Organic Polymer for Highly Efficient Organic-Aqueous Biphasic Catalysis and Convenient Reuse of Catalysts" by Fu, H. X.; Zhang, Z. H.; Fan, W.; Wang, S.; Liu, Y.; Huang, M. H., *J. Mater. Chem. A*, 2019**.** *7* (25), 15048–15053, Copyright 2019 by Royal Society of Chemistry.

Soluble porous polymers, such as the previously described PIMs, are of interest since they can be easily processed with solution techniques such as spin-coating and dip-coating. Additionally, their solubility allows characterization techniques such as solution Nuclear Magnetic Resonance (NMR) and Gel Permeation Chromatography (GPC). These polymers are usually linear with large rigid sections that leave packing voids in the solid state. The degree of rigidity of the polymer backbone and the presence of attached functional groups are usually essential to produce soluble porous polymers. If

the backbone of a soluble polymer is too flexible, it may be able to adopt a stable nonporous packing conformation. Alternatively, if the polymer backbone is too rigid and lacking in rotational freedom, the polymer may be insoluble. An example of this is Azo-POP-7, which is a linear azo-linked diphenylfluorene-based porous polymer **(figure 15)**.[86] Azo-POP-7 is soluble but can be compared to other linear azo-linked polymers such as GA-azo-POP which is insoluble **(figure 15)**. The monomers of the GA-azo-POP are more flexible, with an internal ether linkage and lack the large three-dimensionality of the diphenylfluorene monomers in Azo-POP-7.[86] Balancing the properties to create a soluble porous polymer, as is described in this example, can be challenging. Consequently, the soluble materials are the minority of the two given categories, due presumably to a greater degree of difficulty in their design and synthesis.

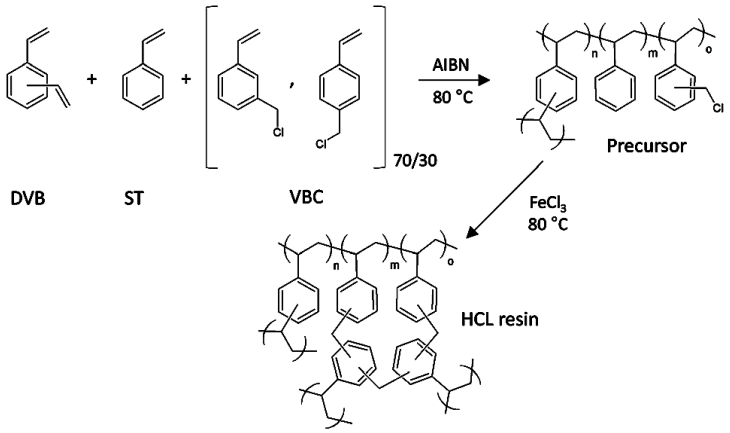

Figure 16. "Davankov resin" prepared from a styrene-based polymer[87]*****

*Reprinted with permission from "Synthesis and Adsorption Study of Hyper-Crosslinked Styrene-Based Nanocomposites Containing Multi-Walled Carbon Nanotubes" by Castaldo, R.; Avolio, R.; Cocca, M.; Gentile, G.; Errico, M. E.; Avella, M.; Carfagna, C.; Ambrogi, V., *RSC Adv.*, 2017**.** *7* (12), 6865–6874, Copyright 2017 Royal Society of Chemistry.

Insoluble porous polymers are the first, more explored, and more diverse of the two categories. The first permanently porous polymers reported were porous hyper-crosslinked polystyrene resins **(figure 16)**. These are sometimes called "Davankov resins" after the discoverer and were copolymers of styrene and divinyl benzene, which underwent a post-synthetic crosslinking step utilizing strong Lewis acids.[88,89] Similarly, many simple porous polymers can be produced from traditional nonporous polymers such as melamine-formaldehyde resins, phenol-formaldehyde resins, and poly(ethylene) through specific synthetic conditions or through various templating methods.[90–92] Since these materials are already produced affordably on the industrial scale, porous versions of these polymers could potentially be scaled accordingly. However, these polymers suffer from limited porosity control and tunability. Since these polymers are based on simple, established polymer chemistries, they are inherently less tailored towards specific applications and usually lack the potential for functionalization and modification. Control of the porosity in these systems is usually limited by the reaction conditions or templating methods utilized.

To produce porous polymers with control over the functionalization and porosity, many specialty porous polymers have been designed, utilizing complex monomers, reaction conditions, and catalysts. Some of these have displayed extremely high surface areas or performances towards targeted applications.

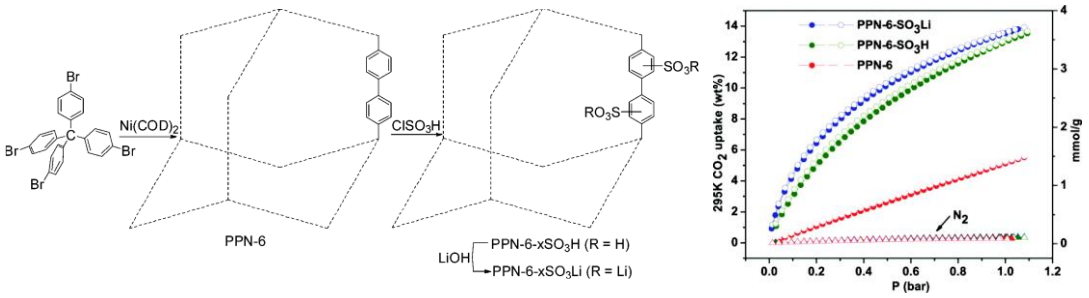

Figure 17. Synthesis PPN-6-xSO_3Li and corresponding CO2 adsorption isotherms[93†]

[†]Reprinted with permission from "Sulfonate-Grafted Porous Polymer Networks for Preferential CO2 Adsorption at Low Pressure" by Lu, W.; Yuan, D.; Sculley, J.; Zhao, D.; Krishna, R.; Zhou, H. C., *J. Am. Chem. Soc.*, 2011**.** *133* (45), 18126–18129, Copyright 2011 by American Chemical Society.

An example of this type of specialty porous polymer is the microporous PPN-6 which can be produced with extremely high surface areas **(figure 17)**.[93–95] This polymer is synthesized from a complex, three-dimensional aromatic monomer, tetrakis(4-bromophenyl)methane, which is coupled through the use of a stoichiometric amounts of an expensive nickel reagent, bis(cyclooctadiene)nickel(0), under scrupulously anhydrous conditions. This specialty porous polymer can be further functionalized towards applications such as CO_2 capture, where it has shown high performance.[93] Other polymers in this category include the Porous Aromatic Frameworks (PAFs)[40,96–98], Porous Organic Polymers (POPs)[99], Porous Polymer Networks (PPNs)[93–95,100–104], Covalent Organic Polymers (COPs)[105], and Hyper-Crosslinked Polymers (HCP)[88,106]. Some distinctions between these designations may be made, but they can be generalized as insoluble porous polymer networks. Overall, the use of complex monomers,

expensive catalysts, solvents, and processing steps limits most specialty porous polymers such as PPN-6 to production and study on the lab-scale.

One relevant strategy for the production of specialty porous polymers focuses on utilizing large, rigid three-dimensional monomers to create voids in the structure.[6,42,107] This approach can lead to enhanced porosity in polymers but is not infallible. Often, utilizing larger extended monomers does not result in a direct increase in porosity due to network interpenetration. Nevertheless, this strategy has been employed with a diverse number of monomers including tetraarylmethanes, triptycenes, triphenylbenzenes, porphyrins, phthalocyanines, aryladamantanes, arylfluorenes, triarylamines, and triphenylenes **(figure 18)**.[42]

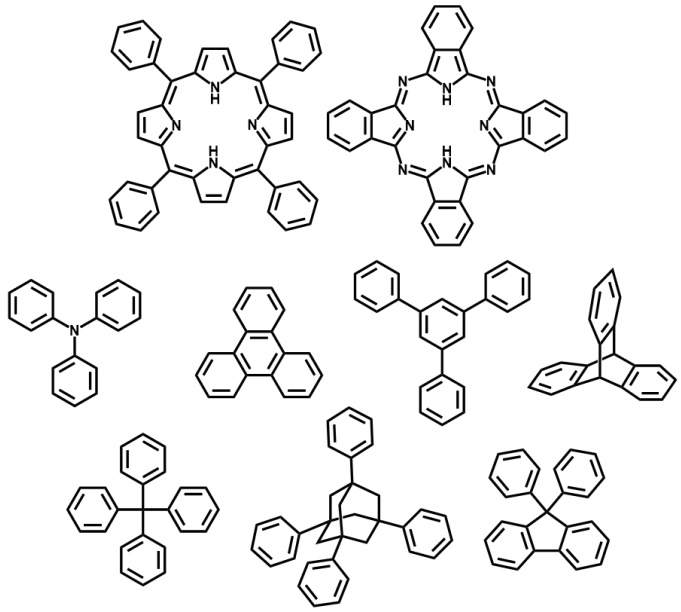

Figure 18. Large, rigid molecules utilized as monomers for porous polymers

A subset of monomers utilized for this approach are macrocycles and monomers with intrinsic porosity, which will be discussed at length in the following section.

I.v Macrocycle porous polymers

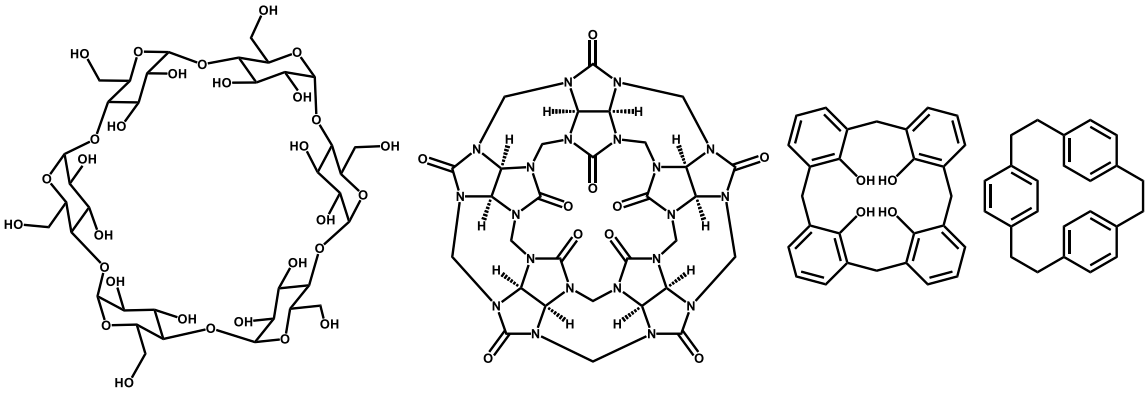

Figure 19. α-cyclodextrin, cucurbit[5]uril tetrahydroxycalix[4]arene, [2.2.2]paracyclophane macrocycles

There are many classes of organic macrocycles, such as cyclodextrins, cyclophanes, cucurbiturils, and calixarenes **(figure 19)**. Macrocycles have several properties which are beneficial for porous polymer construction; many macrocycles can be considered single molecular pores, exhibiting intrinsic porosity before being linked into polymers networks. Macrocycles with high affinities for binding molecular species have been developed in the well-studied field of host-guest chemistry.[108–114] Utilizing these as monomers for porous polymer synthesis allows for high performing materials for adsorption of specific species in targeted applications. Moreover, rigid macrocyclic rings, unlike other large molecular structures, are not amenable to self-interpenetration which often reduces porosity in porous polymers.

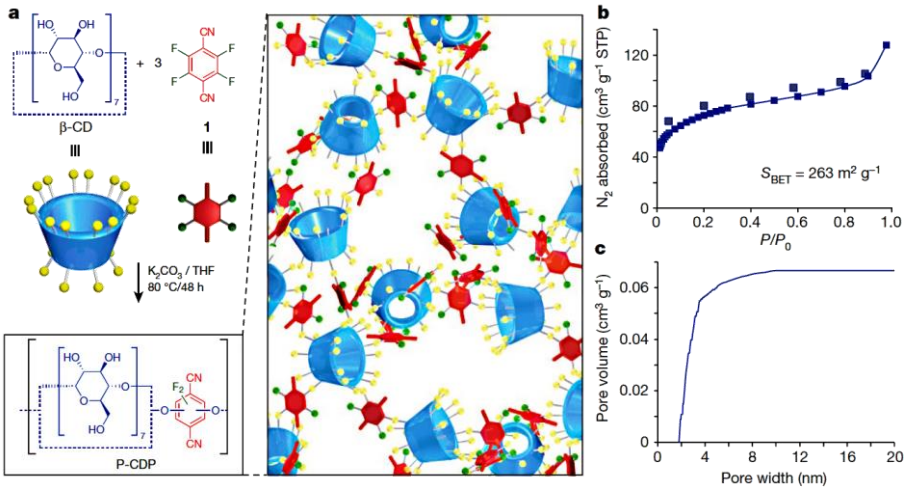

Figure 20. P-CDP, a cyclodextrin-based porous polymer[115‡]

‡Reprinted with permission from "Rapid Removal of Organic Micropollutants from Water by a Porous β-Cyclodextrin Polymer" by Alsbaiee, A.; Smith, B. J.; Xiao, L.; Ling, Y.; Helbling, D. E.; Dichtel, W. R., *Nature*, 2016**.** *529* (7585), 190–194, Copyright 2016 by Springer Nature.

Several different classes of macrocycles have been utilized to construct porous polymers.[116] Among these, cyclodextrins and calixarenes are of particular note, as these have successfully been employed to construct high-performing porous polymers towards specific applications.[115,117] A number of porous polymers constructed from cyclodextrins have been reported and have shown promise in water purification applications. An example of these materials is the Porous β-CycloDextrin Containing Polymers, P-CDP, which is constructed from β-Cyclodextrin crosslinked with tetrafuoroterephthalonitrile **(figure 20)**.[115] P-CDP was utilized to remove various organic micropollutants from water, including pesticides, plastic components, and pharmaceuticals. P-CDP showed

enhanced micropollutant removal performance over other sorbents such as activated carbons.[115]

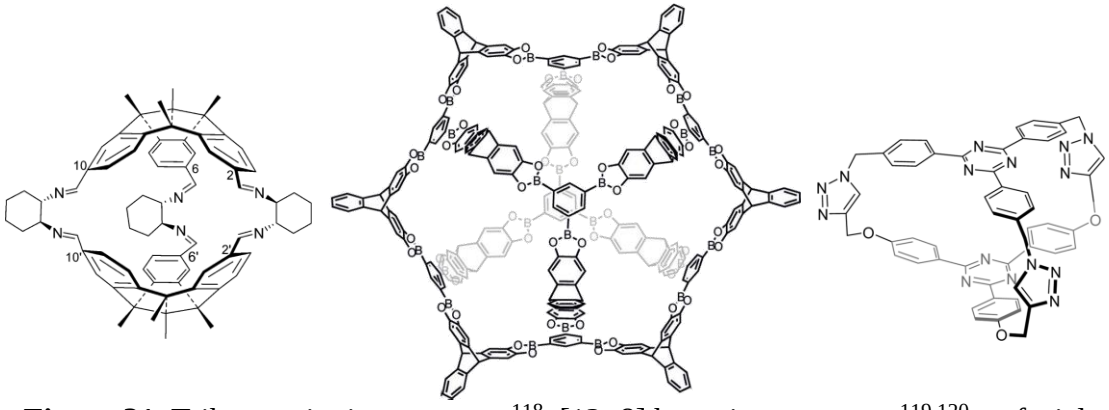

Figure 21. Tribenzotriquinacene cage[118], [12+8] boronic ester cages[119,120], cofacial organic cage[121]*

*Reprinted with permission from "C3-Symmetrical Tribenzotriquinacene Derivatives: Optical Resolution through Cryptophane Synthesis and Supramolecular Self-Assembly into Nanotubes" by Wang, T.; Zhang, Y. F.; Hou, Q. Q.; Xu, W. R.; Cao, X. P.; Chow, H. F.; Kuck, D., *J. Org. Chem.*, 2013**.** *78* (3), 1062–1069, Copyright 2013 by American Chemical Society.

*Reprinted with permission from "A Shape-Persistent Quadruply Interlocked Giant Cage Catenane with Two Distinct Pores in the Solid State" by Zhang, G.; Presly, O.; White, F.; Oppel, I. M.; Mastalerz, M., *Angew. Chemie Int. Ed.*, 2014**.** *53* (20), 5126–5130, Copyright 2014 by John Wiley and Sons.

*Reprinted with permission from "Cofacial Organic Click Cage to Intercalate Polycyclic Aromatic Hydrocarbons" by Samanta, J.; Natarajan, R., *Org. Lett.*, 2016**.** *18* (14), 3394–3397, Copyright 2016 by American Chemical Society.

Similarly, organic cages possess many of the same advantages previously described for macrocyclic monomers. Fundamentally, organic cages can be considered three-dimensional macrocycles, and consequently some can be directly constructed from two or more linked macrocycles **(figure 21)**. All organic cages can be thought of as intrinsically porous if they are rigid enough to maintain their structures and have small

enough pore windows to prevent self-interpenetration into their cavities; this designation may be given regardless of the measurable porosity in the packed molecular solid state, as packing modes often preclude gas access into interior pores. Another point of consideration when comparing organic cages to other starting materials is their pre-defined pore characteristics. The average pore window size in most porous polymers will be defined by the average, random arrangement of monomers in the structure; when utilizing intrinsically porous starting materials such as cavitands or large rigid monomers, the window sizes may be less distributed due to their structures and a reduced number of possible arrangements based on steric considerations. However, truly defined pores and pore windows are hard to achieve outside of crystalline materials. Organic cages offer potential to access the greatest possible control over pore characteristics in porous polymers. The pore size and window size of intrinsically porous organic cages should, theoretically, affect the porosity in derived polymers. The average pore characteristics of derived porous polymer will most likely be defined by the intrinsic pores of the organic cage starting material and the extrinsic pores between the linked cages.

Examples of porous polymers constructed from organic cages are fewer than those from macrocyclic monomers. In one characteristic example, porous cage frameworks “pCAGEs” were constructed from triangular prismatic cages assembled from triphenylbenzenes and cyanuric chloride **(figure 22)**.[122] The prismatic organic cages were connected via a nucleophilic aromatic substitution with several amine linkers to form polymers. The pCAGEs were compared against a control polymer, constructed

from the "half-cage," lacking intrinsic porosity. In this example, the control polymer and molecular cage had little porosity in comparison to the pCAGEs.[122]

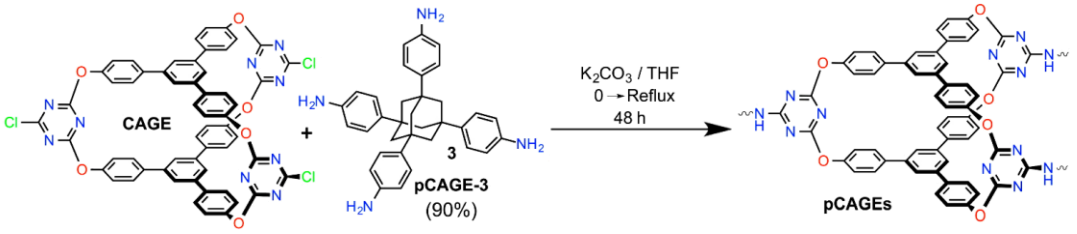

Figure 22. Porous "pCAGE" polymers constructed from prismatic organic cages[122†]

[†]Reprinted with permission from "Thinking Outside the Cage: Controlling the Extrinsic Porosity and Gas Uptake Properties of Shape-Persistent Molecular Cages in Nanoporous Polymers" by Buyukcakir, O.; Seo, Y.; Coskun, A., *Chem. Mater.*, 2015**.** *27* (11), 4149–4155, Copyright 2015 by American Chemical Society.

This is a phenomenon that has been reported for several intrinsically porous molecular compounds: when assessed as solid-state molecular materials, these compounds display little porosity, despite their structures having high void fractions. This is most likely due to close molecular packing, preventing the infiltration of probe gases. However, when utilized to construct porous polymers, an enhancement in the porosity is observed, even over polymers constructed from similar, nonporous monomers. This can be attributed to the rigid polymer network adequately spacing the intrinsically porous monomers so that their voids are accessible to probe gases.

While the approach of utilizing macrocycles and organic cages to construct porous polymers has advantages as described, it is important to compare polymers designed or produced with this method to others in the field. As previously stated, the major advantages of porous polymers are their potential scalability and affordability.

When porous polymers require expensive reagents and synthetic conditions that cannot be feasibly scaled beyond the lab, they enter competition with advanced porous materials such as MOFs and COFs.

Thus, any porous polymers designed utilizing this approach should account for these factors and attempt to utilize scalable polymer chemistries and macrocyclic/OC monomers which can be affordably sourced.

Calixarenes, specifically the subset resorcinarenes, are put forward as being particularly suitable to this end.

I.vi Calixarenes macrocycles

The term "calixarene" is a term derived from the Greek "calix" for a drinking vessel like a chalice and "arene," the common organic chemistry term for aromatic compounds.[123,124] In the pursuit of phenol-formaldehyde resin exploration, Zinke and Ziegler reported the first calixarene, the classic 4-tert-Butylcalix[4]arene, as glistening crystals from a recrystallized waxy-brown base-catalyzed condensate of p-tert-butylphenol and formaldehyde; however, no experimental evidence of the structure was provided at the time of publication.[123,125] For several decades following, Zinke, Cornforth, Kämmerer, Munch, and others worked on procedures the preparation of cyclic phenol-formaldehyde oligomers.[123,125] Due to instrumentation available at the time, definitive structures of the compounds were lacking. In the 1970's David Gutsche began work on these cyclic oligomers.[123] Gutsche presented the term "calixarene" to refer to these compounds at two symposia in 1975.[125] In 1978 he published a paper on a

few calixarenes with ^{1}H and ^{13}C-NMR and mass spectrometry of the compounds to support the proposed structures.[125]

Since that time, a great diversity of calixarenes have been reported. It's not feasible to describe the many derivatives here, but a summary of some of major classes is given as follows. "Calixarene," specifically, is usually used to refer to para-substituted phenols linked by a methylene bridges at the positions ortho to the -OH groups **(figure 23)**. The number of constituent phenol rings in the calixarene can vary, usually from four to eight, depending on the synthetic conditions. The standard notation, calix[*n*]arene, may be used where *n* indicates the number rings to clarify the size of the macrocycle in reference **(figure 23)**.[123–125] Pillararenes are similar to calixarenes, composed of para-substituted arenes where the functional groups are usually phenols or alkoxy groups; the methylene bridging pattern in pillararenes is alternating ortho/meta to each functional group, respectively **(figure 23)**.[126,127] This results in a distorted macrocyclic ring in comparison to the calixarenes. Resorcinarenes and pyrogallolarenes are similar to the calixarenes in their bridging substitution patterns **(figure 23)**. These two classes are derived from resorcinol and pyrogallol, having two or three hydroxy groups instead of the one from the phenol-derived calixarene.[123,124] Resorcinarenes and pyrogallolarenes as usually produced with carbon-based functional groups at the linking bridgeheads.

This is accomplished by utilizing various formyl-containing compounds and is compatible with a great number of groups, including alkyls and aromatics.

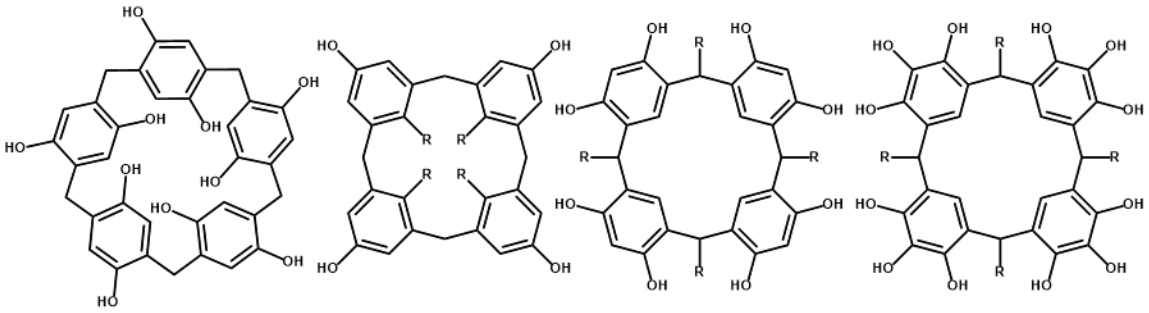

Figure 23. Pillar[5]arene, tetrahydroxycalix[4]arene, calix[4]resorcinarene, and calix[4]pyrogallolarene

Many of the initial syntheses for calixarenes reported by Zinke, Cornforth, Kämmerer, Munch, and Gutsche were performed under alkaline conditions.[125] Yields of calixarenes, depending on functional groups and ring numbers can vary greatly. Nevertheless, calixarenes have relatively facile syntheses and can often be purified adequately by simple methods such as washing and recrystallization. Condensation reactions of calixarenes and the similar macrocycles can often alternatively be catalyzed by acids instead of alkali conditions.

Under acidic conditions in alcohol solvents, many resorcinarenes can be produced in high yields with little modification of standard syntheses. Moreover, a range of R-groups are tolerated at the methine bridgehead in these macrocycles. Starting with resorcinol, many formyl-functionalized compounds can be utilized to produce resorcinarenes, in a modular fashion.[113,124] Perhaps the simplest example of this can be methylcalix[4]resorcinarene which can be produced from resorcinol and acetaldehyde in refluxing ethanol **(figure 24)**.[113] While some published procedures call for air-free,

anhydrous conditions, practically the syntheses are very robust and can be performed in open air and unpurified solvents. Resorcinarenes, depending on solubility, can usually be purified sufficiently by extraction, washing, and recrystallization.

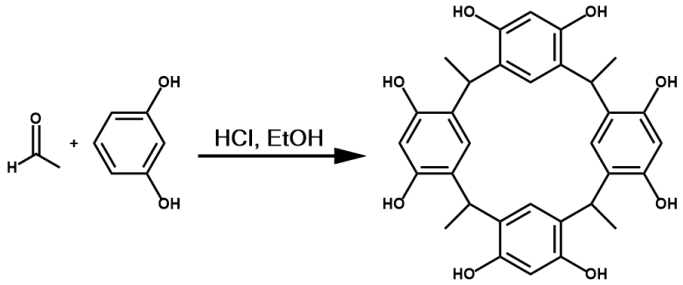

Figure 24. Common synthesis of methylcalix[4]resorcinarene[113]

Bridgehead-substituted calixarenes have four stereocenters that can lead to a number of possible diastereomers. These are commonly given as the crown (*rccc*), chair (*rctt*), diamond (*rcct*), and saddle (*rtct*), where *c* and *t* indicate relative *cis* and *trans* configurations of the bridgehead carbons **(figure 25)**.[125] Most simple syntheses result in several of these, although methods for producing specific diastereomers have been reported, if desired.[128,129] Under elevated temperatures and/or acidic/basic conditions some diastereomers may be interconvertible. Mixtures of the different diastereomers can be separated via common techniques such as chromatography or recrystallization if required.

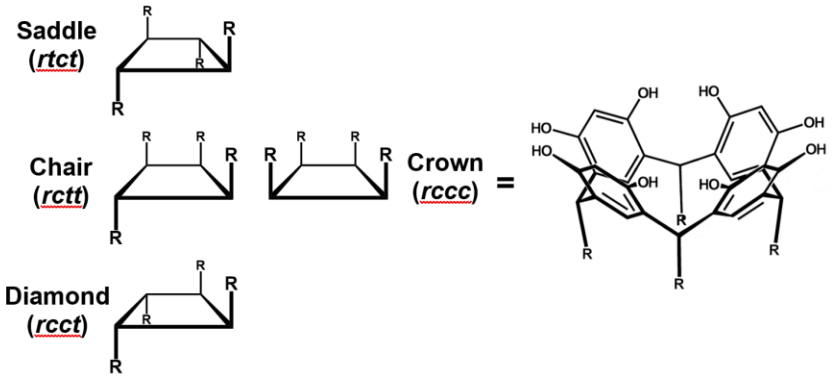

Figure 25. Common conformers of calixarenes with a depiction of the crown (*rccc*) conformers of calix[4]resorcinarene

Calixarenes have been utilized in such applications as host-guest chemistry, separations, sensing, and catalysis. When bridgehead-substituted calixarenes exist in the *rccc* crown conformation, the interior cavity acts as a hydrophobic pocket which can have a variety of interactions with small molecules and ions. One example of this ability of calixarenes to act as selective hosts for species is the use of calixarenes as cesium scavengers from mixtures of alkali metals in water.[110,130,131] Even simple calixarenes such as methylcalix[4]resorcinarene have demonstrated potential for this application **(figure 26)**.[131] Aqueous separations can be designed with calixarenes as dissolved selective agents that bind cesium ions, while eschewing sodium and smaller alkali ions; the cesium@calixarene complex can be separated from other dissolved ions by a nanofiltration membrane via size selectivity, allowing the small uncomplexed ions to pass through while retaining the larger cesium@calixarene.[131]

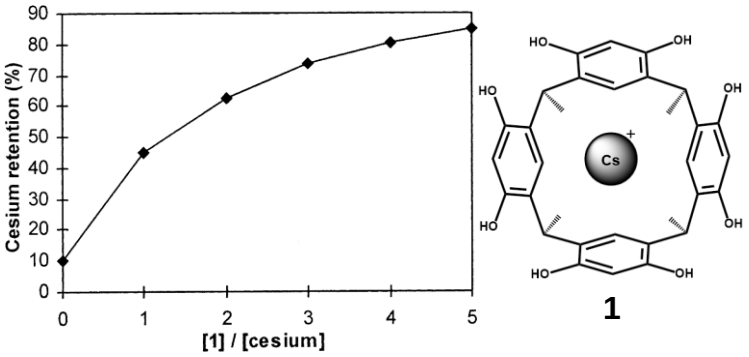

Figure 26. Cesium capture and retention by methylcalix[4]resorcinarene[131‡]

‡Reprinted with permission from "Cesium/Sodium Separation by Nanofiltration-Complexation in Aqueous Medium" by Chitry, F.; Pellet-Rostaing, S.; Nicod, L.; Gass, J. L.; Foos, J.; Guy, A.; Lemaire, M., *Sep. Sci. Technol.*, 2001**.** *36* (5–6), 1053–1066, Copyright 2001 by Taylor and Francis.

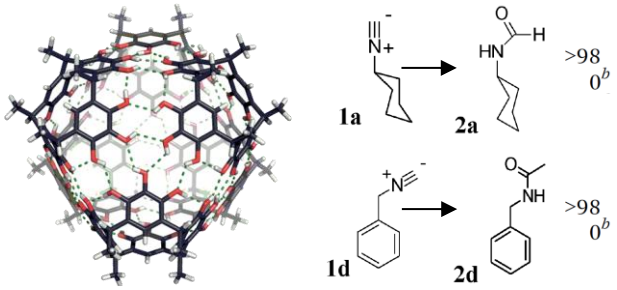

Figure 27. A hexameric hydrogen-bonded pyrogallolarene capsule[132] and several catalyzed isonitrile hydrations[133*]

*Reprinted with permission from "Catalysis inside the Hexameric Resorcinarene Capsule" by Zhang, Q.; Catti, L.; Tiefenbacher, K., *Acc. Chem. Res.*, 2018**.** *51* (9), 2107–2114, Copyright 2018 by American Chemical Society.

*Reprinted with permission from "Efficient Isonitrile Hydration through Encapsulation within a Hexameric Self-Assembled Capsule and Selective Inhibition by a Photo-Controllable Competitive Guest" by Bianchini, G.; Sorella, G. La; Canever, N.; Scarso, A.; Strukul, G., *Chem. Commun.*, 2013**.** *49* (46), 5322–5324, Copyright 2013 by Royal Society of Chemistry.

Beyond only binding guests, calixarenes have been utilized in organic catalysis through a number of different mechanisms. In a series of reactions reported to work

through a similar pathway, catalysis happens inside a hexameric capsule formed from six hydrogen-bonded calixarene molecules in water-saturated organic solvents **(figure 27)**.[132] Different reactions have seen enhancement by these capsules, such as hydration of isonitriles[133] and selective benzylation of aromatics[134]. These reactions usually rely on hydrogen bonding, size, and shape effects that are present within the confined hexameric "nanoreactors."[132] In the isonitrile example, hydration occurs only when the hexamer is present in water-saturated chloroform **(figure 27)**.[133] When the hexamer is absent or when resorcinol was present as a control, no reaction was observed.[133]

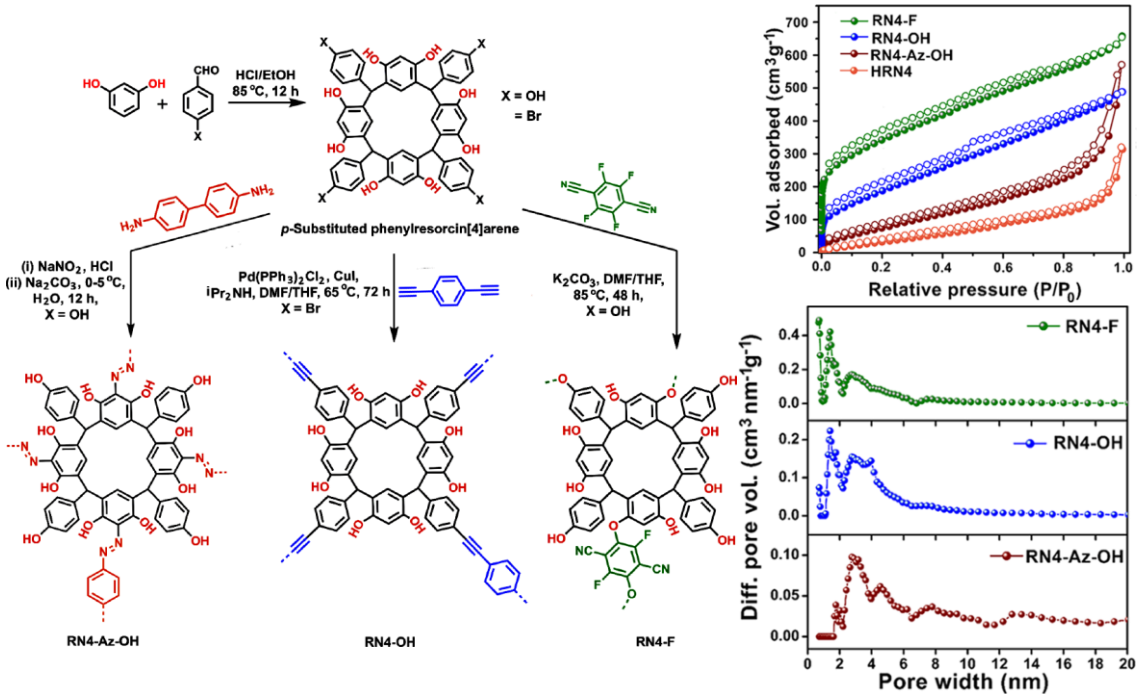

Figure 28. Synthesis of three different phenylresorcinarene-based porous polymers, RN4-AZ-OH, RN4-OH, and RN4-F[135†]

[†]Reprinted with permission from "Connecting the Dots: Knitting c-Phenylresorcin[4]Arenes with Aromatic Linkers for Task-Specific Porous Organic Polymers" by Giri, A.; Hussain, M. W.; Sk, B.; Patra, A., *Chem. Mater.*, 2019**.** *31* (20), 8440–8450, Copyright 2019 by American Chemical Society.

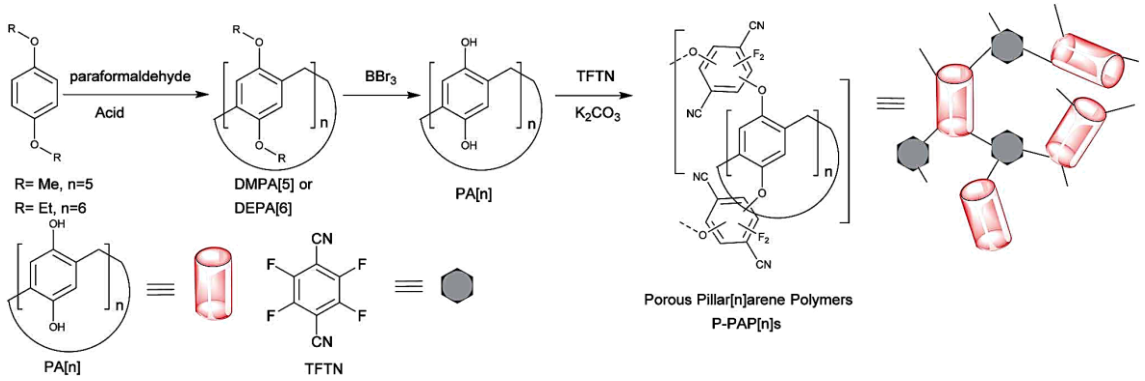

Figure 29. Synthesis of porous P-PAP[*n*]s from pillar[*n*]arene (*n* = 5, 6) crosslinked by tetrafuoroterephthalonitrile[136]‡

‡Reprinted with permission from "Pillar[n]Arene-Based Porous Polymers for Rapid Pollutant Removal from Water" by Lan, S.; Zhan, S.; Ding, J.; Ma, J.; Ma, D., *J. Mater. Chem. A*, 2017**.** *5* (6), 2514–2518, Copyright 2017 by Royal Society of Chemistry.

A number of porous polymers have been constructed from calixarenes-like compounds.[135,136,145–147,137–144] Many of the reported examples fall into similar categories: calixarenes linked via condensation with formaldehyde into porous gels [145,146], halo-functionalized calixarenes linked through palladium-catalyzed couplings[135,137,140–142,147] **(figure 28 and 30)**, calixarenes linked through direct azo coupling[135,138] **(figure 28)**, and calixarenes linked through nucleophilic aromatic substitution with fluoro-aromatics[135,139] **(figure 28 and 29)**. These porous polymers have been applied to a range of applications from the sequestration of organic dyes[135,141] and iodine[138,142,143] to the adsorption and conversion of CO_2.[135]

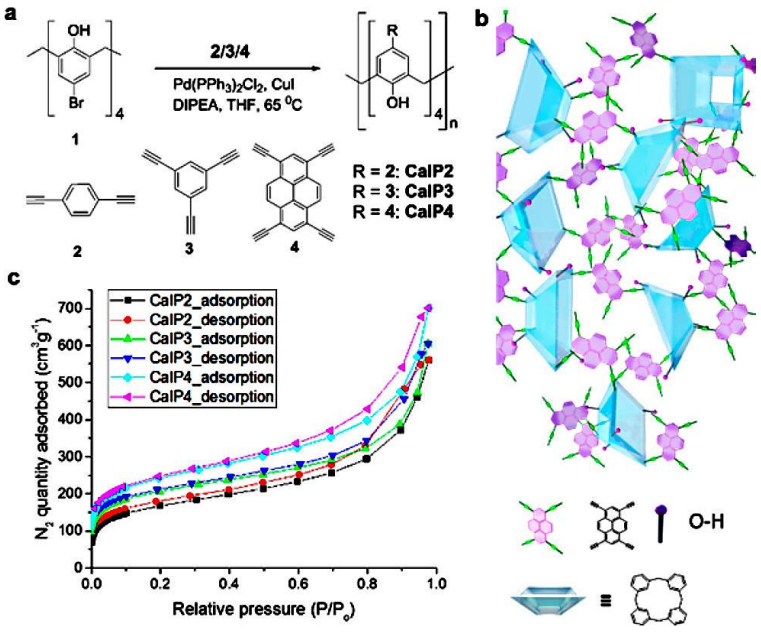

Figure 30. Calix[4]arene-based CalP(*n*)s prepared via a Sonogashira−Hagihara cross-coupling[137]*

*Reprinted with permission from "Porous Polycalix[4]Arenes for Fast and Efficient Removal of Organic Micropollutants from Water" by Shetty, D.; Jahovic, I.; Raya, J.; Asfari, Z.; Olsen, J. C.; Trabolsi, A., *ACS Appl. Mater. Interfaces*, 2018**.** *10* (3), 2976–2981, Copyright 2018 by American Chemical Society.

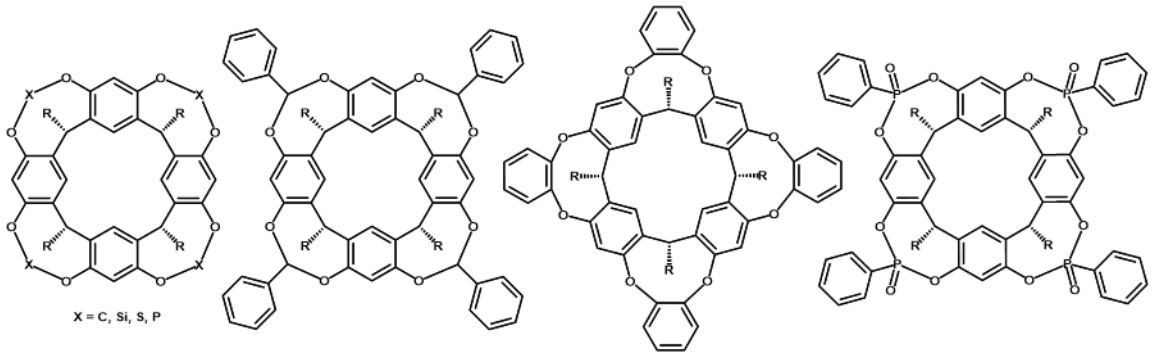

Figure 31. Calixarene-based cavitands with various bridging groups

The broadest definition of "cavitand" is a molecule which contains a cavity **(figure 31)**. However, the term is most often used in literature to refer to molecules

derived from calixarenes-like compounds which have multiple sets of "bridging" or connecting groups.[123–125] In practical synthesis this is usually accomplished by starting with one macrocyclic calixarene-type compound onto which bridging groups are installed to build another level of connection **(figure 32)**.[148–152]

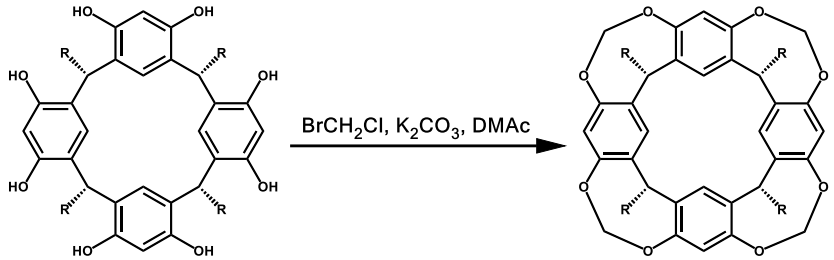

Figure 32. Common methylene bridged cavitand synthesis utilizing bromochloromethane

A number of different bridging groups have been reported including, alkyl and silylethers, phosphates, sulfates, aromatic ethers, and even other calixarenes. Complex cavitands with multiple levels of bridging groups have also been reported and are often referred to as "hemicarcerands"[113,125,153] which is derived from "prison," *carcer*, in Latin. Cavitands are more rigid than the calixarenes from which they are derived since added bridging groups prevent major conformational changes. Cavitands have been utilized for many of the same applications as calixarenes, in host-guest chemistry,[112,148,154,155], sensing,[156,157] and catalysis[108]. Cavitands, even over calixarenes, are known for strongly binding diverse guests[158], sometimes forming stable complexes up to high temperatures. One interesting example of guest binding is a series of clathrates formed in zero-dimensional pores of crystals of dimethylsilyl-bridged

cavitands **(figure 33)**.[114,150] Clathrates of several of these gases such as CO_2 and Ar are stable above 100 °C, indicating the strength of the interactions in these complexes.[114]

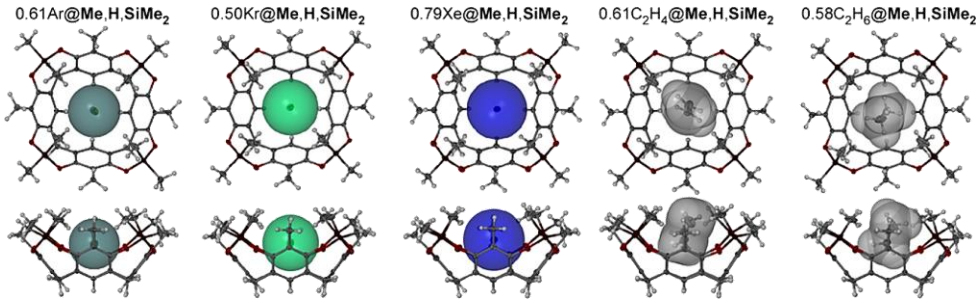

Figure 33. Crystal structures of enclathrated gases in the "0D pores" of dimethylsilyl-bridged cavitands[114†]

[†]Reprinted with permission from "Enclathration and Confinement of Small Gases by the Intrinsically 0D Porous Molecular Solid, Me,H,SiMe2" by Kane, C. M.; Banisafar, A.; Dougherty, T. P.; Barbour, L. J.; Holman, K. T., *J. Am. Chem. Soc.*, 2016**.** *138* (13), 4377–4392, Copyright 2016 by American Chemical Society.

Cavitands have been utilized for interesting catalytic applications. In one reported example a phenylphosphonate-bridged cavitand was found to strongly bind primary alkyl ammonium ions **(figure 34)**.[108] When reacted with methyliodide, the selective formation of the monomethylated products was observed; the cavitand acts as an intermolecular protecting group and prevents further alkylation that would occur under normal reaction conditions.[108]

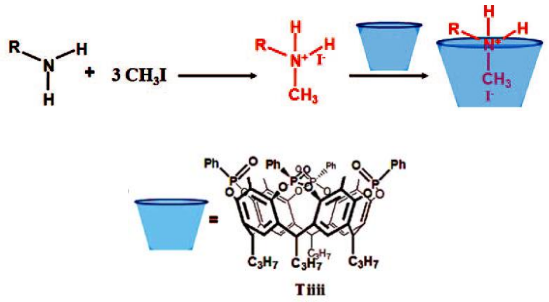

Entry	Amine	*T* (°C)	Yield (%)
1	$C_2H_5NH_2$	25	96
2	$C_3H_7NH_2$	25	98
3	$C_4H_9NH_2$	25	100
4	$C_7H_{15}NH_2$	25	100
5	$C_6H_{11}NH_2$	45	97
6	$C_6H_5NH_2$	45	99

Figure 34. Selective monomethylation of alkylamines in a phosphate-bridged cavitand[108‡]

‡Reprinted with permission from "Highly Selective Monomethylation of Primary Amines through Host-Guest Product Sequestration" by Yebeutchou, R. M.; Dalcanale, E., *J. Am. Chem. Soc.*, 2009**.** *131* (7), 2452–2453, Copyright 2009 by American Chemical Society.

Porous polymers constructed from cavitands are lacking. In one possible example, a similar reaction to the benzene-bridged cavitand-forming reaction was utilized to produce the porous polymer networks **(figure 35)**.[139] Methylcalix[4]resorcinarene was condensed with several 1,2,4,5-tetrafluorobenzene compounds in an attempt to favor the intramolecular ortho-linking of adjacent resorcinol -OH groups and produce a cavitand-based porous polymer.[139] The proposed resulting polymer structure is that of a repeating cavitand and ^{19}F ssNMR evidence of almost complete polymerization was given to support this.[139] However, the linking structure cannot be definitively verified to be the uniform ortho-pattern that would be required to produce a repeating cavitand structure. Unless pre-constructed cavitands are utilized to produce porous polymers or more advanced structural determinations are made, there is an absence such materials reported in literature.

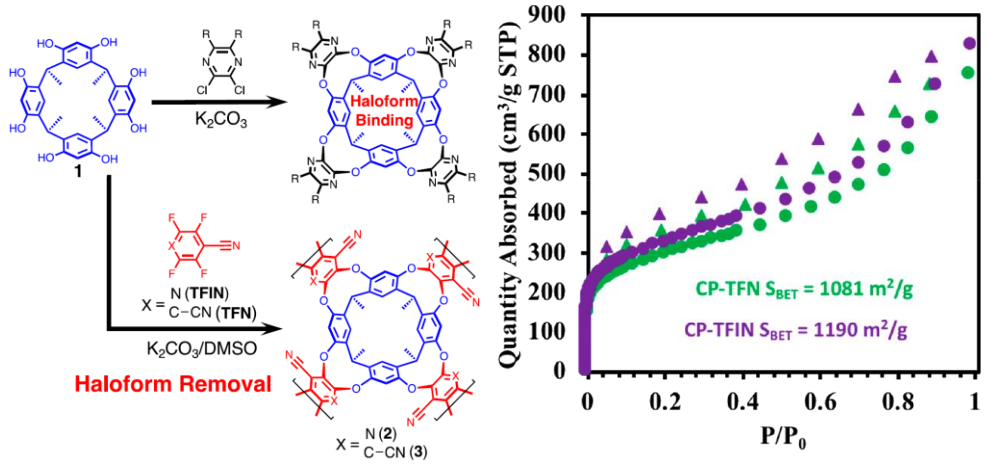

Figure 35. A calixarene-based PPN, CP-TFIN, utilized for haloform removal from water[139]*

*Reprinted with permission from "Resorcinarene Cavitand Polymers for the Remediation of Halomethanes and 1,4-Dioxane" by Skala, L. P.; Yang, A.; Klemes, M. J.; Xiao, L.; Dichtel, W. R., *J. Am. Chem. Soc.*, 2019**.** *141* (34), 13315–13319, Copyright 2019 by American Chemical Society.

Quite a few organic cages have been constructed from calixarenes and calixarene-derived cavitands **(figure 36)**.[159,160,169,161–168] Reported cages have been constructed from one to six macrocyclic units with a variety of "pillar" or connecting groups **(figure 36)**. Many of these reported cages have been formed through dynamic imine chemistry,[163,166,170] **(figure 3)** with some other examples being linked through alkyl ether or thioether groups,[165,168,169] or through Betti/Mannich-type reactions utilizing formaldehyde and alkyldiamines.[159,161,162]

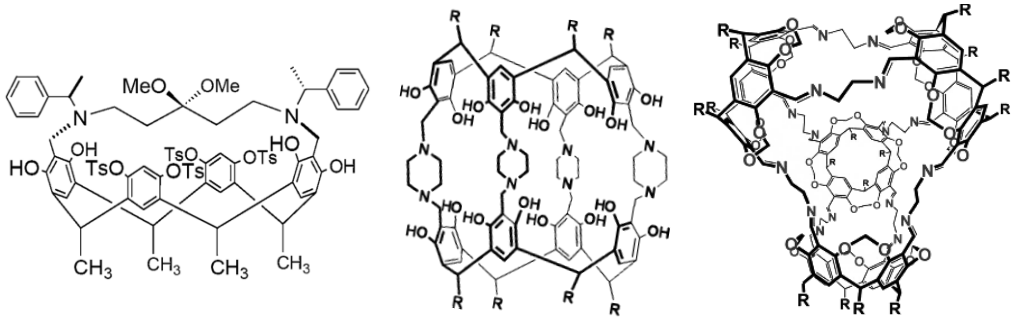

Figure 36. Organic cages derived from one,[161] two,[162] and four calixarenes[167†]

[†]Reprinted with permission from "Enantioselective Addition of Diethylzinc to Benzaldehyde Catalysed by Chiral, Bridged Resorcinarenes: A Stereoselectivity Model Based on Chirality Transfer" by Arnott, G.; Hunter, R., *Tetrahedron*, 2006**.** *62* (5), 992–1000, Copyright 2006 by Elsevier.

[†]Reprinted with permission from "Piperazine Bridged Resorcinarene Cages" by Kodiah Beyeh, N.; Valkonen, A.; Rissanen, K., *Org. Lett.*, 2010**.** *12* (7), 1392–1395, Copyright 2010 by American Chemical Society.

[†]Reprinted with permission from "Solvent Effects in Thermodynamically Controlled Multicomponent Nanocage Syntheses" by Liu, X.; Warmuth, R., *J. Am. Chem. Soc.*, 2006**.** *128* (43), 14120–14127, Copyright 2006 by American Chemical Society.

Many calixarene-derived organic cages can form stable host-guest complexes with small-molecules and solvents.[160,162,169] The encapsulation of small molecules has been utilized to study a phenylnitrene rearrangement reaction;[171] in the study, encapsulated phenyl azide is protected from bimolecular interactions, allowing the observation of the intramolecular rearrangement by NMR.[171] While well-studied for fundamental reasons, there is a lack of reported applications of or materials derived from calixarene-derived organic cages.

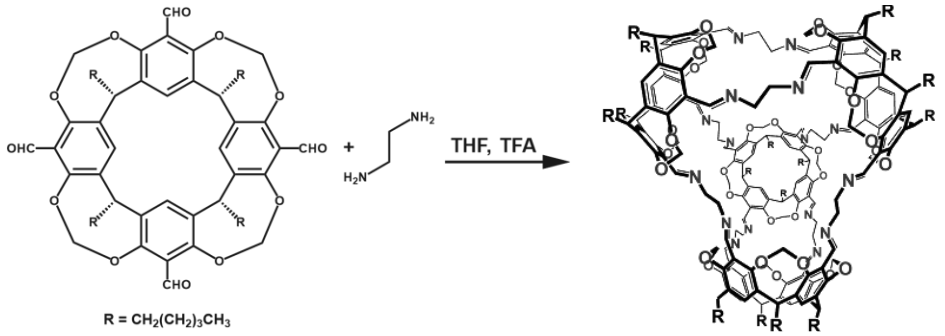

Figure 37. Synthesis of a tetrameric organic cage based on four imine-linked calixarene-cavitands[167]‡

‡Reprinted with permission from "Solvent Effects in Thermodynamically Controlled Multicomponent Nanocage Syntheses" by Liu, X.; Warmuth, R., *J. Am. Chem. Soc.*, 2006**.** *128* (43), 14120–14127, Copyright 2006 by American Chemical Society.

I.vii Novel calixarene porous polymers

As described in previous sections, there are reports of a variety of different porous polymers constructed from calixarene and calixarene-like starting materials. Additionally, the advantages of utilizing macrocyclic starting materials to construct porous polymer were also described, including advantages in porosity control, selectivity towards adsorbents, and structural functionality.

While several classes of calixarene-based porous polymers have been reported, cavitand and organic cage-based porous polymers are lacking. From the reported porous polymers constructed from calixarenes, there is deficiency of materials that are scalable, being based on well-developed polymer chemistries and affordable reagents. Cavitands and organic cages should be particularly promising starting materials for porous polymer due to their strong affinities for specific guest molecules, and their inherent porosities. Additionally, while calixarenes have high degrees of conformational mobility, cavitands

and organic cage starting materials could result in porous polymers with enhanced porosity based on their pre-defined molecular pores.

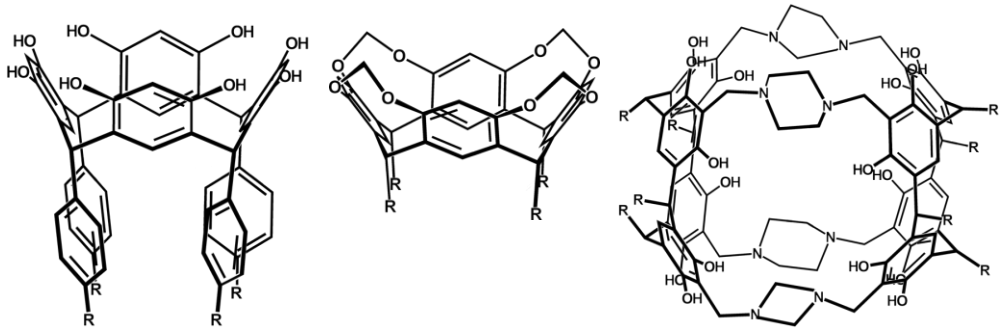

Figure 38. Phenylcalix[4]resorcinarene, methylene-bridged calix[4]resorcinarene cavitand, and piperazine pillared resorcinarene cage

There are many calixarene and calixarene-like macrocycles which could be advantageous as monomers to constructing porous polymers. As described in previous sections, molecular size, shape, and rigidity are important considerations in monomer selection, with large rigid three-dimensional monomers being the most desired. Additional non-property factors that should be kept in consideration when selecting starting materials are affordability and scalability; while scientific explorations of materials are important, designing materials which could be applied to real-world applications is also desirable. Taking these criteria into consideration, phenylcalix[4]resorcinarenes stand out as potential monomers for porous polymers **(figure 38)**.

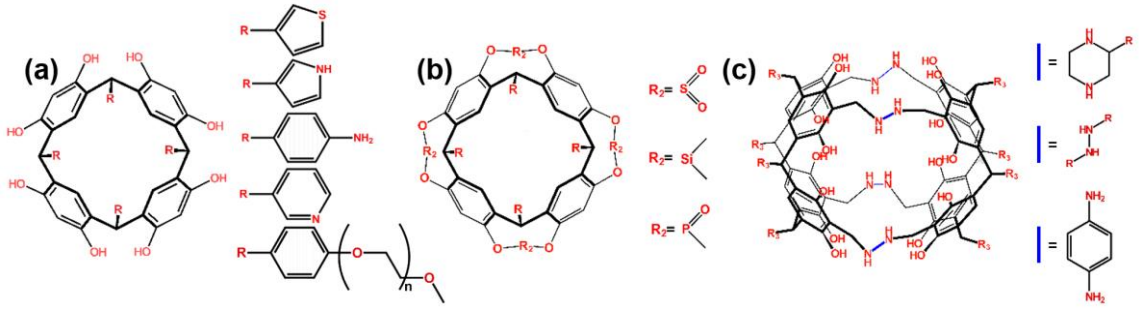

Figure 39. (a) Resorcinarene macrocycle structure with variable R representing "foot" groups. (b) Bridged resorcinarene cavitand with R_2 representing rim-bridging group. (c) Resorcinarene cage with "—" representing the linking group.

Phenylcalix[4]resorcinarenes can be produced from resorcinol and benzaldehydes in simple condensation reactions with high yields.[172] These compounds are large, three-dimensional, somewhat rigid, easily scalable, and can be produced from affordable reagents. Phenyl-resorcinarenes are quite modular, with their syntheses being amenable to substitution of various functionalized benzaldehydes with little modification.[148,173,174] Their porosity in the solid-state porosity can be verified in their open crystal structures, where they form "water channels" and from empirical BET measurements which have confirmed their moderate gas adsorption capacities.[172] Many possible directions of investigation could be pursued, utilizing phenyl-resorcinarenes as starting materials for porous polymers; keeping to the criteria of scalability and affordability, these phenyl-resorcinarenes are directly applicable to well-developed phenol-aldehyde[175] type polycondensation. Investigations of porous "Novalac resins," constructed from the phenyl-resorcinarenes, followed by studies of derivatized examples were examined and described in the following chapter (CHAPTER II).

In comparison to calixarenes, cavitands have reduced conformational mobility which is of potential benefit in the construction of porous polymers. As described in previous sections, a variety of bridging groups and levels may be utilized to construct cavitands. The same criteria used to select a calixarene monomer can be applied to cavitands. Of the different types of cavitands that could potentially be utilized as monomers for porous polymers, methylene bridged-cavitands fit many of these criteria, being simple to produce from resorcinarenes and dihalomethanes in reasonable yields.[151] However, a limited number of cavitands can be produced from resorcinarenes since some functionalities are not tolerated by the bridging reactions. Generally, resorcinarenes with alkyl "feet" groups can be easily converted to the methylene-bridged cavitand, while phenyl-resorcinarenes are not as successful. Speculatively, solubility and steric factors may affect the reaction outcomes. Being limited to alkyl- "footed" resorcinarene cavitands, initial investigations of these as monomers for porous polymers can focus on identifying what effects of the rigid "cup" part of the cavitand has on the porosity of resulting porous polymers, versus those of the flexible calixarene "cup," versus the size and shape "feet" groups. These investigations are described in CHAPTER III.

Organic cages derived from calixarenes, like cavitands are defined three-dimensional structure that can act as molecular pores. As described in previous sections, organic cages offer the potential for additional degrees of control in porous polymer construction due to their pre-defined pore environments. Even over other intrinsically porous and sterically hindered starting materials, the pore structure and window size in

organic cages could, potentially, affect the porosity in resultant porous polymers - a level of control which is generally only archivable in crystalline materials.

When attempting to apply the previously described criteria for monomer selection to organic cages, a common issue to organic cages arises. Generally, organic cages are inherently one of many possible products in their syntheses, resulting in lower yields and requiring complex separations. This directly reduces their scalability and affordability as monomers in porous polymer synthesis. Consequently, a "best-candidate" organic cage monomer is not an obvious selection. Continuing with resorcinarenes as a starting point, piperazine-pillared organic cages can be synthesized from inexpensive reagents and have reasonable yields but are not scalable due to a requirement for very dilute reaction conditions.[162] There are fewer options of polymer reactions to construct porous polymers from organic cages such as the piperazine-pillared resorcinarene; an obvious direction would be to utilize the hydroxyl groups as linking points. Polyether, polyester, and polyphosphazene chemistries are possibilities that were attempted. A description of these attempts is given in Chapter IV.

I.viii Summary and forward

Porosity is a material property which can be utilized for a variety of applications that employ the void space such as storage and separations. There are many classes of porous materials including activated carbons, zeolites, porous polymers, MOFs, COFs, and porous liquids. Of these, porous polymers have some advantages in chemical stability, affordability, and scalability.

Many approaches to producing porous polymers and controlling their porosity have been reported. Utilizing large, rigid, three-dimensional molecules as monomers is a common strategy to enhance porosity. A class of molecules particularly suited to this are macrocycles, which can possess intrinsic porosity.

In this work, a class of macrocycles, calixarenes, are utilized to construct a series of porous polymers. Polymers were made from a flexible calixarenes, a rigid calixarene cavitands, and a calixarene-derived organic cages with the objective of determining effects that size, shape, rigidity and intrinsic porosity of starting monomers have on the porosity of derived porous polymer networks.

CHAPTER II

PRE-STRUCTURED CALIXARENE-BASED PHENOLIC-ALDEHYDE POROUS POLYMER NETWORKS

II.i Introduction to porous Novolac resins and pre-structuring with calixarenes

Porous polymer networks (PPNs) are a class of amorphous organic porous materials that have demonstrated potential for applications such as CO_2 capture,[46,93,182,100,135,176–181] methane storage,[101,183,184] catalysis,[83,135,179] etc., while having advantages in scalability, affordability, and stability over other porous materials such as metal organic framework (MOFs).[40,42,43,88,97,185]

While PPNs with surface areas rivaling the most porous materials have been reported, these polymers are usually constructed from specialty monomers and expensive catalysts that would preclude their use in real-world applications.[40,94,95,98] Alternatively, porous versions of many ubiquitous commercial polymers constructed from affordable commodity chemicals such as melamine-formaldehyde resins,[91,100,180,186–188] phenol-formaldehyde (Novalac/Resol) resins,[176,189] crosslinked polystyrene,[181,190,191] and poly(ethylene)[92,192] have been reported, and these porous polymers have been applied to a number of applications such as CO_2 capture, ^{137}Cs removal, ion exchange, and porous membrane materials. One drawback to these materials is a lack of control over their porosity, which is usually derived from synthetic conditions rather than their limited structural features.

Many methods to control the porosity in PPNs have been explored such as chemical templating[91,92] and phase separation.[193–195] One straightforward method to affect the porosity in PPNs is to utilize large "pre-structured" three-dimensional monomers, providing some control over the local structure within the network and introducing additional functionality to the polymer backbone. Notable examples of this approach include work utilizing rigid three-dimensional molecules,[6,81,83,196] organic cages,[122] and macrocycles[106,115,117,197,198] to construct porous polymers.

One class of chemically diverse macrocyclic "cup-shaped" molecules that may have potential as monomers for a pre-structuring approach are calixarenes.[123,124,199] These large molecules can be synthesized from inexpensive phenols and aldehydes and display extensive "host" chemistry, acting as binding sites for small molecule "guests" which could be ideal for porous material applications.[108,112,114,155,200] Indeed, several calixarene-containing porous polymers have been reported to this end, with recent examples showing significant promise towards the sequestration of common pollutants and toxicants.[135,137–139,141,201]

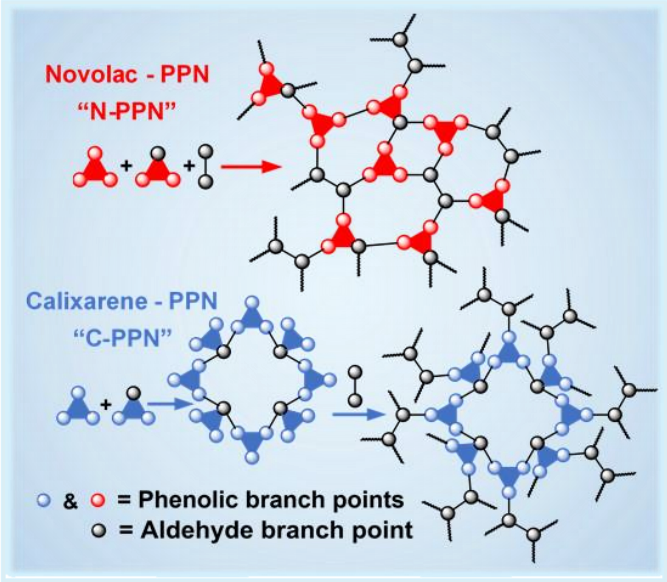

Figure 40. Depictions of Calixarene and Novolac polymer networks

In this work, a series of calixarene-based PPNs, **C-PPNs**, were constructed via the well-developed phenol-aldehyde-type polycondensation to assess if a pre-structing approach could be combined with simple and affordable PPN systems which are based on commercial polymers. For comparison purposes, a series of chemically similar "Novolac resin" PPNs, **N-PPNs,** were constructed from the same set aromatic subunits, but lacking the pre-structured calixarene macrocycles. The porosity of the PPNs was systematically studied with respect to synthetic conditions and monomer structure, utilizing 77 K N_2, 77 K Ar, and 273 K CO_2 gas adsorption isotherms, solid state nuclear magnetic resonance (ssNMR), and infrared (IR) spectroscopy to gain insight into the chemical characteristics of the polymers; and, elemental analysis (EA) via combustion and fast neutron activation analysis (FNAA) was utilized to confirm the similar composition of the **C-PPN** and **N-PPN.**

The potential application of structured **C-PPNs** for water remediation was explored by the simple sequestration of organic dyes and compared with **N-PPN**'s dye sorption rates and capacities, taking into account their respective porosities. Organic macromolecular polymers were used to model chemical fouling of PPN-surfaces in polluted water. Finally, sequestration performance by the chemically fouled **C-PPNs** and **N-PPNs** was used to assess how structured-resorcinarene binding sites might resist chemical fouling in complex, polluted matrices.

II.ii Experimental

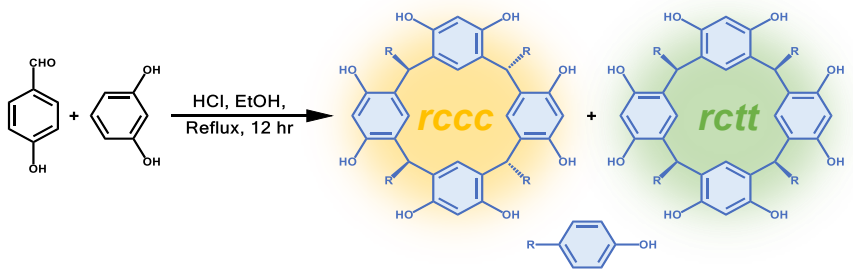

Figure 41. Synthesis of **4-OHPhRsC** via HCl-catalyzed condensation

4-hydroxyphenylcalix[4]resorcinarenes (**4-OHPhRsC**):

4-OHPhRsC was synthesized according to published procedures. 4-hydroxybenzaldehyde and resorcinol were refluxed in ethanol, utilizing HCl as a catalyst. The majority of solvent was removed via rotary evaporation, and the light-pink precipitate was filtered off and washed with cold ethanol. The solid product was analyzed by ^{1}H NMR and found to be close to a 1:1 mixture of the two predominate conformers, *rccc*-crown and *rctt*-chair. The mass was confirmed via FTMS-APCI. The

product was dried in an 80 °C oven for 12 h and used without separation due to the lability of these conformers under further reaction conditions. Average yields >80% were obtained.

General procedure for **C-PPN** synthesis:

0.2 g (0.23 mmol, 1 eqv.) of **4-OHPhRsC** was transferred to a 7 mL Teflon-lined steel autoclave. 0.06 g (0.47 mmol, 2 eqv.) terephthalaldehyde was dissolved in 1.6 mL of 1,4-dioxane and charged into the reactor. A catalyst (0.4 mL 3 M NaOH, 0.2 g t-BuONa, 0.4 mL DBU, 0.2 g TsOH, 0.2 g $AlCl_3$, 0.2 g $ZnCl_2$, 0.4 mL TFA, 0.05 g I_2, or 0.4 mL 12 M HCl) was added and the reactor was sealed and thoroughly agitated. The reactor was placed in a 220 °C oven for 24 h. All solid products were broken into pieces < 1 mm^3 and washed with approximately 100 mL of each, water, methanol, and acetone in order. The products were dried for 3 h at 80 °C in an oven and activated at 120 °C for 12 h under high vacuum (<100 μBar) before further analysis

C-PPN-n Syntheses:

0.2 g (0.23 mmol, 1 eqv.) of **4-OHPhRsC** was transferred to a 7 mL Teflon-lined steel autoclave. An appropriate amount of terephthalaldehyde (e.g. 0.157 g, 1.17 mmol, 5 eqv. for **C-PPN-5**) was dissolved in 1.6 mL of 1,4-dioxane and charged into the reactor. Next, 0.4 mL 12 M HCl was added and the reactor was sealed and thoroughly agitated. The reactor was placed in a 220 °C oven for 24 h. All solid products were broken into pieces < 1 mm^3 and washed with approximately 100 mL of each, water, methanol, and

acetone in order. The red-brown products were dried for 3 h at 80 °C in an oven and activated at 120 °C for 12 h under high vacuum (<100 μBar) before further analysis. Average yields >90% were obtained.

C-PPN-aldehyde variants:

The same procedure for the synthesis of the **C-PPN**s was utilized with the substitution of 0.157 g (1.17 mmol, 5 x 2 eqv.) isophthalaldehyde, 0.070 g (0.78 mmol, 3.33 x 3 eqv.) trioxane (formaldehyde), 0.245 g (1.17 mmol, 5 x 2 eqv.) 4,4'-diformylbiphenyl (**DFBP**), or 0.304 g (0.78 mmol, 3.33 x 3 eqv.) 1,3,5-tris(4-formylphenyl)benzene (**TFPB**) for the respective variants.

N-PPN-n Syntheses:

The same procedure for the synthesis of the **C-PPNs** was utilized with the alteration of 0.102 g (0.93 mmol, 1 eqv.) resorcinol and 0.113 g (0.93 mmol, 1 eqv.) 4-hydroxybenzaldehyde being substituted for **4-OHPhRsC** and combined with the appropriate amount of terephthalaldehyde (0.157 g (1.17 mmol, 5 eqv.) for **N-PPN-5**) before dissolving in 1.6 mL 1,4-dioxane. The products were obtained as dark-brown solids with >90% average yields.

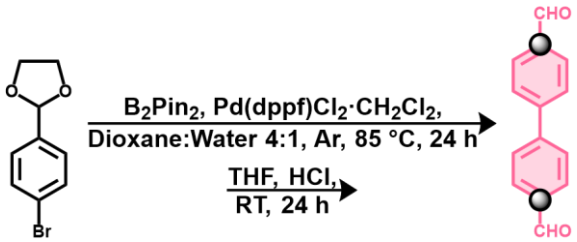

Figure 42. Synthesis of **DFBP** via a one-pot Suzuki-Miyaura coupling

4,4'-diformylbiphenyl (DFBP):

DFBP was synthesized starting from 4.4 g of the ethyl acetal of 4-bromobenzaldehdye, p-bromobenzaldehyde 1,3-dioxolane. This was carried out through a one-pot Suzuki-Miyaura coupling, utilizing 2.44 g Bis(pinacolato)diboron, 0.63 g [1,1′-Bis(diphenylphosphino)ferrocene]dichloropalladium(II)·CH_2Cl_2, 26.5 g K_2CO_3, and 90 mL p-dioxane:water 4:1 under an argon atmosphere at 85 °C for 24 h. Subsequent hydrolysis 2.8 g of the biphenyl acetal was carried out in 30 mL 4 M HCl in 70 mL tetrahydrofuran (THF) at room temperature for 24 h. The reaction was diluted with water and the product was collected as an off-white precipitate, recrystallized, and analyzed via ^{1}H NMR and FTMS-APCI to confirm a match with reported values.

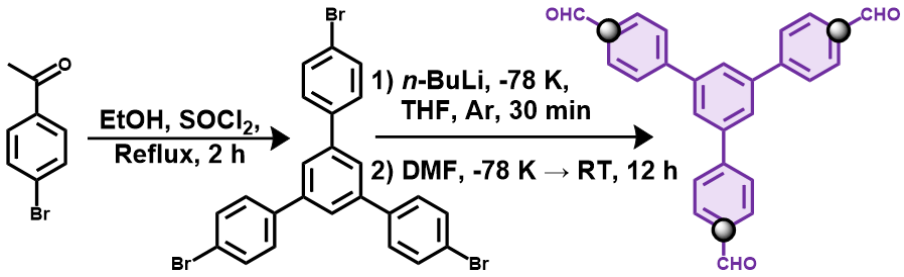

Figure 43. Synthesis of **TFBP** via an aldol cyclization and halo-lithium exchange

1,3,5-tris(4-formylphenyl)benzene (TFPB):

TFPB was synthesized according to published procedures. 10 g 4-bromoacetophenone was condensed through an aldol cyclization by refluxing in 15 mL ethanol and 10 mL thionyl chloride for 2 h to produce 1,3,5-tris(4-bromophenyl)benzene. Subsequently, formylation of 8.4 g of the pure aryl halide in 310 mL THF was carried out via treatment

with 37 mL of a 1.6 M *n*-butyllithium (*n*-BuLi) solution in hexanes at -78 °C under anhydrous conditions and an argon atmosphere. 30 min after the *n*-BuLi addition was complete, the arlylithium was quenched with 12 mL dimethylformamide (DMF) and left under argon overnight. Water and 3 M HCl were added sequentially and the mixture was allowed to stir for 2 h. The product was collected as a cream-colored precipitate, recrystallized, and analyzed via ^{1}H NMR and FTMS-APCI to confirm a match with reported values.

General sample analysis:

FTIR-ATR spectra were collected with an IRAffinity-1 with a PIKE MIRacleQ ATR sampling accessory. PXRD analysis was performed on a BRUKER-AXS D8 diffractometer. Zeta potentials were determined with a Malvern Panalytical Nanosizer ZS. SEM micrographs were collected with a FEI Quanta 600 FE-SEM. ssNMR spectra were collected on a Bruker Avance 400 with a Magnex wide-bore Magnet (^{13}C 101 MHz), and a Varian Inova 500 with an Oxford magnet and a 5 mm 4Nuc (^{1}H/^{19}F/^{31}P/^{13}C) probe was utilized to collect solution ^{1}H (500 MHz) and ^{13}C (126 MHz).

Dye sequestration procedure:

Five 120 mg samples of **C-PPN-5** or **N-PPN-5** from different syntheses were combined and broken into a fine powder with a scapula. The samples were soaked three times in approx. 40 mL of ultrapure water for 24 h followed by centrifugation and fresh water replacement. Finally, a similar one-week soak-wash procedure was followed by drying

in a 120 °C oven for 12 h. 20 mg of dried PPN was loaded into a 20 mL glass scintillation vial and 15 mL of the appropriate stock dye solution of either 60 ppm MeO, 196 ppm MeB, or 301 ppm RhB was added. The sample vials were sonicated for 30 s and placed in a vial shaker. At 12 h, 24 h, and 7 d an appropriate aliquot (300 - 800 μL depending on dye concentration) of solution was removed and centrifuged at 15,000 rpm for 2 min. Some of the pure supernatant was carefully pipetted off and diluted into 3 mL of water in a quartz cuvette. The entire experiments were repeated in triplicate. UV-Vis spectra and colorimetric measurements were collected with a Shimadzu UV-2450 spectrophotometer

BET Analysis:

Approximately 125 mg of pre-dried PPN was placed in a glass sample tube. The samples were evacuated to < 70 μBar for 12 h at 120 °C. The samples were massed and recorded. PPN samples were assessed via N_2 adsorption/desorption analysis on a Micromeritics ASAP 2420. Low pressure 77 K N_2, 77 K Ar, 273 K CO_2 isotherms for **C-PPN-5** and **N-PPN-5** were collected on ASAP 2020 instruments. BJH algorithms were applied to N_2 desorption data and DFT or NLDFT algorithms were applied to N_2, CO_2, and Ar adsorption data in Microactive software

Thermal analysis:

Thermogravimetric analysis (TGA) was carried out on a Mettler Toledo TGA/DSC 1 under either air or nitrogen atmospheres.

M-DSC was performed on a TA Instruments DSC 2500. Approximately 1-2 mg of each sample was ramped at 10 °C/min from -30 to 300 °C in 50 mg aluminum pans. Heating cycles were repeated to ensure reproducibility.

Elemental analysis:

EA (C:H mass fractions) were determined by combustion analysis at Atlantic Microlab (6180 Atlantic Blvd., Ste M Norcross, GA 30071).

Oxygen elemental analysis was determined via 14 MeV fast neutron activation analysis (FNAA) at Texas A&M University Elemental Analysis Laboratory using the direct comparator method. Approximately 500 mg of combined samples of each **C-PPN-5** and **N-PPN-5** were activated at < 100 μBar and 120 °C for 12 h and backfilled with an argon atmosphere. Approx. 500 mg of each sample was weighed and heat-sealed in clean LDPE irradiation vials under an argon atmosphere. Polyethylene cylinders doped with TiO_2 were used as oxygen calibrators. Empty irradiation vials were included in order to assess the oxygen blank contributions of the sample packaging. The $^{16}O(n, p)^{16}N$ reaction was utilized to measure oxygen. Sample aliquots, calibrators, and blanks were irradiated using a Kaman A-711 neutron generator at a nominal 14 MeV neutron fluence rate of 10^{10} $cm^{-2}s^{-1}$. The analysis of oxygen used cyclic (n=5) irradiations/counts of 20 s each. High-energy gamma radiation from the decay of ^{16}N was detected with a BGO spectrometer.

II.iii Results

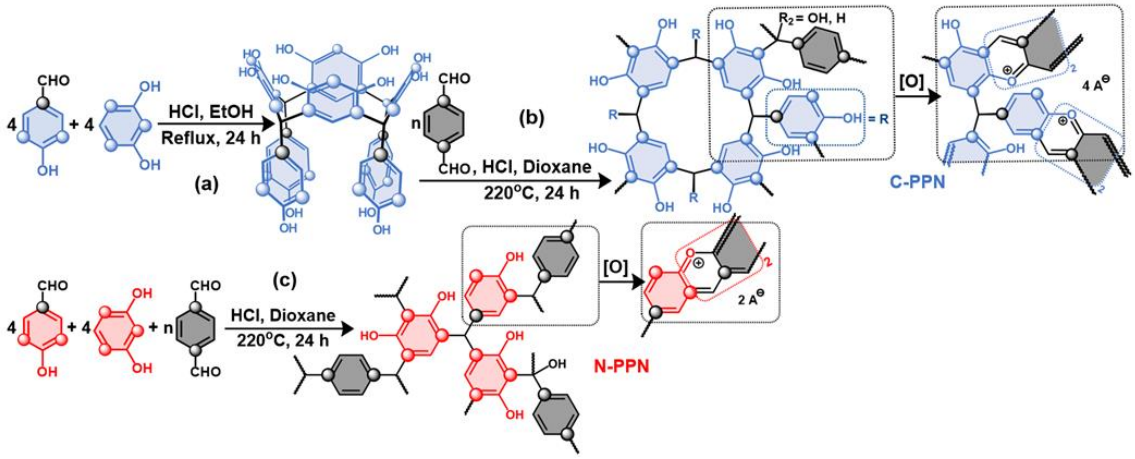

Figure 44. **Blue (○)/ red (○)** spheres indicate activated phenolic branch points and **grey (○)** spheres indicate formyl branch points. **(a)** Synthesis of 4-OHPhRsC macrocycle (depicted as the *rccc*-crown conformer) from 4-hydroxybenzaldehyde and resorcinol. **(b)** Subsequent condensation of **4-OHPhRsC** and terephthalaldehyde to the **C-PPN** with concurrent oxidation (depicted as a proposed structures). **(c)** Direct condensation of 4-hydroxybenzaldehyde, resorcinol, and terephthalaldehyde to the unstructured Novolac resin, **N-PPN** with concurrent oxidation (depicted as a proposed structure showing a few of many possible branching geometries and linkages).

The calixarene (resorcinarene) macrocycle selected for the synthesis of **C-PPNs** was 4-hydroxyphenylcalix[4]resorcinarene (**4-OHPhRsC**) due to its inherent porosity[135,172] and large, three-dimensional structure which is ideal for a pre-structuring approach. Additionally, this monomer can be produced from economical 4-hydroxybenzaldehyde (a food flavoring additive)[202] and the readily available di-phenol, resorcinol **(figure 41 and 44a)** The pre-structured **4-OHPhRsC** was synthesized according to reported procedures[172] and was isolated as a mixture of two conformers in good yield and purity as confirmed by ^{1}H NMR, Fourier transform mass spectrometry atmospheric pressure chemical ionization (FTMS-APCI), and IR spectroscopy **(figures 60, 61, and 70)**.

To develop conditions for a phenol-aldehyde-type polycondensation of the pre-structured **4-OHPhRsC** monomer and a selected terephthalaldehyde comonomer **(figure 44b)**, conditions for similar PPN syntheses and traditional polymerization reactions were identified from literature.[46,179,182] From the standard conditions, parameters were altered one-at-a-time to identify optimal conditions for the pre-structured **C-PPN** syntheses.

To screen for an effective catalyst, a range of acidic and basic catalysts were examined under the same temperature and solvent conditions. Brunauer-Emmett-Teller (BET) nitrogen gas adsorption isotherms were used to assess the porosity of the products. When no catalyst or when basic catalysts such as sodium hydroxide, sodium *tert*-butoxide, and 1,8-Diazabicyclo[5.4.0]undec-7-ene (DBU) were used, either no solid product or nonporous polymers were obtained. Of the acidic catalysts, tosylic acid (TsOH), aluminum chloride ($AlCl_3$), zinc chloride ($ZnCl_2$), trifluoroacetic acid (TFA), and molecular iodine (I_2) all produced porous polymers **(figure 45a)**. Interestingly, these catalysts all resulted in polymers with similar microporosity, with pore sizes ranging from 12 to 16 Å as calculated from N_2 adsorption isotherms. These pore sizes agree well with the crystallographic sizes of the **4-OHPhRsC** macrocycle, which are on the order of 12 Å.[135,172] Consequently, it is hypothesized that micropore structure of the polymers in these PPNs is significantly influenced by the pre-structuring of the starting calixarene.

12 M hydrochloric acid (HCl) was found to outperform other acid catalysts in producing a porous polymer, resulting in a product that had mixed porosity similar to many typical PPNs with 516 mL/g total porosity and a BET surface area (S_{BET}) of 580

m^2/g **(figure 45a)**, and was subsequently selected as the catalyst to perform further optimization experiments.

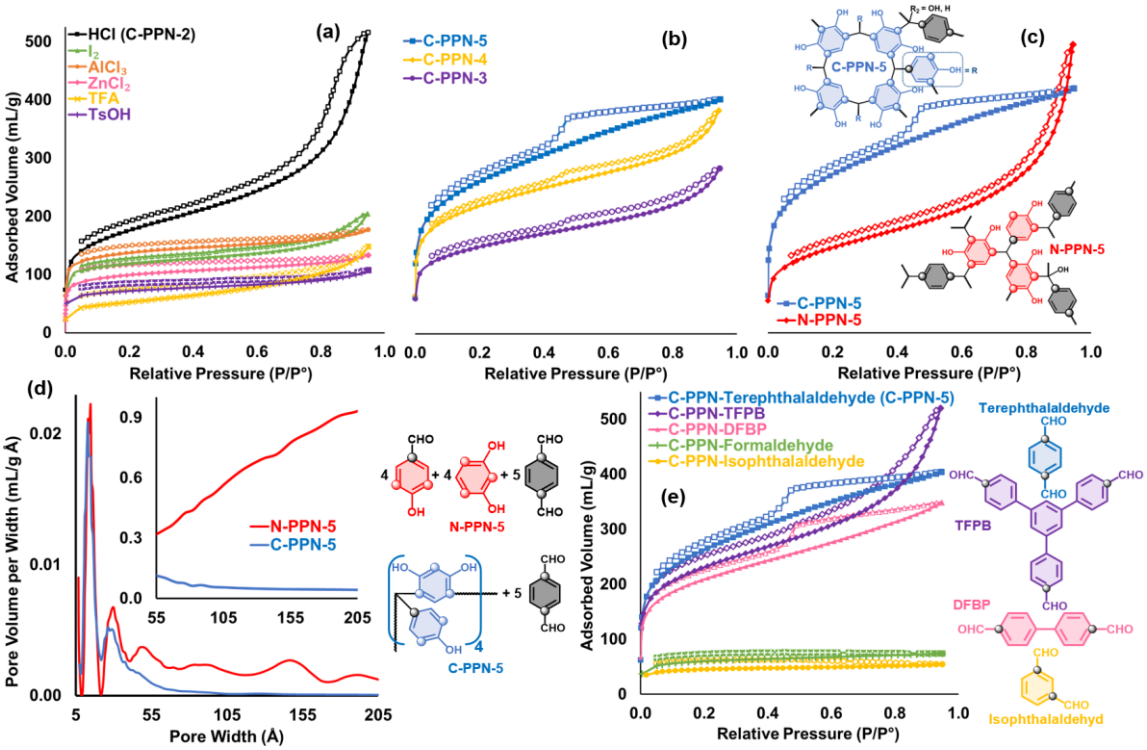

Figure 45. Solid and open marks indicate adsorption and desorption, respectively; **blue (○)/ red (○)** spheres indicate activated phenolic branch points and **grey (○)** spheres indicate formyl branch points. **(a)** N_2 adsorption isotherms of **C-PPN-2**s synthesized with acid catalysts. **(b)** N_2 adsorption isotherms of **C-PPNs** with increasing equivalents of terephthalaldehyde. **(c)** Comparison of N_2 adsorption isotherms of unstructured **N-PPN-5** to resorcinarene-based **C-PPN-5**. **(d)** NLDFT N_2 adsorption pore size distribution of **N-PPN-5** and **C-PPN-5**; inset of Barrett-Joyner-Halenda (BJH) N_2 desorption pore size distribution **(f)** N_2 adsorption isotherms of **C-PPN**-variants depicted with their aldehyde comonomers.

The next factor that was examined was the ratio of comonomers. An interestingly strong dependence of the resultant porosity was observed as the terephthalaldehyde ratio was increased relative to the **4-OHPhRsC**. Initially, the porosity of the PPN dramatically decreased in the higher-pressure regime (516 to 288 mL/g) as the ratio of

terephthalaldehyde was increased from 2 to 3 eqv., **C-PPN-2** and **C-PPN-3**; a subsequent increase to 4 eqv., **C-PPN-4**, increased the overall porosity and microporosity (385 mL/g and 713 m^2/g S_{BET}) **(figure 45b)**. When the ratio was raised to 5 eqv., **C-PPN-5**, the maximum microporosity of the **C-PPN** series was observed with an average S_{BET} of 844 m^2/g and average total porosities of 412 mL/g. Utilizing both the typical Barrett-Joyner-Halenda (BJH) N_2 desorption algorithm and a N_2 non-local density functional theory adsorption (NLDFT) algorithm for carbon surfaces, over 90 % of the porosity of the **C-PPN-5** the of aldehyde sample was determined to be from pores less than 60 Å in width **(figure 45d)**. The micropore size was determined by 77 K N_2, 77 K Ar, and 273 K CO_2 adsorption algorithms to be between 13 - 15 Å, with CO_2 indicating additional pores at 5 - 8 Å **(figures 45d, 64, and 65)**.

As the terephthalaldehyde ratio was further increased to 6 and 7 eqv., **C-PPN-6** and **C-PPN-7 (figure 63)**, it was found that the PPNs' overall porosity decreased to 409 and 385 mL/g, respectively. Once the excess terephthalaldehyde was increased to 8 eqv., **C-PPN-8**, the product developed a Type II isotherm[4] (509 mL/g); this trend continued with 9 eqv., **C-PPN-9**, subsequently, with the porosity decreasing significantly to 358 mL/g **(figure 63)**.

Alteration of other reaction conditions such as solvents, HCl concentration, and temperature resulted in low porosity or nonporous polymers.

After satisfactory identification of reaction conditions which produced PPNs from the calixarene macrocycle, several tests were devised to attempt to probe chemical and structural factors involved in the resultant porosity. For comparison purposes,

chemically equivalent (based on aryl starting materials) unstructured porous resorcinol-based Novolac resins, **N-PPNs**, were constructed to ascertain what affects the **4-OHPhRsC** structure has on the **C-PPNs**. To accomplish this, the same molar equivalents of the individual starting materials used to construct calixarene, resorcinol and 4-hydroxybenzealdehyde, were combined with the corresponding ratio of comonomer terephthalaldehyde under the same reaction conditions used to make the **C-PPNs (figure 44c)**. The resulting **N-PPN-5** was assessed by N_2 adsorption and were found to have different porosities from the equivalent **C-PPN-5 (figure 45c)**; **N-PPN-5** displays a meso/macroporous Type II adsorption isotherm **(figure 45c)** with an average total porosity of 561 mL/g and average surface areas of 656 m^2/g. Utilizing the same methods as the **C-PPNs**, **N-PPN-5's** pores were determined to be broadly distributed across the 20 - 200 Å range, with greater than 50% of the pore volume arising from pores larger than 60 Å **(figure 45d)**. Reproducibility is a common issue in PPN synthesis, as porosity is often dependent on complex reaction conditions such as heating rates. To ensure that the observed differences in porosities between **C-PPN-5** and **N-PPN-5** was consistent and not the result of unaccounted differences in reaction conditions, the sample syntheses were replicated seven times. The significant differences in porosity between **C-PPN-5** and **N-PPN-5** were confirmed in these repeated syntheses, resulting in similar isotherms **(figure 46)**.

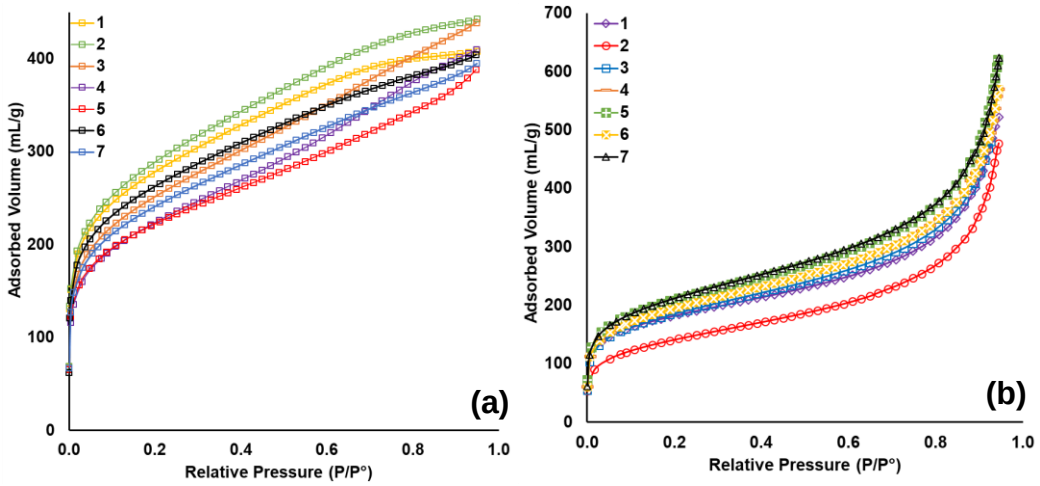

Figure 46. N_2 adsorption isotherms of repeated syntheses of **(a) C-PPN-5** and **(b) N-PPN-5**

The variance in porosity between the equivalent resorcinol and calixarene-based PPNs supports the hypothesis that pre-structured, bulky monomers can affect the porosity of the resulting networks. Furthermore, when the terephthalaldehyde ratio of the **N-PPNs** were varied as with the **C-PPNs** from 2 to 9 equivalents, **N-PPN-2** to **N-PPN-9**, the porosity and isotherm shape were observed to remain a Type II and little change in the porosity was observed (646 and 474 mL/g, respectively) **(figure 77)**. This can be attributed random, tight branching structure of the **N-PPN** where additional equivalents of aldehyde would have less effect on the network structure than in the **C-PPN** network where branching between large pre-structured monomers significant to the porosity.

To further explore the porosity effects of pre-structuring the **C-PPNs**, the identity of the aldehyde comonomer was varied to determine the relationship between the linking structure and the porosity. Terephthalaldehyde was substituted for equimolar (based on reactive aldehyde) amounts of isophthalaldehyde, formaldehyde, 4,4'-diformylbiphenyl (**DFBP**), and 1,3,5-tris(4-formylphenyl)benzene (**TFPB**) comonomers **(figure 45e)**. The

isophthalaldehyde which is similar to terephthalaldehyde with a meta-substituted geometry, resulted in a lower microporous product (55 mL/g) **(figure 45e)**. This indicates the porosity has a strong dependence on the structure of the monomers as opposed to an unidentified chemical or physical factor; the reduced porosity is most likely due to the narrow branching angle between the **4-OHPhRsC** units which results in a more crowded pore environment. Similarly, when formaldehyde was utilized, a low porosity (74 mL/g) polymer resulted, again most likely due to a denser branching structure. The triangular trisubstituted **TFPB** resulted in a polymer with greater mesoporosity and a classic Type II isotherm (520 mL/g) **(figure 45e)**. Finally, the linear **DFBP** comonomer which is equivalent terephthalaldehyde, extended by one benzene ring, resulted in a PPN with a similar isotherm shape to **C-PPN-5**, but lower porosity overall 349 mL/g) which is most likely due to higher interpenetration of the extended network **(figure 45e)**. These results indicate that a variety of PPNs can be derived from the pre-structured calixarene monomer, though the selection of the correct linkage length and geometry is significant to the resultant porosity of the network.

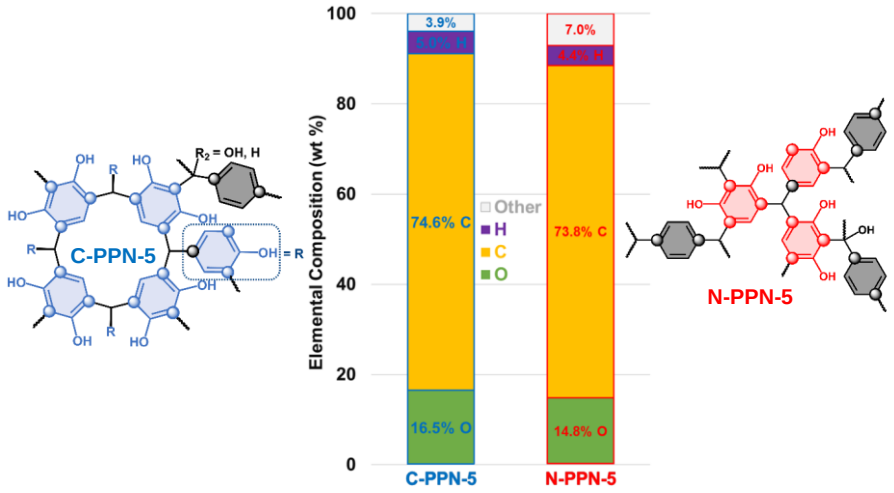

Figure 47. N_2 Combined elemental analysis mass ratio for **C-PPN-5** and **N-PPN-5** (carbon and hydrogen determined via combustion and oxygen determined via FNAA)

To confirm that the expected similar chemical composition between the **C-PPN-5** and **N-PPN-5**s, carbon and hydrogen elemental analysis were carried out via combustion analysis while FNAA was utilized for accurate oxygen determination. Little difference (0.6 - 1.2 %) in the C:H:O ratios was determined between the pre-structure and unstructured polymers as would be expected due to their equivalent starting compositions **(figure 47)**. The differences that are observed can be attributed to variation in oxidation and the expected degree of polymerization between PPNs.

^{13}C cross polarization magic angle spinning ssNMR (^{13}C-CP-MAS-ssNMR) spectra with high-power decoupled (HPDEC), variable contact time, and phasing experiments were employed to gain insight into the chemical structure of produced PPNs. Comparing spectra of the **C-PPN-5** to that of the starting materials, **4-OHPhRsC** and terephthalaldehyde, an expected loss of the downfield aldehyde signal (195 ppm) is observed along with the development of several upfield alkyl signals associated with branching linkages (41 - 11 ppm) **(figure 72)**. From the **C-PPN-5** spectrum **(figures 48a**

and 75) it was determined that several distinct types of crosslinking occur within the polymer network, with secondary (CH_2), tertiary (CH), and quaternary (C) carbons identified in the aliphatic region. This is expected for phenol-aldehyde type condensations due to multiple reaction pathways. Comparing the **C-PPN-5** and **N-PPN-5** ssNMR spectra, little difference is apparent between the spectra other than the intensity of the individual alkyl signals attributed to differences in their crosslinking which would be expected due to their similar chemical compositions **(figure 48a)**.

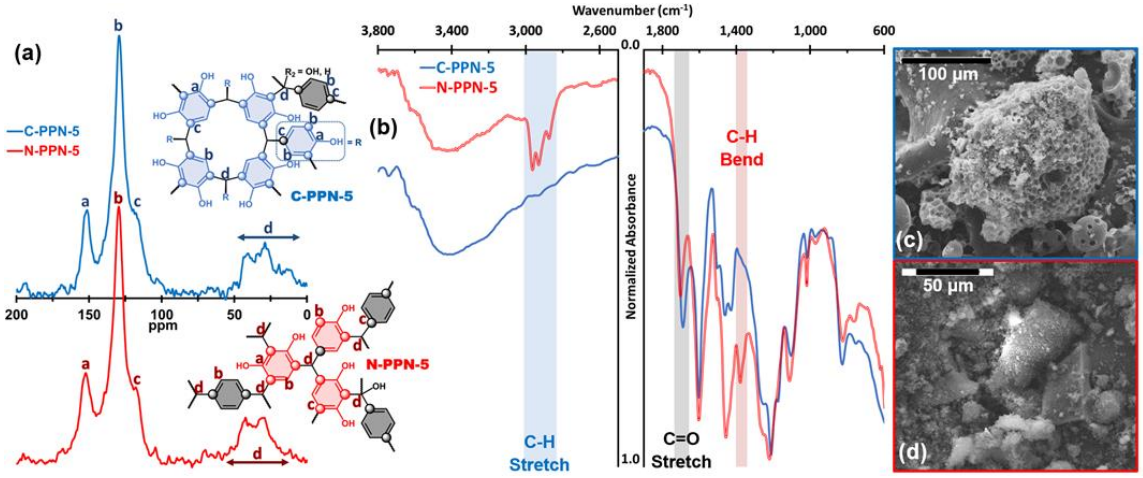

Figure 48. (a) ^{13}C-CP-MAS-ssNMR experiments for **C-PPN-5** and **N-PPN-5. (b)** Overlay of FTIR-ATR spectra of as-synthesized **C-PPN-5** and **N-PPN-5. (c)** SEM image of the **C-PPN-5** (100 µm scale). **(d)** SEM image of the **N-PPN-5** (50 µm scale).

Fourier transform infrared attenuated total reflectance spectroscopy (FTIR-ATR) measurements were used to further examine the chemical structure within the PPNs. The **C-PPN-5** show strong signals for aromatic C=C stretches (1,605 cm^{-1}), O-H stretches (3,000 - 3,700 cm^{-1}), and a carbonyl-type C=O stretch (1,700 cm^{-1}). The **C-PPN-5** spectrum does not display strong aliphatic C-H stretch (2,960 - 2,870 cm^{-1}) or C-H bending bands (1,375 cm^{-1}) that would correspond a high degree of unsaturated linkages

(figure 48b). The **C-PPN-2** spectrum shows stronger aliphatic C-H stretching, while **C-PPN-9** samples show strong signals for the aliphatic C-H bending **(figure 49)**. This most likely indicates samples where the equivalents of terephthalaldehyde differ greatly from 5 eqv. result in varying ratios methylene, methine, and ether-type linkages. In comparison all **N-PPN** spectra, show intense C-H stretch and bending bands due to more aliphatic crosslinking within the network **(figures 48a and 78)**.

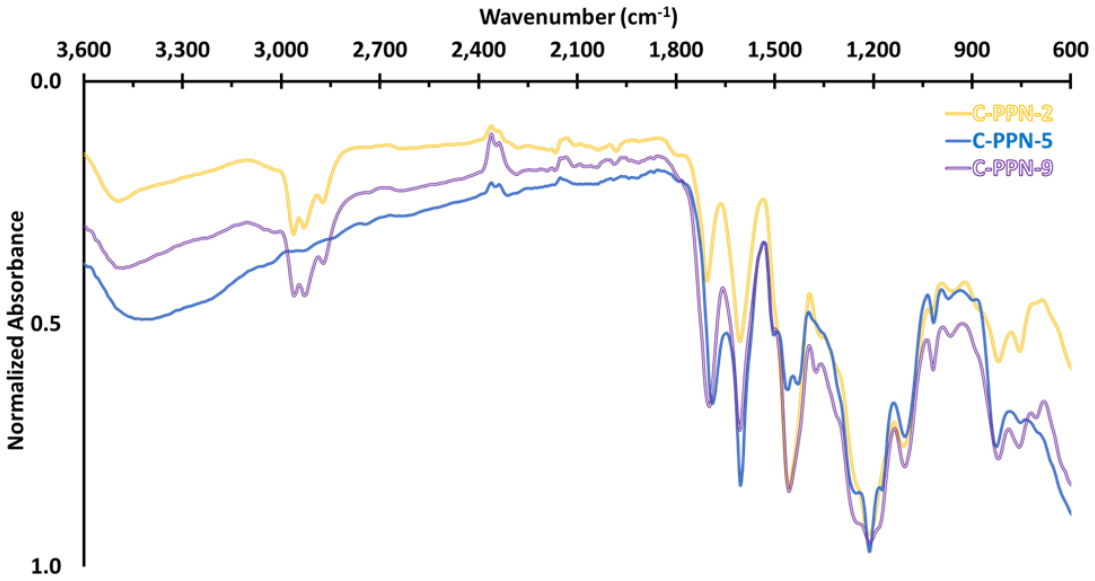

Figure 49. Comparison of normalized FTIR-ATR spectra of **C-PPNs** synthesized with varying equivalents of terephthalaldehyde

Both the **C-PPNs** and **N-PPNs** displayed strong carbonyl-type C=O stretching bands in their IR spectra which did not correspond to significant signals in the ^{13}C-CP-MAS-ssNMR spectra **(figures 48a and 48b)**, consequently a further investigation of this feature was warranted. Oxidation of phenol-aldehyde-type PPNs at high temperatures under atmospheric oxygen has previously been reported to result in such IR bands due to formation of complex pyrylium-like structures.[203] To examine if this type of oxidation

could occur during the high temperature PPN synthesis, samples of **C-PPN-5** and **N-PPN-5** were oxidized via atmospheric oxygen at 250 °C, **C-** and **N-PPN-5-[O],** or reduced in ethanol/KBH_4 at 80 °C, **C-** and **N-PPN-5-[H],** and used to assess the extent and nature of the oxidation in the as-synthesized PPNs. The FTIR-ATR spectrum of **C-PPN-5-[O]** showed the intensification and broadening of the C=O stretch band and an extended absorbance from about 2,000 to 3,600 cm^{-1} which is commonly seen in highly-conjugated graphitic oxide (GO)-like materials **(figure 50)**;[204–206] alternatively, the **C-PPN-5-[H]** spectrum showed the complete disappearance of the C=O stretching band and the emergence of the aliphatic C-H stretching and bending bands **(figure 50)**.

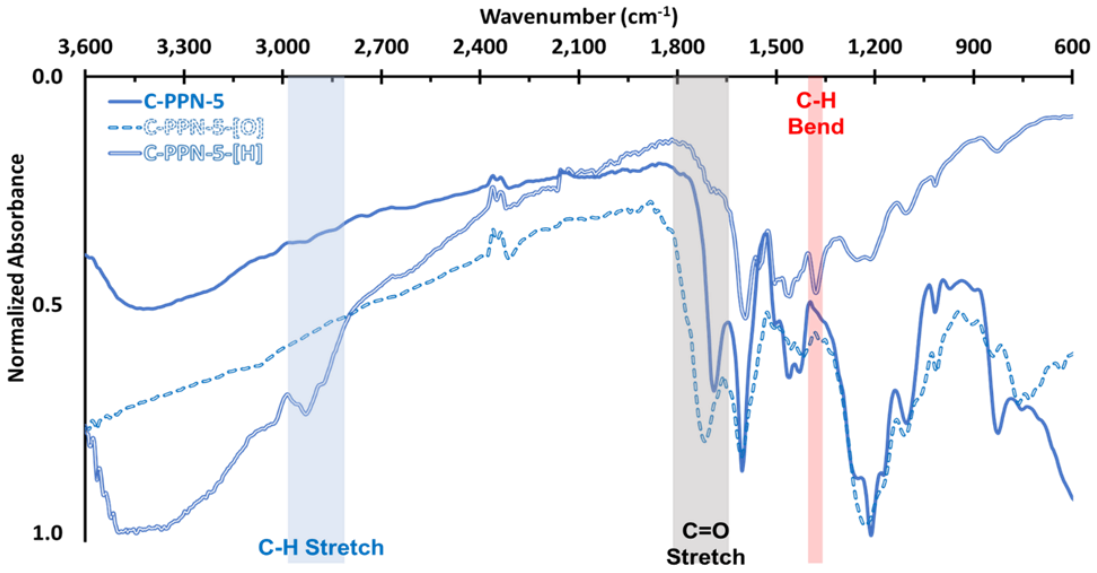

Figure 50. Comparison of normalized FTIR-ATR spectra of 5 eqv. **C-PPN** as synthesized, after oxidation [O], and after reduction [H]

ssNMR spectra of the oxidized **C-PPN-5-[O]** showed a reduction in the alkyl and phenol carbon signals and the emergence several downfield signals which can be attributed to pyrylium and aldehyde-like (192 and 195 ppm), quinoidal, carboxylic acid,

and ester-like functionalities (168 - 166 ppm) **(figure 51)**;[203,206–208] alternatively, the only significant change in the **C-PPN-5-[H]** spectrum was the increase in a signal at 64 ppm which is attributed to a quaternary alcohol or ether linkages arising from the reduction of pyrylium-like structures **(figure 51)**. Similar observations were made in the **N-PPN-5-[O]** and **N-PPN-5-[H]** samples **(figures 85 and 51)**. Thermogravimetric analysis (TGA) of **C-PPN-5** showed little (approx. 2 %) mass loss over the 4 h oxidation under air at 250 °C, and modulated differential scanning calorimetry (M-DSC) showed an expected exothermic peak over the 200 - 300 °C range under air but no exotherm under nitrogen **(figures 52, 82, and 83)**.

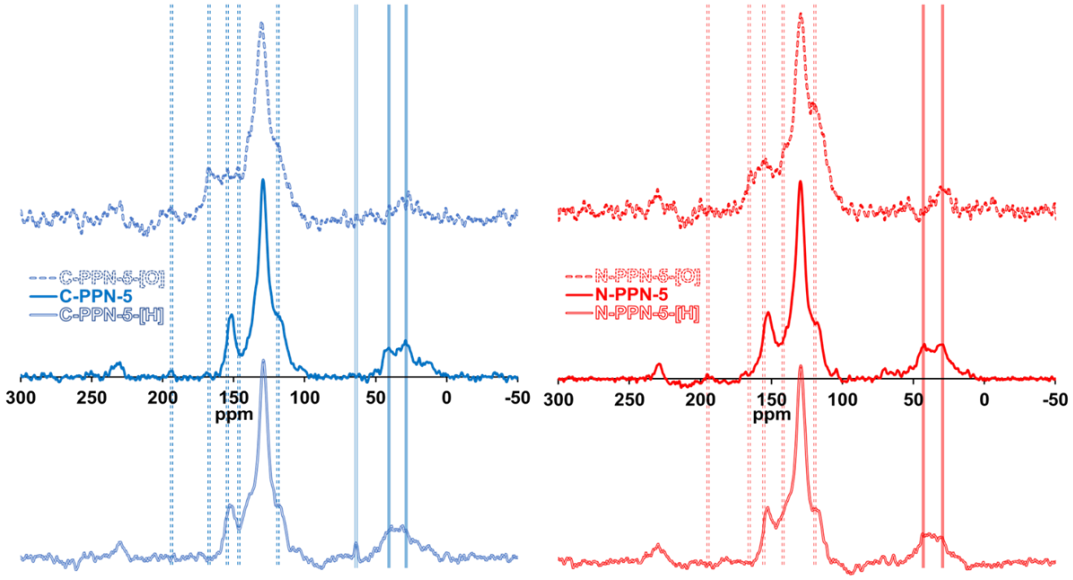

Figure 51. Comparison of offset ^{13}C-CP-MAS-ssNMR spectra of **C-PPN-5** and **N-PPN-5** as synthesized, after oxidation [O], and after reduction [H]

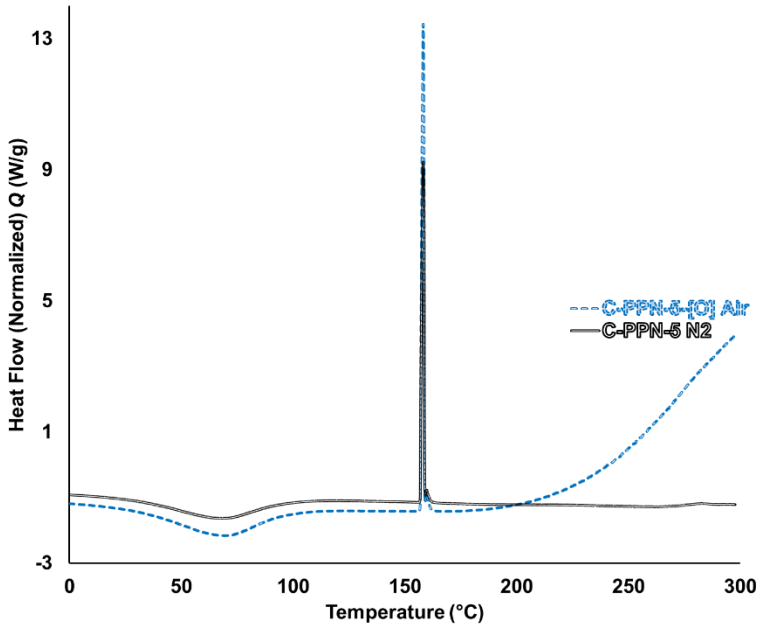

Figure 52. M-DSC exotherms for **C-PPN-5** heated at 10 °C/min to 300 °C under air and N_2 atmospheres

Scanning electron microscopy (SEM) imaging of the **C-PPN**s and the **N-PPN**s was used to examine their morphologies. As a series starting with the lowest equivalent terephthalaldehyde samples, **C-PPN-2** displays a "block-like" morphology commonly observed in PPNs **(figures 53a and 86a)**. As the ratio of equivalents increased, approaching that of **C-PPN-5**, the emergence of several complex morphologies is apparent, including sponge-like structures, spheres, and indented spheres with cavities on the order of 10 μm **(figures 53c, 87, and 88a)**. As the ratio of equivalents was increased past 5 eqv., these complex morphologies were observed to decrease up to **C-PPN-9** which again display the typical block-like structure **(figures 53 and 88c)**. In comparison, regardless of the aldehyde ratio the **N-PPNs** samples do not display the complex morphologies of the **C-PPNs**, exhibiting the block-like morphology with small particulates of approx. 1 μm observed in addition to large fragments on the order of 20 -

200 μm in all samples **(figures 53 and 89)**. The observation of the complex morphologies exclusively in the **C-PPNs** is not easily explained but may be due to differences in the solubility of the **4-OHPhRsC**, resulting in a phase separation during the synthesis.

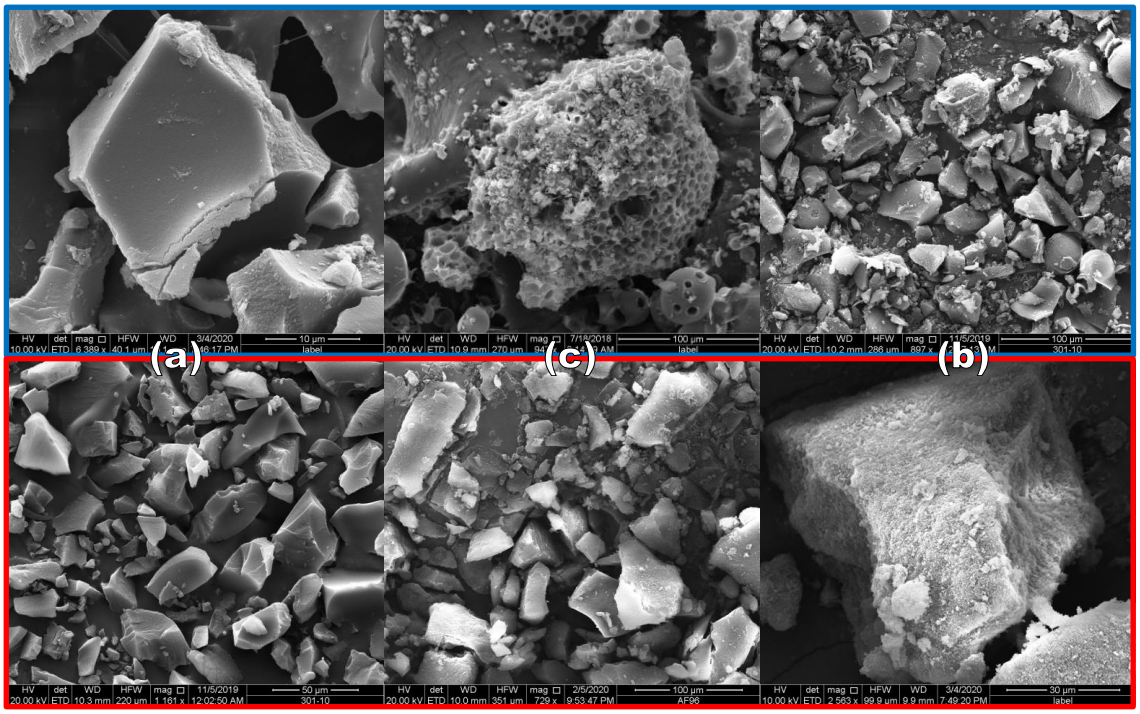

Figure 53. SEM micrographs of **(a) PPN-2 (b) PPN-5 (c) PPN-9** of **C-PPNs** (**blue**) and **N-PPNs** (**red**)

To further characterize the obtained PPNs TGA and PXRD were performed. The thermal stability in air of the **C-PPN-5** and the **N-PPN-5** were assessed by TGA showed no significant (90 wt %) thermal decomposition till 295 and 355 °C, respectively **(figure 54)**. PXRD analysis confirmed amorphicity of the products as none of the PPN samples displayed diffraction peaks.

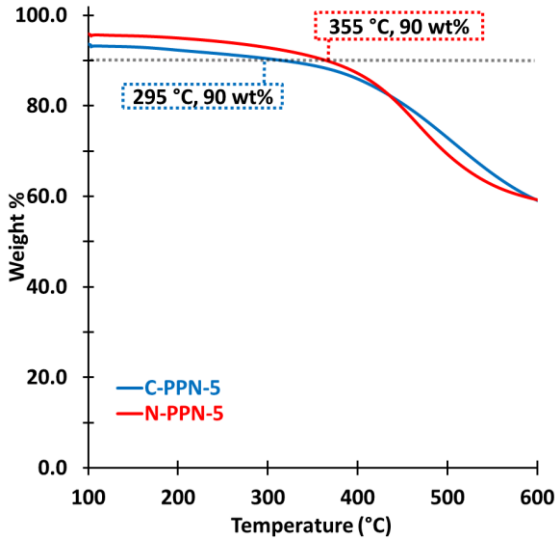

Figure 54. Comparison thermal decomposition of **C-PPN-5** and **N-PPN-5** under nitrogen

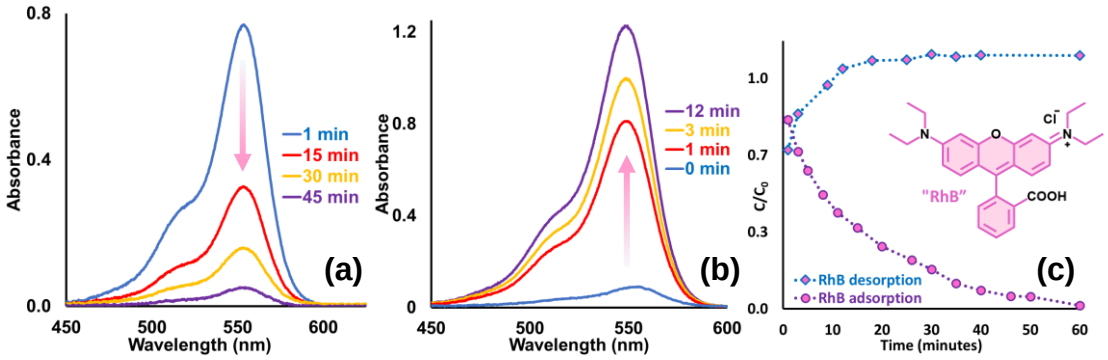

Figure 55. (a) UV-Vis absorbance spectra of 110 ppm aqu. RhB adsorption onto 10 mg of **C-PPN-5** over 45 min. **(b)** Desorption of 135 ppm RhB from 10 mg of **C-PPN-5** by 1:1 ethanol:water solution of 1.5 M NaOH over 12 min. **(c)** Corresponding relative concentrations of RhB for adsorption/desorption experiments over 60 min from UV-Vis spectra

A common analysis of porous materials' potential as sorbents for aqueous toxicants sequestration is accomplished through the adsorption of organic dyes. As can be seen in **(figure 58a)**, samples of **C-PPN-5** were found to rapidly adsorb organic dyes

such as rhodamine B; a process that could be reversed by suspension in ethanol **(figure 58b)**.

To determine their saturation capacities, samples of **C-PPN-5** and **N-PPN-5** were suspended in agitated aqueous solutions of several different types and sizes of organic dyes, rhodamine B (RhB), methylene blue (MeB), and methyl orange dyes (MeO) **(figure 56)**, and the concentrations were monitored via UV-Vis spectroscopy over the period of a week. For all the dyes with **C-PPN-5**, the adsorption capacities reached within 12 h were found to moderately increase in subsequent 24 h and 7 d measurements **(figure 57)**.

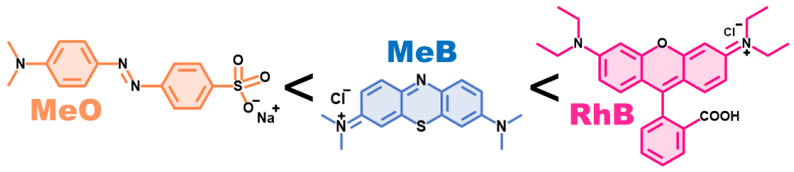

(wt %)	MeO	MeB	RhB
C-PPN	2.0	10.0	20.0
N-PPN	1.8	8.3	18.9

Figure 56. 1-week dye adsorption capacities of **C-PPN-5** and **N-PPN-5** for MeO, MeB, and RhB

C-PPN-5 was found to have the greatest affinity for the larger cationic triarylmethane dye, RhB, followed by the smaller cationic phenothiazine dye, MeB, and finally the anionic azo dye, MeO **(figure 56)**. The results indicate some dependence of dye adsorption on molecular charge but little dependence on the sizes in those examined. To support this analysis, the zeta potential of **C-PPN-5** in aqueous solution was found to be -35 mV, which should result in a greater affinity for cationic adsorbates **(figure 58)**.

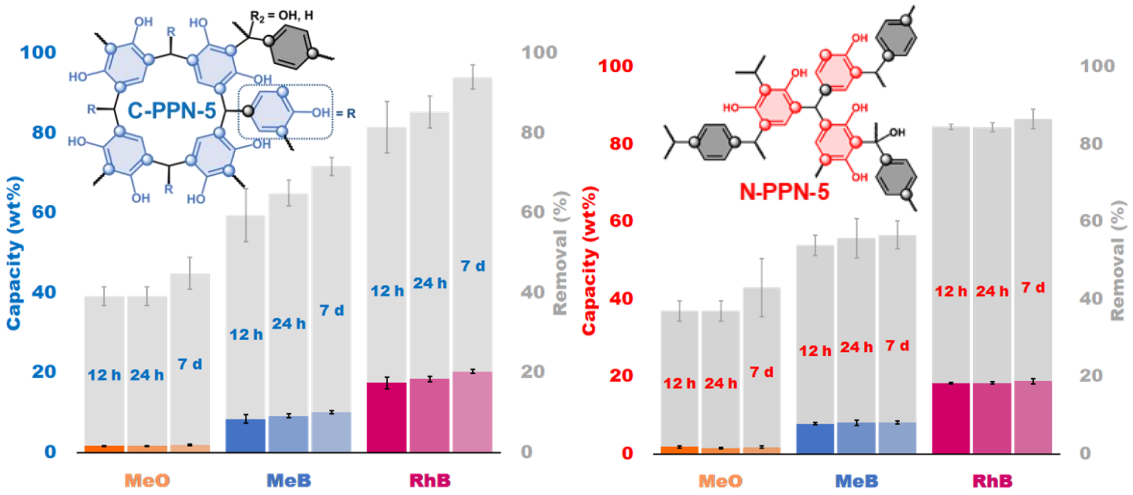

Figure 57. Comparison of **C-PPN-5** and **N-PPN-5** dye adsorption capacities and percent removals of MeO, MeB, and RhB over 1 week

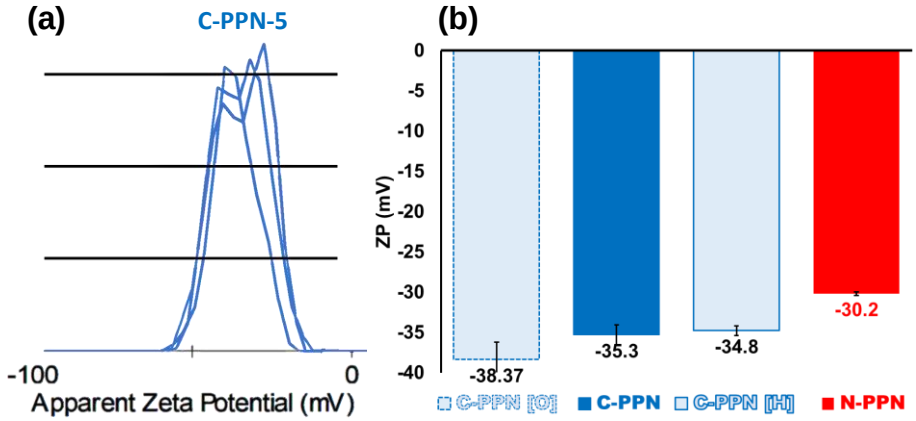

Figure 58. Zeta potential traces in triplicate for **C-PPN-5**. Comparison of measured zeta potentials for as **C-PPN-5** and **N-PPN-5,** as well as **C-PPN-5-[O]** and **C-PPN-5-[H]**

Similarly, **N-PPN-5s** were found to have the same trend in dye affinities but reached their moderately lower saturation capacities within 12 h **(figure 57)**. The differences in adsorption between the **C-PPNs** and **N-PPNs** are attributed to their differences in zeta potential and their distinct pore size distributions; where the more meso- and macroporous **N-PPN-5** allows rapid saturation of its more modest surface

area, the more micro/mesoporous **C-PPN-5** has a higher saturation capacity and allows dye molecules to continue to diffuse into the particle interior over a week.

When examining the rates of MeB sequestration by **C-PPNs** and **N-PPNs** over 1 h, interestingly, the MeB sequestration over 1 h for **C-PPN-5** is approximately twice that of **N-PPN-5** which has higher total porosity than the pre-structured polymer **(figure 59a)**. This is attributed to the enhanced microporosity of the pre-structured **C-PPN-5s**.

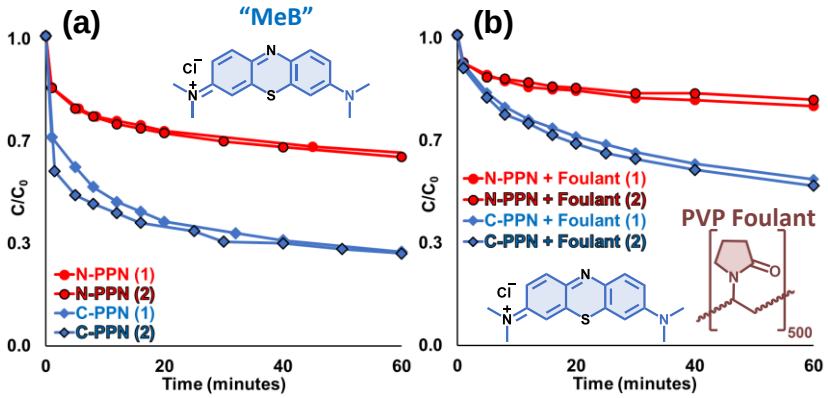

Figure 59. Repeated removal of MeB dye from water by **C-PPN-5** and **N-PPN-5** in the absence **(a)** and presence **(b)** of a "macromolecular foulant" PVP

Chemical fouling is a process that hinders the rate of pollutant sequestration by adsorbent-based materials by coating the sorbent surface in high molecular weight organic matter such as naturally-occurring humic acids. Adsorption of macromolecular foulants into larger mesopores of sorbents can result in pore-blocking which will reduce sorption rates and capacities. To examine how chemical fouling would affect the dye sequestration rates of **N-PPN-5** and **N-PPN-5**, the sorbents were incubated in high concentrations (1,000 ppm) of a model water-soluble macromolecule, 55 kDa Poly(VinylPyrrolidone) (PVP), for several hours. Comparing the dye sequestration

performance of the **C-PPN-5** to the **N-PPN-5** after treatment with a PVP foulant, a difference in their resistance to fouling was observed **(figure 59b)**. On a relative basis, the **N-PPN-5** dye adsorption performance over 1 h was reduced by about 44%, in comparison to 32% for the **C-PPN-5**. These differences were attributed to the mesopores of the **C-PPN-5s** being narrower than those of the **N-PPN-5s,** preventing foulant penetration into the surface pores.

II.iv Summary

Two series of porous phenol-aldehyde polymers, **C-PPNs** and **N-PPNs**, were constructed from the same set of aromatic subunits. In the **C-PPNs**, a pre-structuring approach was employed where aromatic subunits were formed into macrocyclic calixarenes which were subsequently polymerized; **N-PPNs** were polymerized directly from the aromatic subunits without pre-structuring to serve as a comparison to typical porous Novolac resins. Despite having similar chemical compositions, confirmed by elemental analysis and ssNMR studies, the **C-PPN-5** displayed major differences from the **N-PPN-5** in porosity and morphology, with minor differences in thermal stability, degrees of oxidation, network connectivity, dependence on linking aldehyde equivalents, zeta potentials, dye sorption capacities, etc. The more microporous **C-PPN-5** was also found to resist fouling by macromolecular organics in dye sequestration experiments. These results demonstrate how the application of a pre-structured monomer to typical PPNs based on well-developed commercial polymers such as Novalac resins offers an additional route to control material properties. Furthermore, a series of **C-PPN** variants

were produced utilizing several different aryl aldehyde comonomers paired with the pre-structured calixarene which demonstrates a potential for wider application of this method in the future.

II.v Supplemental information

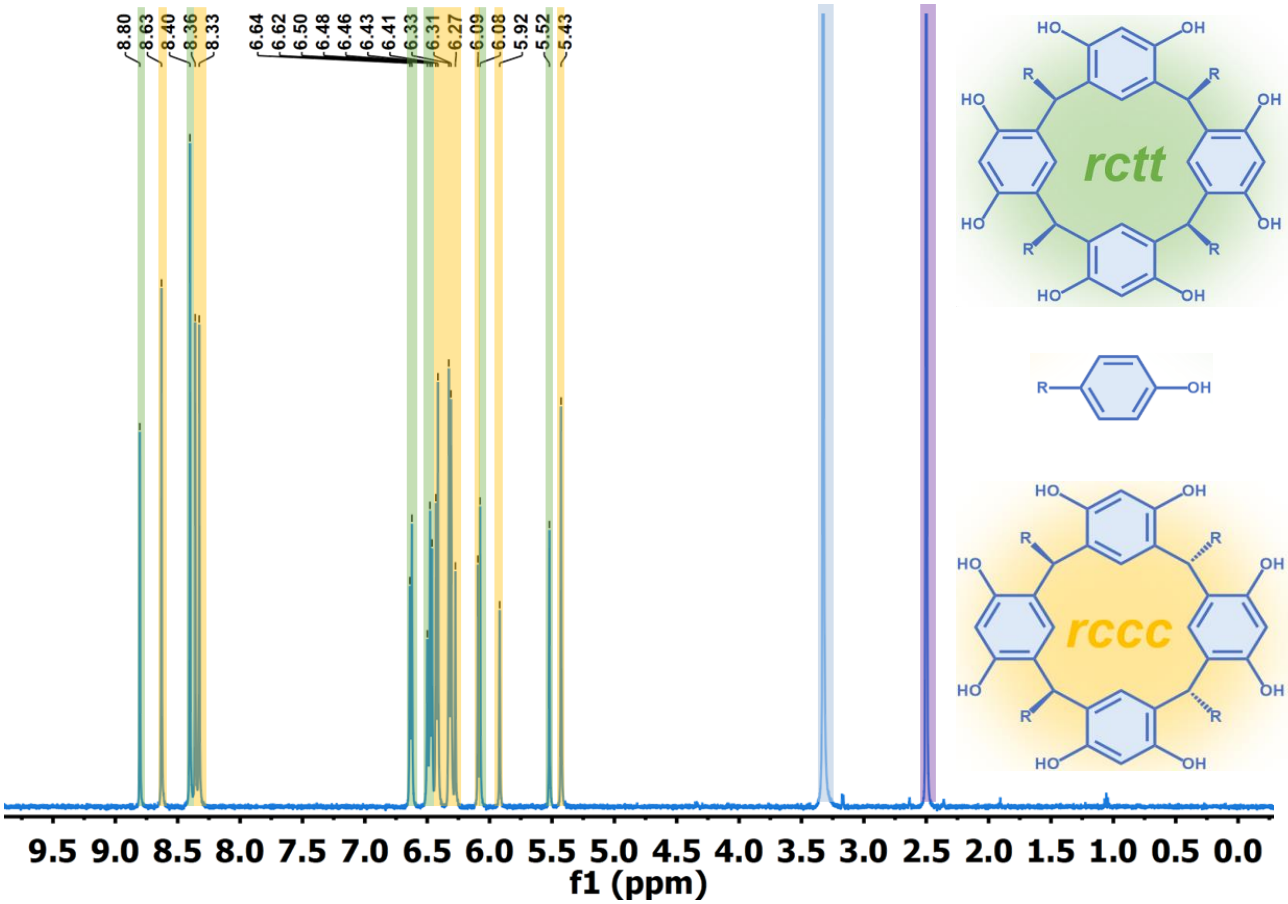

Figure 60. 500 MHz ^{1}H NMR spectra of **4-OHPhRsC** in D_6-DMSO green and yellow overlays correspond to signals from the *rctt* and *rccc* diastereomers, respectively; blue overlay indicates water and purple overlay indicates residual solvent

Figure 61. Optical photograph of **4-OHPhRsC**

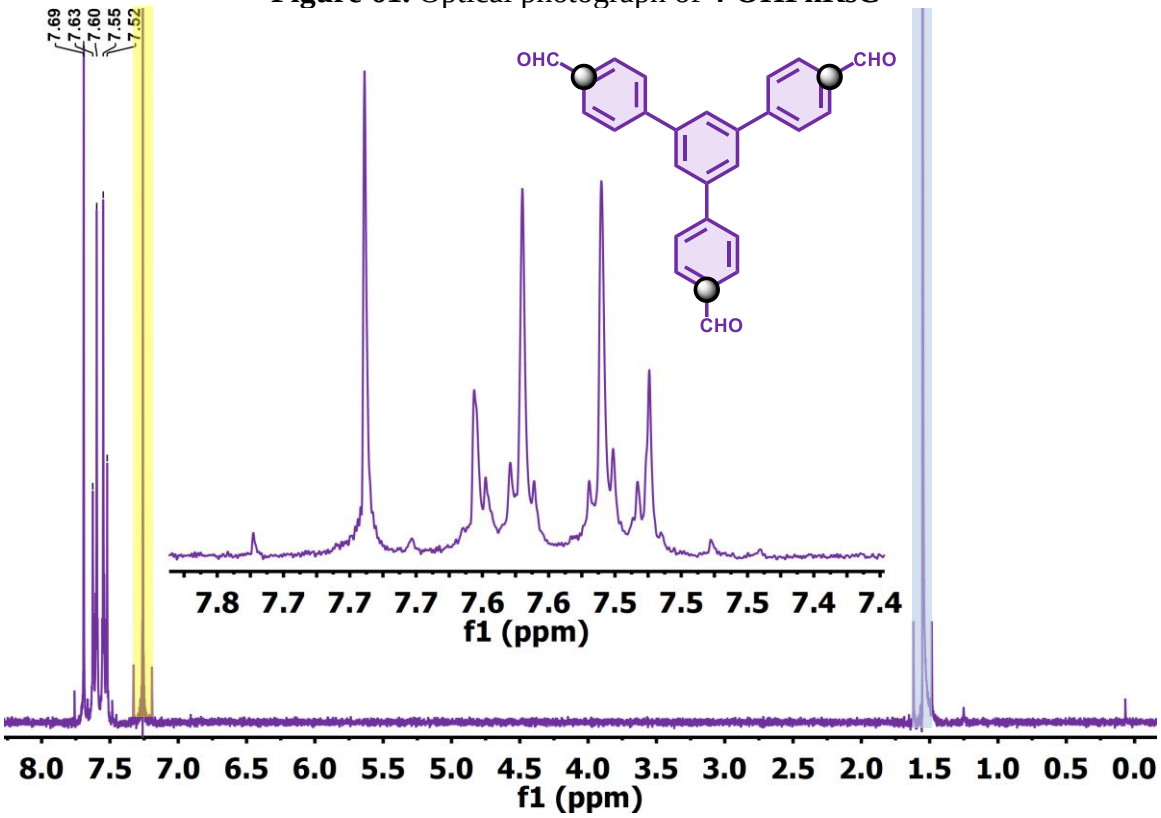

Figure 62. 500 MHz ^{1}H NMR spectra of **TFPB** in $CDCl_3$, blue overlay indicates water and yellow overlay indicates residual solvent

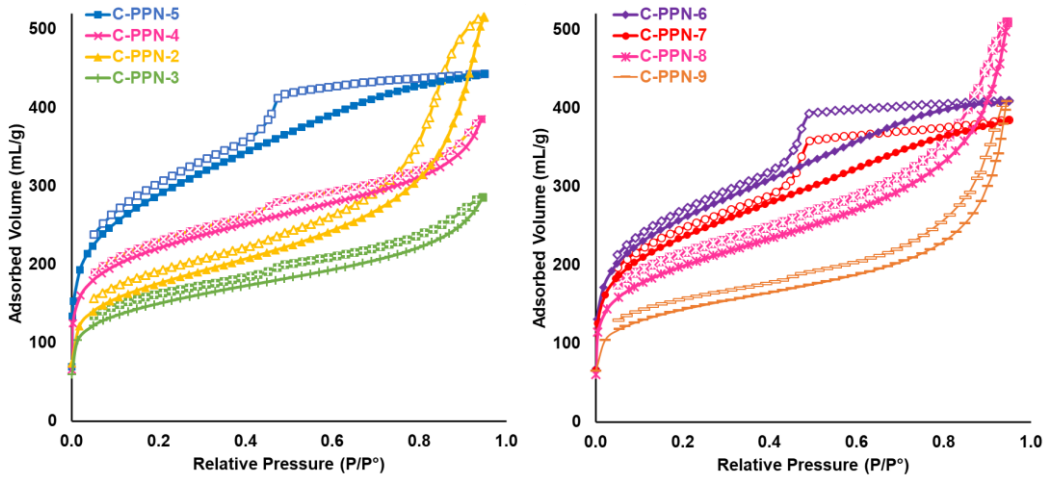

Figure 63. N_2 isotherms of **C-PPN**s synthesized with varying equivalents of terephthalaldehyde

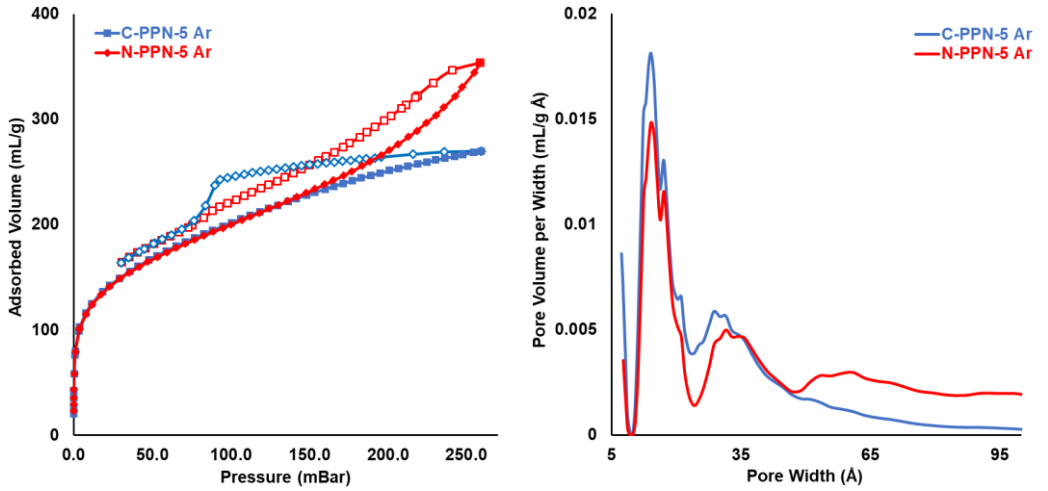

Figure 64. (a) Comparison of 77 K Ar isotherms for **C-PPN**-5 and **N-PPN**-5. **(b)** Comparison of calculated PSDs based on 77 K Ar

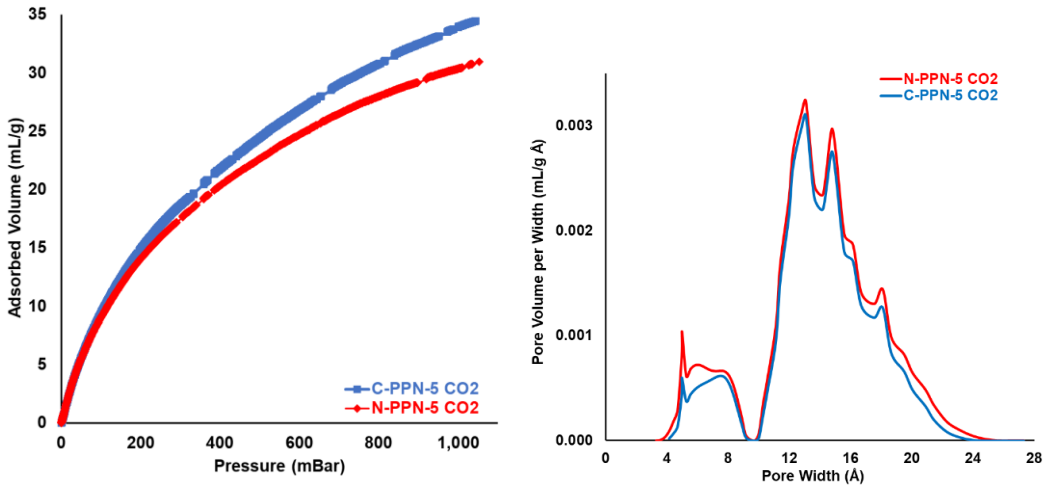

Figure 65. (a) Comparison of CO_2 isotherms for **C-PPN**-5 and **N-PPN**-5. **(b)** Comparison of calculated PSDs based on the CO_2 isotherms

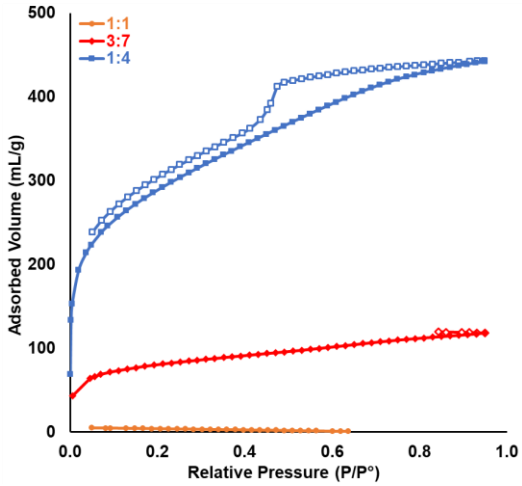

Figure 66. Comparison of N_2 isotherms of **C-PPN-5** produced with different HCl:Dioxane ratios

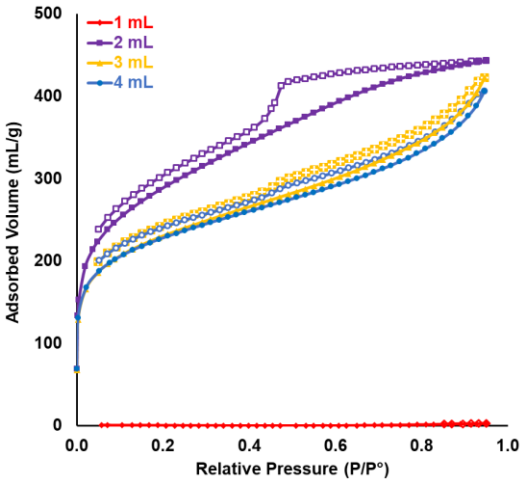

Figure 67. Comparison of N_2 isotherms of **C-PPN-5** produced with different total volumes of dioxane and HCl

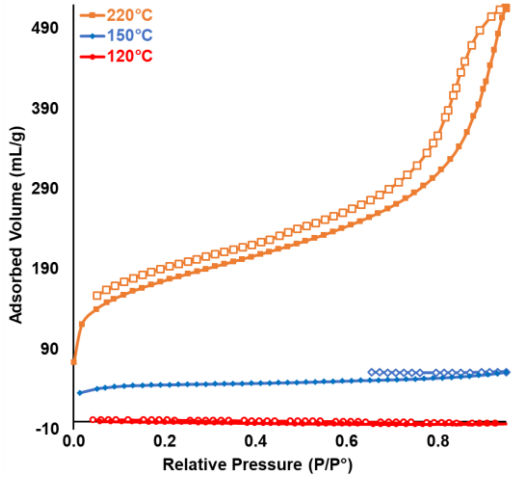

Figure 68. Comparison of N_2 isotherms of **C-PPN-5** produced with different reaction temperatures

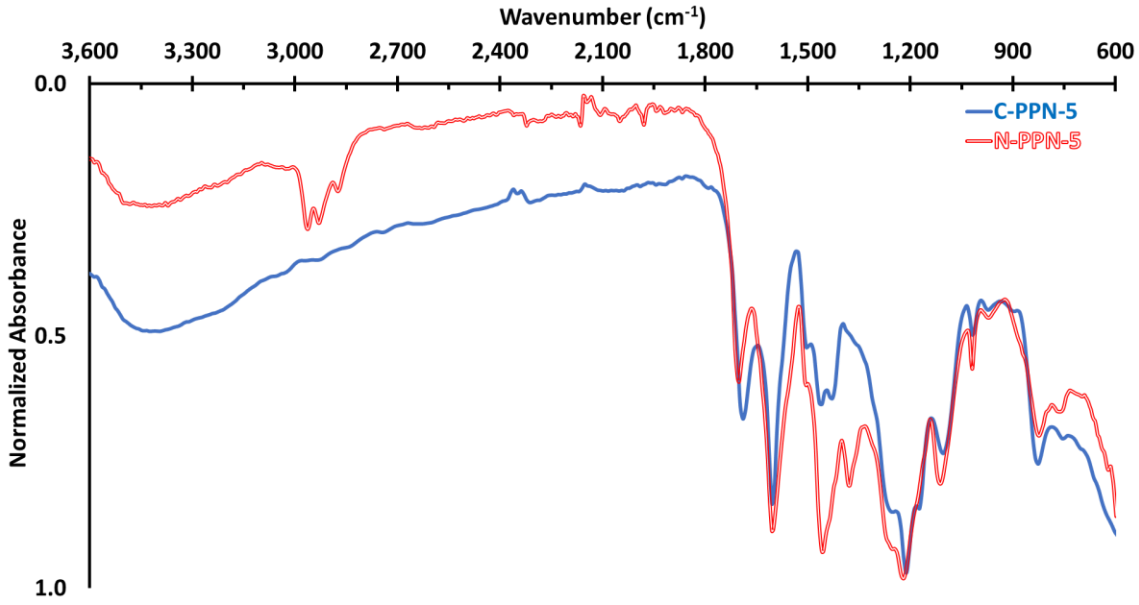

Figure 69. Comparison of normalized FTIR-ATR spectra of **C-PPN-5** and **N-PPN-5**

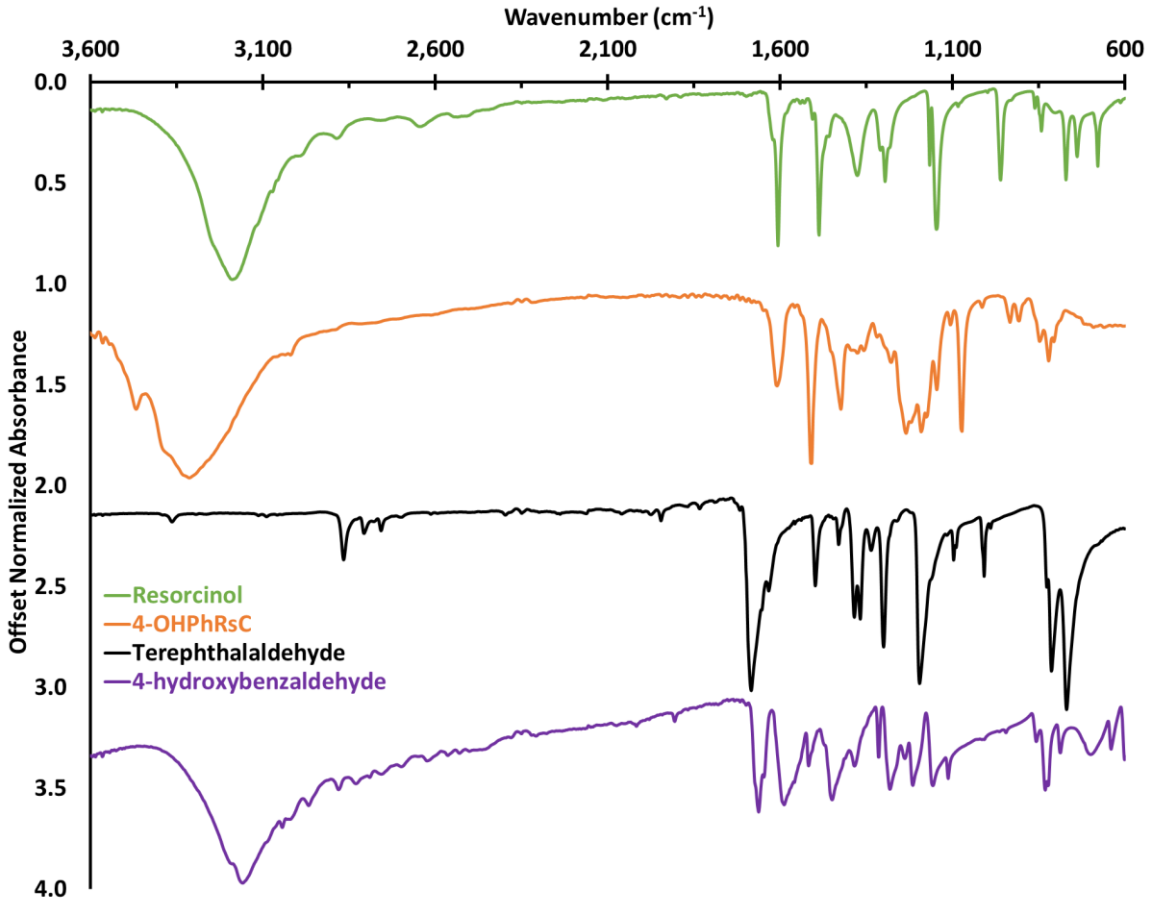

Figure 70. Comparison of normalized offset FTIR-ATR spectra resorcinol, **4-OHPhRsC**, terephthalaldehyde, and 4-hydroxybenzaldhyde

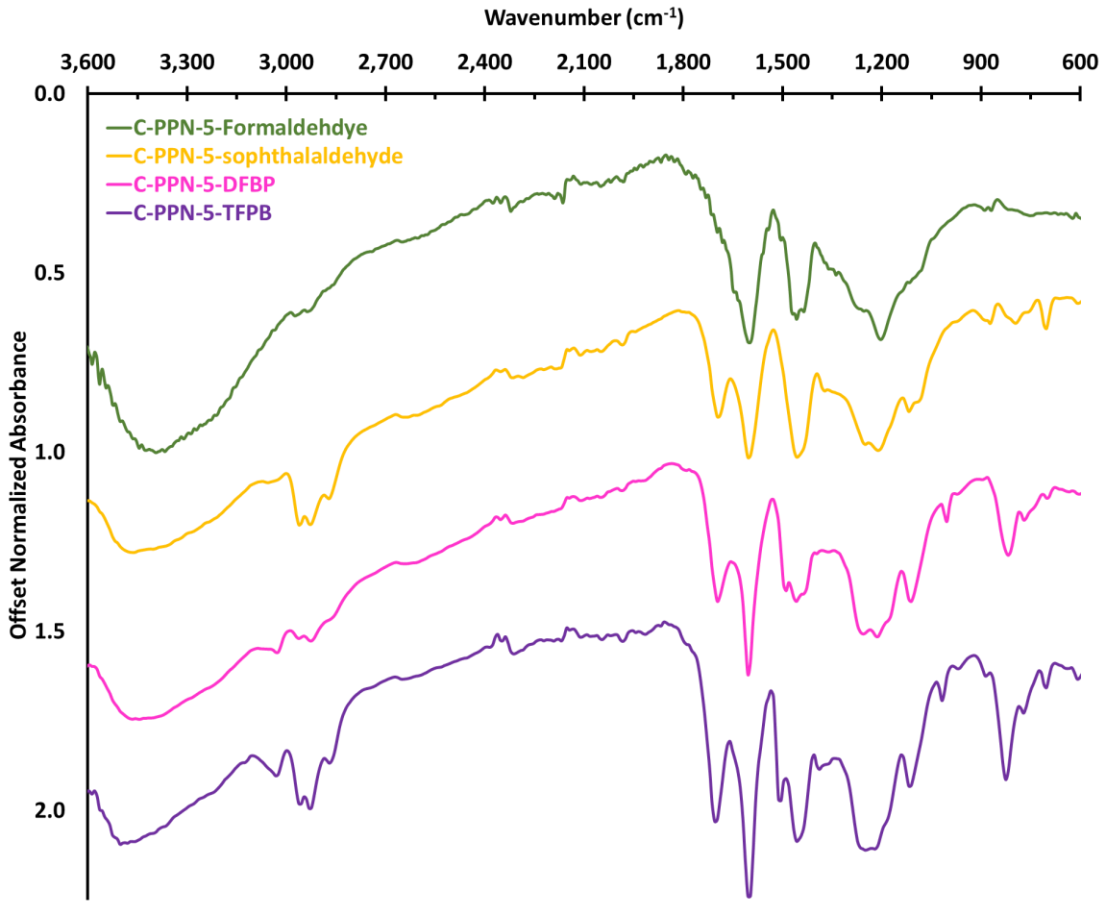

Figure 71. Comparison of FTIR-ATR normalized spectra offset by 0.5 of **C-PPN-5-formaldehyde**, **C-PPN-5-isophthalaldehyde**, **C-PPN-5-DFBP**, and **C-PPN-5-TFPB**

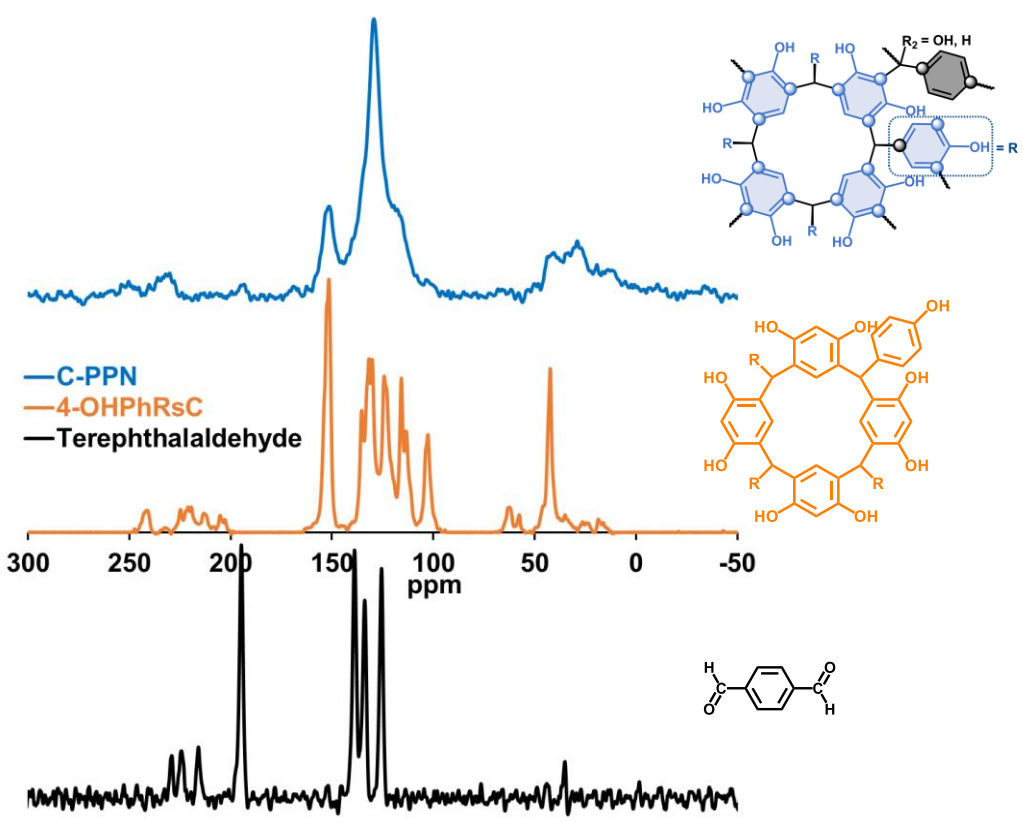

Figure 72. Comparison of offset ^{13}C-CP-MAS-ssNMR spectra of 5 eqv. **C-PPN**, **4-OHPhRsC**, and terephthalaldehyde

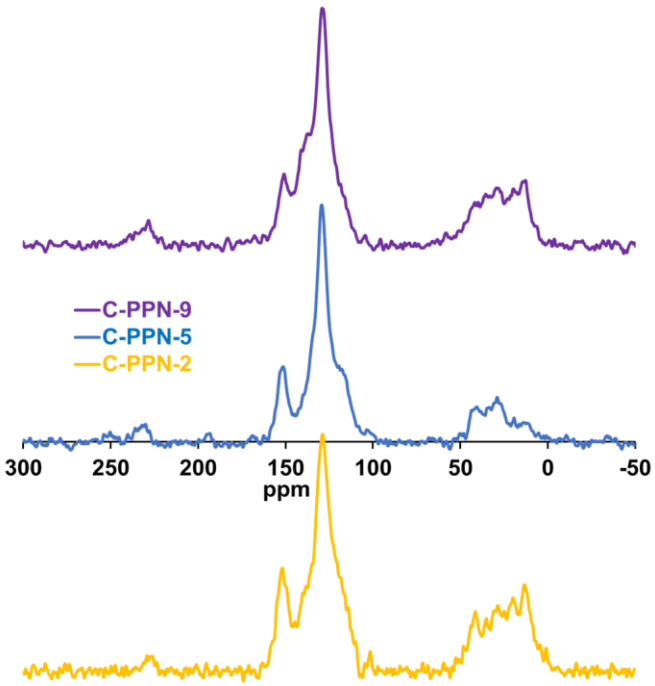

Figure 73. Comparison of offset ^{13}C-CP-MAS-ssNMR spectra of **C-PPNs** synthesized with varying equivalents of terephthalaldehyde

Figure 74. Optical photograph of **C-PPN-5**

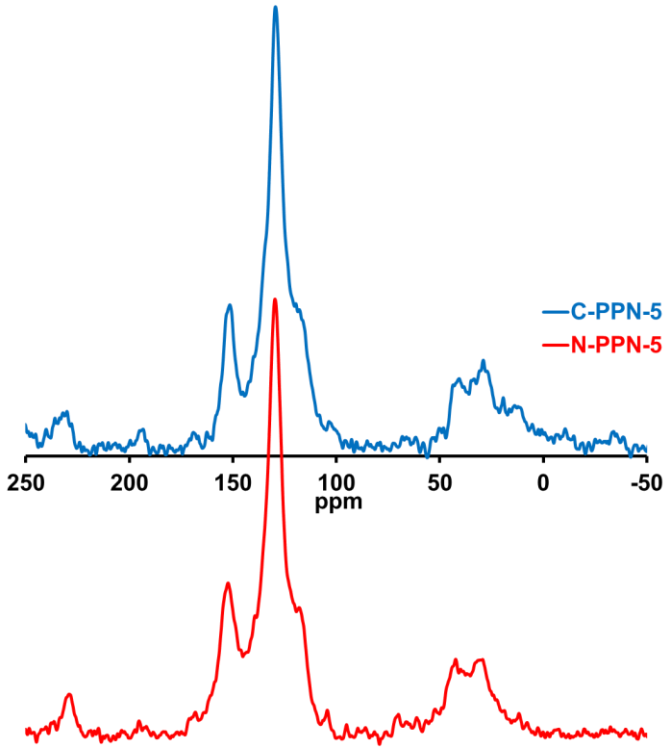

Figure 75. Comparison of offset ^{13}C-CP-MAS-ssNMR spectra of **C-PPN-5** and **N-PPN-5**

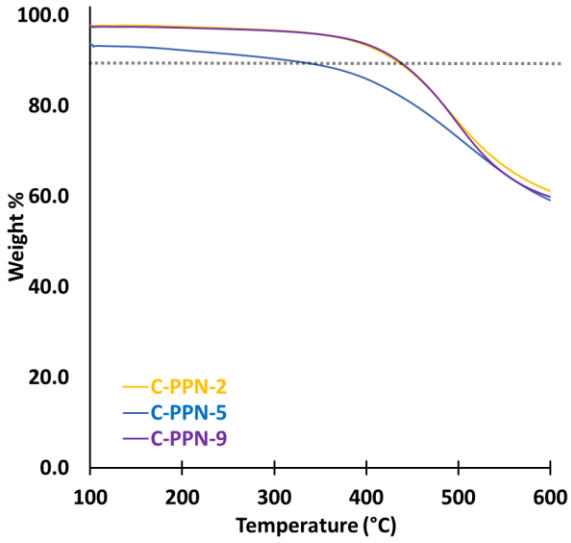

Figure 76. Comparison thermal decomposition of **C-PPNs** under nitrogen

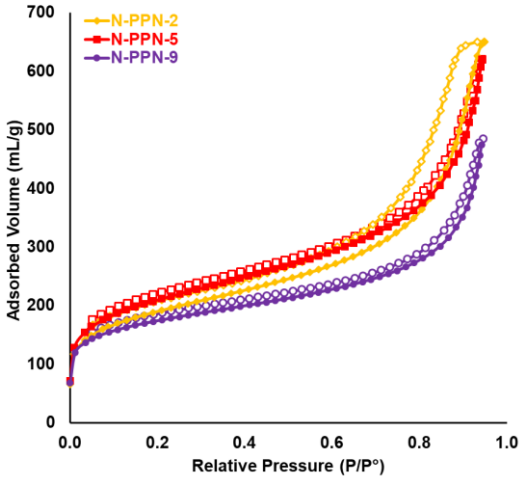

Figure 77. N_2 isotherms of **N-PPN**s synthesized with varying equivalents of terephthalaldehyde

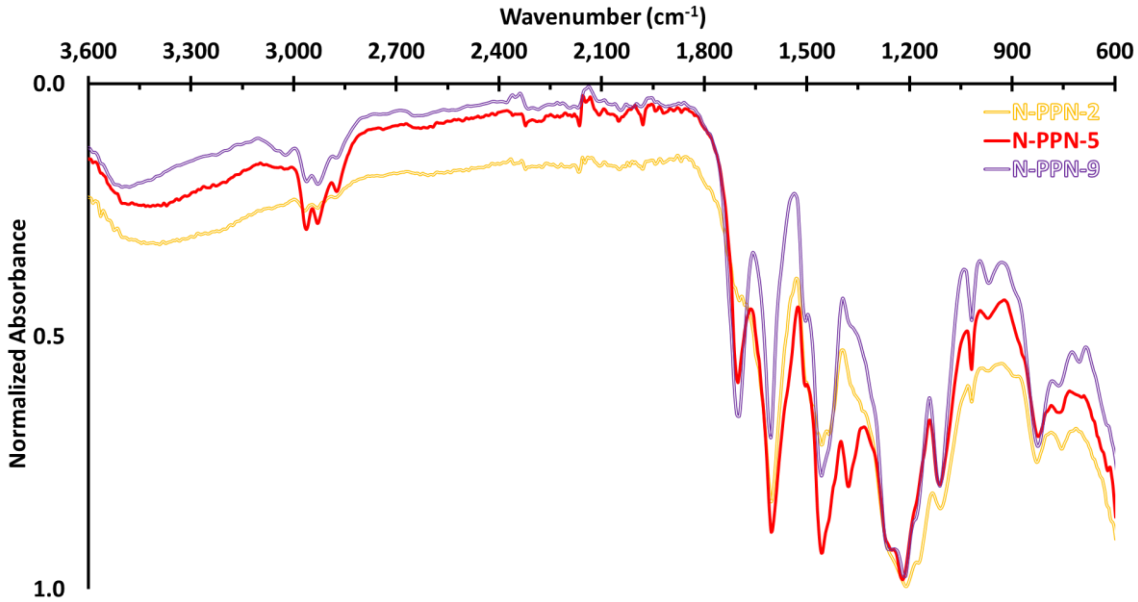

Figure 78. Comparison of normalized FTIR-ATR spectra of **N-PPN**s synthesized with varying equivalents of terephthalaldehyde

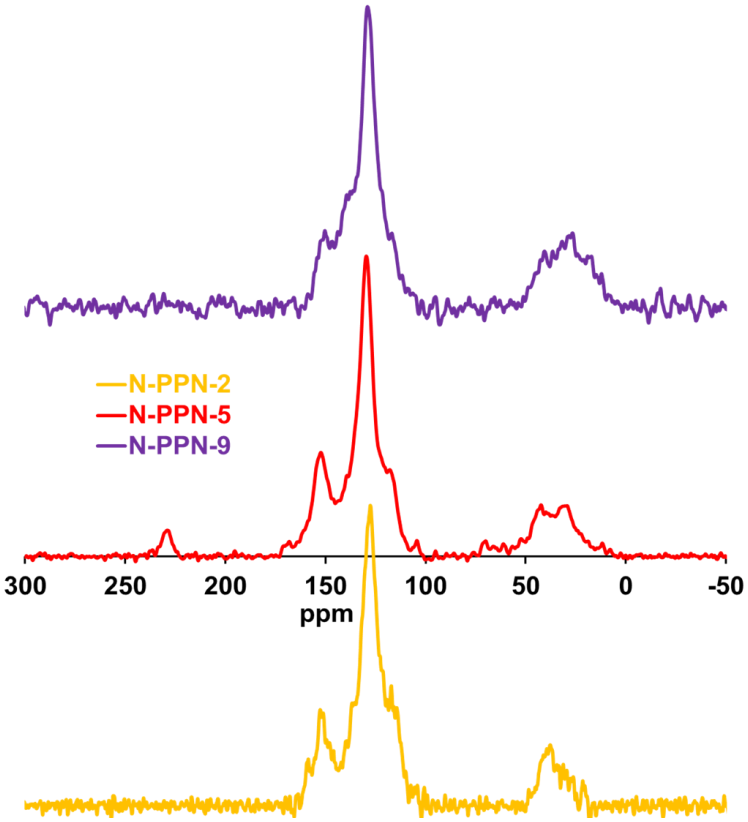

Figure 79. Comparison of offset ^{13}C-CP-MAS-ssNMR spectra of N-PPNs synthesized with varying equivalents of terephthalaldehyde

Figure 80. Optical photograph of **N-PPN-5**

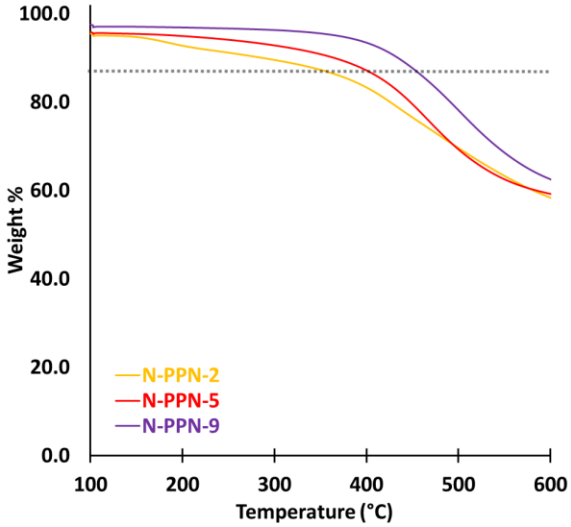

Figure 81. Comparison thermal decomposition of **N-PPNs** under nitrogen

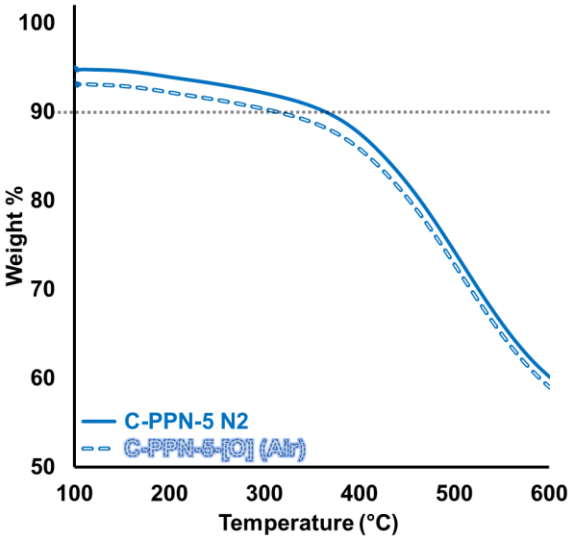

Figure 82. Comparison of the thermal decomposition of **C-PPN-5** under nitrogen and air

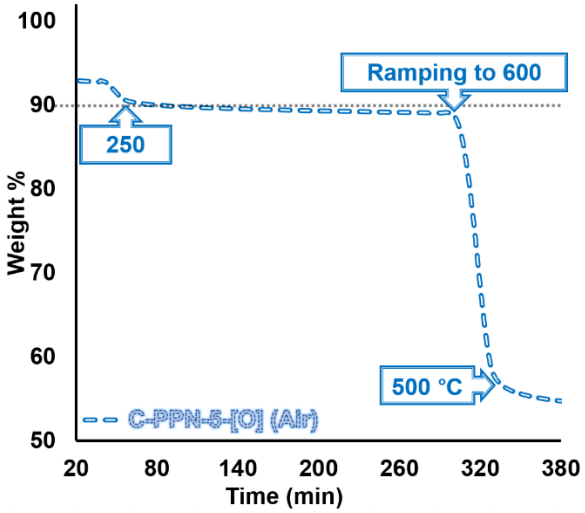

Figure 83. Thermal decomposition of **C-PPN-5** under air with an isothermal hold at 250 °C for 4 h, followed by ramping to 600 °C

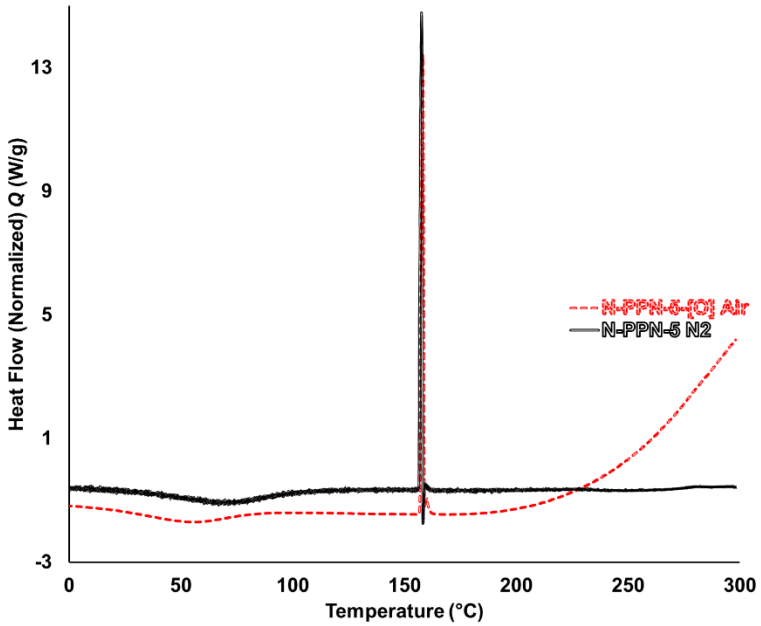

Figure 84. M-DSC exotherms for **N-PPN-5** heated at 10 °C/min to 300 °C under air and N_2 atmospheres

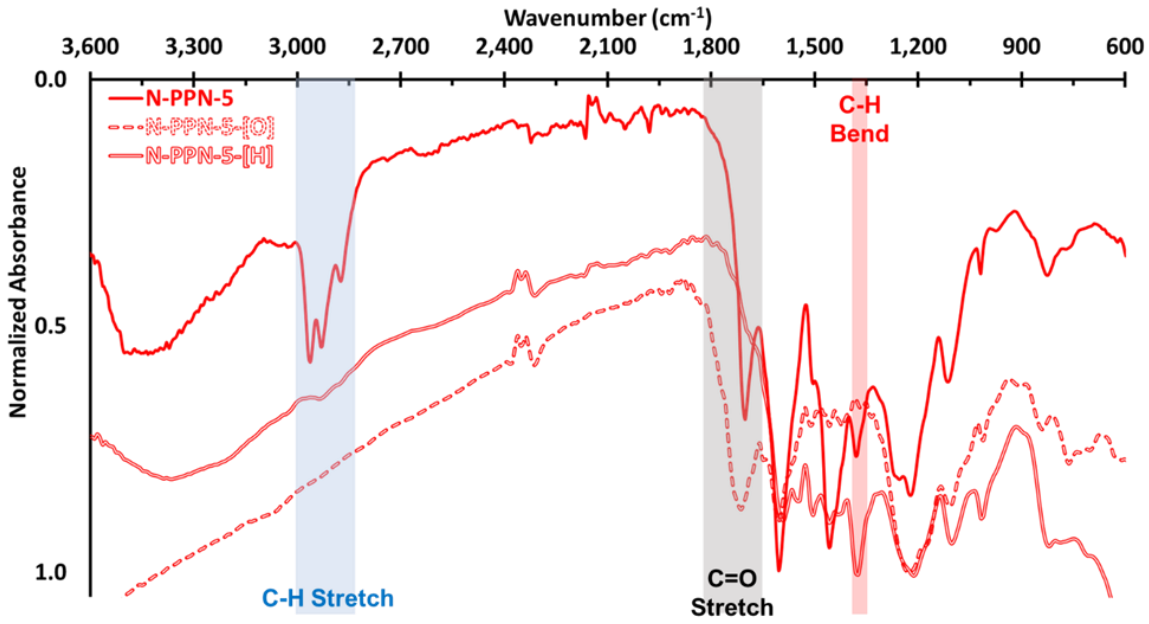

Figure 85. Comparison of normalized FTIR-ATR spectra of **N-PPN-5** as synthesized, after oxidation [O], and after reduction [H]

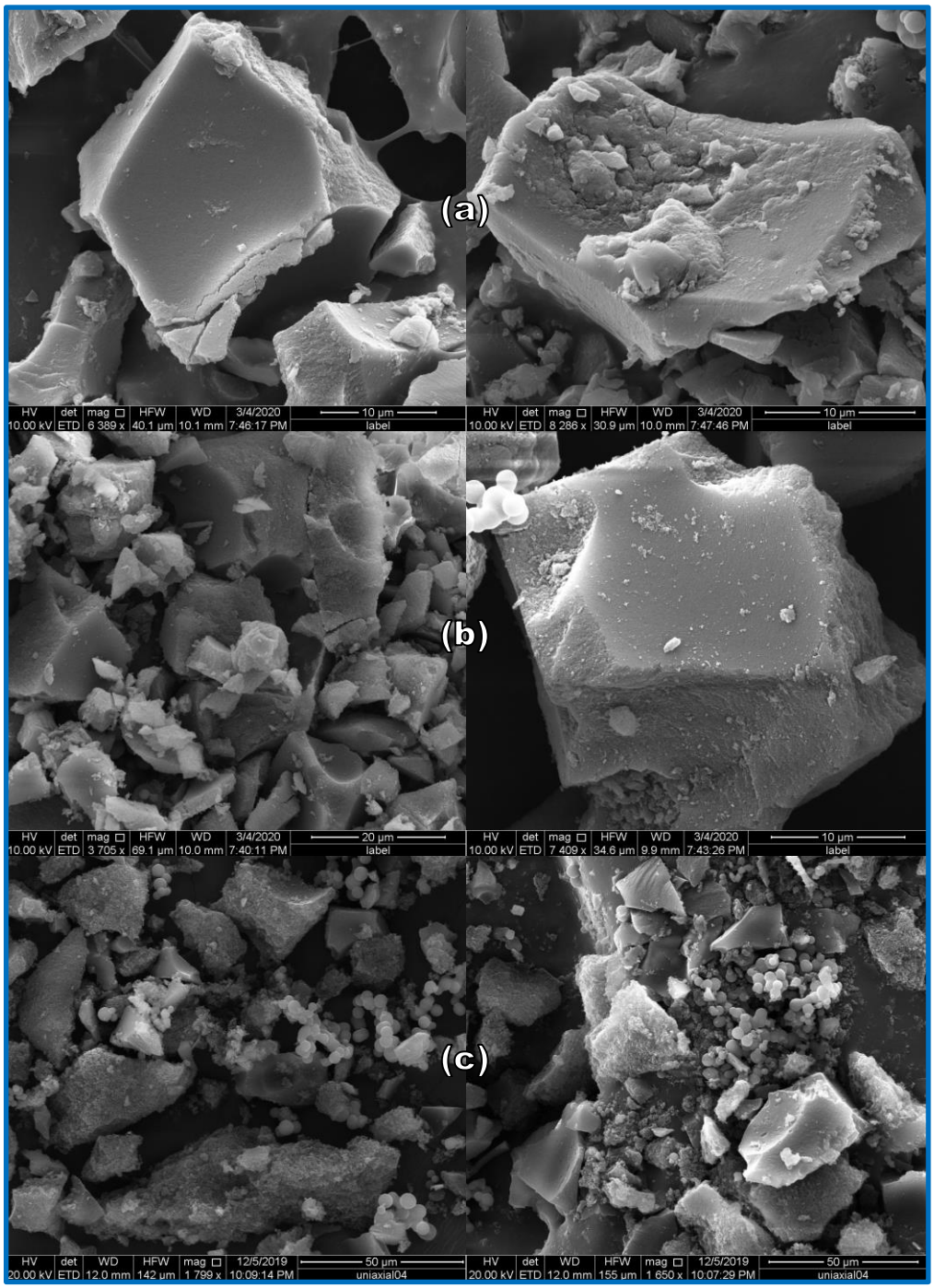

Figure 86. SEM micrographs of **(a) C-PPN-1 (b) C-PPN-2 (c) C-PPN-3**

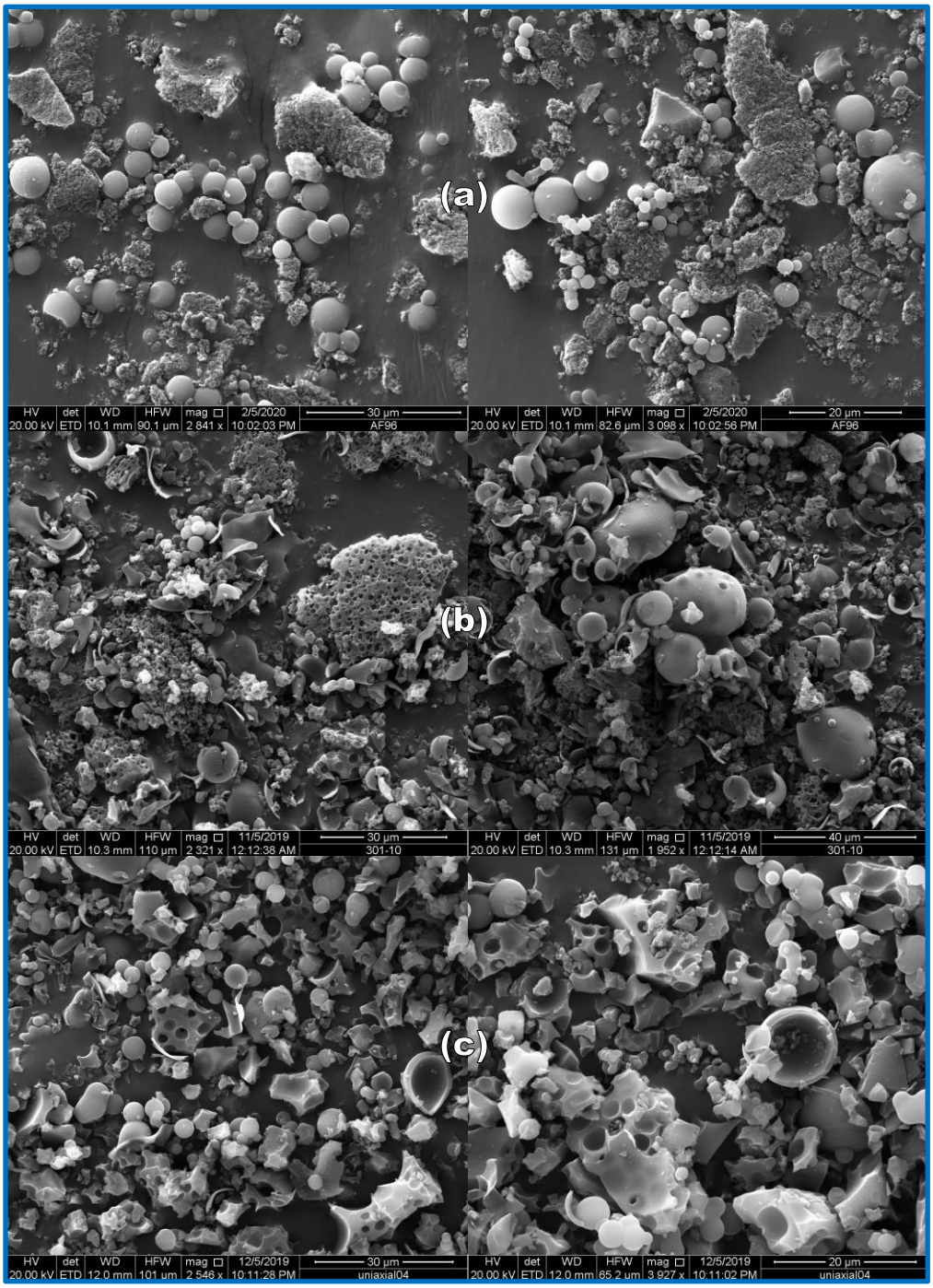

Figure 87. SEM micrographs of **(a) C-PPN-4 (b) C-PPN-5 (c) C-PPN-6**

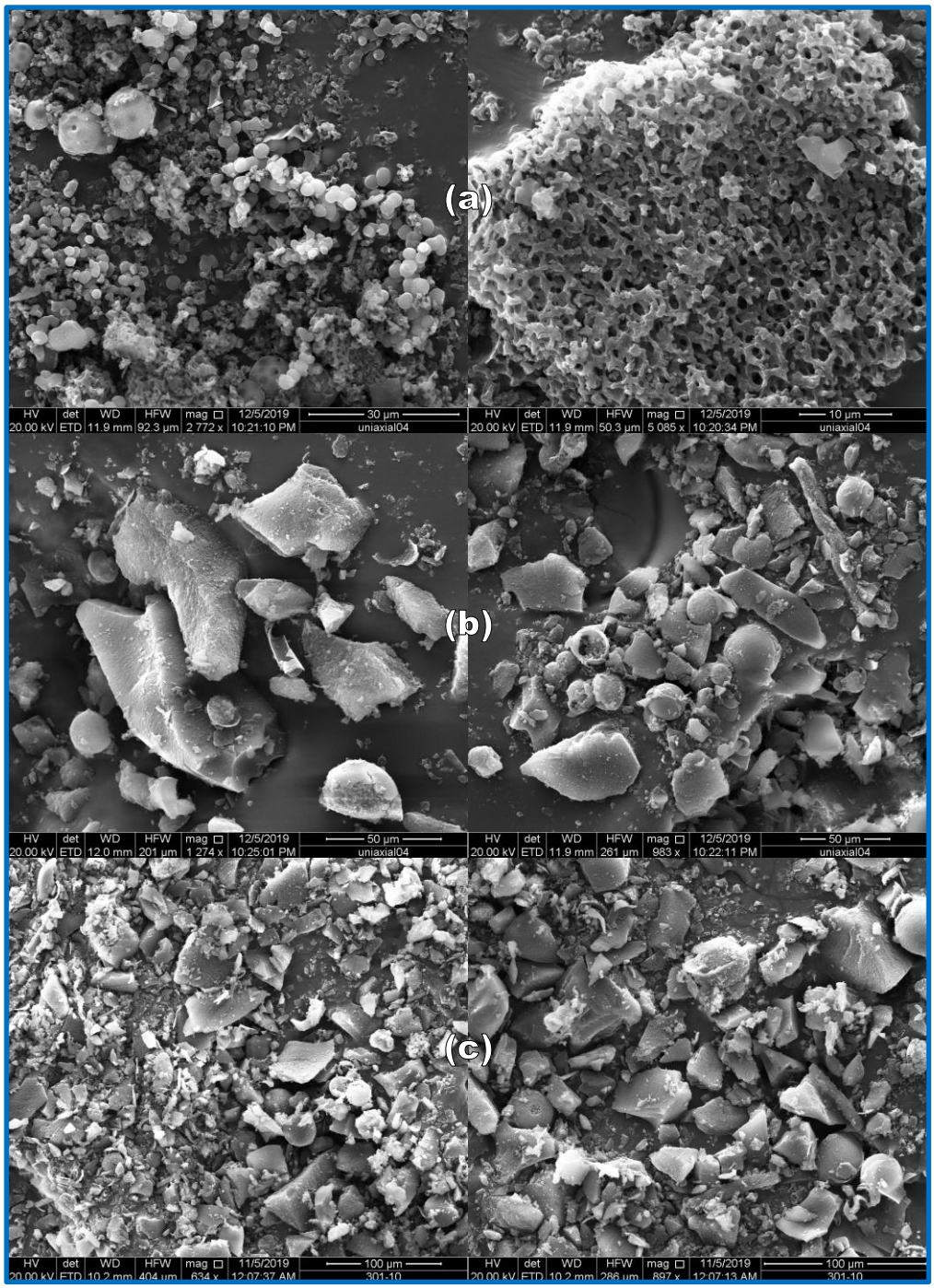

Figure 88. SEM micrographs of **(a) C-PPN-7 (b) C-PPN-8 (c) C-PPN-9**

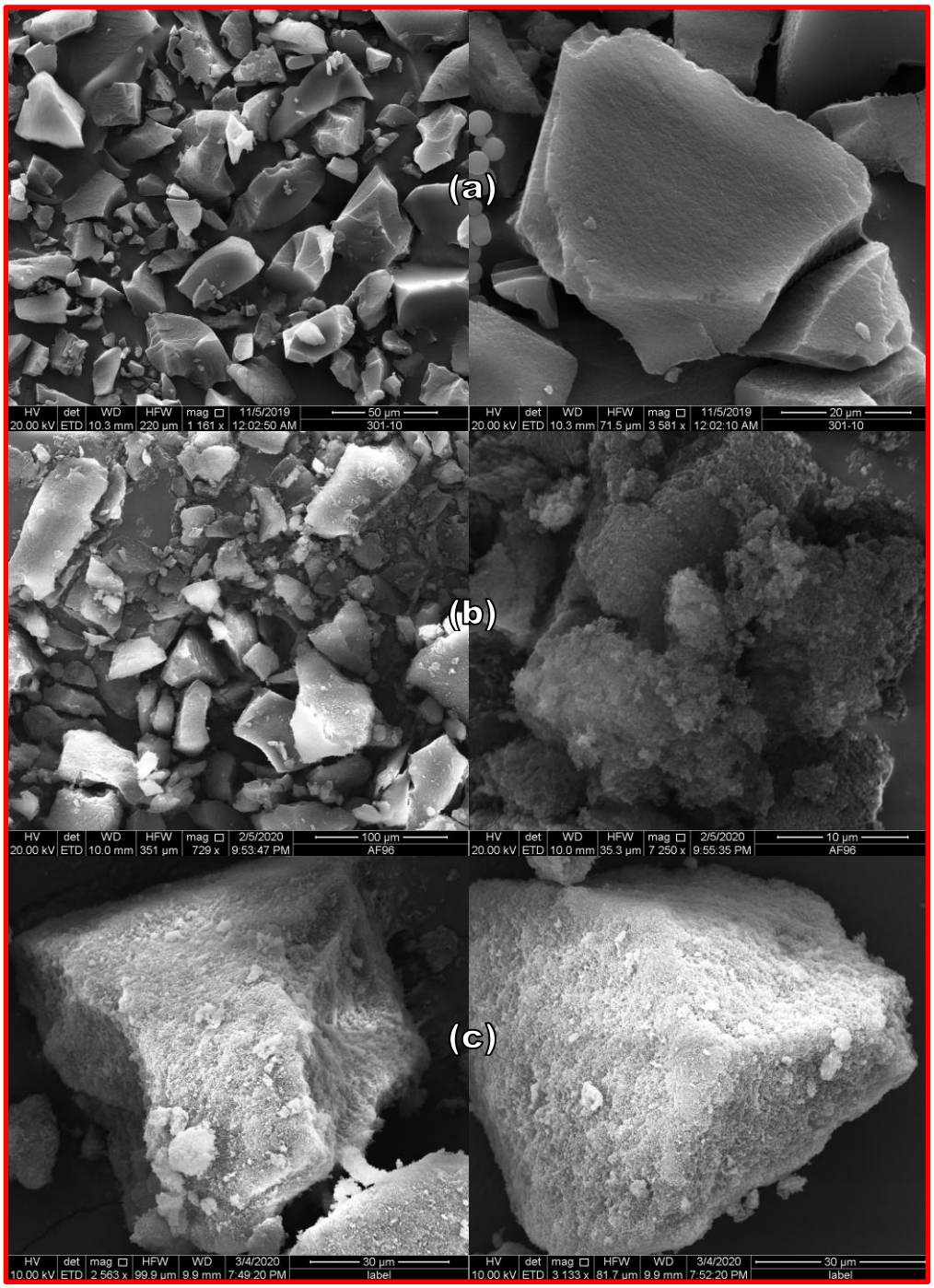

Figure 89. SEM micrographs of **(a) N-PPN-2 (b) N-PPN-5 (c) N-PPN-9**

CHAPTER III

POROUS POLYMERS NETWORKS CONSTRUCTED FROM RIGID BRIDGED CAVITANDS

III.i Introduction to rigid cavitands and their polymer networks

The pre-structuring approach to constructing PPNs, utilized calixarene macrocycles' large three-dimensional structures to modify the porosity of the resultant network. However, calixarenes have many possible conformations which are interconvertible at elevated temperatures.[124] While the molecular size will inherently be beneficial to this approach regardless of the exact conformation assumed during synthesis, the ability to control the conformation would be desirable. One way to approach this would be to "lock" the calixarene into one conformation during the pre-structuring process before PPN synthesis.

One method to lock the calixarene into a conformation is to add "bridging" groups to the structure to reduce their conformational mobility. In resorcinarenes this can be accomplished by ether-type linkages spanning the phenolic groups of the macrocycle in the *rccc*-crown conformation. The resulting compounds are called "cavitands" and are known for forming stable clathrate-like complexes with gasses and solvents molecules, properties which would be beneficial to many porous polymer applications.[114,150] To this end, "bridged" calixarene cavitands were synthesized and utilized to construct a series of porous polymer networks, **B-PPNs**. Comparisons were made to PPNs constructed from unbridged, conformationally flexible calixarenes, **C-PPNs**.

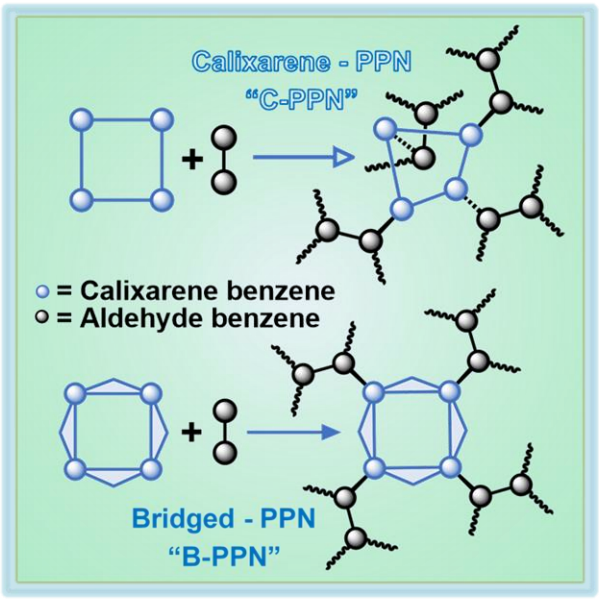

Figure 90. Depictions of polymer networks constructed from calixarenes (**C-PPNs**) and bridged cavitands (**B-PPNs**)

By removing degrees of freedom in the rigid **B-PPN** systems, a better study of factors which affect the porosity can be made. The most obvious factors for calixarene monomers that could be significant to the resulting porosity are the size and shape of the "cup" and "feet" groups. To examine these factors, chain length of the "feet" groups was altered from methyl to *n*-propyl to *n*-heptyl to determine the effects on the porosity of the resulting PPNs. Alternatively, an independent examination cup size could have been made.

For the **C-PPNs** it was found that the gas adsorption isotherms varied greatly and irregularly with calixarene "feet" groups and had large hystereses indicative of their flexibility. The gas adsorption isotherms of the **B-PPNs** had narrower hystereses and revealed an inverse relationship between the S_{BET} and the carbon chain lengths of the cavitand "feet" groups. The results indicate that rigid cavitands can be utilized to

construct PPNs with a degree regular, predictable porosity derived from their macrocyclic shape and intrinsic molecular porosity.

III.ii Experimental

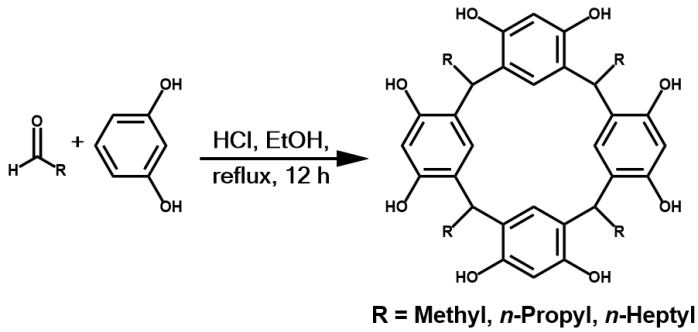

Figure 91. General synthesis of resorcinarenes (**(R)RsC)**

General synthesis of resorcinarenes ((R)RsC):

(R)RsC was synthesized according to published procedures.[112,113,124] Aldehydes and resorcinol were refluxed in ethanol, utilizing HCl as a catalyst. The solution was concentrated by rotary evaporation and the resulting precipitates were filtered off and washed with cold ethanol. The solid products were analyzed by ^{1}H NMR and FTMS-APCI. The products were dried in an 80 °C oven for 12 h and utilized for further syntheses.

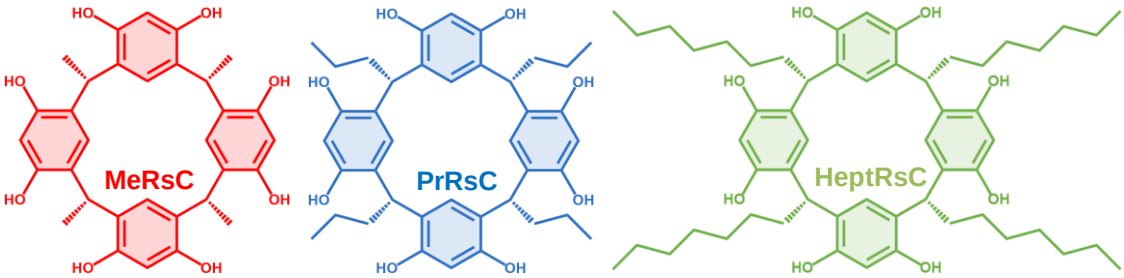

Figure 92. Chemical structures of methyl, *n*-propyl, and *n*-heptyl resorcinarenes from left to right (**MeRsC, PrRsC,** and **HeptRsC** respectively)

Methyl resorcinarene (MeRsC):

MeRsC was synthesized according to the general and reported procedures.[112] Products were confirmed via ^{1}H NMR and FTMS-APCI.

n-Propyl resorcinarene (PrRsC):

PrRsC was synthesized according to the general and reported procedures.[112,209–211] Products were confirmed via ^{1}H NMR and FTMS-APCI.

Figure 93. Optical photograph of **PrRsC**

Example synthesis of *n*-heptyl resorcinarene (HeptRsC):

HeptRsC was synthesized according to the general and reported procedures.[212,213] (0.71 mL, 4.54 mmol) octanal and (0.5 g, 4.5 mmol) resorcinol were refluxed for 12 h in 10 mL ethanol, utilizing 1.8 mL 12 M HCl as a catalyst. The majority of solvent was removed via rotary evaporation, and the off-white precipitate was filtered off and washed with cold ethanol. The solid product was analyzed by ^{1}H NMR and FTMS-APCI. The product was dried in an 80 °C oven for 12 hours and used and utilized for further syntheses.

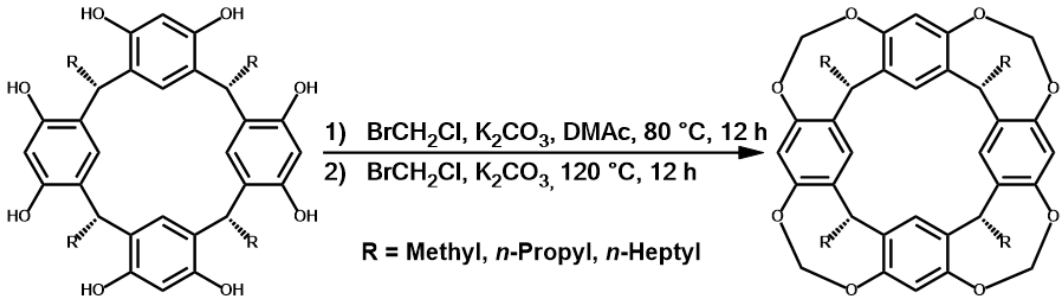

Figure 94. General synthesis of bridged resorcinarene cavitands (**B-(R)RsC**)

General synthesis of bridged resorcinarene cavitands (B-(R)RsC):

Bridged resorcinarene cavitands, **B-(R)RsC,** were synthesized according to published procedures.[112,151,211,214] Each of the corresponding dried resorcinarenes were charged into anhydrous dimethylacetamide, DMAc, in a heavy-walled glass pressure reactor with a screw-on Teflon stopper. Anhydrous K_2CO_3 was charged into the vessel, resulting in a brightly-colored reddish solution due to phenoxide formation. Excess bromochloromethane, $BrClCH_2$, was added and the vessel was sealed and placed in an 80 °C oil bath for 12 h. After this period another aliquot of K_2CO_3 and $BrClCH_2$ was added, and the solution was heated to 120 °C for an additional 8 h. At the this stage the

bright reddish color diminished and the solutions took on dark colors, indicating the absence of phenolate ions. The vessel was removed from the heat and allowed to cool to room temperature. The solution was poured into a large beaker; water and 3M HCl were added with vigorous stirring till bubbling stopped. The solution was covered and allowed to stand for a several hours in a refrigerator (4 °C). Lightly-colored tan to brown precipitates were collected via vacuum filtration and washed thoroughly with water. The products were dissolved in ethyl acetate:diethyl ether 5:1 and washed once with dilute sodium hydroxide to remove impurities and 3 times with water to remove remaining DMAc. The organic phase was subjected to rotary evaporation and the obtained products were products were analyzed by ^{1}H NMR and FTMS-APCI. The products were dried in an 80 °C oven for 24 hours

Bridged methyl resorcinarene cavitand (B-MeRsC):

B-MeRsC was synthesized according to the general and reported procedures.[112] Products were analyzed by ^{1}H NMR and FTMS-APCI.

Bridged *n*-Propyl resorcinarene cavitand (B-PrRsC):

B-PrRsC was synthesized according to the general and reported procedures.[108] Products were analyzed by ^{1}H NMR and FTMS-APCI.

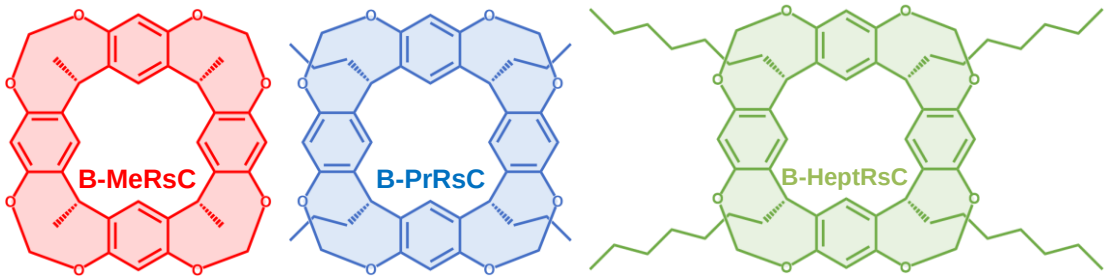

Figure 95. Chemical structures of bridged methyl, *n*-propyl, and *n*-heptyl resorcinarene cavitands from left to right (**B-MeRsC, B-PrRsC,** and **B-HeptRsC** respectively)

Bridged *n*-heptyl resorcinarene cavitand (B-HeptRsC):

B-HeptRsC was synthesized according to general and published procedures.[215] (0.3 g, 0.34 mmol, 1eqv.) dried **HeptRsC** was charged into 12 mL anhydrous dimethylacetamide, DMAc, in a heavy-walled glass pressure reactor with a screw-on Teflon stopper. (1.4 g, 10.2 mmol, 30 eqv.) dry K_2CO_3 was charged into the vessel, resulting in a brightly-colored reddish solution due to phenoxide formation. (0.68 mL, 10.2 mmol, 30 eqv.) bromochloromethane, $BrClCH_2$, was added and the vessel was sealed and placed in an 80 °C oil bath for 12 h. After this period another 1.4 g aliquot of K_2CO_3 and 0.68 mL $BrClCH_2$ was added, and the solution was heated to 120 °C for an additional 8 h. At the this stage the bright reddish color diminished and the solutions took on dark colors, indicating the absence of phenolate ions. The vessel was removed from the heat and allowed to cool to room temperature. The solution was poured into a large beaker; water and 3M HCl were added with vigorous stirring till bubbling stopped. The solution was covered and allowed to stand for a several hours in a refrigerator (4 °C). A tan precipitate was collected via vacuum filtration and washed thoroughly with water. The product was dissolved in ethyl acetate:diethyl ether 5:1 and washed once with

dilute sodium hydroxide to remove impurities and 3 times with water to remove remaining DMAc. The organic phase was subjected to rotary evaporation and the obtained products were products were analyzed by ^{1}H NMR and FTMS-APCI. The products were dried in an 80 °C oven for 24 hours

General Procedure for R C-PPN-n synthesis:

R C-PPN-ns were synthesized according to the procedures developed in the previous section (CHAPTER II) 0.1 g (1 eqv.) of each calixarene (**R)RSC** was transferred to a 7 mL Teflon-lined steel autoclave. An appropriate amount of terephthalaldehyde (e.g. 0.074 g, 0.55 mmol, 3 eqv. for **Methyl C-PPN-3**) was dissolved in 1 mL of 1,4-dioxane and charged into the reactor. Next, 0.3 mL 12 M HCl was added and the reactor was sealed and thoroughly agitated. The reactor was placed in a 220 °C oven for 24 h. All solid products were broken into pieces < 1 mm^3 and washed with approximately 100 mL of each, water, methanol, and acetone in order. The darkly-colored products were dried for 3 h at 80 °C in an oven and activated at 120 °C for 12 h under high vacuum (<100 μBar) before further analysis. Average yields >90% were obtained.

General Procedure for R B-PPN-n synthesis:

R B-PPN-ns were synthesized according to the procedures developed in the previous section (CHAPTER II) 0.1 g (1 eqv.) of each bridged cavitand, **B-(R)RsC,** was transferred to a 7 mL Teflon-lined steel autoclave. An appropriate amount of terephthalaldehyde (e.g. 0.068 g, 0.51 mmol, 3 eqv. for **Methyl B-PPN-3**) was dissolved

in 1 mL of 1,4-dioxane and charged into the reactor. Next, 0.3 mL 12 M HCl was added and the reactor was sealed and thoroughly agitated. The reactor was placed in a 220 °C oven for 24 h. All solid products were broken into pieces < 1 mm^3 and washed with approximately 100 mL of each, water, methanol, and acetone in order. The darkly-colored products were dried for 3 h at 80 °C in an oven and activated at 120 °C for 12 h under high vacuum (<100 μBar) before further analysis. Average yields >90% were obtained.

Figure 96. Optical photograph of **Propyl C-PPN-3**

BET Analysis:

Approximately 125 mg of pre-dried PPN was placed in a glass sample tube. Samples were evacuated to < 70 μBar for 12 h at 120 °C. **Heptyl B-PPN-3** was solvent exchanged after synthesis with diethyl ether and activated by flushing with supercritical CO_2 for several hours; the washed product was activated the same as other samples. The samples were massed and recorded. PPN samples were assessed via N_2 adsorption/desorption analysis on a Micromeritics ASAP 2420. Low pressure 77 K N_2, 77 K Ar, 273 K CO_2 isotherms were collected on ASAP 2020 instruments. BJH

algorithms were applied to N_2 desorption data and DFT or NLDFT algorithms were applied to N_2, CO_2, and Ar adsorption data in Microactive software.

III.iii Results

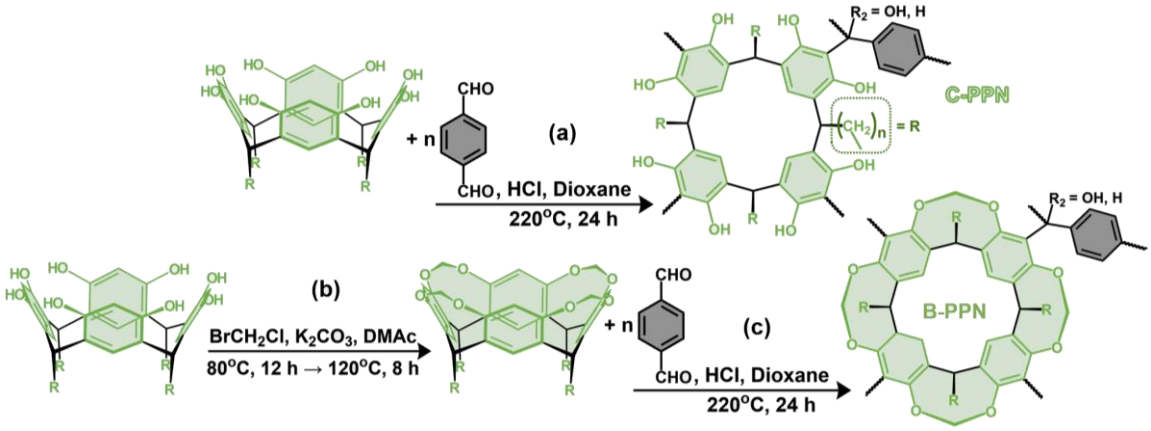

Figure 97. (a) Parent calixarene macrocycle (depicted as the *rccc*-crown conformer) and terephthalaldehyde condensed to form the **C-PPNs,** depicted as proposed structures**. (b)** Bridging of parent calixarenes into rigid cavitands by bromochloromethane. **(c)** Condensation of bridged cavitands into **B-PPNs,** depicted as expected structures.

Calixarenes (resorcinarenes) with methyl, *n*-propyl, and *n*-heptyl (**MeRsC**, **PrRsC**, and **HeptRsC**) "feet" groups were synthesized according to published procedures. Subsequently, the hydroxyl groups of **MeRsC**, **PrRsC**, and **HeptRsC** were bridged by methylene groups to form rigid cavitands, **B-MeRsC, B-PrRsC,** and **B-HeptRsC**. Starting from the three-pairs of flexible and rigid bridged calixarenes as monomers, a corresponding series of **C-PPNs** and **B-PPNs** were constructed. Due to the success of the previously explored phenol-aldehyde synthesis of **C-PPNs** in previous section (CHAPTER II), the similar conditions were utilized to construct the PPNs for this study. The calixarene and bridged cavitand monomers were linked with

terephthalaldehyde to form the PPNs **(figure 97)**, utilizing the same catalyst, concentrations, solvent, temperature, etc.

The one factor that was re-explored was linking aldehyde equivalents, due to the change in the number reactive phenolic branching points in the alkyl-footed monomers in this study in comparison to the **4-OHPhRsC** monomer utilized in CHAPTER II. Starting with the **B-PrRsC**, a series of **B-PPN-(n)s** were constructed where **(n)** designates the number of equivalents of terephthalaldehyde ranging from one to five **(figure 98)**. All equivalent samples were found to produce porous polymers but with greatly varying isotherm shapes. Starting from the **Propyl B-PPN-1**, the lowest porosity of the series was observed with a total porosity of 77 mL/g with a large hysteresis loop; increasing the equivalents **Propyl B-PPN-2** more than double the porosity to 184 mL/g, maintaining the isotherm shape and hysteresis. **Propyl B-PPN-3** and **Propyl B-PPN-4** sequentially had increased porosity to 284 and 283 mL/g, respectively, and produced new isotherm shapes with very wide hystereses **(figure 98)**. Finally, **Propyl B-PPN-5** produced the highest porosity in the series, resulting in 405 mL/g and developing a fairly standard Type II isotherm with little hysteresis **(figure 98)**.

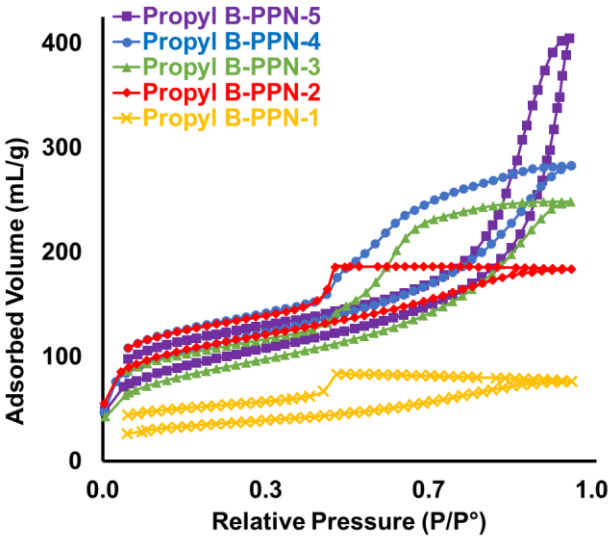

Figure 98. N_2 isotherms of **Propyl B-PPNs** synthesized with varying equivalents of terephthalaldehyde

From these results, it was determined that 3 to 5 eqv. of aldehyde should be examined in the further PPN syntheses due to these samples' high porosities. Some trends were apparent between the 4 eqv. and 5 eqv. series of **C-** and **B-PPNs (figure 99)**, with the highest porosities of the PPN pairs being those with the smallest methyl foot groups, followed by the larger *n*-propyl groups producing moderate porosity, and finally the largest *n*-heptyl groups produced nonporous polymers. These results are interpreted as qualitative evidence that the flexible alkyl feet groups do indeed decrease the porosity of the PPNs.

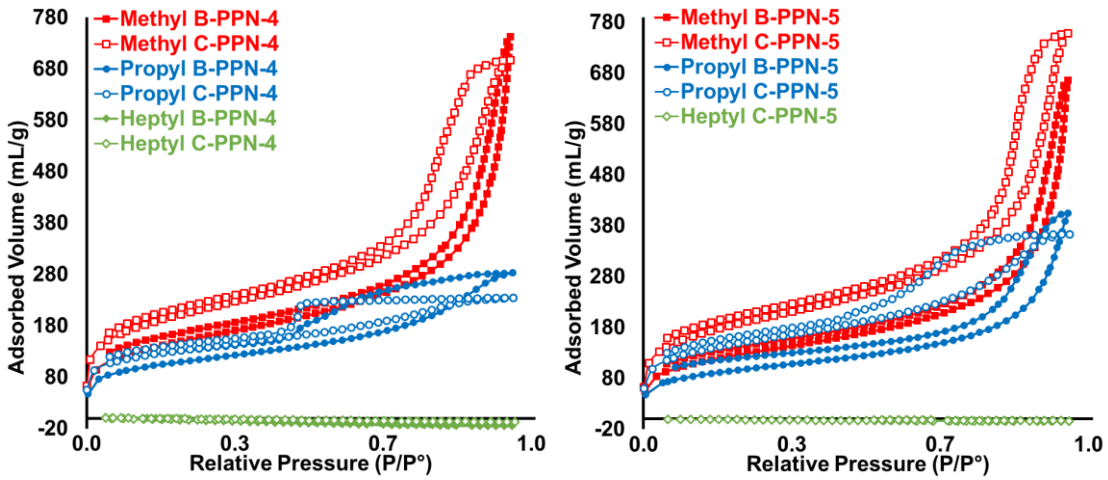

Figure 99. N_2 isotherms of **(a) B-PPN-4s** and **C-PPN-4s (b) B-PPN-5s** and **C-PPN-5s**

For the 3 eqv. series, the **C-PPNs** show a similar trend to what was previously observed with decreasing porosities with increasing foot chain length and moderate hystereses loops **(figure 100a)**. Due to all samples with *n*-heptyl feet groups producing non-porous polymers, the **Heptyl B-PPN-3** was activated via washing with supercritical CO_2. Comparing the pairs, **B-PPN-3s** displayed the clear differences from their **C-PPN-3** pairs for this series, maintaining a uniform Type II isotherm shape with narrow hystereses **(figure 100b)**. The total porosities of **B-PPN-3s** decreased from 542 to 517 to 392 mL/g with the methyl, propyl, heptyl series, respectively **(figure 100b)**. The differences in isotherm shape and hystereses between the **C-PPN-3s** and **B-PPN-3s** can be attributed the differences in conformational flexibility between the calixarene and bridged cavitand monomers, as was predicted.

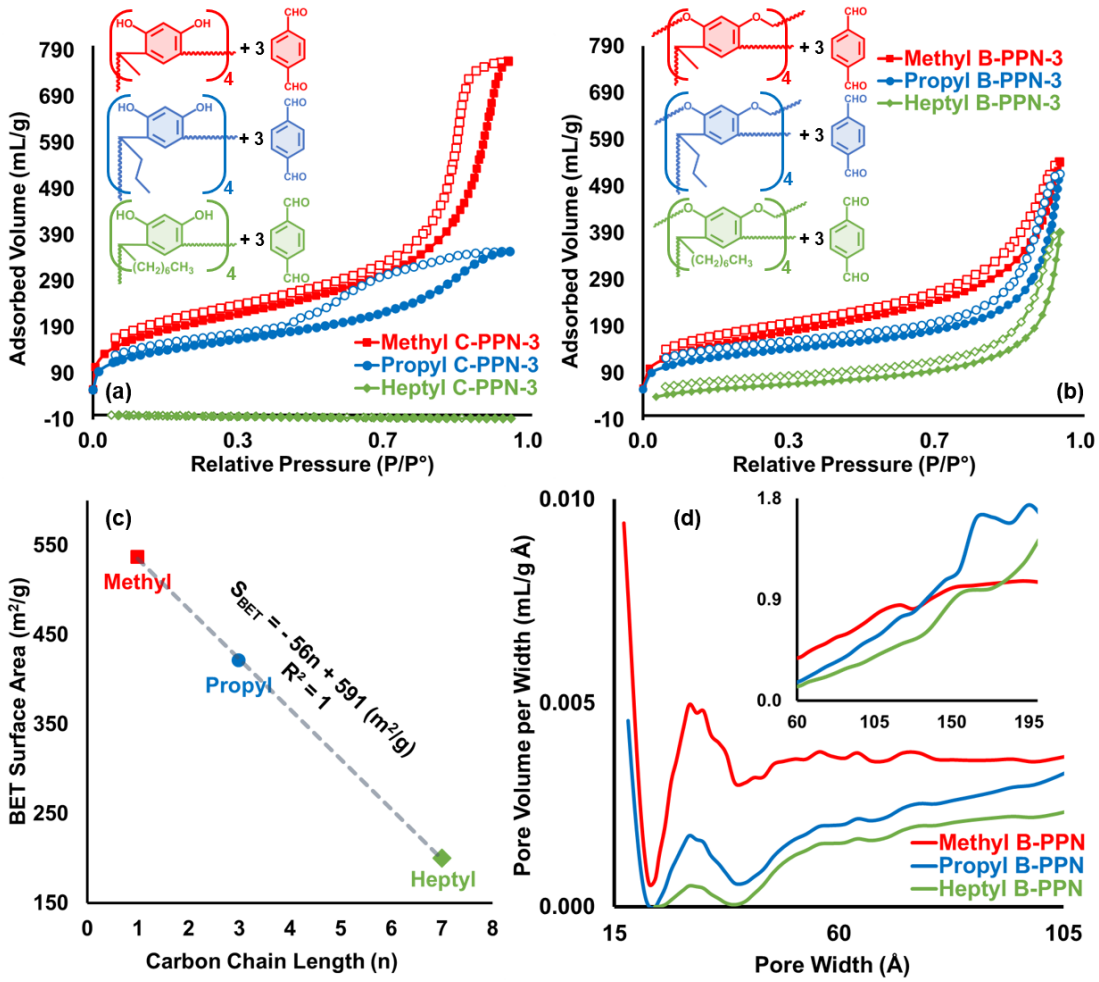

Figure 100. **(a)** N_2 adsorption isotherms of the **C-PPN-3s** with different foot chain lengths **(b)** N_2 adsorption isotherms of the **B-PPN-3s** with different foot chain lengths. **(c)** A linear plot of the BET micropore surface areas, S_{BET}, of each **B-PPN**. **(d)** NLDFT N_2 adsorption pore size distribution of **B-PPNs**; inset of Barrett-Joyner-Halenda (BJH) N_2 desorption pore size distribution**.**

To quantify the effect of the foot chain length on the PPN porosity, **B-PPN-3s** were utilized to make a comparison due to their uniform isotherm shapes. The calculated S_{BET} values, being derived from the microporosity**,** should provide a metric of the **B-PPN-3s'** porosity as modified by the feet groups. For the **B-PPN-3** series, for methyl, propyl, and heptyl, the S_{BET} values were determined to be 536, 421, and 200 m^2/g,

respectively. Plotting the carbon chain lengths of the feet groups versus the calculated S_{BET} values gave a linear relationship with a high correlation coefficient (R = 0.999901, a value that is likely anomalously high accounting for error in the BET method) **(figure 100c)**. Overall, the determined relationship provides significant evidence to support a hypothesis that the volume of the feet groups within the cavitand directly reduce the porosity in the PPNs due to occupied pore space.

Examining pore size distributions calculated via NLDFT algorithms from 77 K N_2 gas adsorption isotherms for the **B-PPN-3s,** a pore centered at 32 Å is apparent as well as pores distributed from 4 to above 10 nm **(figure 100d)**. The BJH algorithm applied to the N_2 desorption isotherm indicates the mesoporosity of all three **B-PPN-3s** increases from 6 to 30 nm.

To assess the effect of the cavitands on the micropore structures of the **B-PPN-3s** 273 K CO_2 and 77 K Ar adsorption isotherms were collected. Nitrogen gas adsorption is commonly used to analyze porous materials but has some disadvantages when assessing microporous materials with very narrow pores (< 1 nm). Argon, unlike quadropolar N_2, has lower interaction with charged, polar, or reactive surface chemistries and a lower cross-sectional area than N_2. Likewise, CO_2 at 273 K has much faster kinetics of diffusion into narrow micropores which allows analyses that would be time-prohibitive for larger gases at lower temperatues.

Examining 273 K CO_2 adsorption isotherms of the **B-PPN-3s** show the same trend in total porosity as observed in the N_2 adsorption isotherms **(figure 101)**. Applying a NLDFT algorithm to these isotherms revealed that all the **B-PPN-3s** showed narrow

micropores between 4 and 9 Å and a larger pore between 11 and 16 Å, with the volume of both pores decreasing with the foot chain length **(figure 101)**. The pore at 11 - 16 Å is comparable to pores of **C-PPN-5** observed in CHAPTER II which were attributed to the resorcinarene macrocycle and can likewise be assigned here.

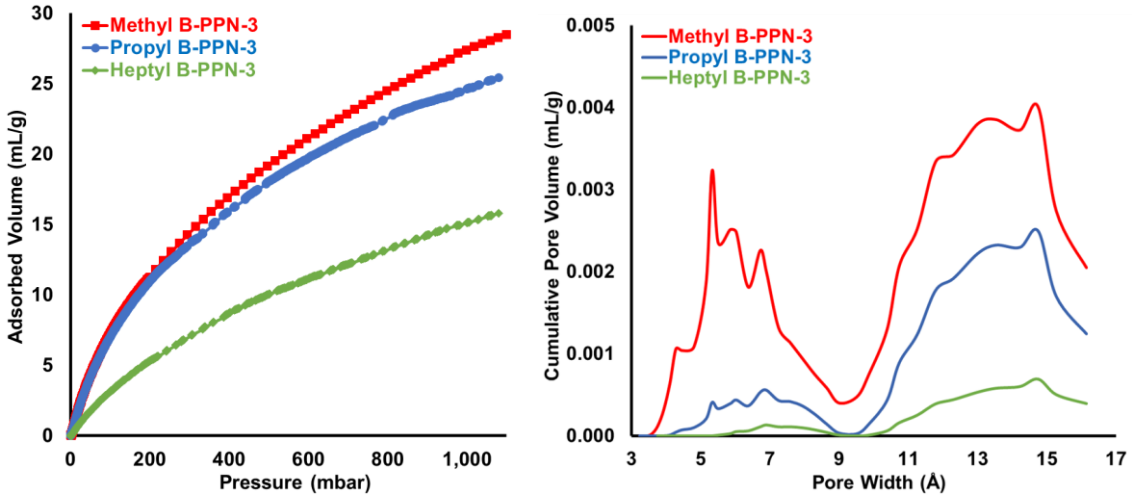

Figure 101. 273 K CO_2 isotherms of **B-PPN-3s** and NLDFT pore size distributions

77 K Ar isotherms repeated the trends observed in the N_2 and CO_2 analyses with regular decreases in total porosity with respect to the foot chain lengths from the methyl to *n*-heptyl functionalized PPNs **(figure 102)**. Examining the PSDs calculated via an NLDFT algorithm, these isotherms showed that all **B-PPN-3s** had pores between 11 and 17 Å, similar to the CO_2 determination; the PSDs also display a pore between 17 and 24 Å and pore centered at 31 Å, similar to what was determined from the N_2 PSDs **(figure 102)**.

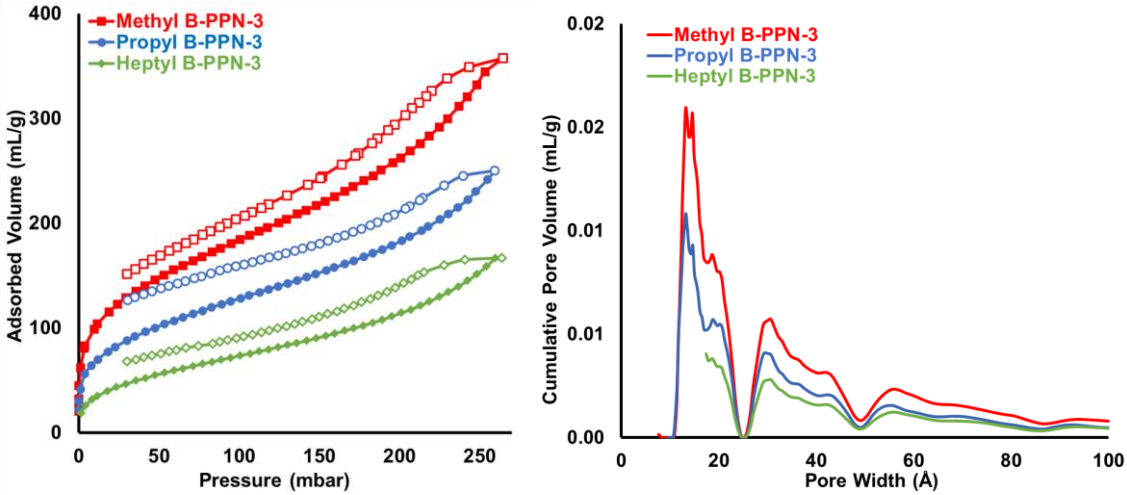

Figure 102. 77 K Ar isotherms of **B-PPN-3s** and NLDFT pore size distributions

As an initial chemical analysis of the produced PPNs, FTIR-ATR was performed. Comparing the spectra of the flexible (**R)RsC** and rigid **B-(R)RsC** monomer pairs, the disappearance of the large O-H stretching bands at 3,000 - 3,700 cm^{-1} and the appearance of an intense C-O-C stretching bands at 900 - 1,020 cm^{-1} indicate the formation of the ether bridging linkages **(figure 119)**. Comparing the spectra of the **C-PPN-3** and the **B-PPN-3** pairs, only small differences in the intensity of the signal bands were observed **(figure 103, 120, and 121)**. The **C-PPN-3** and **B-PPN-3** pairs all displayed strong C=O carbonyl-type stretching bands at 1,705 cm^{-1} as observed for **C-PPNs** in CHAPTER II and maintained their distinct C-H stretching bands at 2,860 - 2,960 cm^{-1} due to their respective alkyl groups. The spectra all displayed moderate O-H stretching bands with the disappearance of the C-O-C stretching bands in the **B-PPN-3s,** indicating the apparent loss of bridging linkages during synthesis **(figure 103, 120, and 121)**.

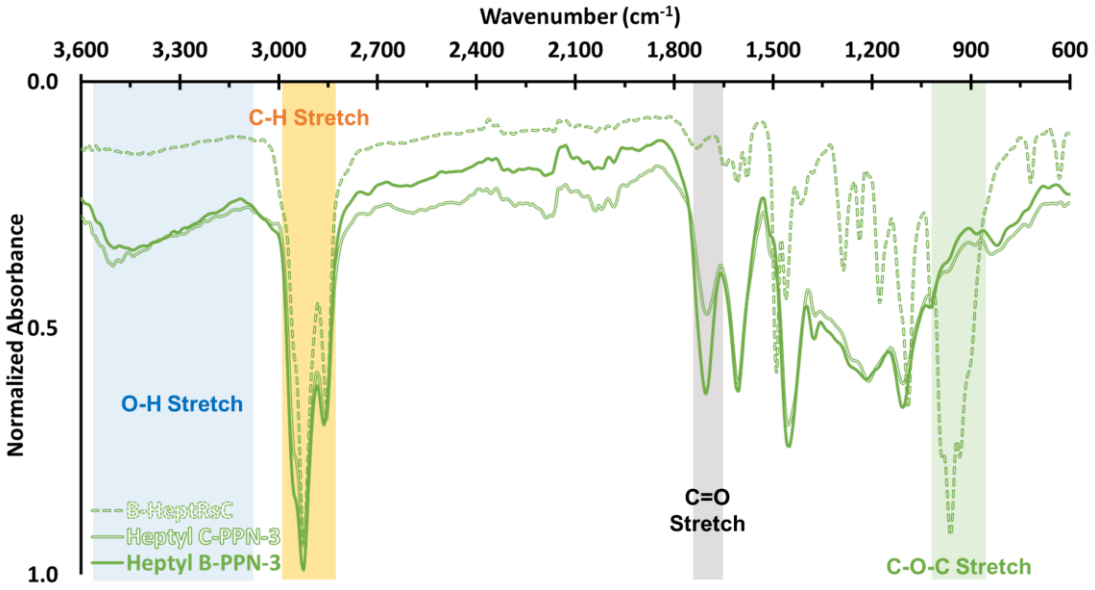

Figure 103. Comparison of normalized FTIR-ATR spectra of the bridged cavitand, **B-HeptRsC**, the **Heptyl C-PPN-3**, and **Heptyl B-PPN-3**

While the porosities of the PPNs were clearly modified by presence or absence of bridging methylene groups, the possibility that these linkages were hydrolyzed or oxidized during the acidic high-temperature syntheses is apparent from the FTIR-ATR spectra. To further examine this, ^{13}C-CP-MAS-ssNMR analyses were performed on the PPNs as previously described in CHAPTER II. Spectra of the **PrRsC** and **B-PrRsC** monomers and **C-PPN-3s** and **B-PPN-3s** polymer pairs were collected and compared. For the monomer pairs, the installation of the bridging methylene groups in the **B-PrRsC** allowed for the resolution of the four unique aromatic ^{13}C signals where only three are visible in the flexible **PrRsC**; moreover, the **B-PrRsC** displayed downfield 2^{o} ^{13}C signals at 101 ppm that correspond to deshielded O-CH_2-O bridging groups **(figure 104)**. Examining the spectra for the **C-PPN-3s** and **B-PPN-3s** with these indicators in mind, a comparison reveals the presence of the alkyl ^{13}C peaks corresponding feet

groups in the final products, as well as a diminished ^{13}C peak near 150 ppm which corresponds to aromatic 4^{o} C-O from either the phenol or bridged ether groups **(figure 104, 122,** and **123)**. Furthermore, the 2^{o} ^{13}C signals at 101 ppm indicating the methylene bridging groups cannot be detected in the **B-PPN-3s** spectra **(figure 104, 122,** and **123)**.

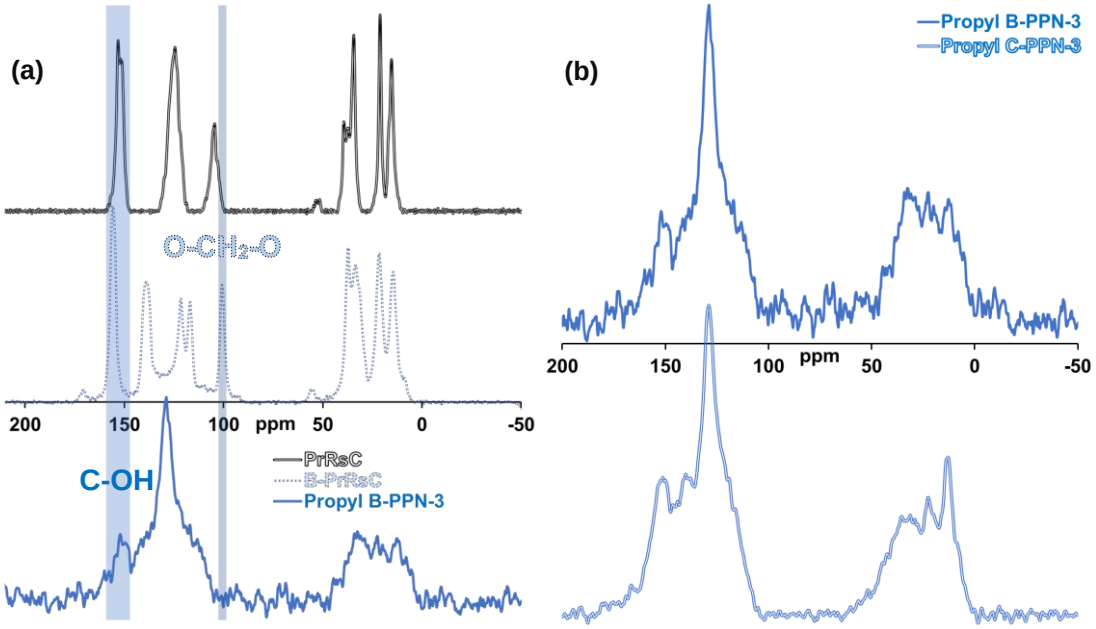

Figure 104. Comparison of ^{13}C-CP-MAS-ssNMR spectra of **(a) B-PrRsC**, **PrRsC**, and **Propyl B-PPN-3 (b) Propyl B-** and **Propyl C-PPN-3**

Summarizing results from IR and ssNMR analyses, it can be concluded that the alkyl feet groups survive the PPN syntheses but the methylene bridging groups are either hydrolyzed, oxidized, or otherwise reacted during the polymerizations. The high-temperature acid-catalyzed synthesis employed to construct the **C-PPNs** and **B-PPNs** is an efficient and convenient route to highly-crosslinked porous phenol-aldehyde polymers; however, this method may have been detrimental to the objective of producing bridged cavitand-based PPNs (**B-PPNs**) in comparison to milder polymerization techniques.

Nevertheless, if the methylene-bridged “cup” of the cavitands do not survive the syntheses, it is apparent that their conformational restriction on the network structures had an affect on the resulting polymers’ porosities. The clear differences in isotherm shape and hystereses between the **C-PPNs** and **B-PPNs** are indicative of the flexibility and rigidity their respective monomers during the polymerization. Hypothetically, the rapid network formation could proceed significantly before the loss of the bridging structures. If this is the case, the bridging groups acted more as templates that are labalized during the polymerization.

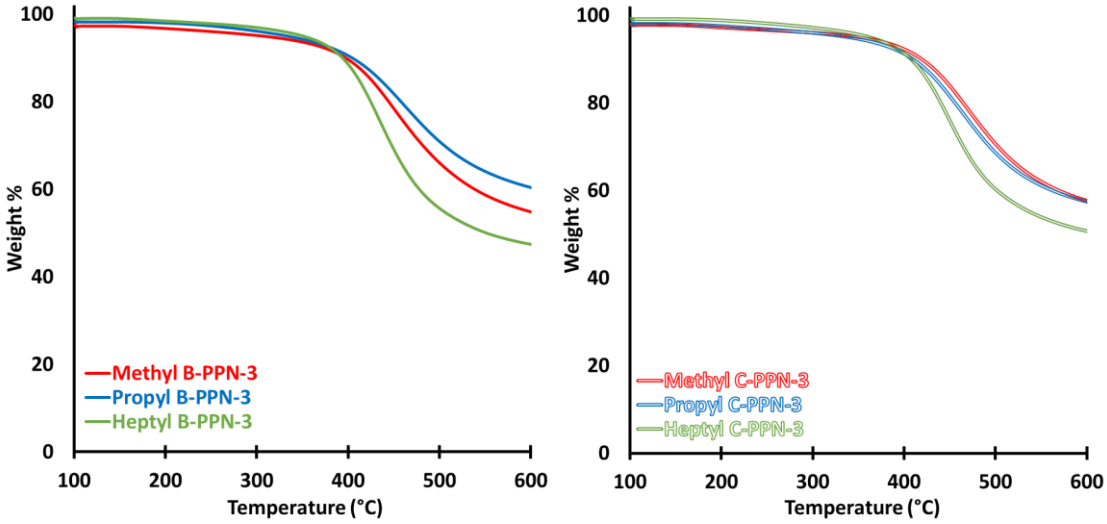

Figure 105. Comparison of the thermal decomposition of **C-** and **B-PPN-3s** under nitrogen

Thermal stability of the **C-PPN-3s** and **B-PPN-3s** was assessed via TGA under nitrogen atmospheres. All the **C-PPN-3s** and **B-PPN-3s** had similar thermal stabilities (90 wt %) between 395 and 415 °C **(figure 105)**. The **Heptyl C-PPN-3s** and **B-PPN-3s** did have a noticeably greater mass loss during degradation which may be due to the partial loss of these significantly larger feet groups during pyrolysis.

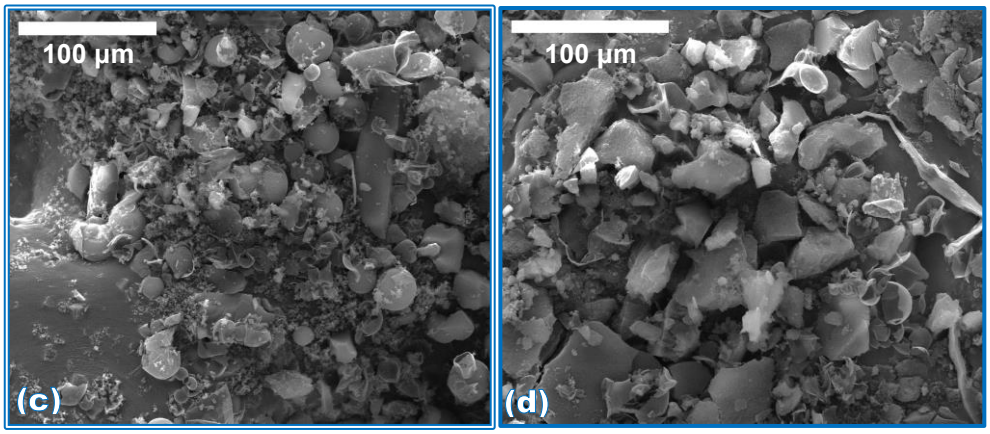

Figure 106. (a) SEM image of the **Methyl C-PPN-3** (100 µm scale). **(b)** SEM image of the **Methyl B-PPN-3** (100 µm scale).

Examining SEM micrographs of the **C-PPN-3s** and **B-PPN-3s**, the propyl and heptyl PPNs all show typical block-like morphology with particle sizes on the order of 10 - 100 µm; the only apparent differences between these being the rougher or more fragmented surface morphology on the **B-PPN-3s (figures 124b, 125b, and 126b)**. Interestingly, **Methyl C-PPN-3s** and **Methyl B-PPN-3s** display complex hollow spheres on the order of 10 - 100 µm **(figure 106)**.

III.iv Further work

The **C-PPN** and **B-PPN** pairs constructed in this study provide evidence that the alkyl feet of the monomers only reduce the porosity of the resulting PPNs. To further examine this, the "footless" or "parent" calixarenes and cavitands could be constructed and utilized produce **C-PPN** and **B-PPN** pairs **(figure 107)**.[216,217] These samples would serve as further evidence of the observed trend linear **(figure 100c)** and would indicate how the porosity of "cup" part of the monomer is significant to the porosity of the PPNs.

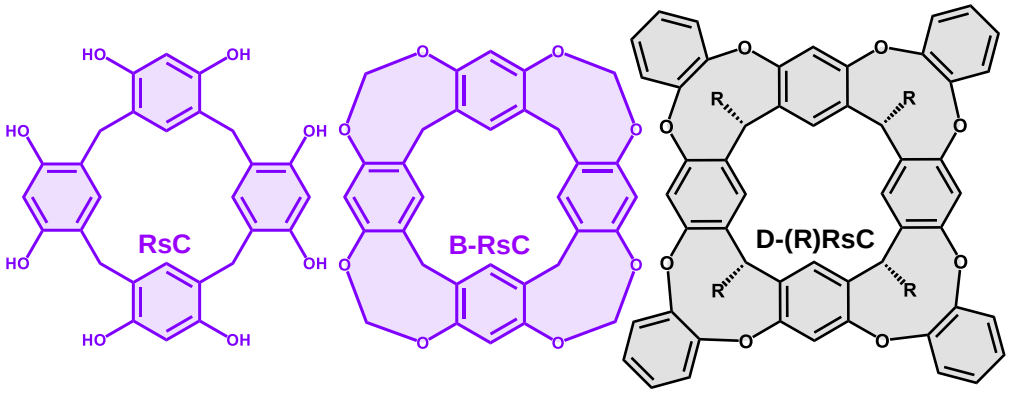

Figure 107. Chemical structures of the parent, bridged parent cavitand, and catechol-deepened cavitand from left to right (**RsC**, **B-RsC**, and **D-(R)RsC** respectively)

Alternatively, with the feet of the calixarene examined, the "cup" of calixarene could be further examined by "deepening" or adding large bridging groups such as a catechols to extend the cavitands **(figure 107)**.[149,152,218–222] Likewise, larger calixarene macrocycles could be synthesized with five or more ring members and utilized to construct PPNs.[217]

An application of the porous polymers constructed in this study could be to the selective sequestration of ^{137}Cs through ion exchange from basic aqueous solutions.[189,223,224] Phenolic ion exchange resins have been applied to radioactive ^{137}Cs sequestration from basic aqueous solutions. Cavitands and resorcinarenes have been reported to show high selectivities (K > 1000) for cesium over sodium which is required for recovering cesium from radioactive waste streams.[110,130,131,225] This is in an application that could be explored in further work.

III.v Summary

Two series of PPNs were constructed from flexible calixarene macrocycles **C-PPNs** and rigid bridged cavitands **B-PPNs**. The calixarene-based **C-PPNs** had large hysteresis in their gas adsorption isotherms and an irregular decreasing trend in the S_{BET} with respect to the carbon chain length of the alkyl feet groups. Bridged cavitand-based **B-PPNs** had narrower hystereses in their gas adsorption isotherms and had regular decreasing trend in the S_{BET} with the alkyl foot carbon chain length. The narrower hystereses in the **B-PPNs** than the **C-PPNs** were attributed to reduced flexibility between the bridged polymers. Chemical analyses of the PPNs through IR and ssNMR spectroscopy revealed that the bridging groups in the **B-PPNs** did not survive the polymerizations but most likely acted to template the network formation. While this work provides a starting point, further work would be required characterize how the "cup" shape and size affects the porosity of calixarene-derived PPNs.

III.vi Supplemental information

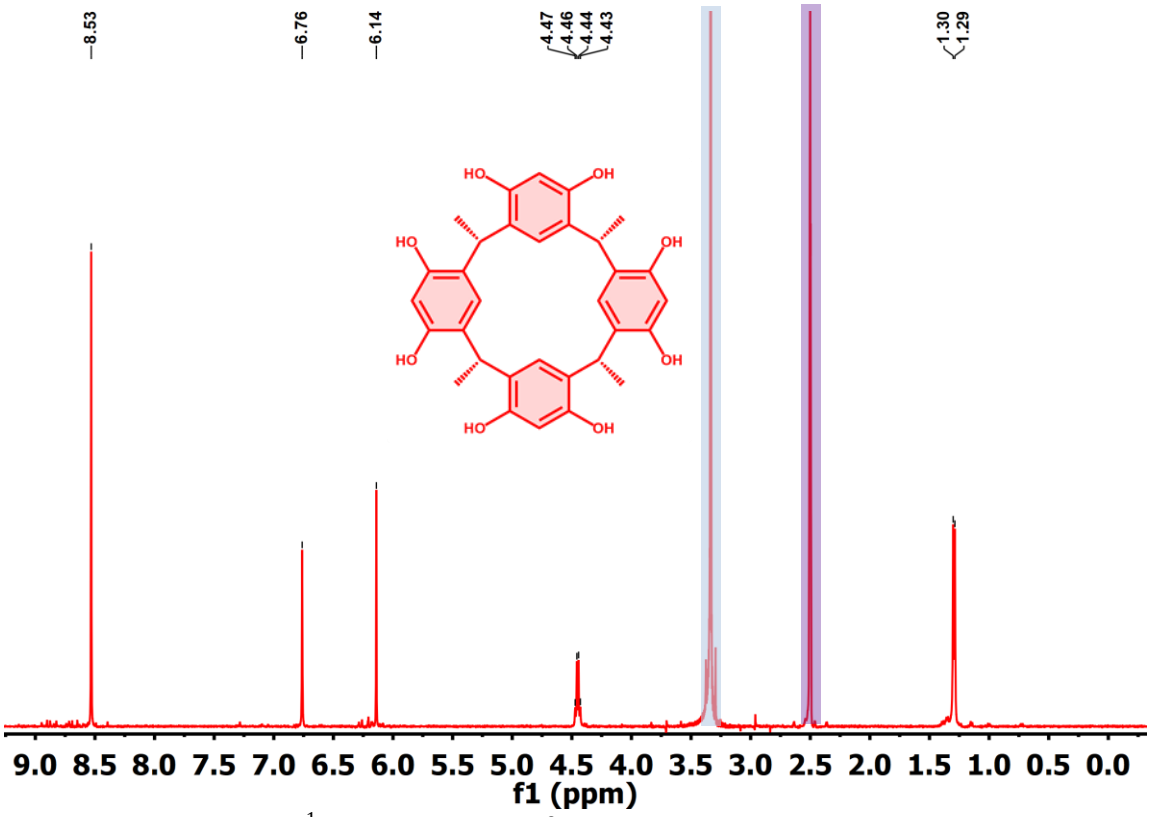

Figure 108. 500 MHz ^{1}H NMR spectra of **MeRsC** in D_6-DMSO, blue overlay indicates residual water and purple overlay indicates residual solvent DMSO

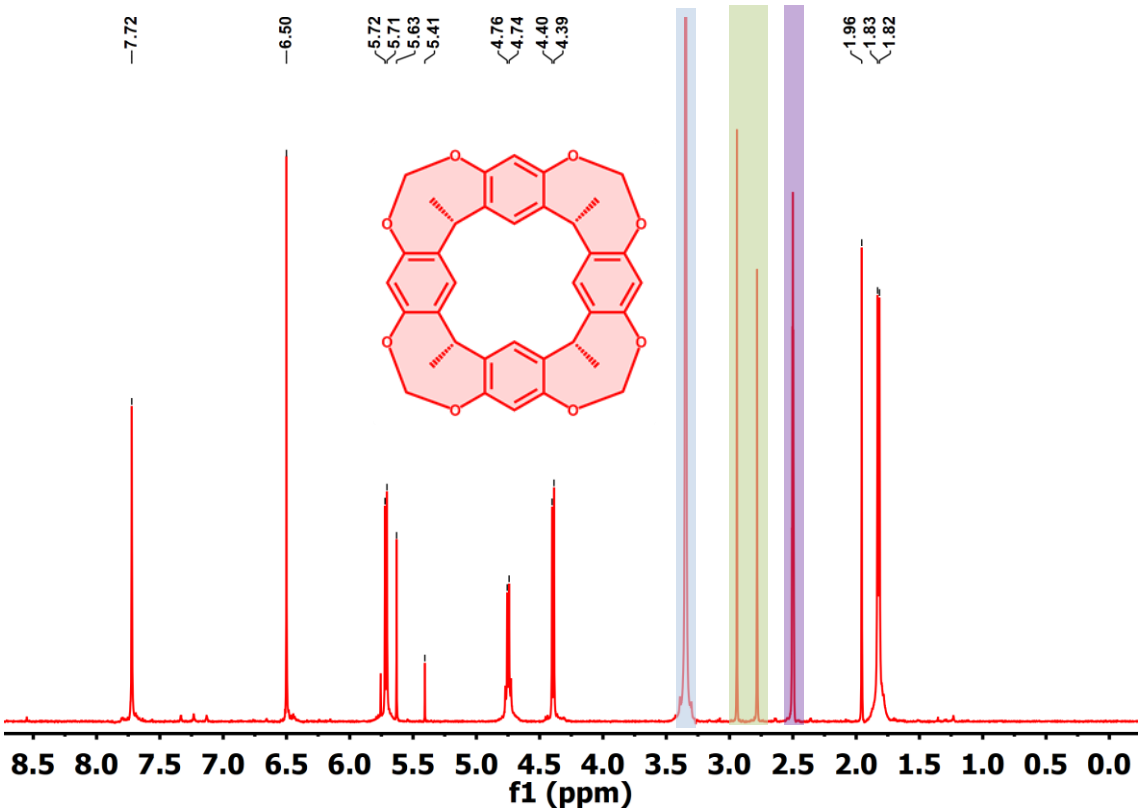

Figure 109. 500 MHz ^{1}H NMR spectra of **B-MeRsC** in D_6-DMSO, blue overlay indicates residual water, purple overlay indicates residual solvent, and green overlay indicates residual DMAc

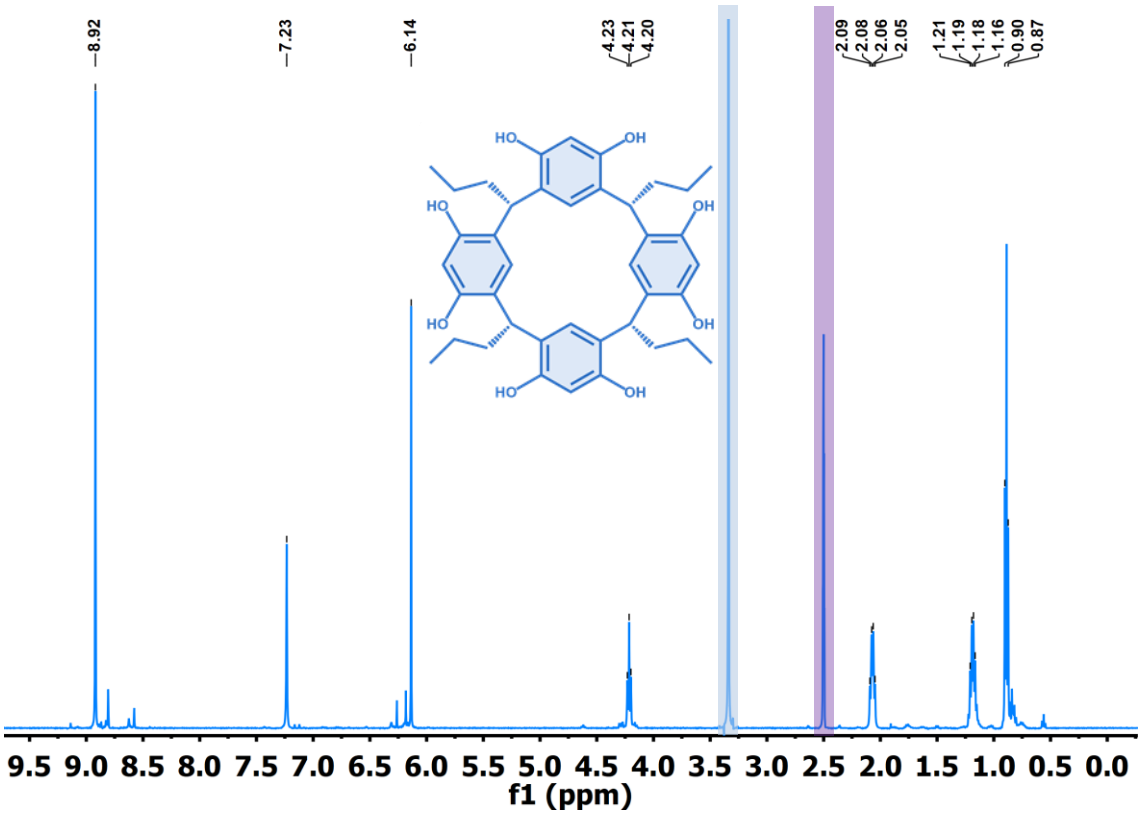

Figure 110. 500 MHz ^{1}H NMR spectra of **PrRsC** in D_6-DMSO, blue overlay indicates residual water and purple overlay indicates residual solvent DMSO

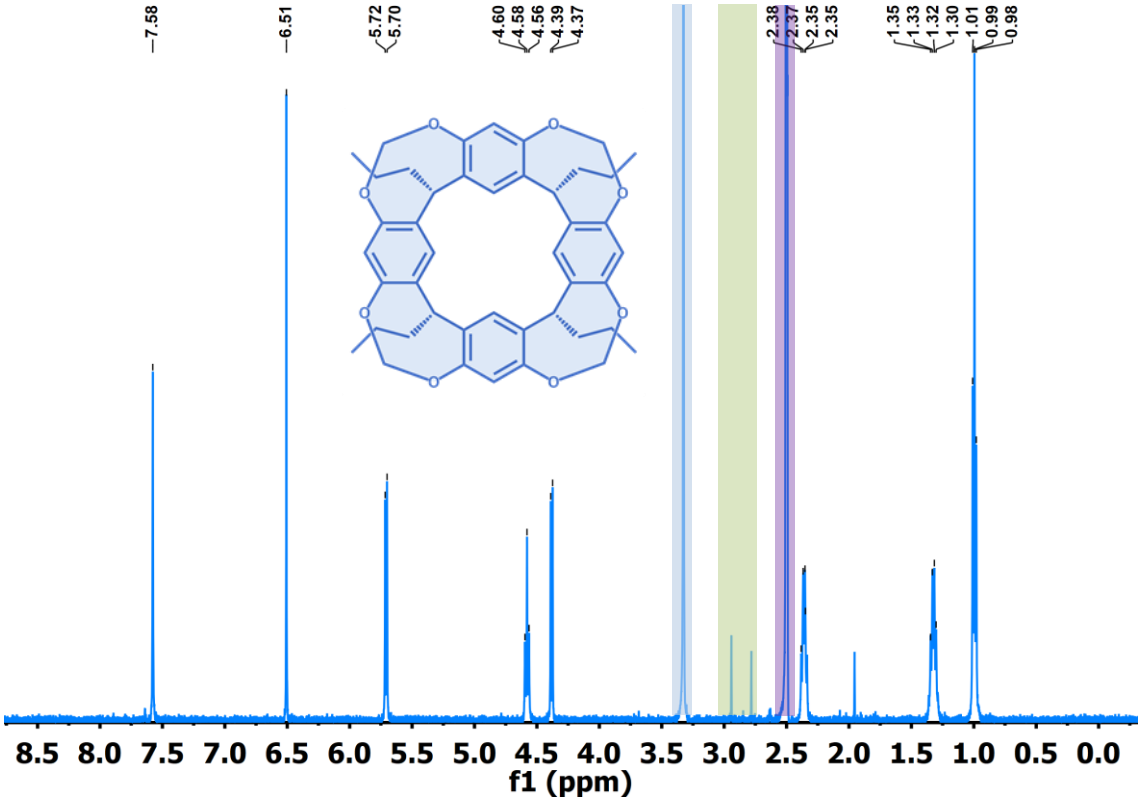

Figure 111. 500 MHz ^{1}H NMR spectra of **B-PrRsC** in D_6-DMSO, blue overlay indicates residual water, purple overlay indicates residual DMSO, and green overlay indicates residual DMAc

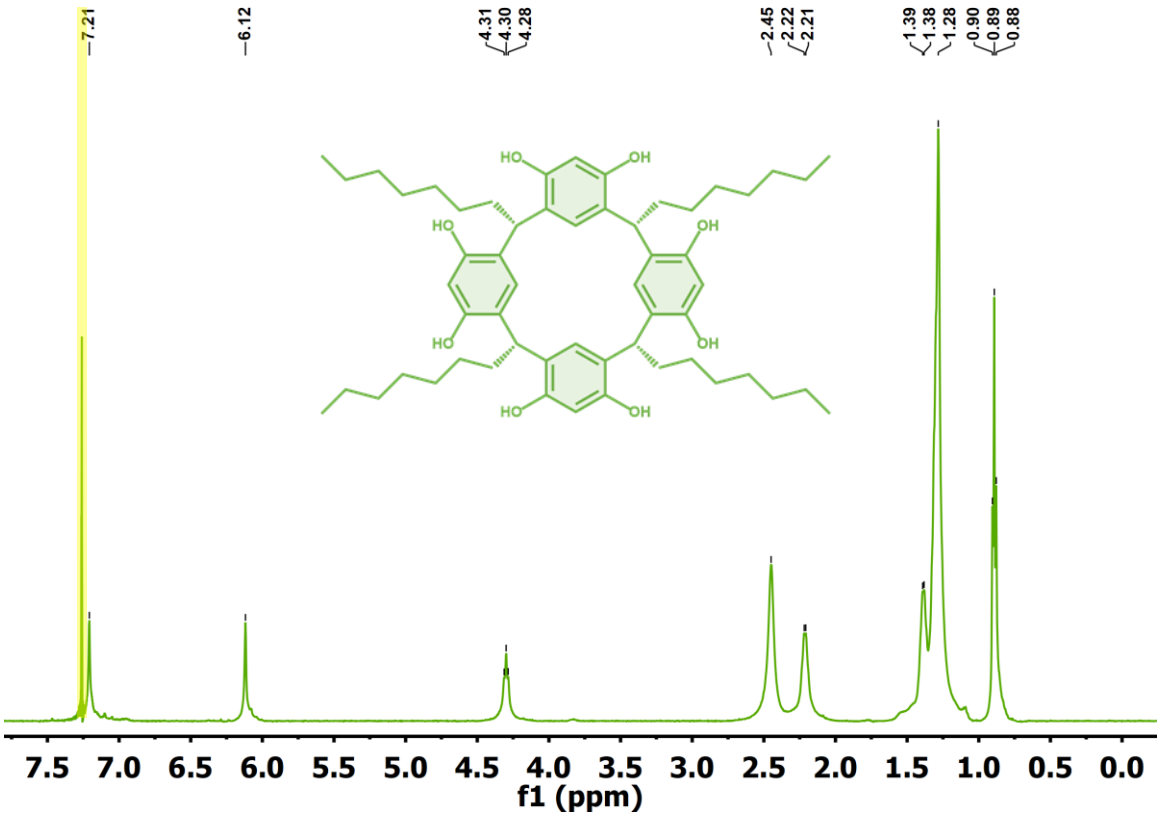

Figure 112. 500 MHz ^{1}H NMR spectra of **HeptRsC** in $CDCl_3$, yellow overlay indicates residual solvent $CHCl_3$

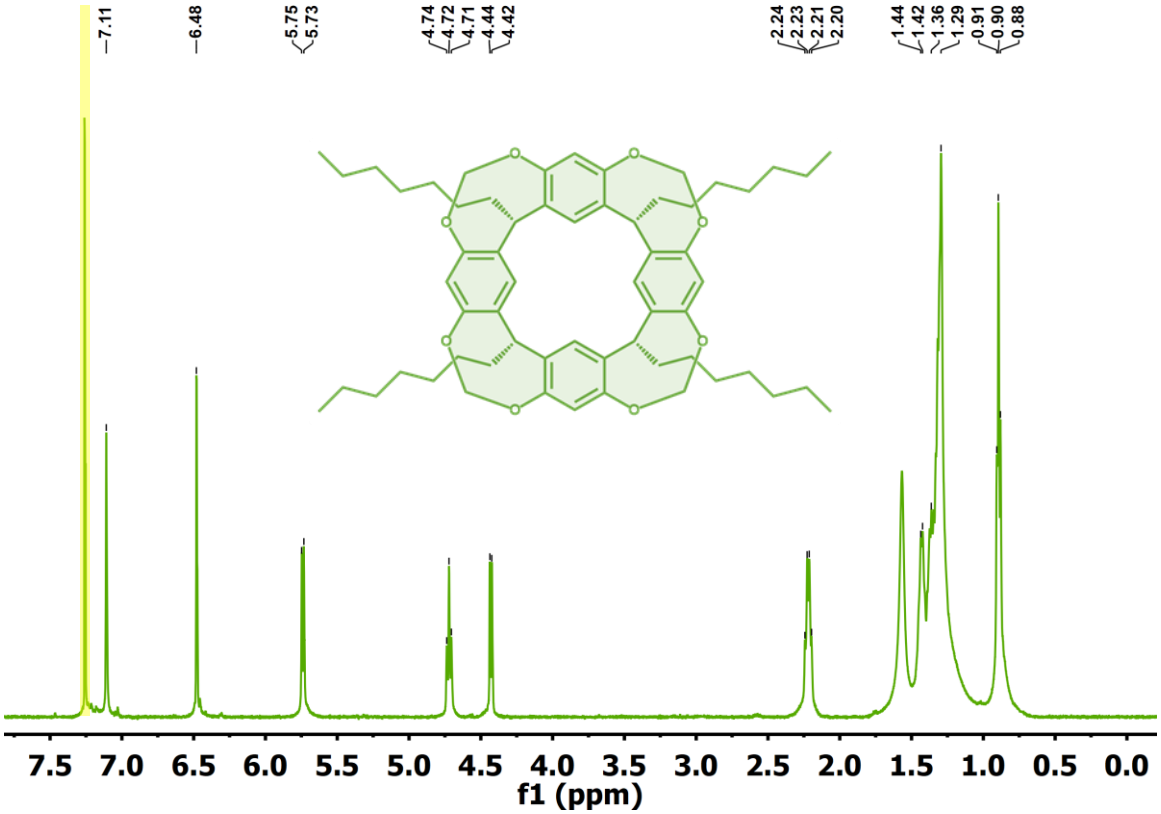

Figure 113. 500 MHz ^{1}H NMR spectra of **B-HeptRsC** in $CDCl_3$, yellow overlay indicates residual solvent $CHCl_3$

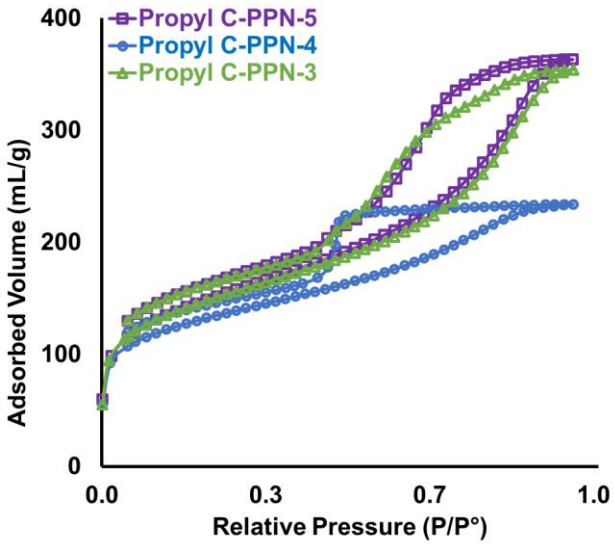

Figure 114. N_2 isotherms of **Propyl C-PPNs** synthesized with varying equivalents of terephthalaldehyde

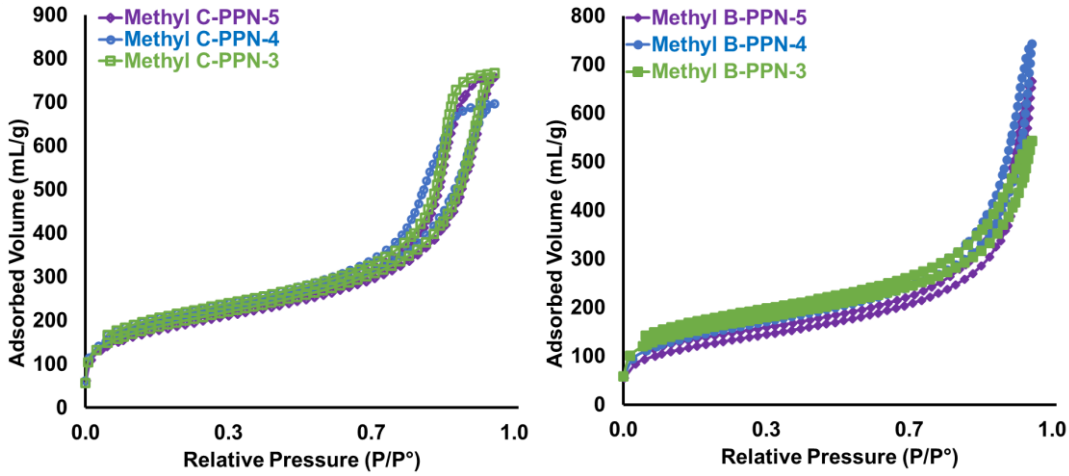

Figure 115. N_2 isotherms of **Methyl C-PPNs** and **Methyl B-PPNs** synthesized with varying equivalents of terephthalaldehyde

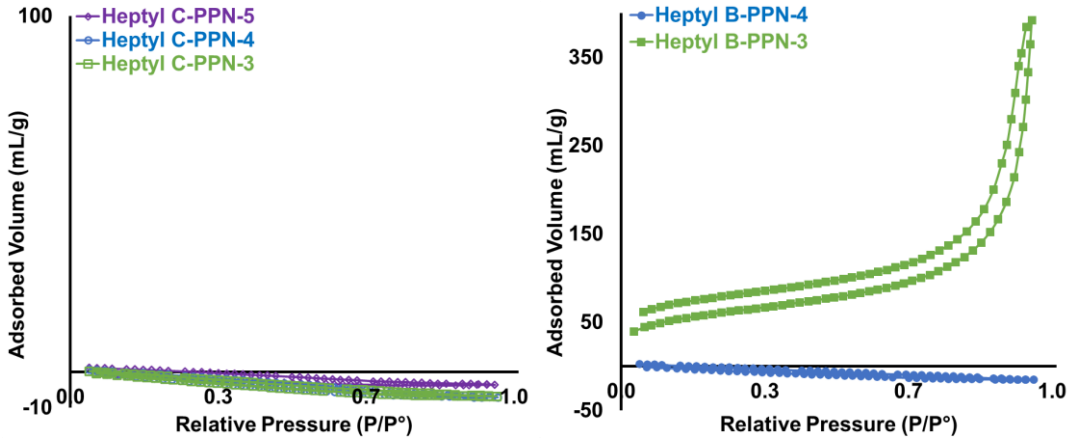

Figure 116. N_2 isotherms of **Heptyl C-PPNs** and **Heptyl B-PPNs** synthesized with varying equivalents of terephthalaldehyde

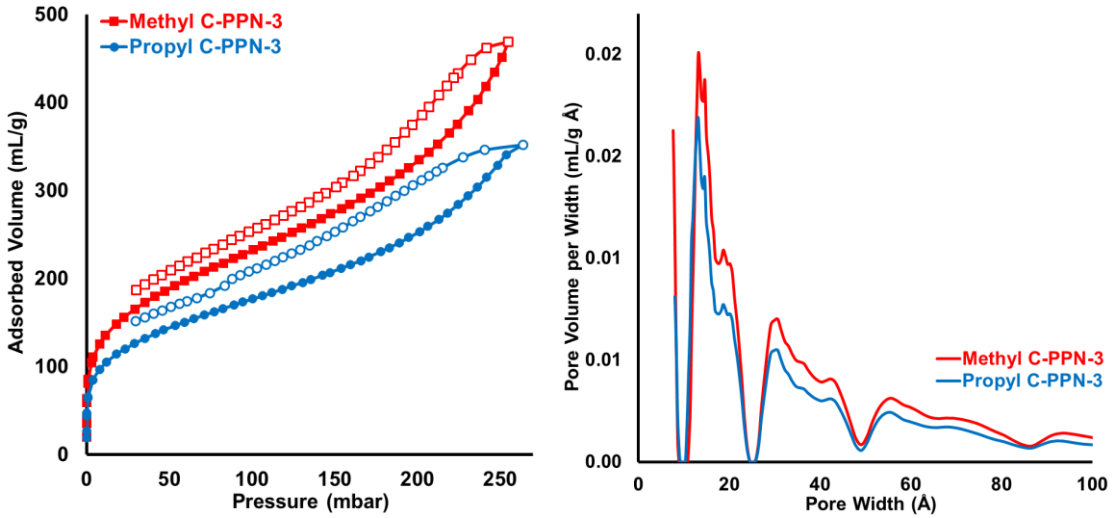

Figure 117. 77 K Ar isotherms of **C-PPN-3s** and derived NLDFT pore size distributions

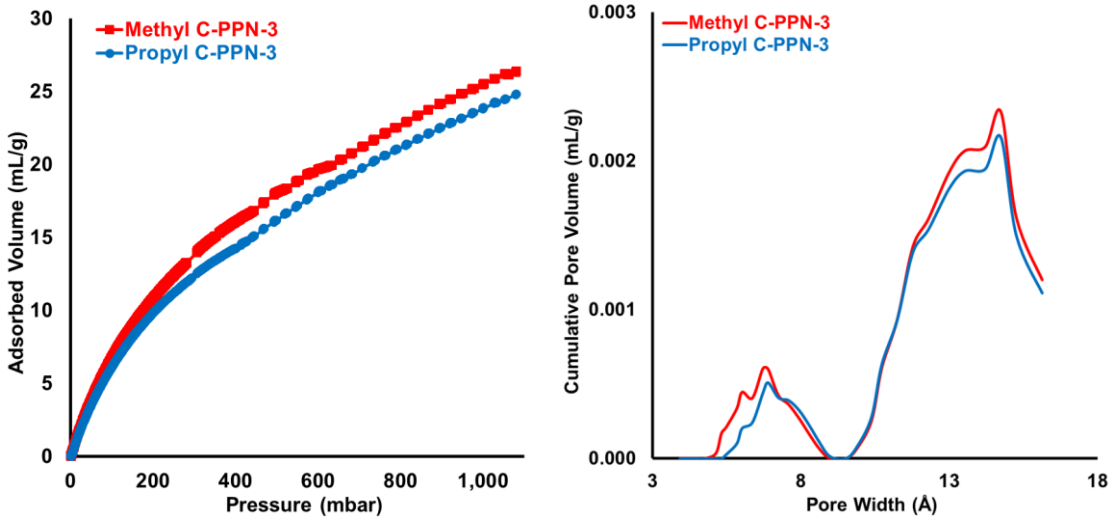

Figure 118. 273 K CO_2 isotherms of **C-PPN-3s** and derived NLDFT pore size distributions

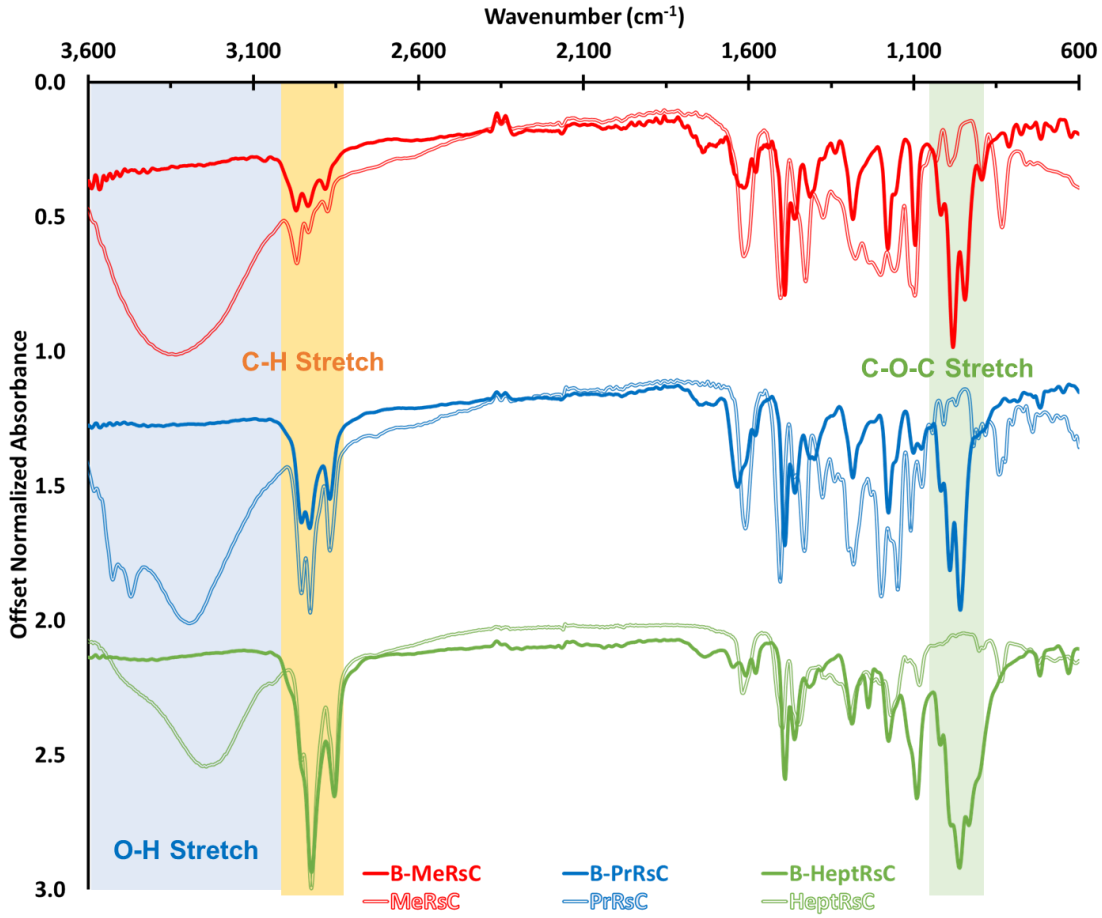

Figure 119. Comparison of normalized offset FTIR-ATR spectra of the bridged cavitands, **B-MeRsC, B-PrRsC**, and **B-HeptRsC** to the calixarenes, **MeRsC, PrRsC**, and **HeptRsC**

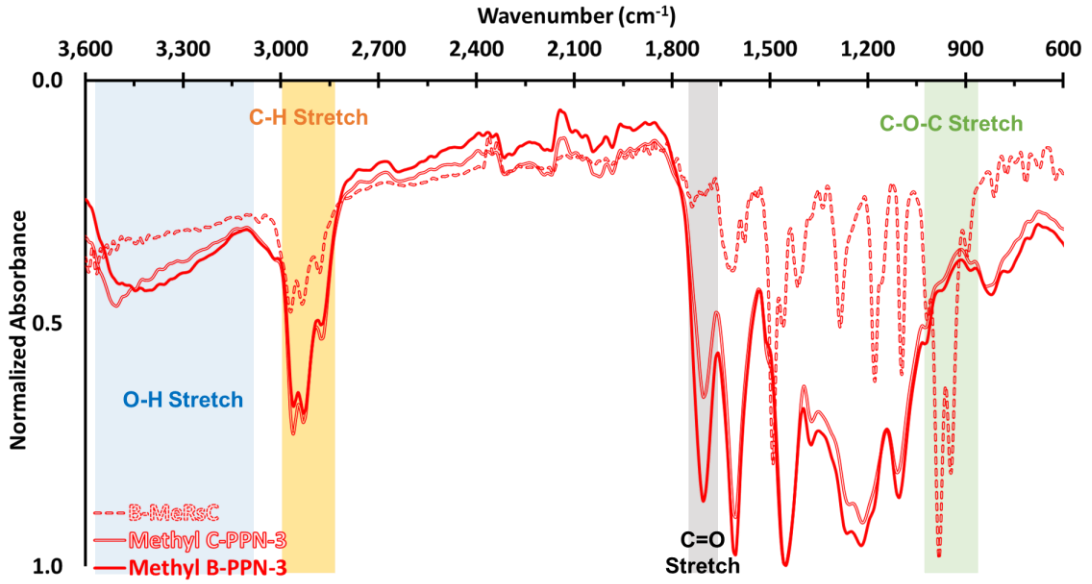

Figure 120. Comparison of normalized FTIR-ATR spectra of the bridged cavitand, **B-MeRsC**, the **Methyl C-PPN-3**, and **Methyl B-PPN-3**

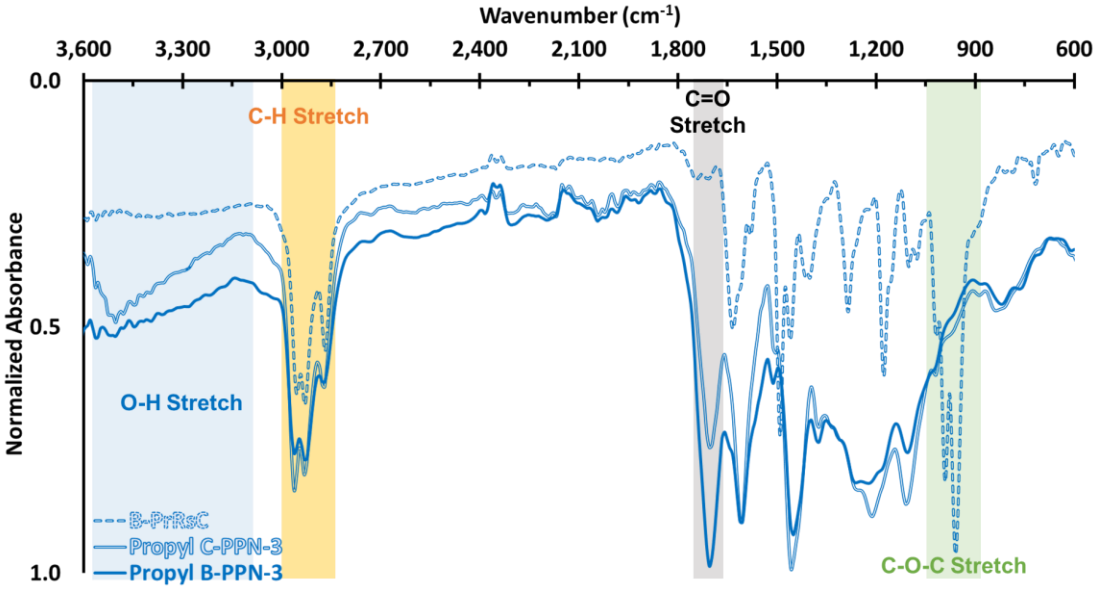

Figure 121. Comparison of normalized FTIR-ATR spectra of the bridged cavitand, **B-PrRsC**, the **Propyl C-PPN-3**, and **Propyl B-PPN-3**

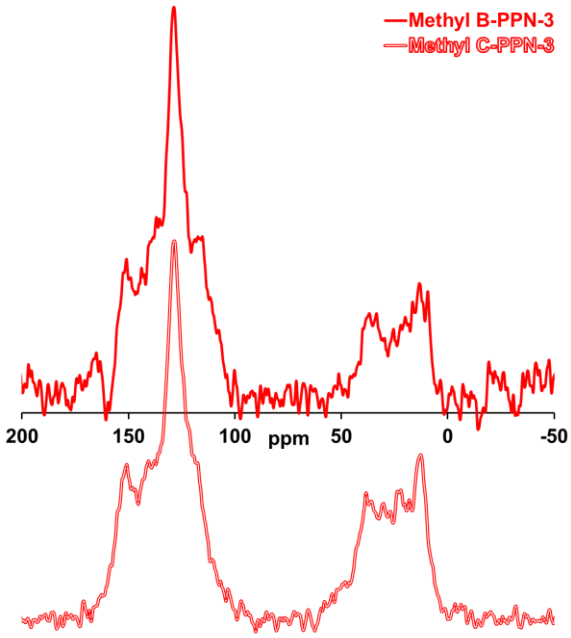

Figure 122. Comparison of ^{13}C-CP-MAS-ssNMR spectra bridged cavitand, **Methyl B-** and **Methyl C-PPN-3**

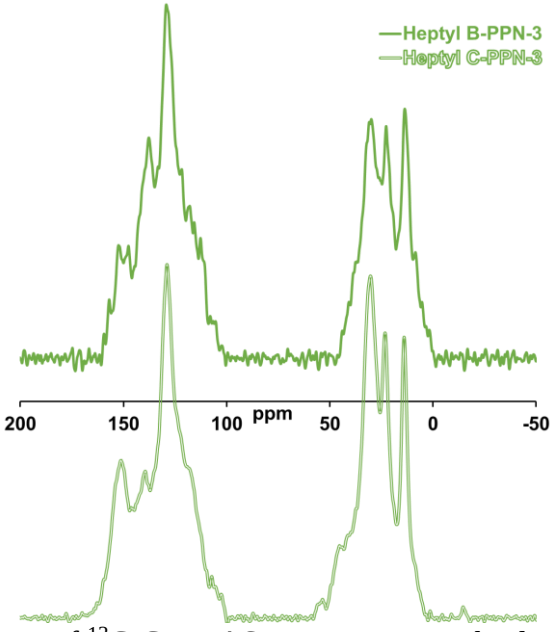

Figure 123. Comparison of ^{13}C-CP-MAS-ssNMR spectra bridged cavitand **Heptyl B-** and **Heptyl C-PPN-3**

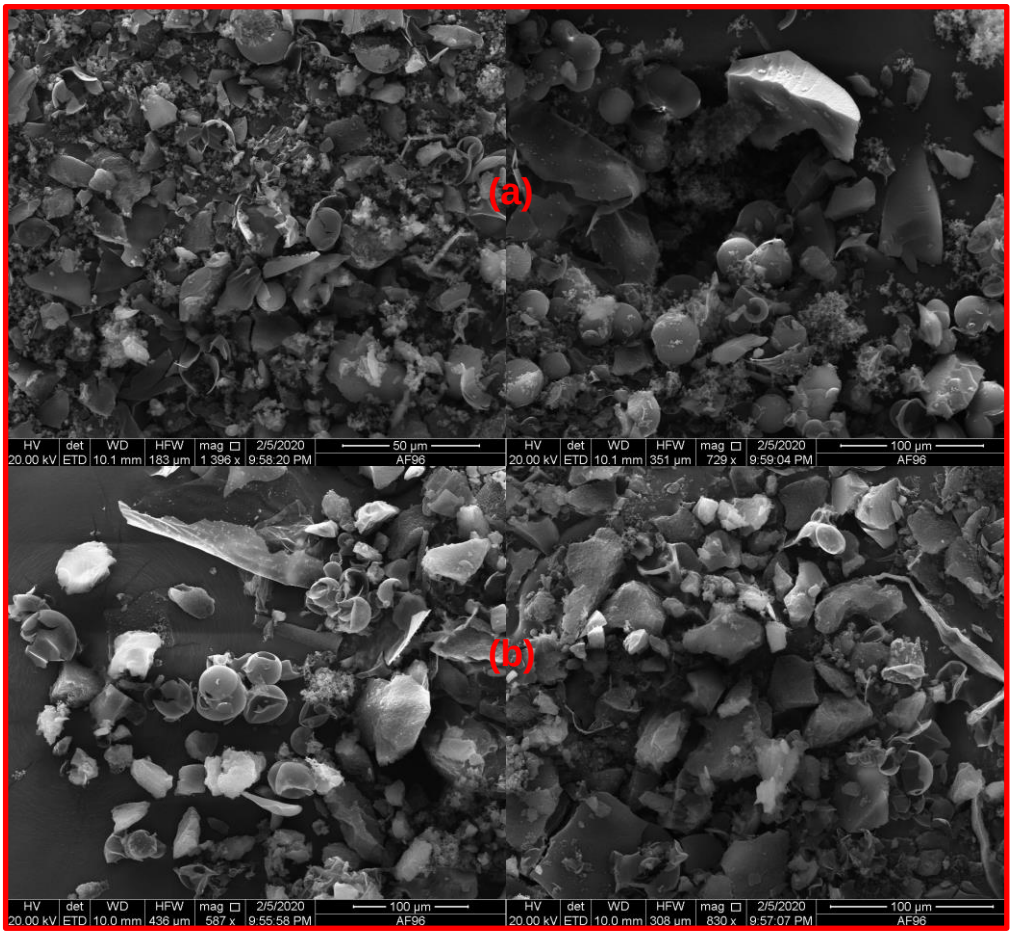

Figure 124. SEM micrographs of **(a) Methyl C-PPN-3** and **(b) Methyl B-PPN-3**

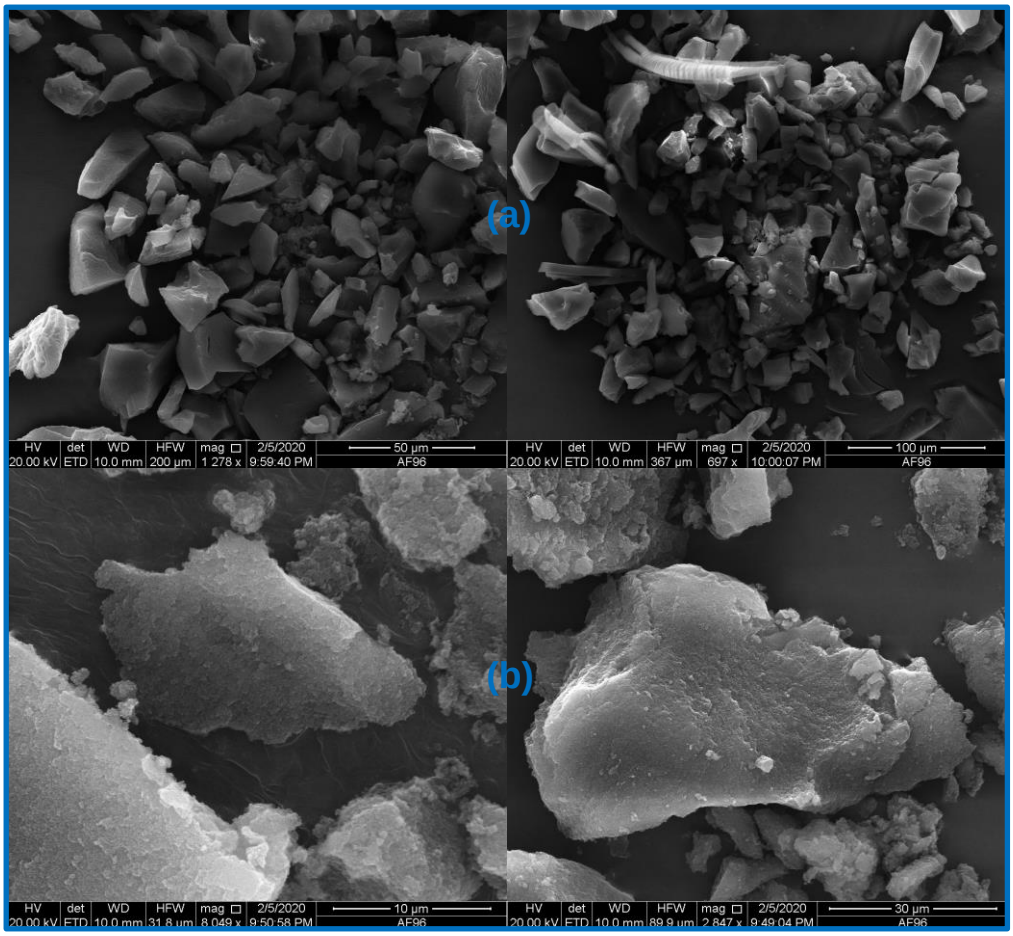

Figure 125. SEM micrographs of **(a) Propyl C-PPN-3** and **(b) Propyl B-PPN-3**

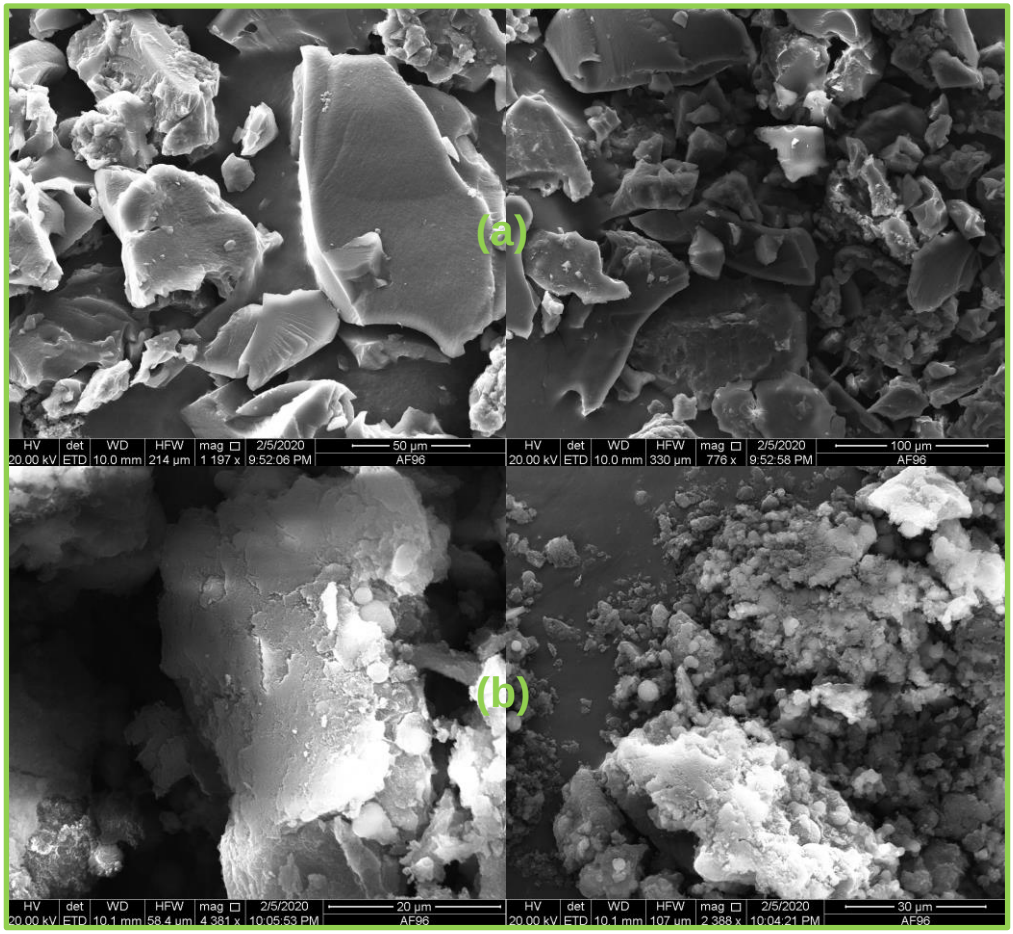

Figure 126. SEM micrographs of **(a) Heptyl C-PPN-3** and **(b) Heptyl B-PPN-3**

CHAPTER IV

POROUS POLYMER NETWORKS CONSTRUCTED FROM CALIXARENE-BASED ORGANIC CAGES

IV.i Introduction to organic cages and their polymer networks

After producing calixarene and cavitand-based porous polymers in an attempt towards increasing control over the local structure in the networks, organic cages can be logical next step in this series of monomers. Organic cages are molecules that have enclosed volumes, sometimes referred to "zero-dimensional" molecular pores.[77,226] While the enclosed volumes are not necessarily accessible to small molecules due to narrow pore windows, many examples of organic cages which can act as typical porous materials have been reported. These types of organic cages can be called "intrinsically" porous since they possess porosity derived from their structures as opposed to their molecular packing.[226]

Utilizing organic cages as monomers for PPN construction should allow another degree of control over the network porosity, due to the intrinsic pores of the starting materials. There have been few reported examples of organic cages utilized to construct PPNs[122] and COFs[227,228], with each showing enhanced CO_2 gas capacities and selectivity which were attributed to the intrinsic molecular pores of the starting materials.

A number of organic cages constructed from calixarenes have been reported but most of these compounds are inherently produced as mixtures with many side products, requiring complex separations.[159,160,169,161–168] Ideally, monomers selected for porous

polymer synthesis should be feasibly scalable; however, since this criterion cannot be met, a simple organic cage should be selected for a study of organic cage-based porous polymer networks **OC-PPNs**. Moreover, many of the reported organic cages do not have functionalities that would be directly amenable towards porous polymer synthesis.

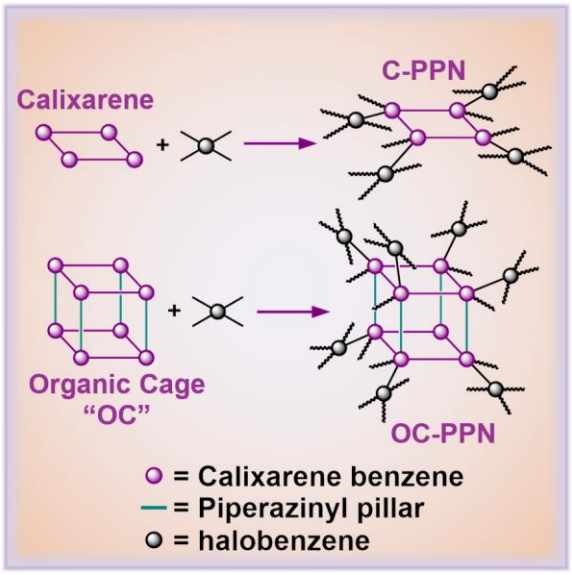

Figure 127. Depiction of polymer network constructed from organic cage, **OC-PPNs,** compared to **C-PPNs**

The smaller, simpler enclosed cages that can be produced from calixarenes are those constructed from only two macrocycles connected at the rims. Examining published examples, a series of cages can be produced by linking two resorcinarenes at the rims with piperazine pillars.[162] These cages also possess phenolic groups that could serve as nucleophilic branching sites for polymerization reactions. This series of piperazinyl-pillared cages can be produced in moderate yields (approx. 30%) but require large volumes of solvent for dilute reaction conditions and significant purification of the many oligomeric side products. Nevertheless, based on their advantageous properties,

structural simplicity and reactive functional groups, this class of cages was selected as the monomers for this study.

Porous polymers constructed from organic cages (**OC-PPNs**) could be compared to similar **C-PPNs** to examine the effect of the intrinsic molecular pores on the resulting porosities.

VI.ii Experimental

n-Propyl resorcinarene (PrRsC):

PrRsC was synthesized as described in CHAPTER II.

Piperazinyl-pillared *n*-propyl resorcinarene organic cage (PrRsC-OC):

The *n*-propyl resorcinarene organic cage, **PrRsC-OC,** were synthesized according to published procedures.[162] 1.2 L ethanol, 1.66 mL of 35% aqueous formaldehyde (14 eqv.), and 0.5 mL acetic acid were charged into a 3 L two-neck round bottom flask. 1.0 g **PrRsC (**1 eqv.) and 0.144 g **(**1.1 eqv.) piperazine were dissolved in 300 mL of ethanol and transferred to an addition funnel. The flask was equipped with a reflux condenser and placed in an 85 °C heating mantle, and the addition funnel was set to slowly drip in the contained solution. After 24 h, the reaction was cooled to room temperature. The solvent was removed by rotary evaporation and a reddish solid was obtained. The product was suspended in acetone and THF and sonicated. The suspension was poured over a plug of silica and diatomaceous earth and washed with acetone and THF to remove polymeric side products. The filtrate was subjected to rotary evaporation, and

the solid product was purified with a silica gel flash chromatography column (CH_2Cl_2:MeOH 95:5). The early eluting colored fractions were found to contain a mixture of the **PrRsC-OC** and the cage with one piperazinyl pillar missing. These fractions were combined and the obtained solids were recrystallized from methanol and subjected to another flash column (CH_2Cl_2:EtOH 90:10). A light pink powder was collected from the early eluting fractions **(figure 127)**. This product was suspended in acetonitrile and heated to 80 °C for several hours before the solvent was removed via rotatory evaporation to free trapped guest molecules within the **PrRsC-OC.** The product was obtained in about 30 - 40 % yields. Analysis by ^{1}H NMR and electrospray mass spectrometry (ESI-MS) indicated the product in good purity.

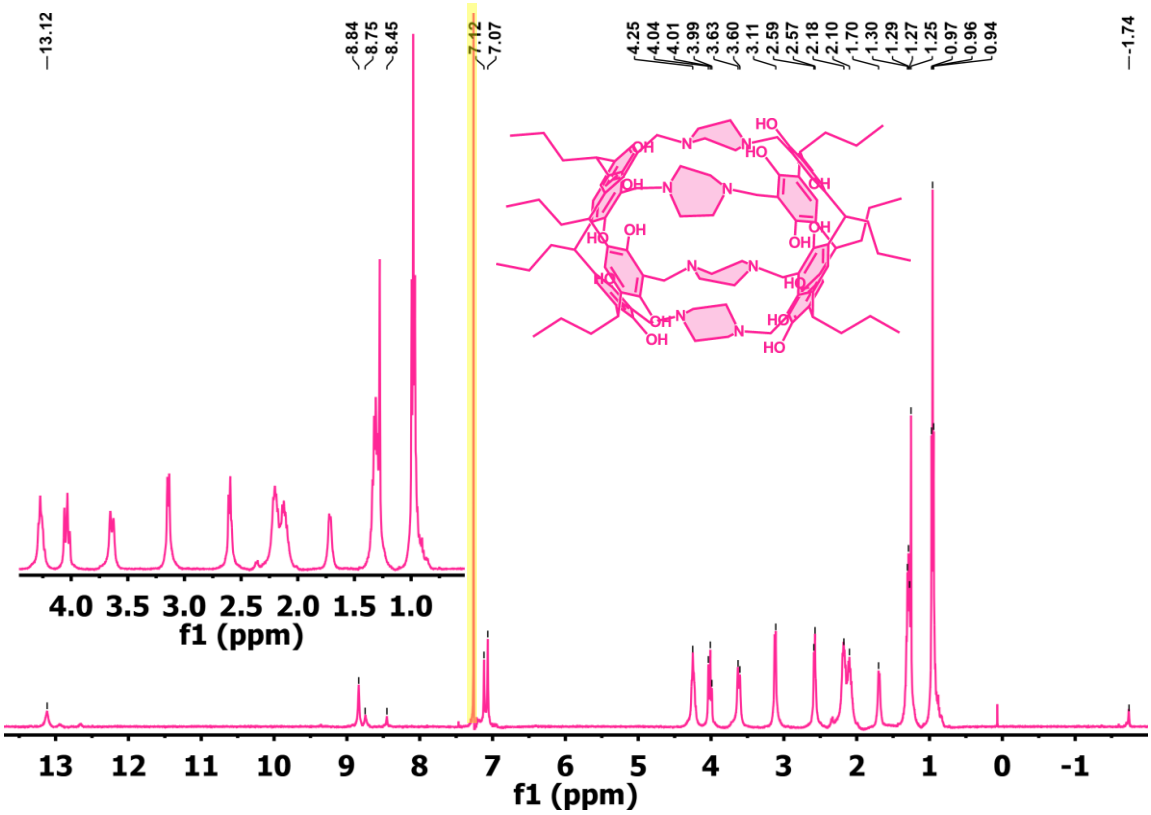

Figure 128. 500 MHz ^{1}H NMR spectra of **PrRsC-OC** in $CDCl_3$, yellow overlay indicates residual solvent

Figure 129. Optical photograph of **PrRsC-OC**

Cyanuric chloride - 4-OHPhRsC polyether:

Multiple reaction conditions for the synthesis of a cyanuric chloride-based polyether were attempted, including in a Teflon-lined steel autoclave at 150 and 220 °C, in scintillation vials with DBU and DIPEA at 0 to 80 °C. An example synthesis is as follows: (0.1 g, 12 mmol) **4-OHPhRsC** was transferred into a 7 mL Teflon-lined steel autoclave. (0.086 g, 0.47 mmol) cyanuric chloride and 2 mL of 1,4-dioxane were charged into the reactor. The reactor was sealed and thoroughly agitated. The reactor was placed in a 150 °C oven for 24 h. All solid products were broken into pieces < 1 mm^3 and washed with approximately 100 mL of each, water, methanol, and acetone in order. The products were dried for 3 h at 80 °C in an oven and activated at 120 °C for 12 h under high vacuum (<100 μBar) before further analysis.

Terephthaloyl chloride - 4-OHPhRsC polyester:

Multiple reaction conditions for the synthesis of a terephthaloyl chloride-based polyester were attempted, including in a Teflon-lined steel autoclave at 150 and 220 °C. An example synthesis is as follows: (0.1 g, 12 mmol) **4-OHPhRsC** was transferred into a 7

mL Teflon-lined steel autoclave. (0.142 g, 0.7 mmol) terephthaloyl chloride and 2 mL of 1,4-dioxane were charged into the reactor. The reactor was sealed and thoroughly agitated. The reactor was placed in a 150 °C oven for 24 h. All solid products were broken into pieces < 1 mm^3 and washed with approximately 100 mL of each, water, methanol, and acetone in order. The products were dried for 3 h at 80 °C in an oven and activated at 150 °C for 12 h under high vacuum (<100 μBar) before further analysis.

Hexachlorophosphazene - 4-OHPhRsC polyphosphazenes:

Multiple reaction conditions for the synthesis of a terephthaloyl chloride-based polyester were attempted, including in a Teflon-lined steel autoclave at 150 and 220 °C, in scintillation vials with various solvents and DIPEA, TEA, NaH, and pyridine bases at 0 to 100 °C. An example synthesis is as follows: (0.1 g, 12 mmol) **4-OHPhRsC** was transferred into a 7 mL Teflon-lined steel autoclave. (0.081 g, 0.23 mmol) hexachlorophosphazene and 2 mL of 1,4-dioxane were charged into the reactor. The reactor was sealed and thoroughly agitated. The reactor was placed in a 150 °C oven for 24 h. All solid products were broken into pieces < 1 mm^3 and washed with approximately 100 mL of each, water, methanol, and acetone in order. The products were dried for 3 h at 80 °C in an oven and activated at 120 °C for 12 h under high vacuum (<100 μBar) before further analysis.

Cyanuric chloride - PrRsC polyether:

An example synthesis is as follows: (0.1 g, 0.15 mmol) **PrRsC** was transferred into a 7 mL Teflon-lined steel autoclave. (0.076 g, 0.41 mmol) cyanuric chloride and 2 mL of 1,4-dioxane were charged into the reactor. The reactor was sealed and thoroughly agitated. The reactor was placed in a 150 °C oven for 24 h. No solid products were obtained.

Cyanuric chloride - PrRsC-OC polyether:

(0.08 g, 0.05 mmol) **PrRsC-OC** was transferred into a 20 mL scintillation vial. (0.034 g, 0.18 mmol) cyanuric chloride, 3 mL of 1,4-dioxane, and 0.08 mL DIPEA were charged into the vial at 0 °C. The reaction was stirred at 0 °C for 2 h, followed by RT for 2 h. The vial was placed in an 85 °C for 20 h. A gel-like product was obtained.

Procedure for TFTN - OC-PPN synthesis:

0.05 g (0.028 mmol, 1 eqv.) of **PrRsC-OC** and 0.023 g (0.114 mmol, 4 eqv.) tetrafluoroterephthalonitrile, **TFTN**, 0.118 g K_2CO_3 (0.856 mmol, 30 eqv.) were loaded into a heavy-walled glass pressure reactor with a screw-on Teflon stopper. 10 mL of 7:3 THF:DMAc was added and the reagents were stirred till dissolution. The pressure reactor was lowered into an oil bath and heated to 85 °C and for 12 h. After this period another aliquot of K_2CO_3 and **TFTN** were added, and the solution was heated to 160 °C for an additional 2 d. The reaction solution was cooled to room temperature and decanted into a beaker. Water and 3 M HCl were added slowly in sequence and the reaction mixture was stirred till bubbling ceased. The lightly-yellow colored solid

products were collected via filtration, and suspended in diethyl ether, centrifuged, and the solvent replaced three successive times. The solid products were found to be somewhat soluble in methanol, DMSO, and acetone, especially mixtures of these solvents. The solid products were dried for 3 h at 80 °C in an oven and activated at 120 °C for 12 h under high vacuum (<100 μBar) before further analysis.

IV.iii Results

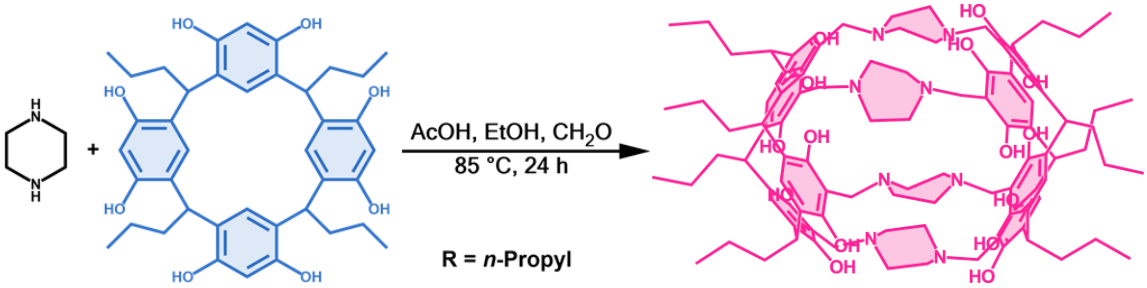

Figure 130. Synthesis of piperazinyl-pillared *n*-propyl resorcinarene organic cage, **PrRsC-OC**

Starting from the *n*-propyl resorcinarene, **PrRsC**, a previously reported Mannich/Betti-type reaction was employed with piperazine and formaldehyde to give a piperazinyl-pillared organic cage, **PrRsC-OC (figure 127)**.[139] After several chromatographic steps, the pure cage was isolated from side products as confirmed by ^{1}H NMR and ESI-MS **(figures 128 and 138)**.

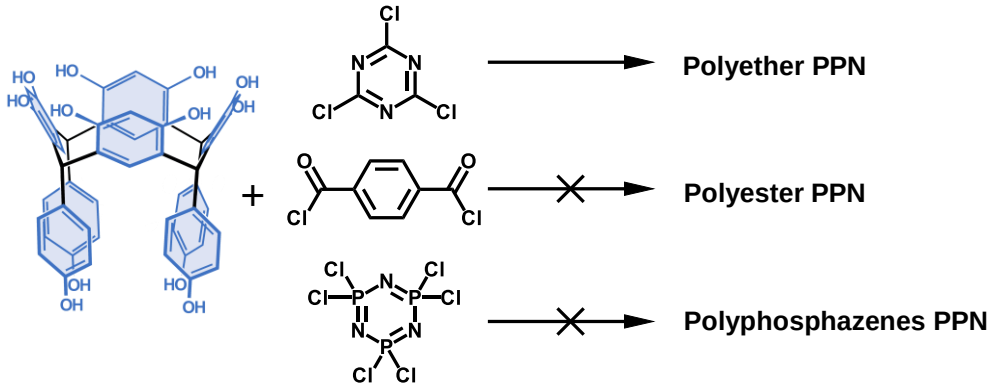

Figure 131. Attempted model syntheses of polyethers, polyesters, and polyphosphazenes C-PPNs

The most direct approaches to polymerization of the **PrRsC-OCs** is through their phenolic groups. These groups can serve as nucleophiles in a variety of linking reactions to produce polyethers, polyesters, polyphosphazenes, etc. These are common approaches to PPN syntheses and several reaction conditions were screened to determine which would be compatible with the **PrRsC-OCs.**

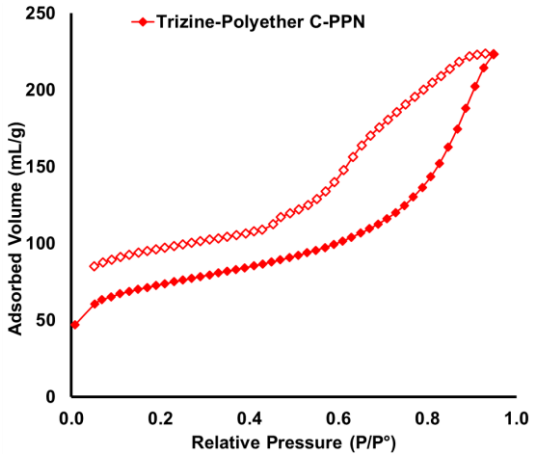

Figure 132. N_2 gas adsorption/desorption isotherms for triazine-linked polyester PPN constructed from cyanuric chloride and **4-OHPhRsC**

Starting with **4-OHPhRsC** as a model resorcinarene due to the previous success in PPN syntheses, cyanuric chloride[143,229], terephthaloyl chloride[230,231], and

hexachlorophosphazene[232,233] were selected as linkers to attempt to construct polyethers, polyesters, and polyphosphazenes PPNs, respectively **(figure 131)**. After several attempted syntheses with these linkers, only the cyanuric chloride produced a porous triazine-linked polyether PPN from **4-OHPhRsC** with a total porosity of about 223 mL/g **(figure 132)**. With this result, attempts were made to produce polyether PPNs from the **PrRsC** and **PrRsC-OCs** utilizing cyanuric chloride **(figure 133)**. Unfortunately, attempts produced soluble or nonporous gels.

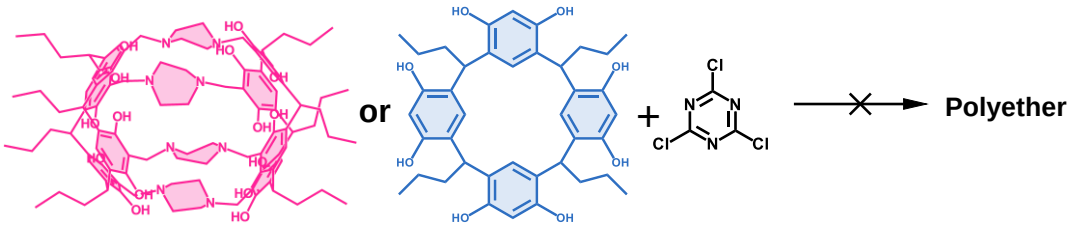

Figure 133. Attempted syntheses of triazine-linked polyethers PPNs from **PrRsC** and **PrRsC-OC**

Since these initial attempts to synthesize PPNs were unsuccessful, a reexamination of literature focusing on polymerizations of calixarenes was undertaken. Based on two recent reports that utilized aryl fluorides to link resorcinarenes, an attempt to construct an **OC-PPN** was made utilizing tetrafluoropthalonitrile, **TFTN**, as a linking reagent.[135,139] Utilizing conditions similar to those reported in literature **(figure 134)**, solid product (**OC-PPN**) was obtained.

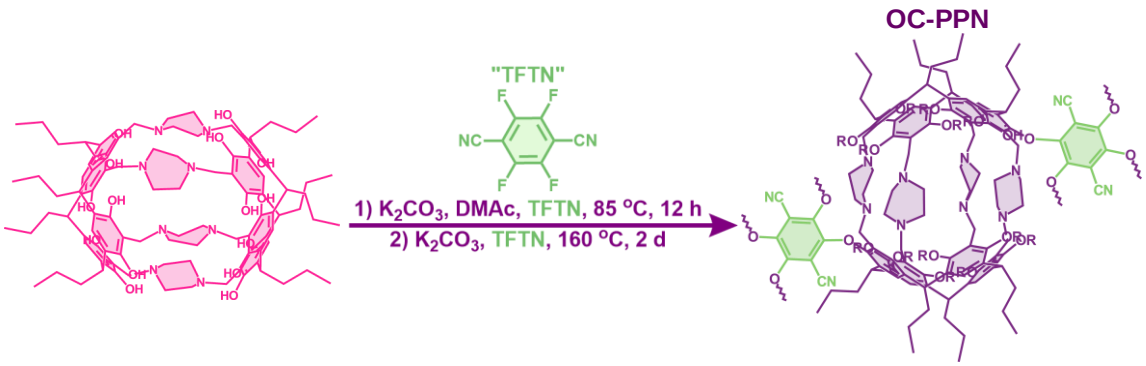

Figure 134. Synthesis of a polyether **OC-PPN** utilizing **TFTN**

To examine the chemical composition of the product, FTIR-ATR analysis of the **OC-PPN**, **TFTN**, and **PrRsC-OC** was performed **(figure 135)**. The **OC-PPN** showed the appearance of a peak at 2240 cm^{-1} indicates the appearance of a nitrile C≡N stretch from the **TFTN** linkages and the reduction of O-H stretch (3,000 - 3,700 cm^{-1}) due to formation of ether linkages; this can be confirmed by appearance of C-O ether stretch bands at 1,240 and 1045 cm^{-1}. These are good indications of the successful polymerization of the **PrRsC-OC**.

Examining the ^{13}C-CP-MAS-ssNMR spectra of the **PrRsC-OC** and **OC-PPN,** signals corresponding to the piperazinyl pillars are present at 51 ppm **(figure 136)**. In the **OC-PPN** spectrum, a nitrile signal from the **TFTN** linkers is present at 100 ppm **(figure 136)**. These are further indications of the successful polymerization.

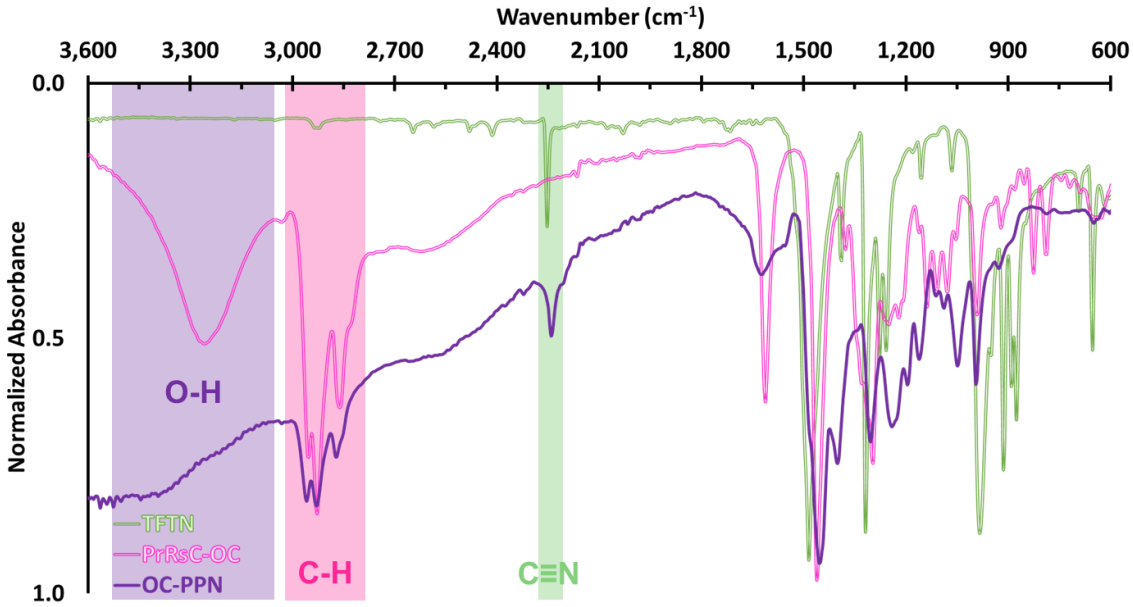

Figure 135. Comparison of normalized FTIR-ATR spectra of **TFTN**, **PrRsC-OC,** and **OC-PPN**

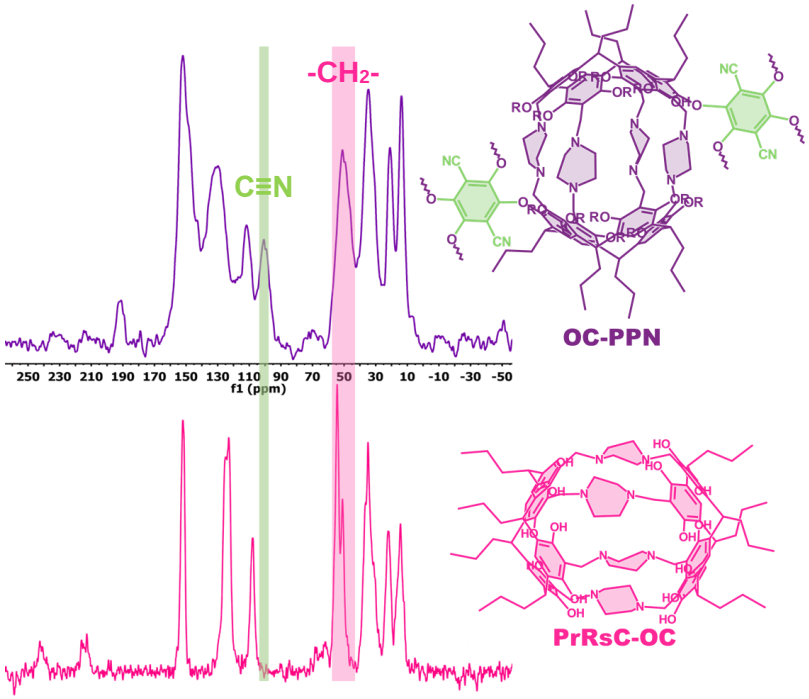

Figure 136. Comparison of offset ^{13}C-CP-MAS-ssNMR spectra of **PrRsC-OC** and **OC-PPN**

Finally, when an attempt to analyze the porosity of the produced **OC-PPN** was made via BET N_2 adsorption, no adsorption was determined.

The summation of these failed attempts to produce a porous polymer from the **PrRsC** and **PrRsC-OCs** through reaction with their nucleophilic phenol groups may indicate that this approach may not be feasible; this may be due to possible steric interactions or it may be that polymers produced through this method have too much gel-character to maintain their porosity after activation. Moreover, the pore windows of the small **PrRsC** organic cage may be too narrow to effectively allow gas adsorption.

IV.iv Further work

Due to the unsuccessful synthesis of porous polymers from the **PrRsC-OCs,** future attempts could utilize previously reported imine-linked cavitand-based organic cages through an alternative approach.[234] The imine linkages of these cages can be reduced to secondary amines which could be utilized to construct porous polymers through several approaches such as reaction with aldehyde linkers **(figure 137)**.[234]

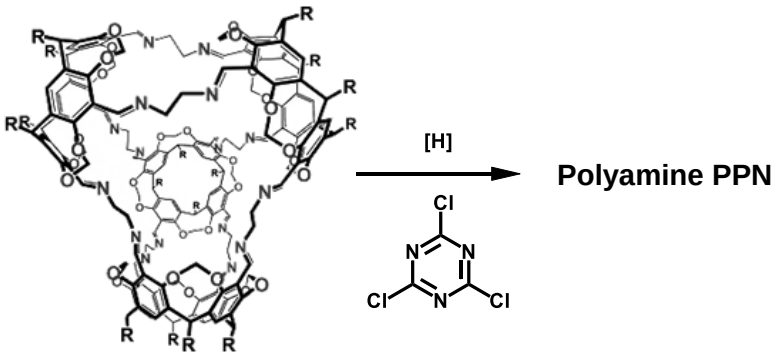

Figure 137. Distorted tetrahedron imine-linked cavitand organic cage[234] with a proposed polyamine synthesis*

*Reprinted with permission from "Solvent Effects in Thermodynamically Controlled Multicomponent Nanocage Syntheses" by Liu, X.; Warmuth, R., *J. Am. Chem. Soc.*, 2006**.** *128* (43), 14120–14127, Copyright 2006 by American Chemical Society.

IV.v Summary

Several unsuccessful attempts were made to produce **OC-PPNs** from calixarene-derived **PrRsC-OCs.** A synthetic approach previously reported for the synthesis of calixarene PPNs, utilizing aryl fluorides as liking reagents was attempted. The products were characterized with IR and ssNMR spectroscopy and indicated that the polymerization was successful and the structure of the **PrRsC-OC** was most likely maintained. Nevertheless, this polymer was also found to be nonporous.

It is hypothesized that either *n*-propyl groups of the calixarene, steric crowding of phenol groups, and/or narrow pore windows of the **PrRsC-OCs** are not amenable to PPN synthesis.

Future work that attempts to construct PPNs from calixarene-derived organic cages may be more successful if larger cavitand-based imine-linked organic cages are utilized as monomers.

IV.vi Supplemental information

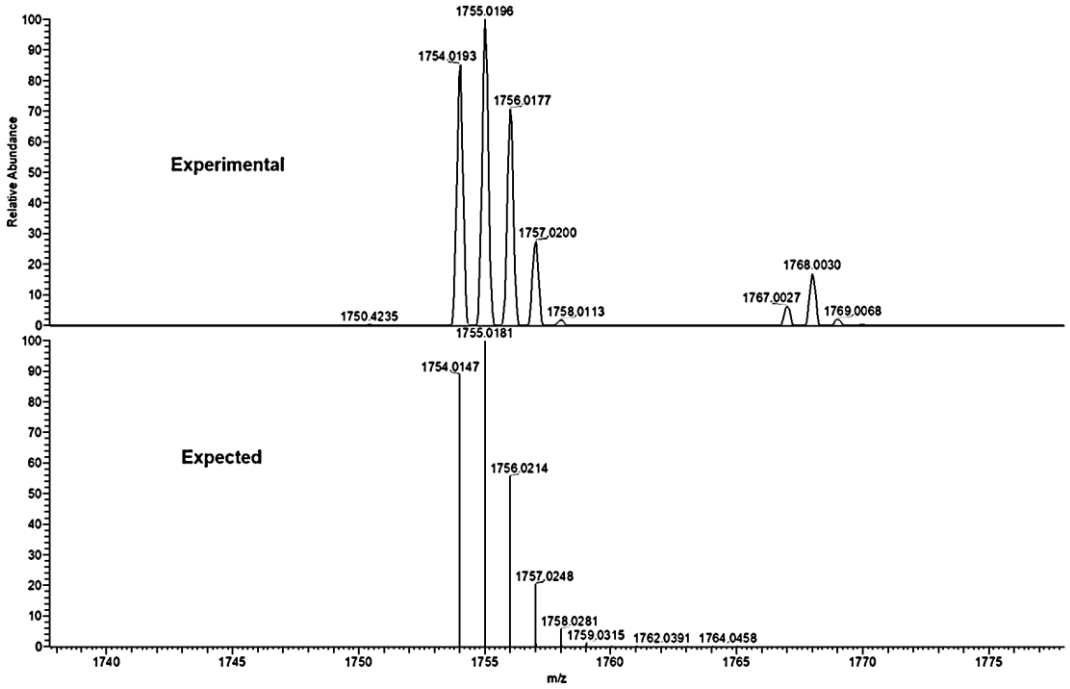

Figure 138. Expected and experimental ESI mass spectra of **PrRsC-OC**

CHAPTER V

CONCLUSIONS AND PROSPECTIVE

V.i Summary

Porosity is the property of materials that describes the amount of empty space or voids it contains and is an important property for separating and storing mater and many other applications. Porous materials have been utilized by humankind since antiquity, for such applications as treating poisoning via the ingestion charcoal. In modern times, a number of types of porous materials have been developed for many applications, one being porous polymers which have some advantages in stability, affordability, and scalability. Porous polymers have seen their greatest application as ion exchange resins in water purification but can be applied to many of the same applications as other porous materials.

Many specialized porous polymers have been constructed through the years, targeted towards specific applications. Research on porous polymers often focuses on controlling their porosity and functionality, which can be more challenging than in other porous materials.

One common approach to controlling the porosity in polymers to utilize large, three-dimensional monomers to modify the local network structures, and within this approach there have been many different specific monomers employed. One class of monomers that have successfully been applied in this approach are macrocyclic monomers. One particular series of very diverse macrocycles that have many properties that would be beneficial for this approach are the “cup-shaped” calixarenes and their

derivatives. Recently these macrocycles have seen increased interest for porous polymer synthesis due to their ability to bind many small molecules and their porous structures.[135–137,139,143,147]

In this study a series of calixarenes and derived cavitands and organic cage were utilized to construct polymers to explore the resulting porosity. Phenol-aldehyde calixarene-based PPNs were studied and compared to unstructured resins. A series of rigid cavitand-based PPNs were synthesized and compared to calixarene-based PPNs to examine the significance of flexibility on the resulting porosity. Additionally, calixarene-derived organic cages were utilized as monomers in an attempt to construct porous polymers with pre-defined pores.

V.ii Conclusions

In this study, it was found that pre-structured phenol-aldehyde porous polymers constructed from calixarenes are chemically similar typical Novalac resins but have greater microporosity and modified properties. Moreover, the pre-structured calixarene was utilized to construct several variant phenol-aldehyde polymers which had porosity modified by the linking aldehyde comonomers.

The porosity in a series of cavitand-based polymers was determined to decrease regularly with increasing chain length of the attached functional “feet” groups. This indicates that the flexible alkyl functional groups served only to occupy space within porous polymers. Further work could reveal how the “cup” size and shape modifies polymer porosity.

Attempts to construct porous polymers from small calixarene-based organic cages were unsuccessful. A number of disadvantageous structural factors may be the culprit to these failures. Future work to produce porous polymers from organic cages may have better success with larger organic cages with wider pore windows.

V.iii Prospective

A number of porous polymers derived from calixarenes have recently been reported.[135–137,139,143,147] Additionally, in this study several series of phenol-aldehyde calixarene-derived porous polymers were produced and examined. Calixarene-derived porous polymers have been found to have modified porosities and enhanced performance towards aqueous sequestration of small molecule pollutants and toxicants.

While the reported examples are promising initial explorations, the great diversity of calixarene derivatives and the modularity of their syntheses should allow for many porous polymers to be produced, targeting specific applications. These functionalized derivatives are as of yet unexplored and could be promising materials for future applications such as water remediation.

REFERENCES

(1) Rouquerol, J.; Avnir, D.; Fairbridge, C. W.; Everett, D. H.; Haynes, J. M.; Pernicone, N.; Ramsay, J. D. F.; Sing, K. S. W.; Unger, K. K. Recommendations for the Characterization of Porous Solids (Technical Report). *Pure Appl. Chem.* **1994**, *66* (8), 1739–1758.

(2) Klobes, P.; Meyer, K.; Munro, R. G.; (U.S.), N. I. of S. and T.; Peter Klobes, K. M. and R. G. M. *Porosity and Specific Surface Area Measurements for Solid Materials*; NIST recommended practice guide; U.S. Department of Commerce, Technology Administration, National Institute of Standards and Technology, 2006; Vol. 14.

(3) Lowell, S.; Shields, J. E.; Thomas, M. A.; Thommes, M. *Characterization of Porous Solids and Powders: Surface Area, Pore Size, and Density*; Springer Science & Business Media, 2005; Vol. 42.

(4) Thommes, M.; Kaneko, K.; Neimark, A. V.; Olivier, J. P.; Rodriguez-Reinoso, F.; Rouquerol, J.; Sing, K. S. W. Physisorption of Gases, with Special Reference to the Evaluation of Surface Area and Pore Size Distribution (IUPAC Technical Report). *Pure and Applied Chemistry*. 2015, pp 1051–1069.

(5) Bojdys, M. J.; Briggs, M. E.; Jones, J. T. A.; Adams, D. J.; Chong, S. Y.; Schmidtmann, M.; Cooper, A. I. Supramolecular Engineering of Intrinsic and Extrinsic Porosity in Covalent Organic Cages. *J. Am. Chem. Soc.* **2011**, *133* (41), 16566–16571.

(6) McKeown, N. B. Polymers of Intrinsic Microporosity. *ISRN Mater. Sci.* **2012**,

2012, 1–16.

(7) Cooper, A. I. Porous Molecular Solids and Liquids. *ACS Cent. Sci.* **2017**, *3* (6), 544–553.

(8) Keller, J. U.; Staudt, R. *Gas Adsorption Equilibria: Experimental Methods and Adsorptive Isotherms*; 2005.

(9) Fricke, E.; Stüwe, H. P.; Vibrans, G. Dissolution of Hydrogen from the Gas in Steel at Room Temperature. *Metall. Trans.* **1971**, *2* (9), 2697–2700.

(10) Lowell, S.; Shields, J. E.; Thomas, M. A.; Thommes, M. *Surface Area Analysis from the Langmuir and BET Theories*; 2004.

(11) Weiss, J. N. The Hill Equation Revisited: Uses and Misuses. *FASEB J.* **1997**, *11* (11), 835–841.

(12) Hill, A. V. The Combinations of Haemoglobin with Oxygen and with Carbon Monoxide. I. *Biochem. J.* **1913**, *7* (5), 471–480.

(13) Schneemann, A.; Bon, V.; Schwedler, I.; Senkovska, I.; Kaskel, S.; Fischer, R. A. Flexible Metal-Organic Frameworks. *Chem. Soc. Rev.* **2014**, *43* (16), 6062–6096.

(14) Zhang, J. P.; Zhou, H. L.; Zhou, D. D.; Liao, P. Q.; Chen, X. M. Controlling Flexibility of Metal-Organic Frameworks. *Natl. Sci. Rev.* **2018**, *5* (6), 907–919.

(15) Foo, M. L.; Matsuda, R.; Hijikata, Y.; Krishna, R.; Sato, H.; Horike, S.; Hori, A.; Duan, J.; Sato, Y.; Kubota, Y.; Takata, M.; Kitagawa, S. An Adsorbate Discriminatory Gate Effect in a Flexible Porous Coordination Polymer for Selective Adsorption of CO2 over C2H2. *J. Am. Chem. Soc.* **2016**, *138* (9), 3022–3030.

(16) Giri, N.; Del Pópolo, M. G.; Melaugh, G.; Greenaway, R. L.; Rätzke, K.; Koschine, T.; Pison, L.; Gomes, M. F. C.; Cooper, A. I.; James, S. L. Liquids with Permanent Porosity. *Nature* **2015**, *527* (7577), 216–220.

(17) Pierre, A. C.; Pajonk, G. M. Chemistry of Aerogels and Their Applications. *Chem. Rev.* **2002**, *102* (11), 4243–4265.

(18) Harris, P. J. F. Structure of Non-Graphitising Carbons. *Int. Mater. Rev.* **1997**, *42* (5), 206–218.

(19) Hong, S.; Rohman, M. R.; Jia, J.; Kim, Y.; Moon, D.; Kim, Y.; Ko, Y. H.; Lee, E.; Kim, K. Porphyrin Boxes: Rationally Designed Porous Organic Cages. *Angew. Chemie - Int. Ed.* **2015**, *54* (45), 13241–13244.

(20) Fayon, P.; Trewin, A. Formation Mechanism of Ultra Porous Framework Materials. *Phys. Chem. Chem. Phys.* **2016**, *18* (25), 16840–16847.

(21) Smith, B. J.; Hwang, N.; Chavez, A. D.; Novotney, J. L.; Dichtel, W. R. Growth Rates and Water Stability of 2D Boronate Ester Covalent Organic Frameworks. *Chem. Commun.* **2015**, *51* (35), 7532–7535.

(22) Rudd, N. D.; Wang, H.; Fuentes-Fernandez, E. M. A.; Teat, S. J.; Chen, F.; Hall, G.; Chabal, Y. J.; Li, J. Highly Efficient Luminescent Metal–Organic Framework for the Simultaneous Detection and Removal of Heavy Metals from Water. *ACS Appl. Mater. Interfaces* **2016**, *8* (44), 30294–30303.

(23) Lutz, W. Zeolite Y: Synthesis, Modification, and Properties—A Case Revisited. *Adv. Mater. Sci. Eng.* **2014**, *2014*, 724248.

(24) Ströck, M. Amorphous Carbon

https://upload.wikimedia.org/wikipedia/commons/9/90/Amorphous_Carbon.png (accessed Oct 10, 2020).

(25) Harris, P. J. F. Fullerene-Related Structure of Commercial Glassy Carbons. *Philos. Mag.* **2004**, *84* (29), 3159–3167.

(26) Marsh, H.; Rodríguez-Reinoso, F. *Activated Carbon*; Elsevier, 2006.

(27) Harris, P. On Charcoal. *Interdiscip. Sci. Rev.* **1999**, *24* (4), 301–306.

(28) Derlet, R. W.; Albertson, T. E. Activated Charcoal - Past, Present and Future. *West. J. Med.* **1986**, *145* (4), 493–496.

(29) Harris, P. J. F.; Tsang, S. C. High-Resolution Electron Microscopy Studies of Non- Graphitizing Carbons. *Philos. Mag. A Phys. Condens. Matter, Struct. Defects Mech. Prop.* **1997**, *76* (3), 667–677.

(30) Shen, W.; Zhang, S.; He, Y.; Li, J.; Fan, W. Hierarchical Porous Polyacrylonitrile-Based Activated Carbon Fibers for CO2 Capture. *J. Mater. Chem.* **2011**, *21* (36), 14036–14040.

(31) Mozammel, H. M.; Masahiro, O.; SC, B. Activated Charcoal from Coconut Shell Using ZnCl2 Activation. *Biomass and Bioenergy* **2002**, *22* (5), 397–400.

(32) Tsai, W. T.; Chang, C. Y.; Lee, S. L. A Low Cost Adsorbent from Agricultural Waste Corn Cob by Zinc Chloride Activation. *Bioresour. Technol.* **1998**, *64* (3), 211–217.

(33) Tseng, R. L.; Tseng, S. K.; Wu, F. C. Preparation of High Surface Area Carbons from Corncob with KOH Etching plus CO2 Gasification for the Adsorption of Dyes and Phenols from Water. *Colloids Surfaces A Physicochem. Eng. Asp.* **2006**,

279 (1–3), 69–78.

(34) Tang, S.; Chen, Y.; Xie, R.; Jiang, W.; Jiang, Y. Preparation of Activated Carbon from Corn Cob and Its Adsorption Behavior on Cr(VI) Removal. *Water Sci. Technol.* **2016**, *73* (11), 2654–2661.

(35) Khodaie, M.; Ghasemi, N.; Moradi, B.; Rahimi, M. Removal of Methylene Blue from Wastewater by Adsorption onto Znclactivated Corn Husk Carbon Equilibrium Studies. *J. Chem.* **2013**, *2013*, 383985.

(36) Yang, C.-S.; Jang, Y. S.; Jeong, H. K. Bamboo-Based Activated Carbon for Supercapacitor Applications. *Curr. Appl. Phys.* **2014**, *14* (12), 1616–1620.

(37) Ikemoto, Y.; Nakano, T.; Kuno, M.; Nozue, Y. Magnetic and Optical Properties of K and Na Clusters Arrayed in a Diamond Structure in Zeolite FAU. *Phys. B Condens. Matter* **2000**, *281–282*, 691–693.

(38) Czárán, E. Introduction to Zeolite Science and Practice. *Reaction Kinetics & Catalysis Letters*. Elsevier 1991, pp 161–163.

(39) Silverstein, M. S.; Cameron, N. R.; Hillmyer, M. *Porous Polymers*; 2011.

(40) Ben, T.; Pei, C.; Zhang, D.; Xu, J.; Deng, F.; Jing, X.; Qiu, S. Gas Storage in Porous Aromatic Frameworks (PAFs). *Energy Environ. Sci.* **2011**, *4* (10), 3991–3999.

(41) Qiu, S.; Teng, B. *Porous Polymers : Design, Synthesis and Applications. Shilun Qiu, Teng Ben*; Cambridge, UK : Royal Society of Chemistry, [2016], 2016.

(42) Xu, Y.; Jin, S.; Xu, H.; Nagai, A.; Jiang, D. Conjugated Microporous Polymers: Design, Synthesis and Application. *Chem. Soc. Rev.* **2013**, *42* (20), 8012–8031.

(43) Wu, J.; Xu, F.; Li, S.; Ma, P.; Zhang, X.; Liu, Q.; Fu, R.; Wu, D. Porous Polymers as Multifunctional Material Platforms toward Task-Specific Applications. *Adv. Mater.* **2019**, *31* (4), 1–45.

(44) Myers, R. J.; Eastes, J. W.; Myers, F. J. Synthetic Resins as Exchange Adsorbents. *Ind. Eng. Chem.* **1941**, *33* (6), 697–706.

(45) Ilnicka, A.; Kamedulski, P.; Skorupska, M.; Lukaszewicz, J. P. Metal-Free Nitrogen-Rich Carbon Foam Derived from Amino Acids for the Oxygen Reduction Reaction. *J. Mater. Sci.* **2019**, *54* (24), 14859–14871.

(46) Katsoulidis, A. P.; Kanatzidis, M. G. Phloroglucinol Based Microporous Polymeric Organic Frameworks With-OH Functional Groups and High CO2 Capture Capacity. *Chem. Mater.* **2011**, *23* (7), 1818–1824.

(47) Yuan, S.; Feng, L.; Wang, K.; Pang, J.; Bosch, M.; Lollar, C.; Sun, Y.; Qin, J.; Yang, X.; Zhang, P.; Wang, Q.; Zou, L.; Zhang, Y.; Zhang, L.; Fang, Y.; Li, J.; Zhou, H.-C. Stable Metal–Organic Frameworks: Design, Synthesis, and Applications. *Adv. Mater.* **2018**, *30* (37), 1704303.

(48) Yuan, S.; Sun, X.; Pang, J.; Lollar, C.; Qin, J. S.; Perry, Z.; Joseph, E.; Wang, X.; Fang, Y.; Bosch, M.; Sun, D.; Liu, D.; Zhou, H. C. PCN-250 under Pressure: Sequential Phase Transformation and the Implications for MOF Densification. *Joule* **2017**, *1* (4), 806–815.

(49) Ertas, I. E.; Gulcan, M.; Bulut, A.; Yurderi, M.; Zahmakiran, M. Metal-Organic Framework (MIL-101) Stabilized Ruthenium Nanoparticles: Highly Efficient Catalytic Material in the Phenol Hydrogenation. *Microporous Mesoporous Mater.*

2016, *226*, 94–103.

(50) Wang, Q.; Astruc, D. State of the Art and Prospects in Metal-Organic Framework (MOF)-Based and MOF-Derived Nanocatalysis. *Chem. Rev.* **2020**, *120* (2), 1438–1511.

(51) Furukawa, H.; Cordova, K. E.; O'Keeffe, M.; Yaghi, O. M. The Chemistry and Applications of Metal-Organic Frameworks. *Science* **2013**, *341* (6149), 1230444.

(52) Li, H.; Eddaoudi, M.; O'Keeffe, M.; Yaghi, O. M. Design and Synthesis of an Exceptionally Stable and Highly Porous Metal-Organic Framework. *Nature* **1999**, *402* (6759), 276–279.

(53) Bai, Y.; Dou, Y.; Xie, L.-H.; Rutledge, W.; Li, J.-R.; Zhou, H.-C. Zr-Based Metal–Organic Frameworks: Design, Synthesis, Structure, and Applications. *Chem. Soc. Rev.* **2016**, *45* (8), 2327–2367.

(54) Yuan, S.; Qin, J.-S.; Lollar, C. T.; Zhou, H.-C. Stable Metal-Organic Frameworks with Group 4 Metals: Current Status and Trends. *ACS Cent. Sci.* **2018**, *4* (4), 440–450.

(55) Wang, K.; Lv, X.-L.; Feng, D.; Li, J.; Chen, S.; Sun, J.; Song, L.; Xie, Y.; Li, J.-R.; Zhou, H.-C. Pyrazolate-Based Porphyrinic Metal–Organic Framework with Extraordinary Base-Resistance. *J. Am. Chem. Soc.* **2016**, *138* (3), 914–919.

(56) Colombo, V.; Galli, S.; Choi, H. J.; Han, G. D.; Maspero, A.; Palmisano, G.; Masciocchi, N.; Long, J. R. High Thermal and Chemical Stability in Pyrazolate-Bridged Metal–Organic Frameworks with Exposed Metal Sites. *Chem. Sci.* **2011**, *2* (7), 1311–1319.

(57) Winarta, J.; Shan, B.; Mcintyre, S. M.; Ye, L.; Wang, C.; Liu, J.; Mu, B. A Decade of UiO-66 Research: A Historic Review of Dynamic Structure, Synthesis Mechanisms, and Characterization Techniques of an Archetypal Metal–Organic Framework. *Cryst. Growth Des.* **2020**, *20* (2), 1347–1362.

(58) Cavka, J. H.; Jakobsen, S.; Olsbye, U.; Guillou, N.; Lamberti, C.; Bordiga, S.; Lillerud, K. P. A New Zirconium Inorganic Building Brick Forming Metal Organic Frameworks with Exceptional Stability. *J. Am. Chem. Soc.* **2008**, *130* (42), 13850–13851.

(59) Férey, G.; Mellot-Draznieks, C.; Serre, C.; Millange, F.; Dutour, J.; Surblé, S.; Margiolaki, I. A Chromium Terephthalate-Based Solid with Unusually Large Pore Volumes and Surface Area. *Science* **2005**, *309* (5743), 2040 LP – 2042.

(60) Kandambeth, S.; Dey, K.; Banerjee, R. Covalent Organic Frameworks: Chemistry beyond the Structure. *J. Am. Chem. Soc.* **2019**, *141* (5), 1807–1822.

(61) Lyle, S. J.; Waller, P. J.; Yaghi, O. M. Covalent Organic Frameworks: Organic Chemistry Extended into Two and Three Dimensions. *Trends Chem.* **2019**, *1* (2), 172–184.

(62) Lohse, M. S.; Bein, T. Covalent Organic Frameworks: Structures, Synthesis, and Applications. *Adv. Funct. Mater.* **2018**, *28* (33).

(63) Ding, S. Y.; Wang, W. Covalent Organic Frameworks (COFs): From Design to Applications. *Chem. Soc. Rev.* **2013**, *42* (2), 548–568.

(64) Côté, A. P.; Benin, A. I.; Ockwig, N. W.; O'Keeffe, M.; Matzger, A. J.; Yaghi, O. M. Porous, Crystalline, Covalent Organic Frameworks. *Science* **2005**, *310* (5751),

1166–1170.

(65) Uribe-Romo, F. J.; Hunt, J. R.; Furukawa, H.; Klöck, C.; O'Keeffe, M.; Yaghi, O. M. A Crystalline Imine-Linked 3-D Porous Covalent Organic Framework. *J. Am. Chem. Soc.* **2009**, *131* (13), 4570–4571.

(66) Vitaku, E.; Dichtel, W. R. Synthesis of 2D Imine-Linked Covalent Organic Frameworks through Formal Transimination Reactions. *J. Am. Chem. Soc.* **2017**, *139* (37), 12911–12914.

(67) Li, R. L.; Flanders, N. C.; Evans, A. M.; Ji, W.; Castano, I.; Chen, L. X.; Gianneschi, N. C.; Dichtel, W. R. Controlled Growth of Imine-Linked Two-Dimensional Covalent Organic Framework Nanoparticles. *Chem. Sci.* **2019**, *10* (13), 3796–3801.

(68) Kundu, T.; Wang, J.; Cheng, Y.; Du, Y.; Qian, Y.; Liu, G.; Zhao, D. Hydrazone-Based Covalent Organic Frameworks for Lewis Acid Catalysis. *Dalt. Trans.* **2018**, *47* (39), 13824–13829.

(69) Uribe-Romo, F. J.; Doonan, C. J.; Furukawa, H.; Oisaki, K.; Yaghi, O. M. Crystalline Covalent Organic Frameworks with Hydrazone Linkages. *J. Am. Chem. Soc.* **2011**, *133* (30), 11478–11481.

(70) Jiang, S. Y.; Gan, S. X.; Zhang, X.; Li, H.; Qi, Q. Y.; Cui, F. Z.; Lu, J.; Zhao, X. Aminal-Linked Covalent Organic Frameworks through Condensation of Secondary Amine with Aldehyde. *J. Am. Chem. Soc.* **2019**, *141* (38), 14981–14986.

(71) Yang, Y.; Niu, H.; Xu, L.; Zhang, H.; Cai, Y. Triazine Functionalized Fully

Conjugated Covalent Organic Framework for Efficient Photocatalysis. *Appl. Catal. B Environ.* **2020**, *269*, 118799.

(72) Kuhn, P.; Antonietti, M.; Thomas, A. Porous, Covalent Triazine-Based Frameworks Prepared by Ionothermal Synthesis. *Angew. Chemie - Int. Ed.* **2008**, *47* (18), 3450–3453.

(73) Lyu, H.; Diercks, C. S.; Zhu, C.; Yaghi, O. M. Porous Crystalline Olefin-Linked Covalent Organic Frameworks. *J. Am. Chem. Soc.* **2019**, *141* (17), 6848–6852.

(74) Ma, T.; Kapustin, E. A.; Yin, S. X.; Liang, L.; Zhou, Z.; Niu, J.; Li, L. H.; Wang, Y.; Su, J.; Li, J.; Wang, X.; Wang, W. D.; Wang, W.; Sun, J.; Yaghi, O. M. Single-Crystal x-Ray Diffraction Structures of Covalent Organic Frameworks. *Science* **2018**, *361* (6397), 48–52.

(75) Evans, A. M.; Parent, L. R.; Flanders, N. C.; Bisbey, R. P.; Vitaku, E.; Kirschner, M. S.; Schaller, R. D.; Chen, L. X.; Gianneschi, N. C.; Dichtel, W. R. Seeded Growth of Single-Crystal Two-Dimensional Covalent Organic Frameworks. *Science* **2018**, *361* (6397), 52–57.

(76) Niu, J.; Li, L.; Wang, Y.; Su, J.; Li, J.; Wang, X. Organic Frameworks. *Science* **2018**, *52* (July), 48–52.

(77) Tozawa, T.; Jones, J. T. A.; Swamy, S. I.; Jiang, S.; Adams, D. J.; Shakespeare, S.; Clowes, R.; Bradshaw, D.; Hasell, T.; Chong, S. Y.; Tang, C.; Thompson, S.; Parker, J.; Trewin, A.; Bacsa, J.; Slawin, A. M. Z.; Steiner, A.; Cooper, A. I. Porous Organic Cages. *Nat. Mater.* **2009**, *8* (12), 973–978.

(78) McKeown, N. B. Nanoporous Molecular Crystals. *J. Mater. Chem.* **2010**, *20* (47),

10588–10597.

(79) Jones, J. T. A.; Hasell, T.; Wu, X.; Bacsa, J.; Jelfs, K. E.; Schmidtmann, M.; Chong, S. Y.; Adams, D. J.; Trewin, A.; Schiffman, F.; Cora, F.; Slater, B.; Steiner, A.; Day, G. M.; Cooper, A. I. Modular and Predictable Assembly of Porous Organic Molecular Crystals. *Nature* **2011**, *474* (7351), 367–371.

(80) Teng, B.; Little, M. A.; Hasell, T.; Chong, S. Y.; Jelfs, K. E.; Clowes, R.; Briggs, M. E.; Cooper, A. I. Synthesis of a Large, Shape-Flexible, Solvatomorphic Porous Organic Cage. *Cryst. Growth Des.* **2019**, *19* (7), 3647–3651.

(81) Budd, P. M.; Ghanem, B. S.; Makhseed, S.; McKeown, N. B.; Msayib, K. J.; Tattershall, C. E. Polymers of Intrinsic Microporosity (PIMs): Robust, Solution-Processable, Organic Nanoporous Materials. *Chem. Commun.* **2004**, *4* (2), 230–231.

(82) McKeown, N. B.; Budd, P. M. Exploitation of Intrinsic Microporosity in Polymer-Based Materials. *Macromolecules* **2010**, *43* (12), 5163–5176.

(83) Mc Keown, N. B.; Budd, P. M. Polymers of Intrinsic Microporosity (PIMs): Organic Materials for Membrane Separations, Heterogeneous Catalysis and Hydrogen Storage. *Chem. Soc. Rev.* **2006**, *35* (8), 675–683.

(84) Budd, P. M.; McKeown, N. B.; Fritsch, D. Polymers of Intrinsic Microporosity (PIMs): High Free Volume Polymers for Membrane Applications. *Macromol. Symp.* **2006**, *245–246*, 403–405.

(85) Cahir, J.; Tsang, M. Y.; Lai, B.; Hughes, D.; Alam, M. A.; Jacquemin, J.; Rooney, D.; James, S. L. Type 3 Porous Liquids Based on Non-Ionic Liquid Phases-a

Broad and Tailorable Platform of Selective, Fluid Gas Sorbents. *Chem. Sci.* **2020**, *11* (8), 2077–2084.

(86) Fu, H. X.; Zhang, Z. H.; Fan, W.; Wang, S.; Liu, Y.; Huang, M. H. A Soluble Porous Organic Polymer for Highly Efficient Organic-Aqueous Biphasic Catalysis and Convenient Reuse of Catalysts. *J. Mater. Chem. A* **2019**, *7* (25), 15048–15053.

(87) Castaldo, R.; Avolio, R.; Cocca, M.; Gentile, G.; Errico, M. E.; Avella, M.; Carfagna, C.; Ambrogi, V. Synthesis and Adsorption Study of Hyper-Crosslinked Styrene-Based Nanocomposites Containing Multi-Walled Carbon Nanotubes. *RSC Adv.* **2017**, *7* (12), 6865–6874.

(88) Tan, L.; Tan, B. Hypercrosslinked Porous Polymer Materials: Design, Synthesis, and Applications. *Chem. Soc. Rev.* **2017**, *46* (11), 3322–3356.

(89) Tsyurupa, M. P.; Davankov, V. A. Porous Structure of Hypercrosslinked Polystyrene: State-of-the-Art Mini-Review. *React. Funct. Polym.* **2006**, *66* (7), 768–779.

(90) Wu, D.; Xu, F.; Sun, B.; Fu, R.; He, H.; Matyjaszewski, K. Design and Preparation of Porous Polymers. *Chem. Rev.* **2012**, *112* (7), 3959–4015.

(91) Deryło-Marczewska, A.; Goworek, J.; Kusak, R.; Zgrajka, W. Sorption Properties of Porous Melamine-Formaldehyde Resins. *Appl. Surf. Sci.* **2002**, *195* (1–4), 117–125.

(92) Zhang, X.; Yan, W.; Yang, H.; Liu, B.; Li, H. Gaseous Infiltration Method for Preparation of Three-Dimensionally Ordered Macroporous Polyethylene. *Polymer*

(Guildf). **2008**, *49* (25), 5446–5451.

(93) Lu, W.; Yuan, D.; Sculley, J.; Zhao, D.; Krishna, R.; Zhou, H. C. Sulfonate-Grafted Porous Polymer Networks for Preferential CO2 Adsorption at Low Pressure. *J. Am. Chem. Soc.* **2011**, *133* (45), 18126–18129.

(94) Yuan, D.; Lu, W.; Zhao, D.; Zhou, H. C. Highly Stable Porous Polymer Networks with Exceptionally High Gas-Uptake Capacities. *Adv. Mater.* **2011**, *23* (32), 3723–3725.

(95) Lu, W.; Sculley, J. P.; Yuan, D.; Krishna, R.; Wei, Z.; Zhou, H.-C. Polyamine-Tethered Porous Polymer Networks for Carbon Dioxide Capture from Flue Gas. *Angew. Chemie* **2012**, *124* (30), 7598–7602.

(96) Yuan, Y.; Zhu, G. Porous Aromatic Frameworks as a Platform for Multifunctional Applications. *ACS Cent. Sci.* **2019**, *5* (3), 409–418.

(97) Tian, Y.; Zhu, G. Porous Aromatic Frameworks (PAFs). *Chem. Rev.* **2020**, *120* (16), 8934–8986.

(98) Ben, T.; Ren, H.; Ma, S.; Cao, D.; Lan, J.; Jing, X.; Wang, W.; Xu, J.; Deng, F.; Simmons, J. M.; Qiu, S.; Zhu, G. Targeted Synthesis of a Porous Aromatic Framework with High Stability and Exceptionally High Surface Area. *Angew. Chemie* **2009**, *121* (50), 9621–9624.

(99) Sun, Q.; Dai, Z.; Meng, X.; Xiao, F. S. Porous Polymer Catalysts with Hierarchical Structures. *Chem. Soc. Rev.* **2015**, *44* (17), 6018–6034.

(100) Day, G. S.; Drake, H. F.; Joseph, E. A.; Bosch, M.; Tan, K.; Willman, J. A.; Carretier, V.; Perry, Z.; Burtner, W.; Banerjee, S.; Ozdemir, O. K.; Zhou, H. C.

Improving Alkylamine Incorporation in Porous Polymer Networks through Dopant Incorporation. *Adv. Sustain. Syst.* **2019**, *3* (12), 1900051.

(101) Che, S.; Pang, J.; Kalin, A. J.; Wang, C.; Ji, X.; Lee, J.; Cole, D.; Li, J.-L.; Tu, X.; Zhang, Q.; Zhou, H.-C.; Fang, L. Rigid Ladder-Type Porous Polymer Networks for Entropically Favorable Gas Adsorption. *ACS Mater. Lett.* **2020**, *2* (1), 49–54.

(102) Lu, W.; Wei, Z.; Yuan, D.; Tian, J.; Fordham, S.; Zhou, H. C. Rational Design and Synthesis of Porous Polymer Networks: Toward High Surface Area. *Chem. Mater.* **2014**, *26* (15), 4589–4597.

(103) Lu, W.; Yuan, D.; Zhao, D.; Schilling, C. I.; Plietzsch, O.; Muller, T.; Bräse, S.; Guenther, J.; Blümel, J.; Krishna, R.; Li, Z.; Zhou, H. C. Porous Polymer Networks: Synthesis, Porosity, and Applications in Gas Storage/Separation. *Chem. Mater.* **2010**, *22* (21), 5964–5972.

(104) Yang, X.; Zou, L.; Zhou, H. C. Anchor Installation on Porous Polymer Networks (PPNs) for High CO2 Uptake. *Polymer (Guildf).* **2017**, *126*, 303–307.

(105) Xiang, Z.; Cao, D.; Dai, L. Well-Defined Two Dimensional Covalent Organic Polymers: Rational Design, Controlled Syntheses, and Potential Applications. *Polym. Chem.* **2015**, *6* (11), 1896–1911.

(106) Li, H.; Meng, B.; Chai, S. H.; Liu, H.; Dai, S. Hyper-Crosslinked β-Cyclodextrin Porous Polymer: An Adsorption-Facilitated Molecular Catalyst Support for Transformation of Water-Soluble Aromatic Molecules. *Chem. Sci.* **2016**, *7* (2), 905–909.

(107) McKeown, N. B.; Budd, P. M.; Msayib, K. J.; Ghanem, B. S.; Kingston, H. J.;

Tattershall, C. E.; Makhseed, S.; Reynolds, K. J.; Fritsch, D. Polymers of Intrinsic Microporosity (PIMs): Bridging the Void between Microporous and Polymeric Materials. *Chem. - A Eur. J.* **2005**, *11* (9), 2610–2620.

(108) Yebeutchou, R. M.; Dalcanale, E. Highly Selective Monomethylation of Primary Amines through Host-Guest Product Sequestration. *J. Am. Chem. Soc.* **2009**, *131* (7), 2452–2453.

(109) Topkaya, D.; Dumoulin, F.; Ahsen, V.; Işci, Ü. Axial Binding and Host-Guest Interactions of a Phthalocyanine Resorcinarene Cavitand Hybrid. *Dalt. Trans.* **2014**, *43* (5), 2032–2037.

(110) Chitry, F.; Pellet-Rostaing, S.; Nicod, L.; Gass, J. L.; Foos, J.; Guy, A.; Lemaire, M. New Cesium-Selective Hydrophilic Ligands: UV Measures of Their Interactions toward Cs and Cs/Na Separation by Nanofiltration Complexation. *J. Phys. Chem. A* **2000**, *104* (17), 4121–4128.

(111) Dionisio, M.; Maffei, F.; Rampazzo, E.; Prodi, L.; Pucci, A.; Ruggeri, G.; Dalcanale, E. Guest-Controlled Aggregation of Cavitand Gold Nanoparticles and N-Methyl Pyridinium-Terminated PEG. *Chem. Commun.* **2011**, *47* (23), 6596–6598.

(112) Cram, D. J.; Karbach, S.; Kim, H. E.; Knobler, C. B.; Maverick, E. F.; Ericson, J. L.; Helgeson, R. C. Host-Guest Complexation. 46. Cavitands as Open Molecular Vessels Form Solvates. *J. Am. Chem. Soc.* **1988**, *110* (7), 2229–2237.

(113) Tunstad, L. M.; Sherman, J. C.; Helgeson, R. C.; Weiser, J.; Knobler, C. B.; Cram, D. J.; Bryant, J. A.; Dalcanale, E.; Tucker, J. A. Host-Guest Complexation.

48. Octol Building Blocks for Cavitands and Carcerands. *J. Org. Chem.* **1989**, *54* (6), 1305–1312.

(114) Kane, C. M.; Banisafar, A.; Dougherty, T. P.; Barbour, L. J.; Holman, K. T. Enclathration and Confinement of Small Gases by the Intrinsically 0D Porous Molecular Solid, Me,H,SiMe2. *J. Am. Chem. Soc.* **2016**, *138* (13), 4377–4392.

(115) Alsbaiee, A.; Smith, B. J.; Xiao, L.; Ling, Y.; Helbling, D. E.; Dichtel, W. R. Rapid Removal of Organic Micropollutants from Water by a Porous β-Cyclodextrin Polymer. *Nature* **2016**, *529* (7585), 190–194.

(116) Ji, X.; Wang, H.; Wang, H.; Zhao, T.; Page, Z. A.; Khashab, N. M.; Sessler, J. L. Removal of Organic Micropollutants from Water by Macrocycle-Containing Covalent Polymer Networks. *Angew. Chemie - Int. Ed.* **2020**, *n/a* (n/a).

(117) Klemes, M. J.; Ling, Y.; Chiapasco, M.; Alsbaiee, A.; Helbling, D. E.; Dichtel, W. R. Phenolation of Cyclodextrin Polymers Controls Their Lead and Organic Micropollutant Adsorption. *Chem. Sci.* **2018**, *9* (47), 8883–8889.

(118) Wang, T.; Zhang, Y. F.; Hou, Q. Q.; Xu, W. R.; Cao, X. P.; Chow, H. F.; Kuck, D. C3-Symmetrical Tribenzotriquinacene Derivatives: Optical Resolution through Cryptophane Synthesis and Supramolecular Self-Assembly into Nanotubes. *J. Org. Chem.* **2013**, *78* (3), 1062–1069.

(119) Mastalerz, M.; Hähsler, M. A Giant [8+12] Boronic Ester Cage with 48 Terminal Alkene Units in The Periphery for Postsynthetic Alkene Metathesis. *Chem. – A Eur. J.* **2020**, *n/a* (n/a).

(120) Zhang, G.; Presly, O.; White, F.; Oppel, I. M.; Mastalerz, M. A Permanent

Mesoporous Organic Cage with an Exceptionally High Surface Area. *Angew. Chemie Int. Ed.* **2014**, *53* (6), 1516–1520.

(121) Samanta, J.; Natarajan, R. Cofacial Organic Click Cage to Intercalate Polycyclic Aromatic Hydrocarbons. *Org. Lett.* **2016**, *18* (14), 3394–3397.

(122) Buyukcakir, O.; Seo, Y.; Coskun, A. Thinking Outside the Cage: Controlling the Extrinsic Porosity and Gas Uptake Properties of Shape-Persistent Molecular Cages in Nanoporous Polymers. *Chem. Mater.* **2015**, *27* (11), 4149–4155.

(123) Gutsche, C. D. The Calixarenes. *Host Guest Complex Chem. / Macrocycles* **1985**, 375–421.

(124) Scott, M. P.; Sherburn, M. S. Resorcinarenes and Pyrogallolarenes. In *Comprehensive Supramolecular Chemistry II*; Atwood, J. L., Ed.; Elsevier: Oxford, 2017; pp 337–374.

(125) Vicens, J.; Asfari, M.-Z.; Harrowfield, J. *Calixarenes 50th Anniversary: Commemorative Issue*; Springer Science & Business Media, 1994.

(126) Ogoshi, T.; Kanai, S.; Fujinami, S.; Yamagishi, T. A.; Nakamoto, Y. Para-Bridged Symmetrical Pillar[5]Arenes: Their Lewis Acid Catalyzed Synthesis and Host-Guest Property. *J. Am. Chem. Soc.* **2008**, *130* (15), 5022–5023.

(127) Ogoshi, T.; Sueto, R.; Yoshikoshi, K.; Yamagishi, T. One-Dimensional Channels Constructed from per-Hydroxylated Pillar[6]Arene Molecules for Gas and Vapour Adsorption. *Chem. Commun.* **2014**, *50* (96), 15209–15211.

(128) Weinelt, F.; Schneider, H. J. Mechanisms of Macrocycle Genesis. The Condensation of Resorcinol with Aldehydes. *J. Org. Chem.* **1991**, *56* (19), 5527–

5535.

(129) Patil, R. S.; Zhang, C.; Atwood, J. L. Process Development for Separation of Conformers from Derivatives of Resorcin[4]Arenes and Pyrogallol[4]Arenes. *Chem. - A Eur. J.* **2016**, *22* (43), 15202–15207.

(130) The Selective Flotation of Cesium Ion with Resorcinol-Type Calix[4]Arenes with Alkyl Side Chains.Pdf.

(131) Chitry, F.; Pellet-Rostaing, S.; Nicod, L.; Gass, J. L.; Foos, J.; Guy, A.; Lemaire, M. Cesium/Sodium Separation by Nanofiltration-Complexation in Aqueous Medium. *Sep. Sci. Technol.* **2001**, *36* (5–6), 1053–1066.

(132) Zhang, Q.; Catti, L.; Tiefenbacher, K. Catalysis inside the Hexameric Resorcinarene Capsule. *Acc. Chem. Res.* **2018**, *51* (9), 2107–2114.

(133) Bianchini, G.; Sorella, G. La; Canever, N.; Scarso, A.; Strukul, G. Efficient Isonitrile Hydration through Encapsulation within a Hexameric Self-Assembled Capsule and Selective Inhibition by a Photo-Controllable Competitive Guest. *Chem. Commun.* **2013**, *49* (46), 5322–5324.

(134) La Manna, P.; Talotta, C.; Floresta, G.; De Rosa, M.; Soriente, A.; Rescifina, A.; Gaeta, C.; Neri, P. Mild Friedel–Crafts Reactions inside a Hexameric Resorcinarene Capsule: C−Cl Bond Activation through Hydrogen Bonding to Bridging Water Molecules. *Angew. Chemie - Int. Ed.* **2018**, *57* (19), 5423–5428.

(135) Giri, A.; Hussain, M. W.; Sk, B.; Patra, A. Connecting the Dots: Knitting c-Phenylresorcin[4]Arenes with Aromatic Linkers for Task-Specific Porous Organic Polymers. *Chem. Mater.* **2019**, *31* (20), 8440–8450.

(136) Lan, S.; Zhan, S.; Ding, J.; Ma, J.; Ma, D. Pillar[n]Arene-Based Porous Polymers for Rapid Pollutant Removal from Water. *J. Mater. Chem. A* **2017**, *5* (6), 2514–2518.

(137) Shetty, D.; Jahovic, I.; Raya, J.; Asfari, Z.; Olsen, J. C.; Trabolsi, A. Porous Polycalix[4]Arenes for Fast and Efficient Removal of Organic Micropollutants from Water. *ACS Appl. Mater. Interfaces* **2018**, *10* (3), 2976–2981.

(138) Su, K.; Wang, W.; Li, B.; Yuan, D. Azo-Bridged Calix[4]Resorcinarene-Based Porous Organic Frameworks with Highly Efficient Enrichment of Volatile Iodine. *ACS Sustain. Chem. Eng.* **2018**, *6* (12), 17402–17409.

(139) Skala, L. P.; Yang, A.; Klemes, M. J.; Xiao, L.; Dichtel, W. R. Resorcinarene Cavitand Polymers for the Remediation of Halomethanes and 1,4-Dioxane. *J. Am. Chem. Soc.* **2019**, *141* (34), 13315–13319.

(140) Talapaneni, S. N.; Kim, D.; Barin, G.; Buyukcakir, O.; Je, S. H.; Coskun, A. Pillar[5]Arene Based Conjugated Microporous Polymers for Propane/Methane Separation through Host-Guest Complexation. *Chem. Mater.* **2016**, *28* (12), 4460–4466.

(141) Shetty, D.; Jahovic, I.; Raya, J.; Ravaux, F.; Jouiad, M.; Olsen, J. C.; Trabolsi, A. An Ultra-Absorbent Alkyne-Rich Porous Covalent Polycalix[4]Arene for Water Purification. *J. Mater. Chem. A* **2017**, *5* (1), 62–66.

(142) Shetty, D.; Raya, J.; Han, D. S.; Asfari, Z.; Olsen, J. C.; Trabolsi, A. Lithiated Polycalix[4]Arenes for Efficient Adsorption of Iodine from Solution and Vapor Phases. *Chem. Mater.* **2017**, *29* (21), 8968–8972.

(143) Zhang, Z.; Li, L.; An, D.; Li, H.; Zhang, X. Triazine-Based Covalent Organic Polycalix[4]Arenes for Highly Efficient and Reversible Iodine Capture in Water. *J. Mater. Sci.* **2020**, *55* (4), 1854–1864.

(144) Abadast, F.; Mouradzadegun, A.; Ganjali, M. R. Rational Design, Fabrication and Characterization of a Thiol-Rich 3D-Porous Hypercrosslink Polymer as a New Engineered Hg2+ Sorbent: Enhanced Selectivity and Uptake. *New J. Chem.* **2017**, *41* (13), 5458–5466.

(145) Mouradzadegun, A.; Alsadat Mostafavi, M. Copper-Loaded Hypercrosslinked Polymer Decorated with Pendant Amine Groups: A Green and Retrievable Catalytic System for Quick [3 + 2] Huisgen Cycloaddition in Water. *RSC Adv.* **2016**, *6* (48), 42522–42531.

(146) Mouradzadegun, A.; Elahi, S.; Abadast, F. Synthesis of a 3D-Network Polymer Supported Bronsted Acid Ionic Liquid Based on Calix[4]Resorcinarene via Two Post-Functionalization Steps: A Highly Efficient and Recyclable Acid Catalyst for the Preparation of Symmetrical Bisamides. *RSC Adv.* **2014**, *4* (59), 31239–31248.

(147) Shetty, D.; Jahović, I.; Skorjanc, T.; Erkal, T. S.; Ali, L.; Raya, J.; Asfari, Z.; Olson, M. A.; Kirmizialtin, S.; Yazaydin, A. O.; Trabolsi, A. Rapid and Efficient Removal of Perfluorooctanoic Acid from Water with Fluorine-Rich Calixarene-Based Porous Polymers. *ACS Appl. Mater. Interfaces* **2020**.

(148) Tucker, J. A.; Knobler, C. B.; Trueblood, K. N.; Cram, D. J. Host-Guest Complexation. 49. Cavitands Containing Two Binding Cavities. *J. Am. Chem. Soc.* **1989**, *111* (10), 3688–3699.

(149) Xi, H.; Gibb, C. L. D.; Stevens, E. D.; Gibb, B. C. Deep-Cavity Cavitands: Synthesis and Solid State Structure of Host Molecules Possessing Large Bowl-Shaped Cavities. *Chem. Commun.* **1998**, No. 16, 1743–1744.

(150) Kane, C. M.; Ugono, O.; Barbour, L. J.; Holman, K. T. Many Simple Molecular Cavitands Are Intrinsically Porous (Zero-Dimensional Pore) Materials. *Chem. Mater.* **2015**, *27* (21), 7337–7354.

(151) Roman, E.; Peinador, C.; Mendoza, S.; Kaifer, A. E. Improved Synthesis of Cavitands. *J. Org. Chem.* **1999**, *64* (7), 2577–2578.

(152) Xi, H.; Gibb, C. L. D.; Gibb, B. C. Functionalized Deep-Cavity Cavitands. *J. Org. Chem.* **1999**, *64* (25), 9286–9288.

(153) Sherman, J. C.; Knobler, C. B.; Cram, D. J. Syntheses and Properties of Soluble Carceplexes. *J. Am. Chem. Soc.* **1991**, *113* (6), 2194–2204.

(154) Pellet-Rostaing, S.; Nicod, L.; Chitry, F.; Lemaire, M. Synthesis and Caesium Complexing Properties of Water-Soluble Cavitands. *Tetrahedron Lett.* **1999**, *40* (50), 8793–8796.

(155) Gaeta, C.; Della Sala, P.; Talotta, C.; De Rosa, M.; Soriente, A.; Brancatelli, G.; Geremia, S.; Neri, P. A Tetrasulfate-Resorcin[6]Arene Cavitand as the Host for Organic Ammonium Guests. *Org. Chem. Front.* **2016**, *3* (10), 1276–1280.

(156) Jiang, W.; Zhang, H.; Yang, J.; Liu, Y. Y.; Liu, H. Y.; Ma, J. F. Three Resorcin[4]Arene-Based Complexes with Cu(Ii)-Exchange Characteristics and Fluorescence Sensing of Polyoxometalates in Aqueous Solutions. *CrystEngComm* **2014**, *16* (41), 9638–9644.

(157) Pinalli, R.; Dalcanale, E. Supramolecular Sensing with Phosphonate Cavitands. *Acc. Chem. Res.* **2013**, *46* (2), 399–411.

(158) Tancini, F.; Gottschalk, T.; Bernd Schweizer, W.; Diederich, F.; Dalcanale, E. Ion-Pair Complexation with a Cavitand Receptor. *Chem. - A Eur. J.* **2010**, *16* (26), 7813–7819.

(159) Schmidt, C.; Thondorf, I.; Kolehmainen, E.; Böhmer, V.; Vogt, W.; Rissanen, K. One-Step Synthesis of Resorcarene Dimers Composed of Two Tetra-Benzoxazine Units. *Tetrahedron Lett.* **1998**, *39* (48), 8833–8836.

(160) Nguyen, T. V.; Yoshida, H.; Sherburn, M. S. Selective Binding and Release of Aspirin by an Encapsulating Receptor. *Chem. Commun.* **2010**, *46* (32), 5921–5923.

(161) Arnott, G.; Hunter, R. Enantioselective Addition of Diethylzinc to Benzaldehyde Catalysed by Chiral, Bridged Resorcinarenes: A Stereoselectivity Model Based on Chirality Transfer. *Tetrahedron* **2006**, *62* (5), 992–1000.

(162) Kodiah Beyeh, N.; Valkonen, A.; Rissanen, K. Piperazine Bridged Resorcinarene Cages. *Org. Lett.* **2010**, *12* (7), 1392–1395.

(163) Sun, J.; Warmuth, R. Rational Design of a Nanometre-Sized Covalent Octahedron. *Chem. Commun.* **2011**, *47* (33), 9351–9353.

(164) Mendoza, S.; Godínez, L. A.; Kaifer, A. E. Tetrathiafulvalene-Functionalized Cavitands as Building Blocks for Redox Active Hemicarcerands. *Supramol. Chem.* **2004**, *16* (3), 165–169.

(165) Morikawa, O.; Nakanishi, K.; Miyashiro, M.; Kobayashi, K.; Konishi, H.

Thiomethylation of Distal-Dibromoresorcinarene. Synthesis of Resorcinarenes with Two Different Resorcinol Units in Alternating Sequence and Thiacrown-Resorcinarenes. *Synthesis (Stuttg).* **2000**, No. 2, 233–236.

(166) Ro, S.; Rowan, S. J.; Pease, A. R.; Cram, D. J.; Stoddart, J. F. Dynamic Hemicarcerands and Hemicarceplexes. *Org. Lett.* **2000**, *2* (16), 2411–2414.

(167) Liu, X.; Warmuth, R. Solvent Effects in Thermodynamically Controlled Multicomponent Nanocage Syntheses. *J. Am. Chem. Soc.* **2006**, *128* (43), 14120–14127.

(168) Moran, J. R.; Karbach, S.; Cram, D. J. Cavitands: Synthetic Molecular Vessels. *J. Am. Chem. Soc.* **1982**, *104* (21), 5826–5828.

(169) Chapman, R. G.; Sherman, J. C. Templation in the Formation of Carceplexes. *J. Org. Chem.* **1998**, *63* (12), 4103–4110.

(170) Sun, J.; Bennett, J. L.; Emge, T. J.; Warmuth, R. Thermodynamically Controlled Synthesis of a Chiral Tetra-Cavitand Nanocapsule and Mechanism of Enantiomerization. *J. Am. Chem. Soc.* **2011**, *133* (10), 3268–3271.

(171) Warmuth, R.; Makowiec, S. The Phenylnitrene Rearrangement in the Inner Phase of a Hemicarcerand. *J. Am. Chem. Soc.* **2005**, *127* (4), 1084–1085.

(172) Patil, R. S.; Zhang, C.; Sikligar, K.; Baker, G. A.; Atwood, J. L. Formation of Water Channels in the Crystalline Hydrates of Macrocyclic Compounds. *Chem. - A Eur. J.* **2018**, *24* (13), 3299–3304.

(173) Darvish, F.; Khazraee, S. Molecular Iodine: An Efficient and Environment-Friendly Catalyst for the Synthesis of Calix[4]Resorcinarenes. *Comptes Rendus*

Chim. **2014**, *17* (9), 890–893.

(174) Moore, D.; Watson, G. W.; Gunnlaugsson, T.; Matthews, S. E. Selective Formation of the Rctt Chair Stereoisomers of Octa-O-Alkyl Resorcin[4]Arenes Using Brønsted Acid Catalysis. *New J. Chem.* **2008**, *32* (6), 994–1002.

(175) Crespy, D.; Bozonnet, M.; Meier, M. 100 Years of Bakelite, the Material of a 1000 Uses. *Angew. Chemie - Int. Ed.* **2008**, *47* (18), 3322–3328.

(176) Martín, C. F.; Plaza, M. G.; García, S.; Pis, J. J.; Rubiera, F.; Pevida, C. Microporous Phenol-Formaldehyde Resin-Based Adsorbents for Pre-Combustion CO2 Capture. *Fuel* **2011**, *90* (5), 2064–2072.

(177) Wang, Z.; Luo, Y.; Zhai, T. L.; Ma, H.; Chen, J. J.; Shu, Y.; Zhang, C. Porous Triphenylbenzene-Based Bicyclooxacalixarene Cage for Selective Adsorption of CO2/N2. *Org. Lett.* **2016**, *18* (18), 4574–4577.

(178) Li, S.; Prasetya, N.; Ladewig, B. P. Investigation of Azo-COP-2 as a Photoresponsive Low-Energy CO2 Adsorbent and Porous Filler in Mixed Matrix Membranes for CO2/N2 Separation. *Ind. Eng. Chem. Res.* **2019**, *58* (23), 9959–9969.

(179) Ding, M.; Jiang, H. L. One-Step Assembly of a Hierarchically Porous Phenolic Resin-Type Polymer with High Stability for CO2 Capture and Conversion. *Chem. Commun.* **2016**, *52* (83), 12294–12297.

(180) Yin, F.; Peng, P.; Mo, W.; Chen, S.; Xu, T. The Preparation of a Porous Melamine-Formaldehyde Adsorbent Grafted with Polyethyleneimine and Its CO2 Adsorption Behavior. *New J. Chem.* **2017**, *41* (13), 5297–5304.

(181) Parvazinia, M.; Garcia, S.; Maroto-Valer, M. CO2 Capture by Ion Exchange Resins as Amine Functionalised Adsorbents. *Chem. Eng. J.* **2018**, *331* (August 2017), 335–342.

(182) Lu, W.; Bosch, M.; Yuan, D.; Zhou, H. C. Cost-Effective Synthesis of Amine-Tethered Porous Materials for Carbon Capture. *ChemSusChem* **2015**, *8* (3), 433–438.

(183) Rozyyev, V.; Thirion, D.; Ullah, R.; Lee, J.; Jung, M.; Oh, H.; Atilhan, M.; Yavuz, C. T. High-Capacity Methane Storage in Flexible Alkane-Linked Porous Aromatic Network Polymers. *Nat. Energy* **2019**, *4* (7), 604–611.

(184) Wood, C. D.; Tan, B.; Trewin, A.; Su, F.; Rosseinsky, M. J.; Bradshaw, D.; Sun, Y.; Zhou, L.; Cooper, A. I. Microporous Organic Polymers for Methane Storage. *Adv. Mater.* **2008**, *20* (10), 1916–1921.

(185) Ahmed, D. S.; El-Hiti, G. A.; Yousif, E.; Ali, A. A.; Hameed, A. S. Design and Synthesis of Porous Polymeric Materials and Their Applications in Gas Capture and Storage: A Review. *J. Polym. Res.* **2018**, *25* (3).

(186) Wang, Y.; Xie, Y.; Zhang, Y.; Tang, S.; Guo, C.; Wu, J.; Lau, R. Anionic and Cationic Dyes Adsorption on Porous Poly-Melamine-Formaldehyde Polymer. *Chem. Eng. Res. Des.* **2016**, *114*, 258–267.

(187) Yin, F.; Xu, T.; Wang, S.; Chen, S. Simple Synthesis of Porous Melamine-Formaldehyde Resins by Low Temperature Solvothermal Method and Its CO2 Adsorption Properties. *Express Polym. Lett.* **2017**, *11* (11), 873–884.

(188) Li, Q.; Liu, J. J.; Sun, X.; Xu, L. Hierarchically Porous Melamine-Formaldehyde

Resin Microspheres for the Removal of Nanoparticles and Simultaneously As the Nanoparticle Immobilized Carrier for Catalysis. *ACS Sustain. Chem. Eng.* **2019**, *7* (1), 867–876.

(189) Egorin, A.; Tokar, E.; Palamarchuk, M.; Portnyagin, A.; Tutov, M.; Mis'Ko, D.; Kalashnikova, A.; Sokolnitskaya, T.; Tananaev, I. Synthesis of Porous Resorcinol-Formaldehyde Resins and Study of the Their Sorption Characteristics toward Cs in Highly Mineralized Alkaline Media. *Radiochim. Acta* **2019**, *107* (12), 1145–1153.

(190) Dorfner, K. Ion Exchangers. *Ion Exchangers*. Walter de Gruyter 2011, pp 1–6.

(191) Alesi, W. R.; Kitchin, J. R. Evaluation of a Primary Amine-Functionalized Ion-Exchange Resin for CO 2 Capture. *Ind. Eng. Chem. Res.* **2012**, *51* (19), 6907–6915.

(192) Liu, S.; Zhou, C.; Yu, W. Phase Separation and Structure Control in Ultra-High Molecular Weight Polyethylene Microporous Membrane. *J. Memb. Sci.* **2011**, *379* (1–2), 268–278.

(193) Wang, J.; Xu, S.; Wang, Y.; Cai, R.; Lv, C.; Qiao, W.; Long, D.; Ling, L. Controllable Synthesis of Hierarchical Mesoporous/Microporous Nitrogen-Rich Polymer Networks for CO2 and Cr(vi) Ion Adsorption. *RSC Adv.* **2014**, *4* (31), 16224–16232.

(194) Dorin, R. M.; Sai, H.; Wiesner, U. Hierarchically Porous Materials from Block Copolymers. *Chem. Mater.* **2014**, *26* (1), 339–347.

(195) Yang, X. Y.; Chen, L. H.; Li, Y.; Rooke, J. C.; Sanchez, C.; Su, B. L.

Hierarchically Porous Materials: Synthesis Strategies and Structure Design. *Chem. Soc. Rev.* **2017**, *46* (2), 481–558.

(196) Li, M.; Ren, H.; Sun, F.; Tian, Y.; Zhu, Y.; Li, J.; Mu, X.; Xu, J.; Deng, F.; Zhu, G. Construction of Porous Aromatic Frameworks with Exceptional Porosity via Building Unit Engineering. *Adv. Mater.* **2018**, *30* (43), 1804169.

(197) Yu, T.; Xue, Z.; Zhao, X.; Chen, W.; Mu, T. Green Synthesis of Porous β-Cyclodextrin Polymers for Rapid and Efficient Removal of Organic Pollutants and Heavy Metal Ions from Water. *New J. Chem.* **2018**, *42* (19), 16154–16161.

(198) Ling, Y.; Klemes, M. J.; Xiao, L.; Alsbaiee, A.; Dichtel, W. R.; Helbling, D. E. Benchmarking Micropollutant Removal by Activated Carbon and Porous β-Cyclodextrin Polymers under Environmentally Relevant Scenarios. *Environ. Sci. Technol.* **2017**, *51* (13), 7590–7598.

(199) Gutsche, C. D.; Gutsche, C. D. *Calixarenes : An Introduction. 2nd Ed. C. David Gutsche*; Cambridge : RSC Publishing, [2008]2nd ed., 2008.

(200) Delangle, P.; Dutasta, J. P. Tetraphosphonate-Calix[4]Resorcinarene. A Powerful Host for Alkali Metal and Ammonium Cations Encapsulation. *Tetrahedron Lett.* **1995**, *36* (51), 9325–9328.

(201) Lo Meo, P.; Lazzara, G.; Liotta, L.; Riela, S.; Noto, R. Cyclodextrin-Calixarene Co-Polymers as a New Class of Nanosponges. *Polym. Chem.* **2014**, *5* (15), 4499–4510.

(202) Bell, A. A. 4-hydroxybenzaldehyde and vanillin as toxins formed in leaf wound sap of Phaseolus lunatus. *Phytopathology* **1970**, *60* (1), 161–165.

(203) Far, H. M.; Donthula, S.; Taghvaee, T.; Saeed, A. M.; Garr, Z.; Sotiriou-Leventis, C.; Leventis, N. Air-Oxidation of Phenolic Resin Aerogels: Backbone Reorganization, Formation of Ring-Fused Pyrylium Cations, and the Effect on Microporous Carbons with Enhanced Surface Areas. *RSC Adv.* **2017**, *7* (81), 51104–51120.

(204) Naebe, M.; Wang, J.; Amini, A.; Khayyam, H.; Hameed, N.; Li, L. H.; Chen, Y.; Fox, B. Mechanical Property and Structure of Covalent Functionalised Graphene/Epoxy Nanocomposites. *Sci. Rep.* **2014**, *4*, 1–7.

(205) Emiru, T. F.; Ayele, D. W. Controlled Synthesis, Characterization and Reduction of Graphene Oxide: A Convenient Method for Large Scale Production. *Egypt. J. Basic Appl. Sci.* **2017**, *4* (1), 74–79.

(206) Dékány, I.; Szabó, T.; Berkesi, O.; Forgó, P.; Josepovits, K.; Sanakis, Y.; Petridis, D. Evolution of Surface Functional Groups in a Series of Progressively Oxidized Graphite Oxides. *Chem. Mater.* **2006**, *18* (11), 2740–2749.

(207) Khan, M. B.; Parvaz, M.; Khan, Z. H. Graphene Oxide: Synthesis and Characterization. In *Advanced Structured Materials*; Khan, Z. H., Ed.; Springer Singapore: Singapore, 2017; Vol. 83, pp 1–28.

(208) Cai, W.; Piner, R. D.; Stadermann, F. J.; Park, S.; Shaibat, M. A.; Ishii, Y.; Yang, D.; Velamakanni, A.; Sung, J. A.; Stoller, M.; An, J.; Chen, D.; Ruoff, R. S. Synthesis and Solid-State NMR Structural Characterization of 13C-Labeled Graphite Oxide. *Science* **2008**, *321* (5897), 1815–1817.

(209) Jose, T.; Cañellas, S.; Pericàs, M. A.; Kleij, A. W. Polystyrene-Supported

Bifunctional Resorcinarenes as Cheap, Metal-Free and Recyclable Catalysts for Epoxide/CO2 Coupling Reactions. *Green Chem.* **2017**, *19* (22), 5488–5493.

(210) Russo, M.; LoMeo, P. Binding Abilities of a Chiral Calix[4]Resorcinarene: A Polarimetric Investigation on a Complex Case of Study. *Beilstein J. Org. Chem.* **2017**, *13*, 2698–2709.

(211) Mendez-Arroyo, J.; d'Aquino, A. I.; Chinen, A. B.; Manraj, Y. D.; Mirkin, C. A. Reversible and Selective Encapsulation of Dextromethorphan and β-Estradiol Using an Asymmetric Molecular Capsule Assembled via the Weak-Link Approach. *J. Am. Chem. Soc.* **2017**, *139* (4), 1368–1371.

(212) Koide, Y.; Oka, T.; Imamura, A.; Shosenji, H.; Yamada, K. Studies of Collectors. XIII. The Selective Flotation of Cesium Ion with Resorcinol-Type Calix[4]Arenes with Alkyl Side Chains. *Bull. Chem. Soc. Jpn.* **1993**, *66* (8), 2137–2142.

(213) Aoyama, Y.; Tanaka, Y.; Sugahara, S. Molecular Recognition. 5.1 Molecular Recognition of Sugars via Hydrogen-Bonding Interaction with a Synthetic Polyhydroxy Macrocycle2. *J. Am. Chem. Soc.* **1989**, *111* (14), 5397–5404.

(214) Kass, J. P.; Slasor, L. A.; Zambrano, C. H.; Dueno, E. E. IMPROVED SYNTHESIS AND PURIFICATION OF CAVITANDS. *Org. Prep. Proced. Int.* **2006**, *38* (5), 480–483.

(215) Nishimura, N.; Kobayashi, K. Self-Assembled Boronic Ester Cavitand Capsule as a Photosensitizer and a Guard Nanocontainer against Photochemical Reactions of 2,6-Diacetoxyanthracene. *J. Org. Chem.* **2010**, *75* (18), 6079–6085.

(216) Morikawa, O.; Nagamatsu, Y.; Nishimura, A.; Kobayashi, K.; Konishi, H.

Scandium Triflate-Catalyzed Cyclocondensation of 1,3-Dialkoxybenzenes with 1,3,5-Trioxane. Formation of Resorcin[4]Arenes and Confused Resorcin[4]Arenes. *Tetrahedron Lett.* **2006**, *47* (24), 3991–3994.

(217) Della Sala, P.; Gaeta, C.; Navarra, W.; Talotta, C.; De Rosa, M.; Brancatelli, G.; Geremia, S.; Capitelli, F.; Neri, P. Improved Synthesis of Larger Resorcinarenes. *J. Org. Chem.* **2016**, *81* (13), 5726–5731.

(218) Csók, Z.; Kégl, T.; Párkányi, L.; Varga, Á.; Kunsági-Máté, S.; Kollár, L. Facile, High-Yielding Synthesis of Deepened Cavitands: A Synthetic and Theoretical Study. *Supramol. Chem.* **2011**, *23* (10), 710–719.

(219) Cram, D. J.; Choi, H. J.; Bryant, J. A.; Knobler, C. B. Solvophobic and Entropic Driving Forces for Forming Velcraplexes, Which Are Four-Fold, Lock-Key Dimers in Organic Media. *J. Am. Chem. Soc.* **1992**, *114* (20), 7748–7765.

(220) Cram, D. J.; Tunstad, L. M.; Knobler, C. B. C- and Z-Shaped Ditopic Cavitands, Their Binding Characteristics, and Monotopic Relatives. *J. Org. Chem.* **1992**, *57* (2), 528–535.

(221) Purse, B. W.; Gissot, A.; Rebek, J. A Deep Cavitand Provides a Structured Environment for the Menschutkin Reaction. *J. Am. Chem. Soc.* **2005**, *127* (32), 11222–11223.

(222) Menozzi, E.; Onagi, H.; Rheingold, A. L.; Rebek Jr., J. Extended Cavitands of Nanoscale Dimensions. *European J. Org. Chem.* **2005**, *2005* (17), 3633–3636.

(223) Hassan, N. M.; Marra, J. C.; Adu-Wusu, K.; Marra, J. C. Resorcinol - Formaldehyde Adsorption of Cesium from Hanford Waste Solutions, Part I. Batch

Equilibrium Study. *J. Radioanal. Nucl. Chem.* **2004**, *262* (3), 579–586.

(224) Samanta, S. K.; Ramaswamy, M.; Misra, B. M. Studies on Cesium Uptake by Phenolic Resins. *Sep. Sci. Technol.* **1992**, *27* (2), 255–267.

(225) Pellet-Rostaing, S.; Nicod, L.; Chitry, F.; Lemaire, M. Synthesis and Caesium Complexing Properties of Water-Soluble Cavitands. *Tetrahedron Lett.* **1999**, *40* (50), 8793–8796.

(226) Hasell, T.; Cooper, A. I. Porous Organic Cages: Soluble, Modular and Molecular Pores. *Nat. Rev. Mater.* **2016**, *1* (9), 16053.

(227) Zhu, Q.; Wang, X.; Clowes, R.; Cui, P.; Chen, L.; Little, M. A.; Cooper, A. I. 3D Cage COFs: A Dynamic Three-Dimensional Covalent Organic Framework with High-Connectivity Organic Cage Nodes. *J. Am. Chem. Soc.* **2020**, *142* (39), 16842–16848.

(228) Ma, J. X.; Li, J.; Chen, Y. F.; Ning, R.; Ao, Y. F.; Liu, J. M.; Sun, J.; Wang, D. X.; Wang, Q. Q. Cage Based Crystalline Covalent Organic Frameworks. *J. Am. Chem. Soc.* **2019**, *141* (9), 3843–3848.

(229) Audouin, F.; Birot, M.; Pasquinet, É.; Deleuze, H.; Besnard, O.; Poullain, D. Synthesis of Porous Materials by 2-Nitroresorcinol/Cyanuric Chloride Thermal Polycondensation in Emulsions. *J. Appl. Polym. Sci.* **2008**, *108* (5), 2808–2813.

(230) Zhao, Q.; Liu, Y. Macrocycle Crosslinked Mesoporous Polymers for Ultrafast Separation of Organic Dyes. *Chem. Commun.* **2018**, *54* (53), 7362–7365.

(231) Zhai, Z.; Jiang, C.; Zhao, N.; Dong, W.; Li, P.; Sun, H.; Niu, Q. J. Polyarylate Membrane Constructed from Porous Organic Cage for High-Performance Organic

Solvent Nanofiltration. *J. Memb. Sci.* **2020**, *595* (September 2019), 117505.

(232) Xiong, S.; Tao, J.; Wang, Y.; Tang, J.; Liu, C.; Liu, Q.; Wang, Y.; Yu, G.; Pan, C. Uniform Poly(Phosphazene-Triazine) Porous Microspheres for Highly Efficient Iodine Removal. *Chem. Commun.* **2018**, *54* (61), 8450–8453.

(233) Zhang, M.; Li, Y.; Bai, C.; Guo, X.; Han, J.; Hu, S.; Jiang, H.; Tan, W.; Li, S.; Ma, L. Synthesis of Microporous Covalent Phosphazene-Based Frameworks for Selective Separation of Uranium in Highly Acidic Media Based on Size-Matching Effect. *ACS Appl. Mater. Interfaces* **2018**, *10* (34), 28936–28947.

(234) Liu, X.; Warmuth, R. Solvent Effects in Thermodynamically Controlled Multicomponent Nanocage Syntheses. *J. Am. Chem. Soc.* **2006**, *128* (43), 14120–14127.